Size dependent mechanical behavior of Zr-Ni thin metallic glass films

Matteo Ghidelli

UNIVERSITÉ GRENOBLE ALPES

THÈSE

Pour obtenir le grade de

DOCTEUR DE L'UNIVERSITÉ DE GRENOBLE ALPES

Spécialité : **Matériaux, Mécanique, Génie Civil, Electrochimie**
Arrêté ministériel : 7 août 2006

Et de

DOCTEUR DE L'UNIVERSITÉ CATHOLIQUE DE LOUVAIN

Spécialité : **Science de l'ingénieur**

Présentée par
Matteo GHIDELLI

Thèse dirigée par **Jean-Jacques BLANDIN** et **Jean-Pierre RASKIN**
codirigée par **Sébastien GRAVIER** et **Thomas PARDOEN**

préparée au sein du **laboratoire SIMaP** dans **l'école doctorale I-MEP2** et des laboratoires **IMAP** et **ICTEAM** de l'**Université catholique de Louvain**

Effets d'échelle sur le comportement mécanique de films minces en verres métalliques Zr-Ni

UCL
Université catholique de Louvain

Thèse soutenue publiquement le **26 mai 2015**,
devant le jury composé de :

M. Lindsay GREER (*Rapporteur*)
Professeur, Cambridge University, Royaume-Uni

M. David EMBURY (*Rapporteur*)
Professeur émérite, McMaster University, Canada

M. Yannick CHAMPION (*Président, Examinateur*)
Directeur de recherche CNRS, Université de Paris Est, France

M. Pascal JACQUES (*Examinateur*)
Professeur, Université catholique de Louvain, Belgique

M. Jean-Jacques BLANDIN (*Directeur de thèse*)
Directeur de recherche CNRS – Grenoble INP, France

M. Jean-Pierre RASKIN (*Co-Directeur de thèse*)
Professeur, Université catholique de Louvain, Belgique

M. Thomas PARDOEN (*Invité*)
Professeur, Université catholique de Louvain, Belgique

M. Sébastien GRAVIER (*Invité*)
Maître des conférence, Université Joseph Fourier, Grenoble, France

Université catholique de Louvain

Institute of Mechanics, Materials and Civil Engineering

Institute of Information and Communication Technologies, Electronics and Applied Mathematics

Size dependent mechanical behavior of Zr-Ni thin metallic glass films

Matteo GHIDELLI

Composition du jury:

Prof. Lindsay GREER	Cambridge University, United Kingdom
Prof. David EMBURY	McMaster University, Canada
Prof. Yannick CHAMPION (Président)	Université de Paris Est, France
Prof. Pascal JACQUES	Université catholique de Louvain, Belgium
Prof. Jean-Jacques BLANDIN (Promoteur)	Grenoble INP, France
Prof. Jean-Pierre RASKIN (Promoteur)	Université catholique de Louvain, Belgium
Prof. Thomas PARDOEN	Université catholique de Louvain, Belgium
Dr. Sébastien GRAVIER	Université Joseph Fourier, Grenoble, France

Private defense, Université catholique de Louvain, March 11 2015

Public defense, Grenoble INP, May 26 2015

Preamble

This PhD has been performed within the framework of the **International Doctoral School in Functional Materials** (IDS-FunMat) funded by an **ERASMUS MUNDUS** grant awarded by the **European Commission**.

The IDS-FunMat PhD projects are carried out in co-supervision between universities from two different countries. An industry partner is involved as well. The PhD candidates must spend at least 6 months in each university. Moreover, they are required to attend 3 annual training schools developing scientific, transferable, and interdisciplinary skills.

In the present PhD project, the two partner universities were the Grenoble INP (France) and the Université catholique de Louvain (UCL, Belgium). Specifically, I spent 13 months at the Grenoble INP and 28 months at the UCL. AGC Glass Europe was the official industry partner.

The original title of ERASMUS MUNDUS joint PhD project was "*New generation of micro and nano systems using metallic glass thin films"* (2011-12-EM).

Acknowledgments

I'm grateful to my supervisors Prof. Jean-Jacques Blandin and Dr. Sébastien Gravier (Grenoble INP) and Profs. Jean-Pierre Raskin and Thomas Pardoen (UCL) to have introduced me in the field of metallic glasses and mechanical properties of nano-scale materials.

Thank you for your guidance and to have provided continuous support during this PhD. Moreover, I really appreciated the number of experiences (academic exchanges, conferences, and professional travels) which are fundamental to improve my skills and to develop my career.

I want to acknowledge the European Commission which financed the PhD with an ERASMUS MUNDUS grant within the framework of the International Doctoral School in Functional Materials (IDS-FunMat).

I would like also to express my gratitude to the members of the examining jury which were present to both private and public defense. Throughout very interesting questions and detailed comments, they provide new insights to understand the physics of the observed phenomena.

I'm really indebted with a huge number of people (professors, technicians, post-docs, PhD students) which I've met in this more-than-three-year PhD which help me to carry out experiments and to discuss results. The list of this people would be too long to be reported in this short acknowledgment. Thank you also for the patience when teaching me how to use a machine or how to analyze data. Without your precious help this work could not have been completed.

I'm grateful also to many of friends that I met both at SIMaP/GPM2 (Grenoble INP) and at IMAP (UCL). Again, I could write a very long list which overcome the aim of this concise acknowledgment. Thank you to warmly introduce me in the lab as well as to shear personal experiences and support me during this PhD.

I have to thank my mother and my father for their love, patience, and for having encouraged me every day. Thank you for the company when I felt alone and to have helped me to sustain the weight of the stress of my work when it became too heavy. Thank you to my brothers to their constant presence. Thank you to all my relatives for their love they demonstrate to me every time I came back in my country.

Lastly, I thank my girlfriend for her constant support during this long experience, for her patience and – above all – for having shared the weight of the distance.

Résumé étendu en français

Etat de l'art et objectifs de la thèse

Ces 50 à 60 dernières années, il y a eu un très fort développement technologique caractérisé par la recherche de nouveaux matériaux ayant des performances très élevés en termes de propriétés mécaniques, de légèreté ou de tenue à des milieux extrêmes (température, corrosion…) notamment.

La plupart des études sur les alliages métalliques ont mis l'accent sur l'amélioration des propriétés et des performances des matériaux caractérisés par une structure cristalline dont les atomes sont disposés de manière périodique pour former un réseau 3D étendu. Cependant, en 1960, les chercheurs ont réussi à synthétiser le premier verre métallique (ou alliage métallique amorphe) par solidification rapide du liquide (section 1.1). Le principe est d'empêcher les atomes de s'organiser et d'obtenir une structure atomique hors équilibre qui n'est pas ordonnée à longue distance et qui ressemble celle de la phase liquide d'origine.

Les progrès technologiques couplés avec la compréhension de la physique de l'état vitreux ont conduit au développement de verres métalliques massifs (bulk metallic glasses, BMGs) permettant ainsi l'étude de leurs propriétés mécaniques. Les BMGs sont caractérisés par une limite élastique élevée (jusqu'à 5000 MPa pour certains BMGs à base de Co), par une grande déformation élastique (~ 2%) mais également par une grande ténacité (50 MPa $m^{1/2}$ pour de BMGs à base Zr) (section 1.5). Bien que ces propriétés puissent être très différentes selon l'alliage amorphe sélectionnée, leur origine est liée avec la structure atomique désordonnée qui ne présente pas les défauts existants dans les matériaux cristallins, notamment les dislocations, les joints grains ou l'existence de phases différentes. Cependant, le principal inconvénient des BMGs est lié à leur manque de déformation plastique macroscopique étant donné que la déformation plastique se localise sous la forme de bandes de cisaillement (shear bands), ce qui limite leurs applications potentielles (section 1.5).

Pour faire face à cet inconvénient les scientifiques ont commencé à explorer les effets d'échelle (size effects) sur le comportement mécanique qui est un domaine scientifique récent visant à comprendre comment les propriétés (mécaniques) varient lorsque l'échelle caractéristique de l'échantillon diminue en dessous du micromètre. Les essais de compression sur des micropiliers en verres métalliques ont fait l'objet du plus grand nombre d'études dans la littérature (section 1.6). Avec cette méthode, Volkert *et al.* [102] ont étudié les effets d'échelle pour des verres métallique de composition $Pd_{77}Si_{23}$. La Figure 1 montre le résultat d'essai de compression pour des piliers avec des diamètres différents allant de 3.61 μm (Figure 1a) jusqu'à 140 nm (Figure 1d). On observe ainsi une transition dans le mode de déformation qui est hétérogène avec des bandes de cisaillement pour les grands diamètres alors que les micropiliers avec un petit diamètre semblent se déformer en manière homogène.

Tian *et al.* [114] ont analysé le comportement mécanique de films minces en verre métallique (thin film metallic glasses, TFMGs) de composition $Cu_{49}Zr_{51}$ (Figure 2). Les essais ont été conduits en traction *in-situ* au MET (Microscope Electronique en Transmission) avec des échantillons en forme de dogbone (encart dans la Figure 2a). La Figure 2a montre la courbe contrainte-déformation pour un échantillon de 220 nm d'épaisseur. On peut noter que la déformation à rupture est de 5% avec une contrainte qui atteint 3.5 GPa. Ces valeurs sont beaucoup plus élevées que les valeurs des verres métalliques massifs de même composition, par ailleurs, la contrainte à rupture est proche de la limite théorique de décohésion atomique (Figure 2b).

Ces résultats expérimentaux sont confirmés par des simulations de dynamique moléculaires indiquant une probabilité réduite de nucléation et propagation des bandes de cisaillement pour des échantillons de l'ordre de 100 nm (section 1.6). La réduction d'échelle semble pouvoir influencer la capacité de percolation des défauts activés lors de la déformation plastique. En effet, dans un verre métallique, la formation d'une bande de cisaillement est liée à l'activation des zone de cisaillement (ou shear transformation zones, STZs) qui sont des groupes d'atomes qui soumis à une contrainte de cisaillement se déforment d'autant plus facilement que la densité de volume libre est importante. La percolation des STZs est à l'origine de la formation de bandes de cisaillement une fois qu'ils atteignent une longueur caractéristique ($\sim$ 100 nm) se propagent rapidement en produisant une rupture fragile (sections 1.5 et 1.6).

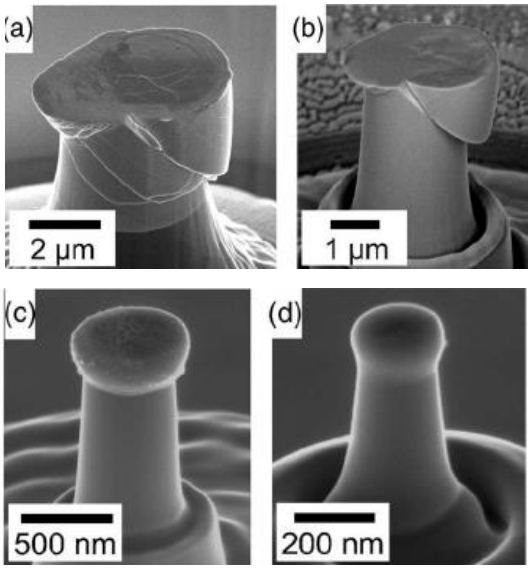

***Figure 1** – Images MEB de micropiliers de diamètres (a) 3.61 μm, (b) 1.84 μm, (c) 440 nm, and (d) 140 nm déformés avec un nanoindenteur. Le mécanisme de déformation passe d'une déformation hétérogène avec bandes de cisaillement à un mécanisme qui semble homogène [102].*

Cependant, il y a plusieurs défis lorsqu'on étudie les propriétés mécaniques de petits échantillons qui sont notamment liés à leur production et à leur manipulation nécessaire à l'extraction des propriétés mécaniques. Les résultats provenant de la compression de micropiliers peuvent être influencés par un mauvais alignement entre la pointe et l'échantillon ou par la forme conique du pilier, alors que l'usinage FIB peut fortement endommager la surface et ainsi affecter les propriétés mécaniques. Bien sûr, ces effets deviennent de plus en plus importants lorsqu'on réduit la taille de l'échantillon. Par conséquent, bien qu'il y ait des preuves concernant l'amélioration du comportement mécanique pour un verre métallique si sa taille caractéristique est en-dessous du micromètre, il reste une certaine confusion dans la littérature liée à l'évolution des propriétés mécaniques et des modes de

déformation avec des résultats contrastés voir contradictoires obtenus par différents auteurs (section 1.6).

Une autre question non résolue touche à l'origine de ces effets d'échelle et à l'existence d'une taille critique en-dessous de laquelle ces effets sont activés (section 1.6). La première question implique la compréhension de la structure atomique du verre métallique et s'il y a des modifications avec la taille (effets d'échelle *intrinsèques*). A l'inverse, les effets d'échelle peuvent avoir une origine *extrinsèque*, c'est-à-dire que les propriétés mécaniques sont influencées par la dimension réduite de l'échantillon et sa géométrie, mais sans changement de la structure atomique.

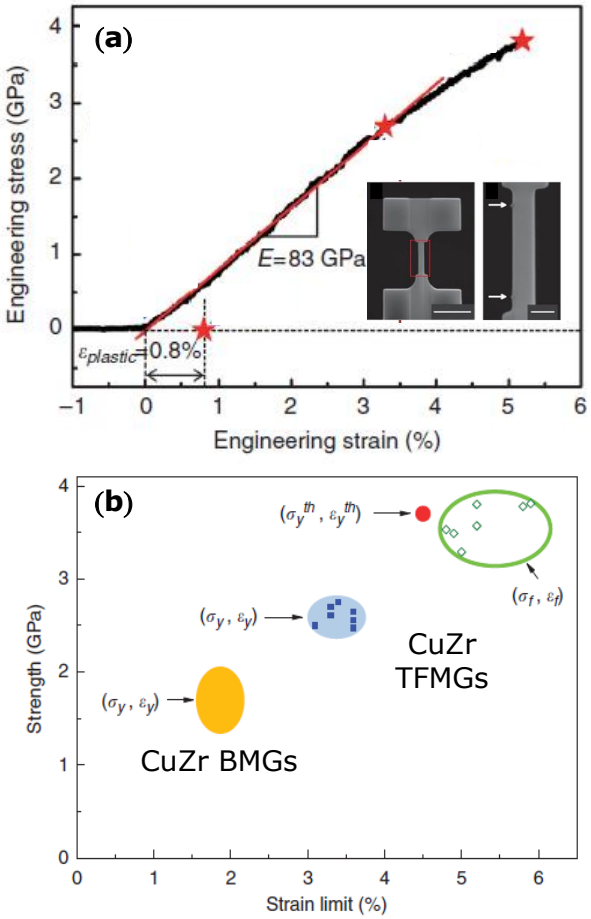

***Figure 2** – (a) Courbe contrainte-déformation pour un échantillon de 220 nm d'épaisseur. (b) Contrainte et déformation pour des Cu-Zr BMGs et pour des films minces (TFMGs). Adapté de [114].*

Dans ce contexte, on peut définir les objectifs de cette thèse visant à étudier les propriétés mécaniques des verres métalliques en film mince (TFMGs). Les films minces de ZrNi ont été déposés par pulvérisation cathodique (section 2.3), puis une analyse complète des propriétés mécaniques a été réalisée en étudiant l'élasticité, les propriétés (visco)plastiques ainsi que le comportement à la rupture.

Plusieurs techniques ont été utilisées aussi (sections 2.4-2.9). Plus précisément, le comportement mécanique des TFMGs a été étudié à la fois sur substrat Si et sur des films libres. Dans le premier cas, on a utilisé la spectroscopie Brillouin de surface (surface Brillouin spectroscopy, SBS) et l'acoustique picoseconde (picosecond ultrasonics, PU) pour obtenir les propriétés élastiques, tandis que le comportement viscoplastique a été étudié par nanoindentation. Le comportement à la rupture a été étudiée par nanoscratch et en analysant l'effet de la propagation d'une fissure activée par une

rayure sur le substrat de Si. Dans le deuxième cas, les propriétés mécaniques des films libres ont été étudiées en utilisant notamment une technique originale de micro-traction actionnée par contrainte interne. Avec cette technique on évite l'usinage FIB, tout en permettant d'extraire avec précision la courbe contrainte-déformation pour différentes géométries de micro-éprouvettes.

En parallèle à cette campagne expérimentale, on a analysé l'effet de la composition sur la structure atomique et sur le comportement mécanique, un sujet sur lequel il n'y a pas de nombreuses études scientifiques. Parmi les techniques employées on a utilisé la diffraction des rayons X (DRX), la microscopie électronique en transmission (MET), la réflectivité des rayons X (XRR), la spectroscopie Brillouin de surface (SBS), l'acoustique picoseconde (PU) ainsi que l'analyse de la résistivité électrique à la température ambiante ou pendant les traitements thermiques.

Dans cette thèse, les effets d'échelle ont été étudiés pour la composition $Zr_{65}Ni_{35}$ (% at.) avec une gamme d'épaisseurs entre 200 et 900 nm, alors que l'effet de la composition a été analysé pour quatre compositions différents : $Zr_{42}Ni_{58}$, $Zr_{65}Ni_{35}$, $Zr_{75}Ni_{25}$, et $Zr_{85}Ni_{15}$ (% at.) avec une épaisseur fixée de 800 nm (Chapitres III-IV).

Déposition et propriétés structurelles de films minces en verre métallique $Zr_{65}Ni_{35}$

Les films minces en verres métalliques (TFMGs) avec composition ZrNi ont été déposés par pulvérisation cathodique (Alliance Concept AC450) dans une salle blanche (classe 1,000) pour limiter la contamination des échantillons (section 2.3). Le bâti de dépôt se trouve au sein de la Plateforme Technologique Amont (PTA) sur le site du Centre Energie Atomique (CEA) de Grenoble.

Sans entrer dans les détails de la physique de la pulvérisation, une vue naïf du procédé de pulvérisation consiste en un plasma – dans notre cas Ar^+– qui bombarde une cible en raison de la présence d'un potentiel appliqué qui accélère les ions Ar^+ (Figure 3a). Le résultat est l'érosion de la cible avec la formation d'un film mince sur le substrat (Figure 3a).

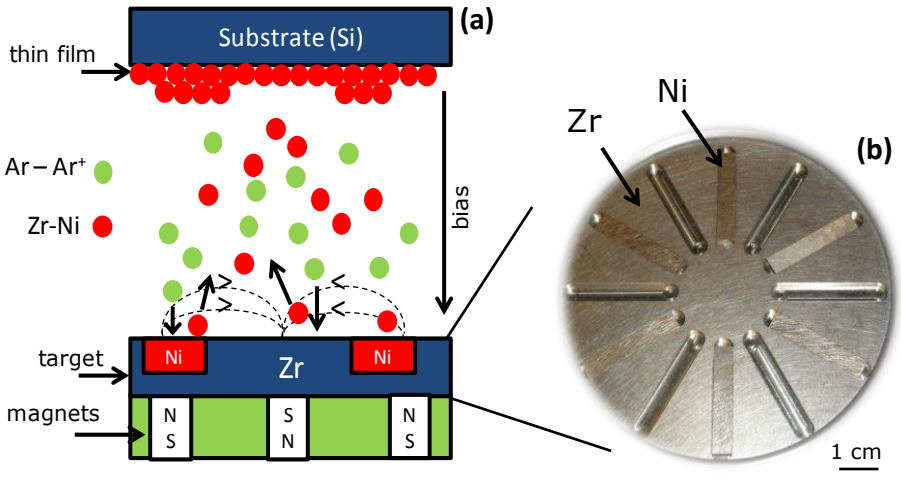

Figure 3 *– (a) Schématique d'une machine de pulvérisation cathodique. (b) La cible utilisée avec six tranches de Ni insérées dans la matrice de Zr.*

La cible qu'on a conçu est constituée par tranches rectangulaires Ni insérées dans une matrice Zr (Figure 3b). Ce design permet de changer facilement la composition du film en ajoutant ou enlevant

les tranches de Ni (section 2.3). Lorsqu'on ajoute 6 tranches de Ni dans la cible on obtient une composition du film $Zr_{65}Ni_{65}$ (Figure 3b). La composition $Zr_{65}Ni_{35}$, mesurée avec plusieurs techniques dont la microsonde du casting (electron probe micro analysis, EPMA), est constante sur le substrat. L'épaisseur du film a été mesurée avec le profilomètre et en regardant la section du film après rupture dans le microscope électronique à balayage (MEB). Les effets d'échelle ont été étudiés pour une gamme d'épaisseurs allant de 900 à 200 nm.

Les spectres DRX pour des TFMGs $Zr_{65}Ni_{35}$ sont rapportés dans la Figure 4a pour différentes épaisseurs (section 3.1). Les échantillons présentent une structure amorphe comme indiqué par la présence des deux bosses, respectivement autour de 36.7° et 65°. Ceci est confirmé par la microdiffraction dans le MET fait pour un échantillon de 900 nm d'épaisseur (encart de la figure 4a). La position de la première bosse de diffraction (Q_p) et sa largeur à demi-hauteur (full width at half maximum, FWHM) ne varie pas avec l'épaisseur avec des valeurs égales à 36.7° et 5.5°. **Cela indique que les échantillons ont la même structure atomique.**

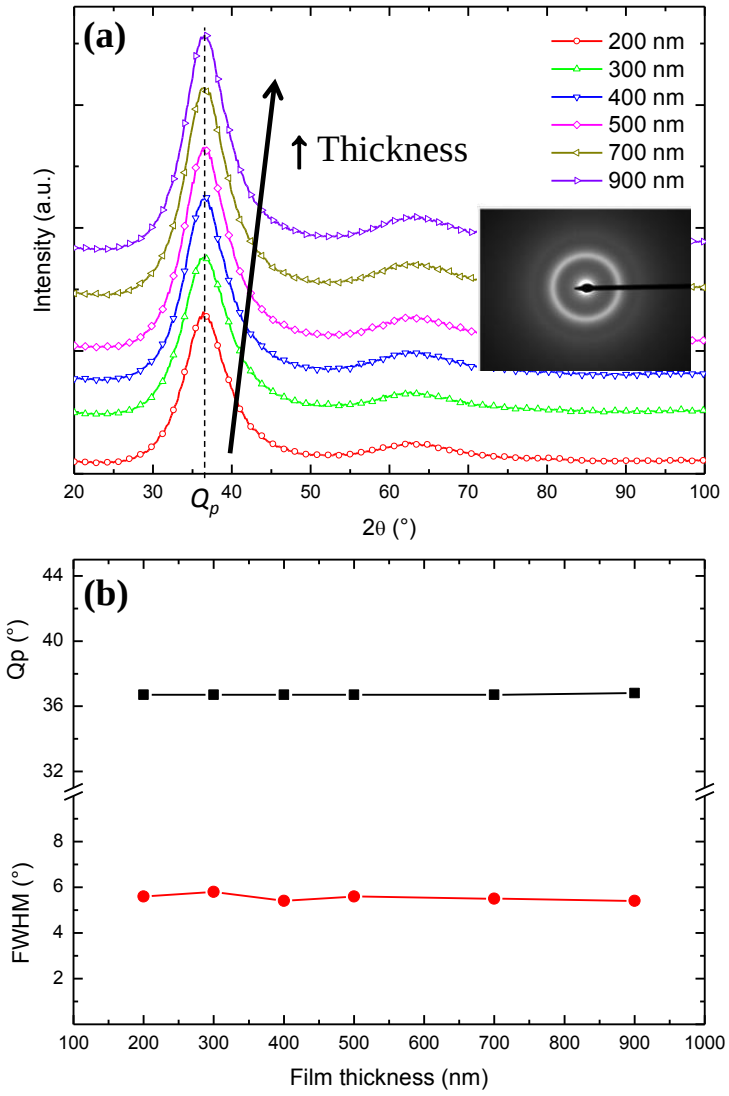

Figure 4 *– (a) Spectres DRX pour des TFMGs $Zr_{65}Ni_{35}$ avec différentes épaisseurs en montrant la présence de deux bosses. Dans l'encart, les résultats de microdiffraction dans le TEM pour un film de 900 nm d'épaisseur. (b) Evolution de la position de la première bosse de diffraction (Q_p) et de la FWHM. Les deux quantités ne varient pas avec l'épaisseur.*

Les constantes élastiques des TFMGs $Zr_{65}Ni_{35}$ ont été obtenues avec la spectroscopie Brillouin de surface (SBS) et l'acoustique picoseconde (PU) (sections 2.5 et 3.3). Ces expériences ont été menées respectivement par Philippe Djemia (de l'Université de Paris XIII) et par Laurent Belliard (de l'Université de Paris VI). La Figure 5 montre l'évolution du module élastique (E) et du coefficient de Poisson (ν) pour différentes épaisseurs. Les valeurs de E et de ν sont constantes et respectivement de 72 GPa et 0.39. **Cela confirme qu'il n'y a pas un changement de la structure atomique pour les différentes épaisseurs et que les effets d'échelle doivent avoir une origine extrinsèque liée à un effet du confinement géométrique.**

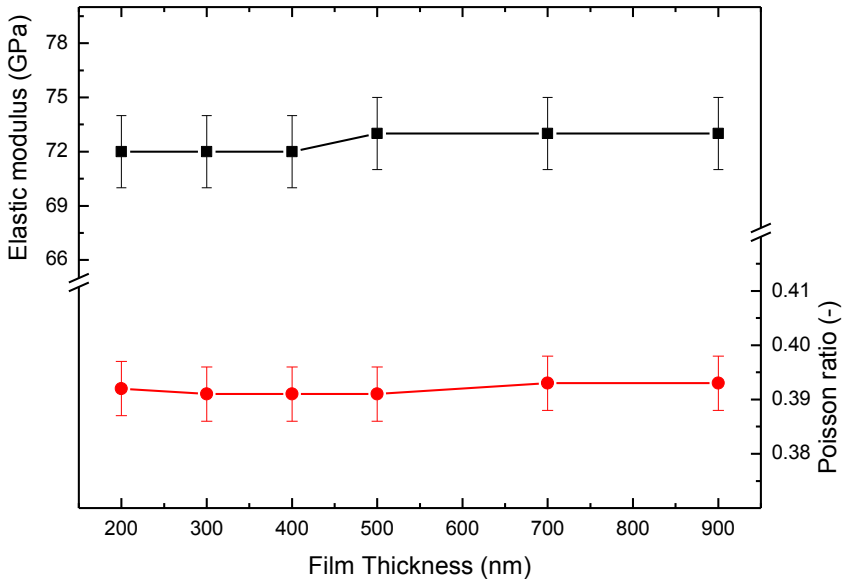

Figure 5 *– Evolution du module élastique (E) et du coefficient de Poisson (ν) avec l'épaisseur du film.*

Propriétés mécaniques de films minces en verre métallique $Zr_{65}Ni_{35}$

Les objectifs de cette section sont de présenter les principaux résultats des effets d'échelle sur la mécanique de films minces $Zr_{65}Ni_{35}$. Pour des films minces déposés sur Si la caractérisation mécanique a été menée par nanoindentation et par l'étude du comportement à rupture, alors que les effets d'échelle mécaniques pour des films libres ont été étudiés avec la technique de « lab-on-chip » qui exploite les contraintes internes d'une couche actuatrice pour générer une déformation dans le film à analyser.

a) Comportement mécanique par nanoindentation

Les expériences de nanoindentation ont été menées dans la configuration CSM (continous stiffness measuremnet) dont la dureté (H) est extraite pour différentes pénétrations. Trois vitesses de déformation ont été étudiées pour mesurer les effets viscoplastiques, respectivement 0.01, 0.025 et 0.1 s^{-1} (section 2.6).

La Figure 6 montre la variation de H avec la vitesse de déformation pour différentes épaisseurs de film (section 4.1.1). On peut noter que la dureté augmente clairement avec la diminution de

l'épaisseur pour toutes les vitesses de déformation. **Ce phénomène a une origine extrinsèque liée à la progressive difficulté de formation des bandes de cisaillement lorsqu'on réduit l'épaisseur du film.** Dans la Figure 6 on peut noter que la dureté augmente lorsqu'on augmente la vitesse de déformation (effet viscoplastique). Ce phénomène a été décrit aussi pour BMGs et il est principalement lié à la nature thermiquement activée des bandes de cisaillement qui se forment plus facilement pour des faibles taux de déformation conduisant à une dureté réduite. Cependant, le coefficient de sensibilité de la vitesse (m_H) est indépendant de l'épaisseur et égal à 0.026. Il est donc possible de calculer le volume d'activation qui est constant et de l'ordre de 120 Å^3.

Il est important d'observer que, en accord avec les résultats présentés dans le cas de la microstructure et les propriétés élastiques, le fait que m_H et donc le volume d'activation ne varie pas avec l'épaisseur indique que les films ont la même structure atomique. L'évolution de la dureté (Figure 6) qui augmente pour des petites épaisseurs est plutôt liée à des effets extrinsèques en raison du confinement dans l'épaisseur.

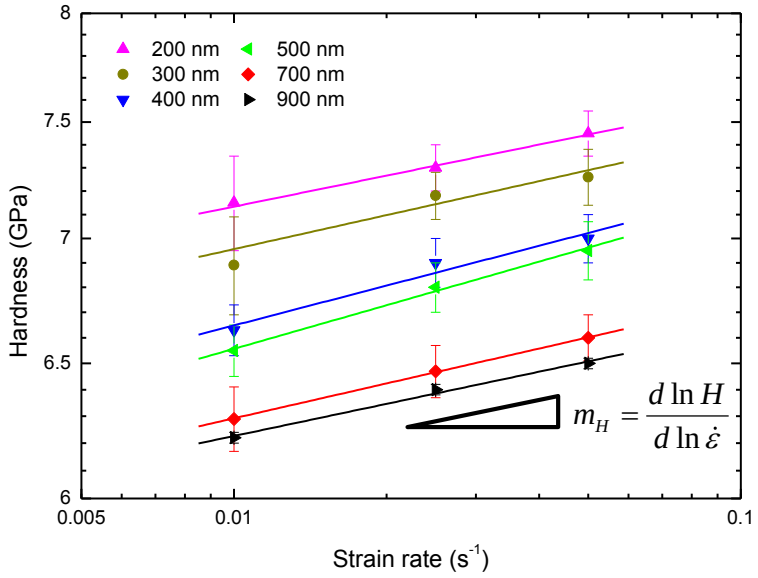

***Figure 6** – Détermination du coefficient de sensibilité de la vitesse (m_H) pour différentes épaisseurs de TFMGs $Zr_{65}Ni_{35}$. Les valeurs de m_H sont constantes et égales à 0.026.*

b) Propriétés mécaniques des films libres avec la technique du «lab-on-chip»

Dans cette section, on présente les principaux résultats qui concernent les propriétés mécaniques des films libres avec composition $Zr_{65}Ni_{35}$. La technique utilisée appelée «lab-on-chip» consiste à recouvrir un film actuateur (Si_3N_4), caractérisé par la présence d'une forte contrainte interne de traction (~ 1 GPa), avec le TFMGs $Zr_{65}Ni_{35}$ (Figure 7a) (plus détails dans la section 2.8). On peut noter que l'échantillon ($Zr_{65}Ni_{35}$) a une forme en dogbone (Figure 7a). Après libération par gravure sélective du substrat (Si), l'échantillon est déformé à cause de la contraction de l'actuateur (Figure 7b). Ensuite, le système atteint une position stable déterminée par l'équilibre des forces.

La déformation dans l'échantillon est calculée en mesurant avec le MEB le déplacement de curseurs spécifiquement conçus sur l'actionneur (Figure 7b). Par contre, la contrainte est déduite par l'application directe du principe d'équilibre des forces étant donné que l'actionneur se déforme élastiquement. Différentes géométries de l'échantillon et de l'actuateur produisent différents niveaux

de contrainte dans l'échantillon qui peuvent se déformer élastiquement ou plastiquement jusqu'à la rupture.

Cette technique a nombreux avantages dont le fait qu'on évite l'usinage FIB et que les échantillons ont une forme régulière de dogbone. En outre il y a la possibilité d'étudier les effets d'échelle pour des dimensions beaucoup plus grandes par rapport à ce qu'on trouve dans la littérature, mais en gardant une gamme d'épaisseurs comparables. Le plus petit échantillon qu'on a étudié à une taille de 25 μm x 1 μm x 200 nm (avec un volume de 5 μm^3 et une surface libre de 60 μm^2) alors que les mircopiliers ont un diamètre entre 140 nm et 3.6 μm avec une hauteur maximale de 10 μm [102]. Les échantillons étudiés par Tian *et al.* [114] pour des tests de traction *in-situ* MET ont une épaisseur et une largeur respectivement de 200 nm et 300 nm. Alors que la longueur est de 1 μm. D'autres avantages sont liés au fait qu'on a une contrainte de traction et par la possibilité d'étudier des effets de relaxation structuraux en mesurant l'évolution de la déformation avec le temps.

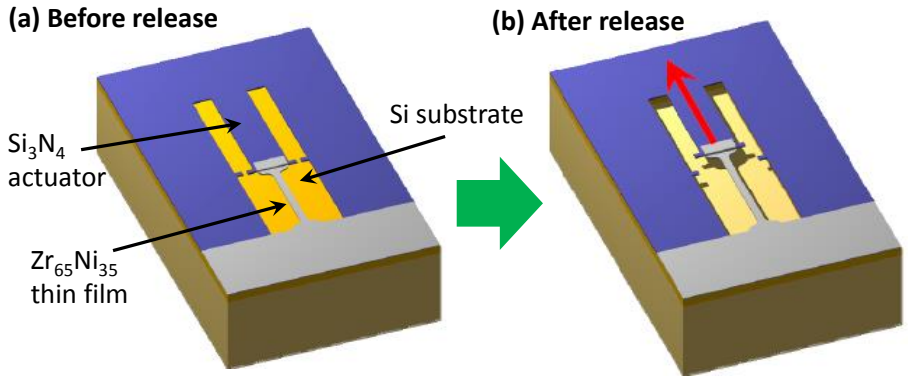

Figure 7 *– La technique « lab-on-chip ». L'échantillons ($Zr_{65}Ni_{35}$) recouvre l'actuateur (Si_3N_4) qui est caractérisé par la présence d'une contrainte interne de traction. (a) Condition avant gravure sélective du substrat. (b) Condition après gravure avec la déformation de l'échantillon.*

La Figure 8 montre la comparaison des courbes de traction pour des échantillons avec une longueur de 25 μm (section 4.2). Les échantillons ont une largeur de 1 μm pour les épaisseurs de 360 nmet 200 nm, tandis qu'une largeur de 2 μm est considérée pour le film de 110 nm d'épaisseur. Dans la Figure 8, on peut noter que :

- **le module élastique** (pente de la ligne noire) **est indépendant de la géométrie de l'échantillon** et égal à 72 GPa, en accord avec les résultats de la spectroscopie Brillouin,
- **la limite d'élasticité est très élevée et passe de 2850 MPa à 3282 MPa et 3300 MPa**, respectivement pour les films d'épaisseurs de 360, 200 et 110 nm,
- **toutes les géométries présentent une grande ductilité** avec une déformation plastique qui atteint le **maximum de 14.3%** pour les poutres de 200 nm d'épaisseur. Une valeur très proche (14.1%) est obtenue pour les échantillons de 360 nm d'épaisseur, tandis que la déformation maximale pour le film de 110 nm est égale à 11.8%,
- l'écrouissage est présent pour toutes les géométries.

La déformation est homogène dans l'échantillon. La Figure 9 montre un film de 25 μm x 2 μm x 110 nm, déformé dans le domaine élastique (Figure 9a) et après avoir subi une déformation totale de 11.8% (Figure 9b). Plus précisément, la Figure 9a correspond au premier point dans le domaine élastique (déformation du 2.3%) dans la Figure 8 (carrés noirs), tandis que la Figure 9b

montre le dernier échantillon avant fracture dans Figure 8 (carrés noirs). A nouveau l, la déformation est homogène et aucun événement de localisation avec des bandes de cisaillement n'est observé même à plus fort grossissement. Ces résultats ont été confirmés aussi par des études à haute résolution MET.

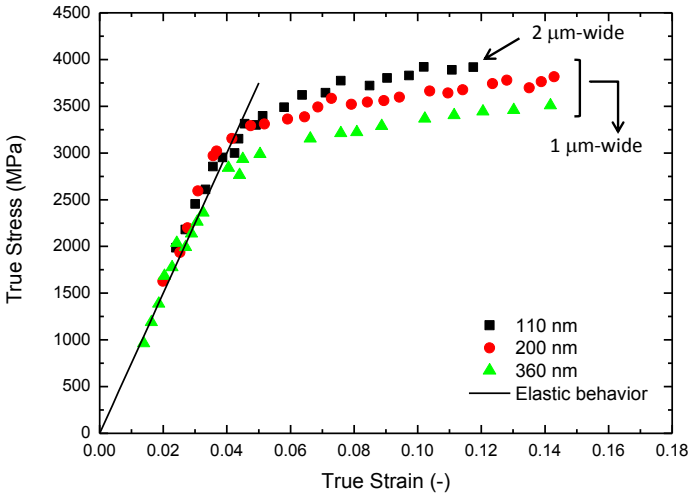

Figure 8 *– Courbes contrainte-déformation pour des échantillons avec épaisseur de 110, 200 et 360 nm. La largeur est donnée dans le graph, tandis que la longueur du faisceau est égale à 25 μm.*

La Figure 10 monte l'évolution de la limite élastique (σ_y) en fonction de la racine de la section transversale de l'échantillon. **On peut noter que σ_y augmente lorsqu'on réduit la section avec une tendance hyperbolique.** Plus précisément, σ_y évolue à partir des valeurs très proches des BMGs à base de Zr (1700-1800 MPa) pour les gros échantillons de 360 nm d'épaisseur et 4 μm-large (1.44 μm^2) jusqu'à des valeurs légèrement supérieures à la limite d'élasticité idéale autour de 3500 MPa pour des sections transversales de 0.2 μm^2). La limite élastique idéale a été estimée avec le modèle de Johnson et Samwer [101] et récemment adapté par Cheng et Ma [100] (section 4.2.4).

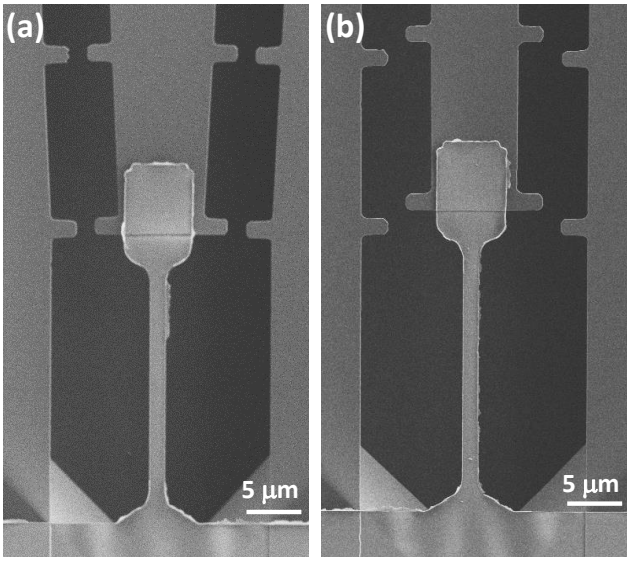

Figure 9 – *Micrographies MEB d'un échantillon de 25 μm x 2 μm x 110 nm soumis à différentes contraintes et déformations. (a) Déformation en régime élastique (2.3%). (b) L'échantillon après une déformation totale de 11.8% indiquant que la déformation se produit de façon homogène.*

Une analyse plus approfondie des données rapportées dans la Figure 10 peut être comprise avec une interpolation des données avec **le critère de propagation de la fissure de Griffith** qui a été utilisé pour modéliser l'évolution de la limite d'élasticité dans le cas de la compression du micropiliers [102] (l'équation est rapportée dans la Figure 10). On peut observer que l'approximation avec ce modèle est très bonne et on peut estimer une énergie de propagation de bandes de cisaillement (Γ) de l'ordre de 16.5 J/m^2, une valeur très proche des valeur de 11 J/m^2 dans la littérature [102].Toutefois, pour les géométries des échantillons étudiés on n'observe aucune déformation inhomogène (avec de bandes de cisaillement) pour les grandes sections et une transition ductile-fragile ne se produit pas. **D'ailleurs, la déformation plastique peut être très grande aussi pour les échantillons ayant des grandes sections transversales** (section 4.2.4).

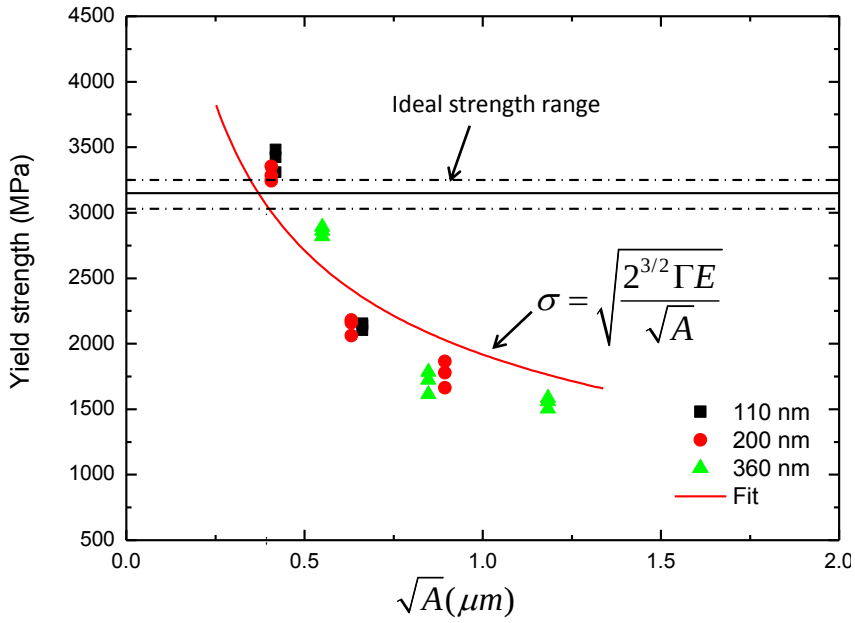

***Figure 10** – Evolution de la limite élastique en fonction de $\sqrt{A}$. Le modèle de Griffith (ligne rouge solide) interpole avec précision les données.*

Sur la base des résultats présentés, une explication claire de la physique derrière ces effets d'échelle peut être tirée (section 4.2.4). Tout d'abord, on suppose que les TFMGs ont la même structure atomique en termes de liaisons Zr-Ni comme indiqué par la valeur constante du module élastique, du coefficient de Poisson et par l'absence de décalage de bosses de diffraction. En outre, les films ont le même volume d'activation qui est lié à la taille des défauts élémentaires, les zones de cisaillement (STZs).

Pour ces raisons, **les changements observés dans la limite élastique en fonction de la surface transversale (Figure 10) doivent être considérés en terme de nombre de STZs potentiellement activées, qui est réduit pour les petites sections transversales. Cela conduit à une augmentation de la limite élastique (qui est proche de la limite idéale) car une contrainte plus élevée est nécessaire pour la percolation de ces défauts afin de former une single bande de cisaillement.** D'ailleurs, ce fait explique aussi la grande plasticité et la déformation homogène. Pour des sections transversales plus grandes, on a une réduction de la limite élastique en raison de la facilité de la percolation des nombreux STZs. Cependant, la présence de multiples événements de cisaillement locaux (opérations STZ) peut expliquer la plasticité et déformation homogène aussi pour les grandes sections transversales.

Les propriétés viscoélastiques des TFMGs ont été étudiées en utilisant la technique de «lab-on-chip». Plus précisément, pour une structure de test particulier, une fois qu'une position stable est atteinte dans le diagramme force-déplacement, la relaxation des contraintes s'effectue avec une cinétique qui dépende des mécanismes de déformation thermiquement activés liés à la microstructure du matériau et à l'épaisseur. Les conditions d'essai avec la technique de «lab-on-chip» correspondent à un essai de fluage réalisés sur un matériau attaché à un ressort (section 4.2.5).

L'étude de la relaxation a été conduit en mesurant la déformation de l'échantillon pour quatre intervalles de temps jusqu'à 51 jours après la gravure. Ce choix a été dicté par la cinétique logarithmique de la relaxation et pour mesurer une variation significative du déplacement. En outre, on montre que la relaxation a lieu seulement si le film est déformé plastiquement à cause de l'activation de STZs.

La relaxation permet aussi l'obtention du volume d'activation qui a été estimé pour différentes géométries d'échantillons soumis à différents niveaux de contrainte à cause du changement de la longueur de l'actionneur. L'évolution du volume d'activation en fonction de la section transversale est rapportée en Figure 11. **On peut noter que ce valeur est constant et entre 110 et 200 Å^3 en accord avec les résultats de nanoindentation. Cela confirme à nouveau que les films ont la même structure atomique et qu'elle n'est pas influencée par la géométrie de l'échantillon.**

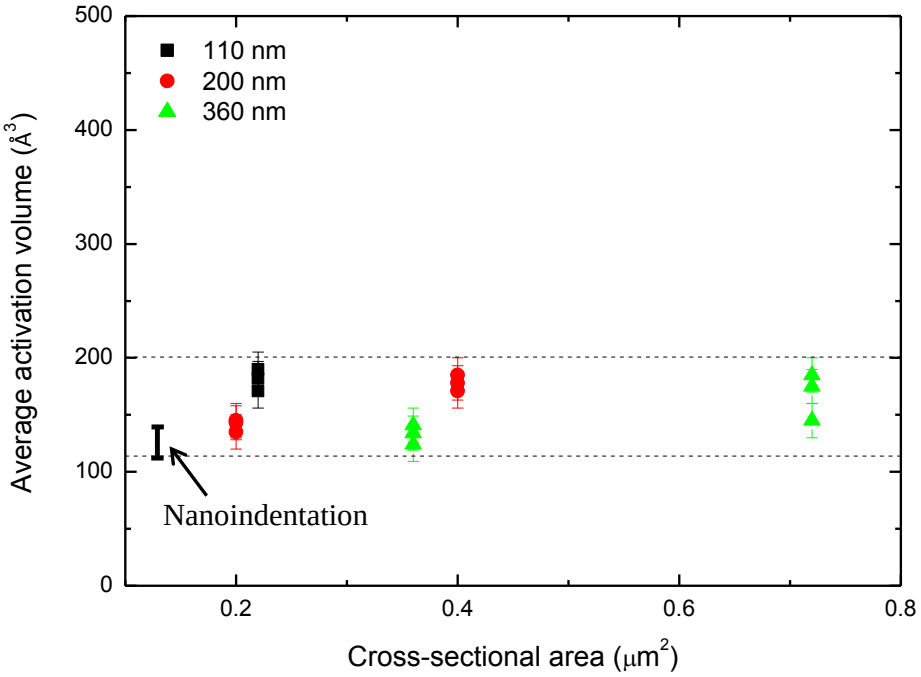

Figure 11 *– Volume d'activation en fonction de la section transversale. Le volume d'activation est constante et compris entre 110 et 200 Å^3.*

L'évolution de la déformation à rupture est montrée dans la Figure 12a (section 5.3). **En particulier, on trouve que la déformation à rupture augmente pour les échantillons avec la plus petite surface libre.** Cette évolution est différente de la limite élastique qui varie en fonction de la section transversale (Figure 10). **Une explication de cette tendance est la présence de défauts dispersés (STZs) qui sont plus nombreux en augmentant les surfaces libres.** Ces défauts ne doivent pas être considérés comme des défauts macroscopiques, car ils ne sont pas détectables par MEB et tous les échantillons se déforment de manière homogène. **Cependant, pour les plus grandes**

surfaces la probabilité d'avoir une percolation de STZ atteignant une taille critique est plus élevée aboutissant une rupture à plus faible niveaux de déformation. On observe aussi que pour les échantillons cassés il y la formation de bandes de cisaillement près de l'ancrage (Figure 12b). Ceci tend à montrer que les échantillons sont capables de soutenir une grande déformation plastique grâce à l'interaction de nombreuses bandes de cisaillement.

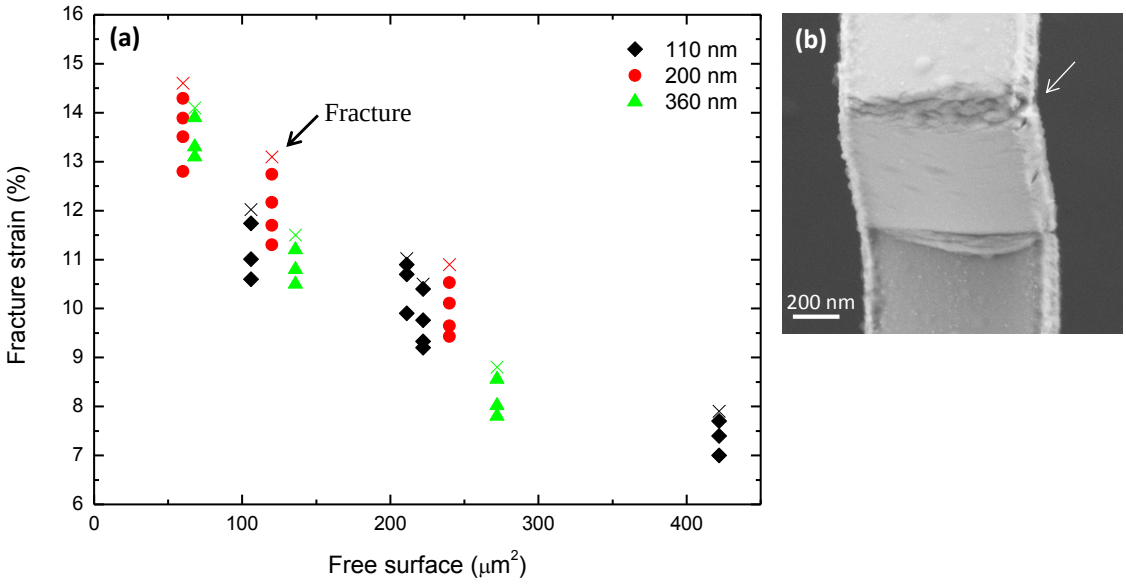

Figure 12 *– (a) Evolution de la déformation à la rupture en fonction de la surface libre. Le symboles «x» indiquent la déformation à la rupture, tandis que les symboles pleins indiquent la déformation totale des derniers échantillons intacts.(b) Exemple d'un échantillon cassé montrant la forte présence de bandes de cisaillements.*

c) Comportement à fracture

La méthode utilisée pour étudier le comportement à rupture des TFMGs déposés sur un substrat Si consiste à faire propager une fissure à partir d'une entaille créée par une pointe de diamant sur la face arrière du Si, la fissure atteignant le TFMG $Zr_{65}Ni_{35}$ (Figure 13a). Ensuite, la zone de fracture est observée au MEB. La configuration de chargement ressemble à un test de flexion à trois points (sections 2.7 et 5.2).

Les surfaces de rupture sont présentées à la Figure 13b-e. **Les films de 300 et 400 nm d'épaisseur montrent une surface uniform**e avec une partie pliée (folded layer) indiquée par une flèche blanche au sommet, Figures 13b-c. **Par contre, les films de 520, 750** (non représenté) **et 900 nm d'épaisseur montrent la présence de corrugations** sauf pour la partie plus haute d'environ 250 nm qui représente la partie pliée, Figures 13d-e.

Pour comprendre ces résultats des simulations par éléments finis (Figure 14) ont été réalisées par Frédéric Lani de l'Université catholique de Louvain (UCL) visant à analyser l'état de contrainte locale et la taille des zones plastiques (fracture process zones, FPZs). A la Figure 14 des résultats sont montrés pour différentes épaisseurs de TFMGs ainsi que diverses longueurs de fissure à épaisseur fixée. La Figure 14a (et le zoom dans la Figure 14h) et 14b montrent la zone plastique en termes de contours de déformation plastique équivalente pour une fissure dans un film de 900 nm situé à 300 nm de la surface et pour un film 300 nm d'épaisseur, respectivement. **On peut noter que la zone**

plastique en tête de fissure et la zone plastique en compression liée à la flexion fusionnent (*plastic collapse*). Pour les films d'épaisseur entre 520 et 900 nm (Figure 14d-e), la fissure peut propager avant la fusion des zones plastiques, alors que pour les petites épaisseurs (300 et 400 nm, Figure 14b-c) il y a tout de suite le *plastic collapse*.

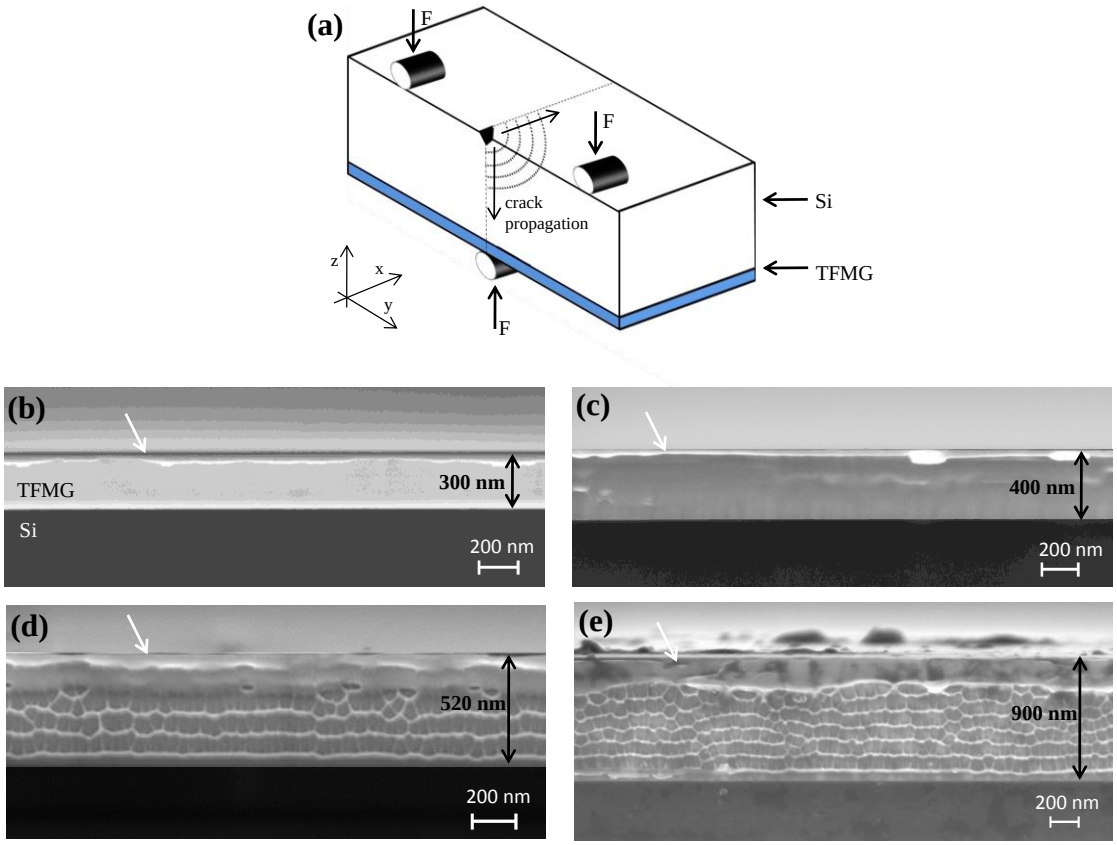

Figure 13 *– (a) Représentation schématique de la configuration de propagation de fissures pour un TFMG déposé sur Si. La figure n'est pas à l'échelle; l'épaisseur de Si est égale à 380 μm, tandis que l'épaisseur maximale du TFMG est de 900 nm. (b) - (e) Micrographies MEB de la surface de fracture pour TFMGs $Zr_{65}Ni_{35}$ avec des épaisseurs différentes de (b) à (e), respectivement, 300 nm, 400 nm, 520 nm et 900 nm. Le substrat en Si est la zone du fond sombre. Les corrugations apparaissent seulement pour des épaisseurs supérieures à 500 nm (d), (e), tandis qu'une couche pliée est observée pour toutes les épaisseurs, comme indiqué par les flèches blanches.*

Par conséquent, on propose que la fissure se propage avec un déplacement de la zone plastique jusqu'au ce que le *plastic collapse* soit rencontré. **Cela explique l'absence de corrugations pour les films les plus minces et pour les parties pliées (folded layers) pour les films plus épais**, Figures 14d-e. Si le *plastic collapse* se produit, le mécanisme de fracture correspond à un déplacement de cisaillement pur.

Avec les simulations par éléments finis on arrive à estimer le gradient de contrainte hydrostatique en tête de la fissure et de le lier – avec le modèle de Argon et Salama [95] – à la présence de corrugations dans les TFMGs épais et à estimer correctement leur taille qu'on mesure avec le MEB, Figure 13.

Cette analyse suggère que les effets d'échelle sur le comportement à rupture ont une origine *extrinsèque* et liée à un confinement géométrique puisque aucun changement dans la

structure atomique n'a été observé. On peut noter que des observations analogues justifient le comportement de nanoindentation ainsi que la grande plasticité, la déformation homogène et l'évolution de la limite élastique étudiées avec la méthode de «lab-on-chip».

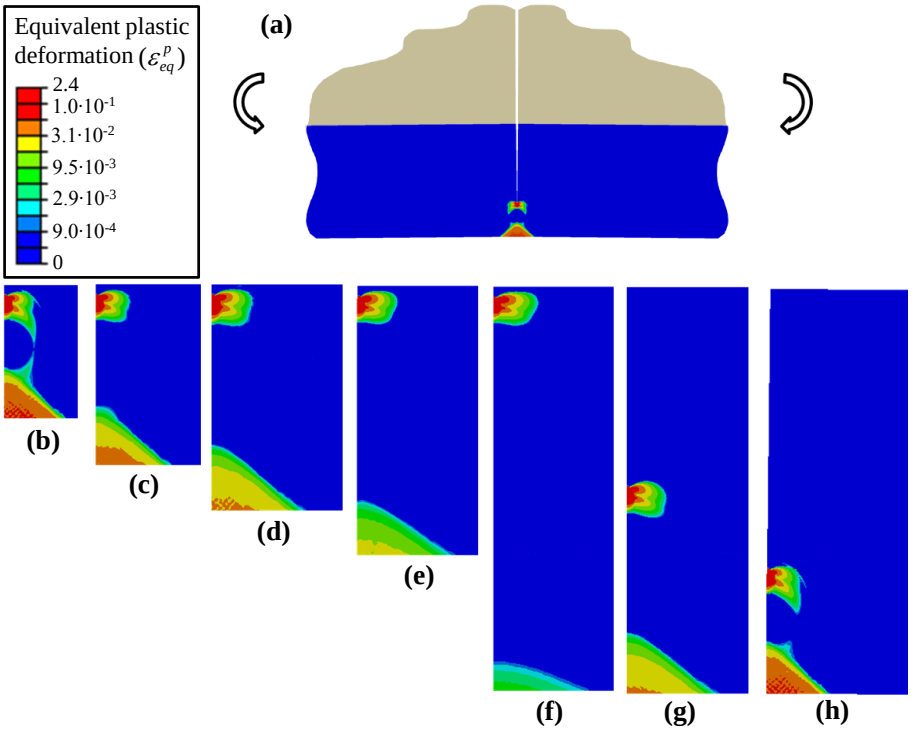

Figure 14 *– Simulations par éléments finis de fissures statiques dans le TFMGs (a) La zone illustrée est un zoom du TFMGs (en bleu) et du substrat Si (en gris) qui est entièrement fissuré. (b) - (h) Zones plastiques estimées en termes de déformation plastique efficace. (b) Film épaisseur t = 300 nm, longueur de la fissure a = 32 nm. (c) t = 400 nm, a = 32 nm. (d) t = 500 nm, a = 32 nm. (e) t = 600 nm, a = 32 nm. (f) t = 900 nm, a = 32 nm. (g) t = 900 nm, a = 450 nm. (h) t = 900 nm, a = 632 nm.*

L'étude du comportement de la fissure des TFMGs $Zr_{65}Ni_{35}$ se conclue avec l'analyse de l'effet du recouvrement avec un film de SiO_2 avec l'objectif de confirmer l'analyse précédemment rapportée indiquant que les effets d'échelle ont une origine extrinsèque (section 5.2).

La Figure 13 montre un changement dans le comportement à rupture à cause du *plastic collapse* qui se produit pour les épaisseurs inferieurs à 400 nm. Ce phénomène empêche de développer le mécanisme de propagation de la zone plastique en tête de la fissure en conduisant à une surface uniforme sans corrugations, Figure 15a. L'objectif du dépôt d'un film de SiO_2 sur le TFMG est de modifier la morphologie de la fracture en décalant la zone plastique de compression dans le SiO_2 lui-même. La surface de rupture d'un TFMG de 400 nm d'épaisseur revêtu d'une couche de SiO_2 de 450 nm est représentée à la Figure 15b démontrant la présence de corrugations. Le même film sans SiO_2 montre une surface plane (Figure 15a). Comme on s'y attendait, **ce changement brusque vient du fait que la zone de compression due à la flexion se situe dans la couche de SiO_2, qui permet à la contrainte hydrostatique de se développer sur une région du film ZrNi suffisamment grande pour déclencher un mécanisme responsable de la formation des corrugations.**

Cela prouve encore que les mécanismes de rupture sont dictés par des facteurs extrinsèques liés à la configuration du chargement et aux contraintes géométriques sur le développement des zones plastiques.

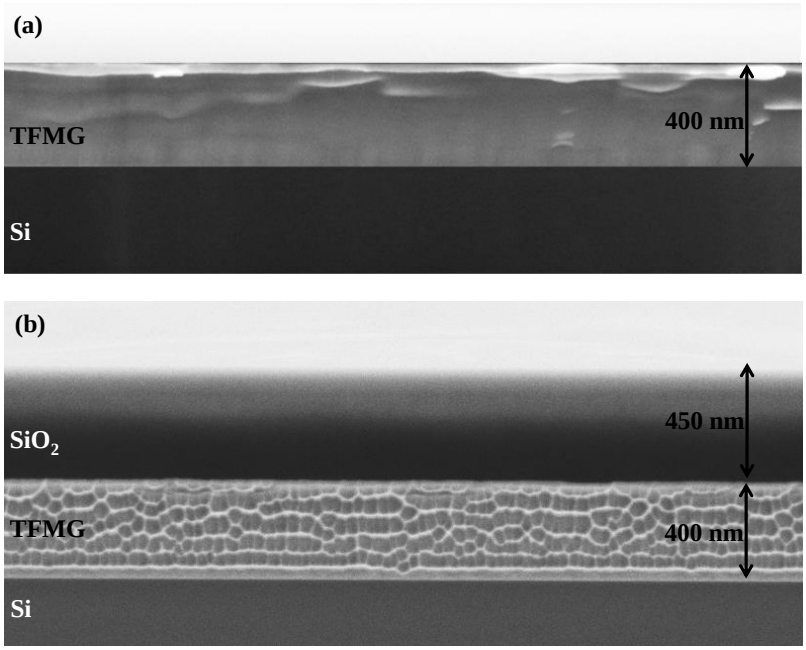

Figure 15 *– Micrographies MEB de surfaces de rupture pour des TFMGs $Zr_{65}Ni_{35}$. (a) Une surface de fracture uniforme est présente pour un film de 400 nm d'épaisseur en raison du plastic collapse. (b) La formation de corrugations sur un film de $Zr_{65}Ni_{35}$ de 400 nm d'épaisseur recouvert par une film de SiO_2 qui déplace en dehors du TFMG la zone plastique de compression liée à la flexion.*

Effet de la composition sur la structure et les propriétés mécaniques de films minces en verre métallique ZrNi

Dans cette section on résume les résultats principaux liés au changement de la structure et des propriétés mécaniques pour les différentes compositions analysées (plus détails dans le Chapitre III et section 4.1.2). Le changement de composition est possible en changeant le nombre de tranches de Ni dans la cible (Figure 3). L'étude de l'effet de la composition a été réalisée pour quatre compositions différentes $Zr_{42}Ni_{58}$, $Zr_{65}Ni_{35}$, $Zr_{75}Ni_{25}$, et $Zr_{85}Ni_{15}$ avec une épaisseur constante et égale à 800 nm.

Les images en section transversale MET montrent l'évolution de la microstructure pour les différentes compositions lors du changement de pourcentage de Zr (Figure 16). **Plus précisément, des petits nanocristaux (~ 3 nm) peuvent être observés pour $Zr_{75}Ni_{25}$ (Figure 16b, flèche rouge), tandis que une cristallisation intense se produit pour $Zr_{85}Ni_{15}$ où des cristallites de 60-70 nm de long sont présents dans une matrice amorphe (Figure 16c, flèche rouge).** Ces observations sont également en accord avec la microdiffraction rapportée dans l'encart, qui montre un *speckle* (flèche blanche) pour $Zr_{75}Ni_{25}$ et des spots de diffraction pour $Zr_{85}Ni_{15}$. D'autre part, la structure de $Zr_{42}Ni_{58}$ (et du $Zr_{65}Ni_{35}$, Figure 4a) sont entièrement amorphe comme prouvé par la microdiffraction (Figure 16a). Des phénomènes de cristallisation sont attendus pour les compositions riches en Zr à cause d'une réduction d'enthalpie de mélange.

Un changement de composition produit aussi un changement dans les propriétés élastiques (Figure 17). Il existe un effet marqué sur le module élastique (E) qui augmente de 65 GPa à 91 GPa lors de la diminution de la teneur en Zr, tandis que le coefficient de Poisson (ν) augmente légèrement pour atteindre la valeur de 0.4 pour $Zr_{42}Ni_{58}$. Les changements de E et ν donnent des informations utiles sur l'évolution de l'ordre local, avec la formation de fortes liaisons Zr-Ni et d'une haute énergie de cohésion pour les échantillons riches en Ni.

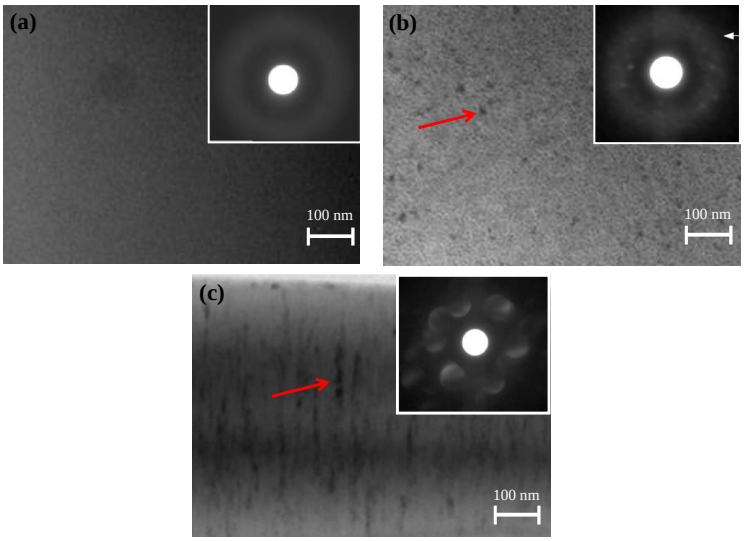

Figure 16 *– Images MET en section transversale de TFMGs Zr_xNi_{100-x} avec une épaisseur égale à 800 nm. Dans l'encart, la microdiffraction. De (a) à (c) les compositions $Zr_{42}Ni_{58}$, $Zr_{75}Ni_{25}$, et $Zr_{85}Ni_{15}$, respectivement. Les flèches rouges indiquent les nanocristaux dispersés d'environ 3 nm et 60 nm de long, respectivement pour $Zr_{75}Ni_{25}$ et $Zr_{85}Ni_{15}$.*

Dans les Chapitres III et IV de la thèse, on montre aussi qu'un changement de composition du film produit un changement de la position des bosses de diffraction, de la dureté, du volume d'activation et de la morphologie des surfaces de rupture. Cela indique qu'un changement de composition comporte un changement dans l'ordre local et particulièrement lié à la formation des liaisons atomiques Zr-Ni qui sont favorisés pour des échantillons riche en Ni.

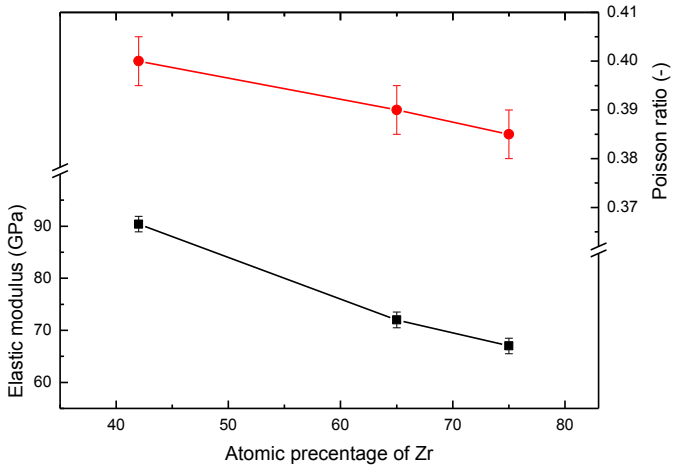

Figure 17 *– Evolution du module élastique et le coefficient de Poisson avec la composition du film.*

Conclusions et perspectives

L'objectif de cette thèse a été d'étudier les propriétés mécaniques des films minces en verre métallique (TFMGs) avec composition $Zr_{65}Ni_{35}$ (% at.) et d'épaisseurs comprises entre 200 et 900 nm. Les échantillons sont déposés par pulvérisation cathodique et une grande campagne d'expériences

structurelles et mécaniques a été menée soit sur des TFMGs déposés sur substrat Si soit sur des TFMGs libres.

Les TFMGs en $Zr_{65}Ni_{35}$ ont la même structure atomique comme indiqué par l'absence de décalage des pics de diffraction et par des valeurs constantes à la fois des propriétés élastiques et du volume d'activation. Cependant, une variation de la dureté est observée couplée à un changement brusque du comportement à la rupture. L'augmentation de la dureté avec la diminution de l'épaisseur est liée à l'effet du substrat sur la formation des bandes de cisaillements. Les surfaces de fracture présentent des corrugations avec des dimensions qui augmentent avec l'épaisseur, sauf pour les épaisseurs inférieures à 400 nm qui présentent des surfaces parfaitement planes. Les corrugations apparaissent à nouveau sur les films les plus minces si on ajoute une couche de recouvrement. L'origine des effets d'échelle est extrinsèque et liée à un effet de confinement de l'épaisseur sur le développement de la zone plastique.

Les propriétés mécaniques des films libres ont été étudiées en utilisant une méthode innovante basée sur un test de micro-traction actionné par une contrainte interne. Les structures d'essai ont été produites en utilisant des techniques de microfabrication avec les éprouvettes soumises à une tension uniaxiale. **Une grande ductilité jusqu'à 14% impliquant 4% de déformation élastique et 10% de déformation plastique homogène est rapportée. Le module élastique mesuré est en accord avec les résultats obtenus pour des TFMGs sur substrat Si, alors que la limite élastique augmente pour les petites surfaces atteignant la limite théorique de 3500 MPa. La variation de la limite élastique a été modélisée avec le modèle de Griffith sur la propagation des fissures.** La relaxation de la contrainte a été étudiée en mesurant la déformation en fonction du temps, conduisant à la détermination du volume d'activation de la déformation plastique. **Le volume d'activation ne dépend pas de la géométrie de l'échantillon, en accord avec les résultats obtenus par nanoindentation pour les TFMGs sur substrat Si. Les effets d'échelle sur la ductilité et sur la limite élastique sont liés à la difficulté accrue pour activer les mécanismes élémentaires de déformation pour les plus petites sections.**

L'effet de la composition sur les propriétés structurelles et mécaniques a été analysé comme suit. La cristallisation se produit pour les échantillons riches en Zr, alors qu'une augmentation du Ni conduit à une augmentation de la densité, des constantes élastiques, de la dureté, et du volume d'activation indiquant la formation de liaisons Zr-Ni et une contribution entropique améliorée.

Perspectives

La plupart des perspectives sont liées à la compréhension de la nature des effets d'échelle avec la technique du «lab-on-chip». En particulier, une campagne d'analyse MET est en cours dans l'objectif de suivre l'évolution de l'ordre local avec la déformation plastique.

D'autres études intéressantes sont liées à l'analyse des propriétés mécaniques avec la technique «lab-on-chip» de TFMGs pour une grande épaisseur (≥ 500 nm). On peut également utiliser cette technique pour tester des éprouvettes de géométries et compositions différentes.

Finalement, l'étude de l'effet de la composition peut être enrichi en analysant la structure atomique et les propriétés mécaniques pour une gamme plus grande de compositions qu'on peut facilement obtenir en jouant avec le nombre de tranches de Ni dans la cible.

.

List of Abbreviations

Metallic Glasses

BMG:	Bulk Metallic Glass
GFA:	Glass Forming Ability
LRO:	Long Range Order
MRO:	Medium Range Order
SRO:	Short Range Order
STZ:	Shear Transformation Zone
TFMG:	Thin Film Metallic Glass
TTZ:	Tensile Transformation Zones
Vit1:	Vitreloy 1

Characterization techniques

AFM:	Atomic Force Microscope
CSM:	Continuous Stiffness Measurements
DSC:	Differential Scanning Calorimetry
EDX:	Energy Dispersive X-ray spectroscopy
EPMA:	Electron Probe Micro Analysis
FIB:	Focus Ion Beam
PU:	Picosecond Ultrasonics
SBS:	Surface Brillouin Spectroscopy
(FE)-SEM:	(Field-Emission)-Scanning Electron Microscope
SPM:	Scanning Probe Microscope
TEM:	Transmission Electron Microscope
XRD:	X-Ray Diffraction
XRR:	X-Ray Reflectivity

Others

COF:	Coefficient of Friction
(LP)-CVD:	(Low Pressure)-Chemical Vapor Deposition
FCC:	Face-Centred Cubic (lattice)
FPZ:	Fracture Process Zone
FSDP:	First Sharp Diffraction Peak
FWHM:	Full Width at Half Maximum

HCP:	Hexagonal-Centred Cubic (lattice)
PVD:	Physical Vapor Deposition
RDF:	Radial Distribution Function
TCR:	Temperature Coefficient of Resistivity
TMAH:	Tetramethyl-ammonium hydroxide
TOF:	Time of Flight

List of Symbols

A: specimen cross-sectional area (lab-on-chip) (m^2)
$A(n)$: wavelength coefficient
$\bar{A}$: average atomic weight
B: bulk modulus (Pa)
C: loading curvature (Pa)
C_{11}: longitudinal elastic constant (Pa)
C_{44}: transversal elastic constant (Pa)
d: diameter (m)
d_p: fracture process zone diameter (m)
$d_{t\text{-}s}$: distance target substrate (m)
D_0: surface diffusion constant ($m^2\ s^{-1}$)
D_S: surface diffusion coefficient ($m^2\ s^{-1}$)
E: elastic modulus (Pa)
E_a: elastic modulus actuator (lab-on-chip) (Pa)
E_{el}: elastic energy ($J\ m^{-3}$)
E_D: activation energy for diffusion ($J\ mol^{-1}$)
ΔG: activation energy for deformation ($J\ mol^{-1}$)
G_c: fracture energy ($J\ m^{-2}$)
h: indentation depth (m)
$\dot{h}$: indentation velocity ($m\ s^{-1}$)
H: hardness (Pa)
I: current (A)
k: Boltzmann constant ($J\ K^{-1}$)
k_f: Fermi wavevector (m^{-1})
k_F: stiffness of testing frame ($N\ m^{-1}$)
k_M: effective stiffness of machine ($N\ m^{-1}$)
k_S: stiffness of sample ($N\ m^{-1}$)
k^*: surface reaction constant (s^{-1})
K_c: fracture toughness ($Pa\ m^{-1/2}$)
l: length, specimen length (lab-on-chip), terrace length (m)
l_0: initial length of the specimen beam (lab-on-chip) (m)
l_{0a}: initial length of the actuator beam (lab-on-chip) (m)
l_{tot}: maximum erosion circumference (m)
L: sample height (m)
m: strain rate sensitivity (lab-on-chip)
m_f: fragility index
m_H: strain rate sensitivity of hardness
M: Taylor factor

n: strain hardening coefficient
N_a: Avogadro number (mol^{-1})
P: indentation load (N)
$\dot{P}$: indentation loading rate ($N\ s^{-1}$)
Q: scattering vector (m^{-1})
Q_p: position of the FSDP (° or m^{-1} in scattering vector coordinates)
R: gas constant ($J\ K^{-1}\ mol^{-1}$)
R_s: sheet resistance (Ω/□)
R_{pre}: substrate curvature without film (m)
R_{post}: substrate curvature with film (m)
$\Delta r/r_0$: variation of surface reflectivity
S: specimen cross section (lab-on-chip) (m^2)
S_a: actuator cross-section (lab-on-chip) (m^2)
S_F: stability factor
t: time (s)
t_f: thickness of the actuator (lab-on-chip) (m)
t_f: thickness of the film (m)
t_s: thickness of the substrate or of the specimen (lab-on-chip) (m)
t_a: thickness of the actuator (lab-on-chip) (m)
T: temperature (K)
T_g: glass transition temperature (K)
T_m: melting temperature (K)
T_s: substrate temperature (K)
T_x: crystallization temperature (K)
u: displacement measured (lab-on-chip) (m)
v_l: longitudinal wave velocity ($m\ s^{-1}$)
v_R: Rayleigh wave velocity ($m\ s^{-1}$)
v_t: transversal wave velocity ($m\ s^{-1}$)
V: voltage (V)
V_a: atomic volume (m^3)
ΔV: apparent activation volume (m^3)
V_{app}: apparent activation volume (m^3)
w: corrugation width (m)
w_a: actuator width (lab-on-chip) (m)
w_s: specimen width (lab-on-chip) (m)
Y: sputtering yield
$\bar{Z}$: average valence

α: temperature coefficient of resistivity (K^{-1})
β: constant which relate v_R with v_T
γ: shear strain
$\dot{\gamma}$: shear strain rate (s^{-1})
γ_y: elastic strain limit in shear
Γ: energy per unit area required to create a shear band ($J\ m^{-2}$)
ε: deformation, uniaxial deformation (lab-on-chip)
ε_f: fracture strain (lab-on-chip)
ε_{el}: elastic strain
ε_p: plastic strain

ε_y: ideal strain limit
ε^{mech}: specimen mechanical deformation (lab-on-chip)
ε^{mis}: specimen mismatch strain (lab-on-chip)
ε_a^{mech}: actuator mechanical deformation (lab-on-chip)
ε_a^{mis}: actuator mismatch strain (lab-on-chip)
$\dot{\varepsilon}$: strain rate, indentation strain rate (s^{-1})
$\dot{\varepsilon}_p$: plastic strain rate (lab-on-chip) (s^{-1})
η: viscosity (Pa s)
θ: angle (°)
λ: radiation wavelength, dominant perturbation wavelength (m)
λ_L: laser wavelength (m)
λ_I: initial perturbation wavelength (m)
λ_s: steady-state perturbation wavelength (m)
μ: shear modulus (Pa)
ν: Poisson ratio
ρ: mass density (kg m^{-3})
$\rho(r)$: microscopic density
ρ_e: electrical resistivity (Ω m)
ρ_{e0}: electrical resistivity at room temperature (Ω m)
σ: stress, uniaxial tensile stress (lab-on-chip) (Pa)
σ_y: yield strength (Pa)
σ_H: hydrostatic stress (Pa)
σ_{homo}: ideal homogeneous stress (Pa)
τ: shear stress (Pa)
τ_y: shear yield strength (Pa)
τ_D: characteristic superficial diffusion time (s)
τ_R: characteristic reaction time (s)
χ: surface energy (J m^{-2})
ω_L: longitudinal wave frequency (s^{-1})
ω_T: transversal wave frequency (s^{-1})

Table of Contents

Introduction

In the last 50-60 years there has been an impressive technological development characterized by the search for new and high performance materials. Specifically, there is an increasing demand for materials with high strength, lightness and toughness, while being also capable to better resist at high temperature and corrosive environment than the existing ones.

Recent investigations have focused on the improvement of the properties and performance of existing materials characterized by a crystalline nature, that is, their atoms are arranged in a periodic manner to form an extended 3D lattice. However, in 1960 researchers succeeded to synthesize the first metallic glass (or amorphous metal) by rapid solidification of the liquid. This process prevents atoms to organize in a crystalline order, leading to an ill-defined atomic structure which shares many common features with the original liquid phase.

The rapid progress of technology coupled with the understanding of the physics of the glassy state led to the development of bulk metallic glasses (BMGs) which enabled measurements of functional and mechanical properties that were previously impossible. Functional properties of metallic glasses involves the superior corrosion resistance in harsh environment, interesting ferromagnetic properties, and a potential biocompatibility. On the other hand, mechanical properties of BMGs are characterized by high strength (2000 MPa for Zr-based BMGs), large elastic strain ($\sim$ 2%), low elastic modulus, and high toughness. Even if functional and mechanical properties can be very different depending on the glassy alloy selected and the imposed cooling rate, their origin is related with the liquid-like atomic structure which can be considered as fully isotropic with no grain boundaries, dislocations and phase segregation which, instead, are present in crystalline materials. However, BMGs Achilles' heel is represented by a brittle-like mechanical behavior in which plastic deformation develops in the form of narrow shear bands leading to abrupt fracture after yielding. This drawback hinders the diffusion of BMGs as structural materials, strongly limiting their applications.

To face this disadvantage scientists started exploring mechanical *size effects* which is a recent scientific domain aiming to understand how (mechanical) properties vary when decreasing the size usually below the micrometer. Obviously, not many applications require structural elements of such small size, but there is a real potential to include them in composite configurations (such as multilayers) or as surface coating whose industry has found a growing number of applications to improve substrate properties such as wettability, adhesion and wear resistance. Moreover, small-scale materials are involved in microelectronics as well which shows a continuous trend toward device miniaturization, while enhancing lifetime, performances and decreasing price. Several applications depend on microfabrication processes including solar cells, light emitting diodes, and MEMS and NEMS (Micro and Nano Electro-Mechanical Systems).

Pioneering results about the mechanical properties of small scale metallic glasses have shown that the brittle-like behavior of the bulk counterparts can be mitigated involving a homogeneous

deformation with large plastic deformation. In parallel, mechanical properties such as the yield strength are enhanced reaching values close to the theoretical limit. These experimental results are confirmed by molecular dynamic simulations showing a reduced likelihood of nucleation and propagation of shear bands for small scale specimens.

Nevertheless, there are several challenges when dealing with micrometer-scale specimens such as the sample production and manipulation to extract mechanical properties. For instance, most studies use compression test of micropillars which are produced by focus ion beam (FIB) milling. In this technique a ionized gas (usually Ga^{+}) bombards the surface of a BMG or of a thick glass coating. The result of a circular erosion is the production of a micropillar which is then deformed in compression by using a nanoindenter, thus obtaining the stress-strain response. Even if this technique has the advantage to be easy to perform, there are several open issues which can alter the results, such as indenter-sample misalignment, pillar taper and the surface damage which occurs during focus ion beam (FIB) milling operations.

Other techniques are represented by *in-situ* transmission electron microscopy (TEM) tensile test, where rectangular dogbone-like specimens are produced by FIB milling and then deformed within a TEM enabling to observe the microstructural evolution. However, in this case sample manipulation is extremely delicate and usually the thicknesses are below 100 nm. More important, the *in-situ* configuration does not allow to extract stress values, limiting the mechanical behavior to the analysis of the deformation.

As a consequence, even though there are evidences about an improvement of the mechanical behavior when moving toward a nanoscale metallic glass, there is some confusion in the literature about the evolution of mechanical properties and the deformation modes resulting from the contrasting results obtained by different authors using the previously cited techniques.

Unsolved questions are also represented by the origin of size effects and by the existence of a critical threshold below which size effects are activated. The former question involves the understanding of the atomic structure of metallic glass at the small scale and if it changes with respect to bulk (*intrinsic* size effects). Here, it can be pointed out that FIB operation can alter the atomic structure with Ga implantation and free volume creation. Alternatively, size effects can have an *extrinsic* nature, namely their mechanical properties are influenced by the reduced sample dimension and geometry, while there are no changes in the atomic structure. The latter question has a non-obvious answer too. In crystalline material size effects are usually triggered when the sample size approaches the internal length scale which dictates the macroscopic behavior such as the grain boundary spacing. In a metallic glass the liquid-like atomic structure prevents to foresee when this transition can occur.

In this contest, we can define the objectives of this PhD thesis aiming to shed light on mechanical properties of small scale metallic glasses. ZrNi thin film metallic glasses (TFMGs) have been deposited by DC-magnetron sputtering and then a complete analysis of mechanical properties has been carried out. This characterization covers elasticity, the analysis of (visco)plastic properties as well as the fracture behavior.

Several techniques have been involved too. Specifically, mechanical tests have been divided into two categories if the mechanical properties are tested on a Si substrate or on freestanding films. In the former case, we use surface Brillouin spectroscopy (SBS) and picosecond ultrasonics (PU) to extract elastic properties, while the viscoplastic behavior have extracted by nanoindentation. The fracture behavior has been investigated by nanoscratch and by analyzing the effect of a crack propagating from the Si substrate. In the latter case, we used the lab-on-chip technique whose basic concept is to use the internal stress generated in a thin layer to actuate another layer (the ZrNi TFMG)

from which the mechanical properties can be extracted. This technique involves the development of dogbone-like freestanding TFMG avoiding the use of FIB operation, while enabling to accurately extract the stress-strain response for different specimen geometries.

In parallel to this experimental campaign, we investigated the effect of the composition on the structure and mechanical response of ZrNi TFMGs, for which there are not many scientific studies. Structural investigation involved several techniques, such as X-ray diffraction (XRD), transmission electron microscopy (TEM), X-ray reflectivity (XRR), surface Brillouin spectroscopy (SBS), picosecond ultrasonics (PU) and the analysis of electrical resistivity at room temperature or during heat treatments.

This PhD thesis work is divided in five chapters:

- **Chapter I** surveys the state-of-the-art, in which the metallic glasses are presented especially focusing on their mechanical properties. The main literature results of size effects are reported, showing the most controversial trends as well. The aim of this chapter is to provide all the key elements to discuss and understand the results presented in Chapters III, IV, and V, as well as to show the novelty of our results with respect to the state-of-the-art.
- **Chapter II** is dedicated to the experimental techniques, analyzing the film growth mechanisms, the sputtering physics as well as all the characterization techniques used to study functional and mechanical properties of ZrNi TFMGs. Particular emphasis is devoted to the description of the lab-on-chip concept involving the mechanical testing on a freestanding film.
- **Chapter III** involves the study of structural and elastic properties of ZrNi TFMGs. The evolution of the atomic structure as a function of composition and thickness is described by using XRD, TEM, XRR, SBS, PU and the analysis of electrical resistivity.
- **Chapter IV** is devoted to the analysis of the viscoplastic properties of ZrNi TFMGs. In the first part, the nanoindentation results are presented involving also the analysis of the effect of the indentation strain rate on the mechanical response with the calculation of the activation volume. In the second part, the analysis of the mechanical properties of freestanding films is reported analyzing the stress-strain curve for different thicknesses as well as stress relaxation phenomena allowing a second estimation of the activation volume.
- **Chapter V** focuses on the fracture behavior of ZrNi TFMGs. This chapter is divided in three parts. Part one is dedicated to the scratch analysis. Part two involves the analysis of fracture of TFMGs on a Si substrate, while part three is devoted to the fracture in tension of freestanding films, competing the analysis of Chapter IV.

Chapter I – State-of-the-art

Metallic glasses (alternatively called amorphous metals) are constituted by metallic or metalloid elements and they are produced by rapidly solidifying the liquid at very high rates (10^6 K/s, section 1.3) [1]. The result of this process is a metallic material lacking long range atomic periodicity, contrary to the crystalline counterparts [1]. The development of high cooling rate techniques coupled with a thorough comprehension of glass formation led to the production of bulk metallic glasses (BMGs) whose larger dimensions enable to probe their functional and mechanical properties [1].

BMGs have outstanding mechanical properties involving high fracture strength close to the theoretical limit and large elastic deformation (~ 2%) arising from their liquid-like atomic structure, with no grain boundaries, dislocations, and phase segregations, contrary to crystalline materials (section 1.5) [2]. Nevertheless, the shear band instability phenomenon that occurs during plastic deformation of BMGs – at room temperature – leads to a lack of ductility, thus drastically undercutting potential use in structural applications (section 1.5) [3].

One way to overcome the BMGs macroscopic brittle-like behavior is to reduce the dimensions (< 1 μm) in order to mitigate the catastrophic effects of instabilities on the mechanical behavior, while also enhancing strength and ductility. This opens the scientific domain of *"size effects"* aiming to investigate the effect of a geometrical confinement on (mechanical) properties, see section 1.6 [4].

However, even though there are theoretic evidences about a change in mechanical behavior when small length scales are involved [3, 4], the preparation and manipulation of very small specimens (∼ μm) led to controversial results in terms of deformation mechanisms as well as on the trend of the main quantities, such as the yield strength, when decreasing the sample size (section 1.6.2). Moreover, the origin of size effects is not unraveled yet since it can results from a change of atomic arrangement (*intrinsic* size effects), or from a geometric confinement (*extrinsic* size effects) both affecting the mechanisms of activation of shear bands (section 1.6.2). The threshold size which activate size effects is matter of debate too. In crystalline materials, mechanical size effects are usually triggered when the characteristic dimensions (*external length scale*) approach the *internal* one which dictate the macroscopic mechanical behavior such as the dislocation or the grain boundaries spacing [4]. In a metallic glass the isotropic liquid-like atomic structure does not enable to predict any obvious change when the external length scale is reduced.

In this chapter, we present the metallic glasses the materials investigated in this PhD thesis work. Firstly, it will be introduced some general notions about the formation of the glassy state and metallic glass atomic structure (sections 1.1 and 1.2). Afterwards, bulk metallic glass (BMGs) properties will be presented especially focusing on the mechanical ones (sections 1.4 and 1.5). The analysis of the theories which describe the formation of the shear bands will play a central role for the understanding of the size effects involving small scale metallic glasses for which the main literature results will be summarized, highlighting the most controversial aspects as well (sections 1.5.8 and 1.6.1).

The objectives of this chapter are to present all the key elements necessary to understand the mechanical properties of thin film metallic glasses (TFMGs) studied in this PhD thesis in Chapters III, IV, and V, while also discussing the literature results involving mechanical size effects. Moreover, the thorough analysis of the relationship composition-atomic structure will enable the understanding of the results for different ZrNi TFMG compositions investigated (again reported in Chapters III, IV, and V).

1.1 The glassy state: thermodynamic aspects

Glasses can be considered as "frozen" liquids obtained by a rapid quenching from the melt state. A glass is thus an amorphous solid which shows a disordered atomic structure (as for liquids) without a long range order (LRO) [5-8]. This is the fundamental difference with respect to a crystalline material whose atomic periodicity allows to identify a *rule of order* that allows to establish the relative position of an atoms within the atomic lattice starting form a point of assigned spatial coordinates. Before focusing on the structure of an amorphous alloys (section 1.2), the basic principles for the formation of the glassy state will be introduced highlighting the concept of glass transition temperature (T_g).

It is well known that when a liquid is cooled below the melting temperature (T_m) it crystallizes through a process of nucleation and growth [9]. This transition is a first-order phase transition and involves discontinuities in several properties such as volume and viscosity. More important, it occurs at fixed temperature (T_m) since the energy is transferred from the liquid to the crystalline seeds for their growth. In Figure 1.1a line 3 is reported the trend of viscosity (η) as function of the temperature during a crystallization process [5, 6]. Viscosity – which can be defined as measure of a material resistance to a shear deformation – shows an abrupt increment of several orders of magnitude from the very low value of the melt up to a solid state where it is almost infinite and arbitrary set at 10^{12} Pa s [6]. A similar trend is reported in the case of volume which experience an abrupt shrinkage at T_m (Figure 1.1b, line 3) [5, 6]. At the end of crystallization process the atomic structure is completely ordered (Figure 1.1a inset on the right). If the cooling rate is fast enough the liquid will enter in the metastable supercooled regime (between T_g and T_m) preventing atoms to rearrange in the crystalline order (Figure 1.1) [5-8]. Reducing the temperature the viscosity continuously increases up to a point that atomic redistributions are no longer possible and the liquid looks frozen ($\eta = 10^{12}$ Pa s). This transition occurs at the glass transition temperature (T_g), Figure 1.1a lines 1 and 2. A glass has been formed in which the high cooling rate prevent to develop a long range order (LRO, Figure 1.1a inset on the left). The glassy phase shows a lower atomic packing efficiency than the crystalline one with a significant content of *free* volume (Figure 1.1b) and higher energy (section 1.2) [5].

The glass transition is affected by kinetic factors (Figure 1.1 branches 1 and 2) [5, 6]. If an high cooling rate is applied, the liquid will result "frozen" at higher temperatures (T_{g1}) since atoms will not have a sufficient time to organize. The result is an highly (meta)stable glassy structure with an higher energy and free volume content [5, 8]. A lower cooling rate allows a certain degree of atomic organization in the supercooled region before freezing which in turn results in a lower value of T_g (T_{g2}) and a denser structure as well (section 1.2) [5, 8].

The cooling rate is a critical process parameter to obtain a glass and is related with the nature of atomic bonds that determine the microscopic structural arrangement rate needed to maintain the equilibrium during cooling [5, 6]. Silicate glasses or polymers, which are constituted by a long macromolecular chains (covalent bonds) with a limited spatial mobility, will easily transform in a glass state at low cooling rate (10^{-2} Ks^{-1}). For these materials, the crystallization needs long times of atomic organization, enhancing the glass forming ability (GFA) [5]. On the other hand, liquid metals –

which have non-directional bonds and high mobility in the melt – need of an large cooling rate to experience glass transition. Typical values, which depend on the alloy composition, are in between 10^3 and 10^8 Ks^{-1}, meaning that these materials have an high aptitude to crystallize exhibiting a lower GFA compared to a covalent glass [5, 8, 10]. In section 1.3 will be presented the empirical rules to obtain a metallic glass.

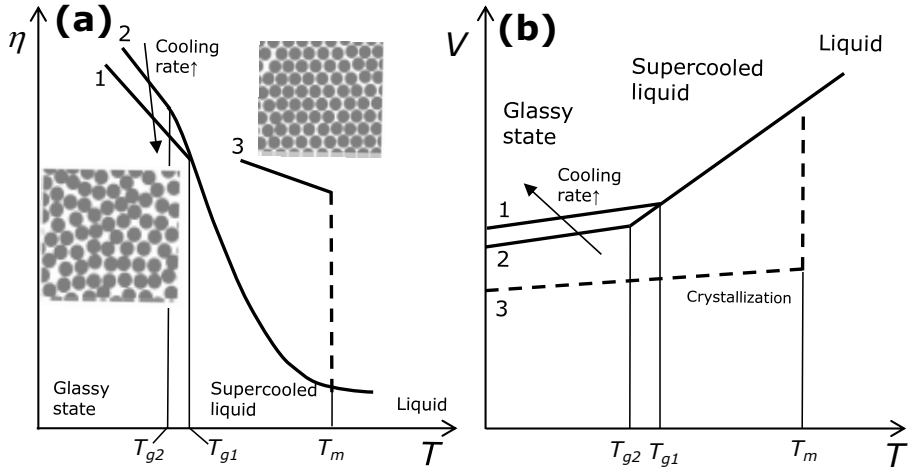

Figure 1.1 *– Viscosity (a) and volume (b) as a function of the temperature for a metallic system. Curves 1 and 2 represent a glass showing the effects of the cooling rate on T_g, while the curve 3 represents a liquid-crystal transition.*

The differences between a covalent glass and a metallic glass – which is constituted only of metallic and metalloid atoms – is appreciable by the analysis of the viscosity (η) in the supercooled region (Figure 1.2) [8]. In covalent glassy systems (SiO_2), *log* (η) linearly increases when reducing the temperature (increasing the ratio T_g/T), while in metallic glass it deviates following a non-linear trend. A fragility index (m_f) indicative of the thermodynamic stability of a glass is defined as [8]

$$m_f = \left.\frac{d\eta(T_g/T)}{d(T_g/T)}\right|_{T=T_g} . \qquad (1.1)$$

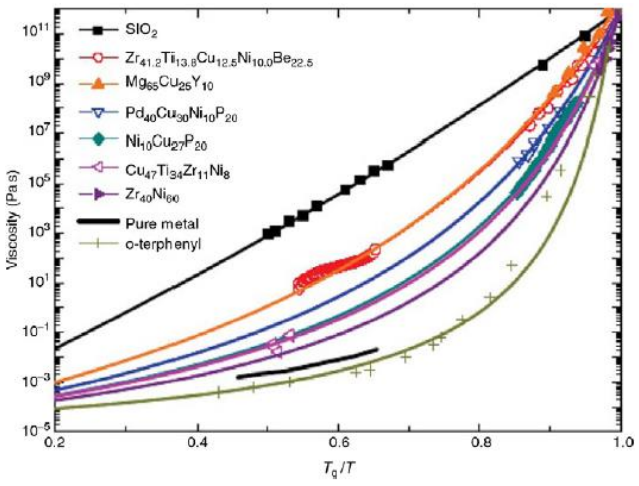

Figure 1.2 *– Viscosity as a function of the temperature for fragile and strong glassy systems [8].*

Liquids with a lower thermodynamic fragility (SiO_2) are called "*strong*", whereas those with a higher m_f are called "*fragile*" (o-terphenyl) [5, 8]. In fragile systems, it is sufficient a small thermal excitation to produce disruption of the local order developed in the supercooled region. In particular, the abrupt fail in viscosity immediately after T_g suggests that the structure of this systems is really *fragile* with an higher tendency to collapse when heated [5, 8]. Strong systems have a network of directional covalent bonds which guarantee a higher (meta)stability, without abrupt changes in viscosity [5, 8]. It is thus reasonable to expect an higher GFA for strong glasses, while metallic glasses have an intermediate behavior (Figure 1.2) which depends on their composition and the structural arrangement reached in the supercooled region (section 1.2).

1.2 Order in metallic glasses

The question of what is the atomic structure in metallic glass has long been a topic of intense research representing a central issue to understand their macroscopic properties. As it has been already mentioned, metallic glasses are constituted only by metallic or metalloid (B, P) atoms. The lack of directional bonds makes difficult to understand the local order on the basis of elementary rules in which the amorphous structure is obtained simply altering the crystalline order (i.e. distorting bond angles) [5, 6].

In Figure 1.3 are reported high resolution transmission electron microscope (TEM) images which compare a crystalline material a low carbon steel (a) with a $Zr_{67}Ni_{33}$ (% at.) metallic glass (b) [11]. While in a crystal it is possible to identify an atomic periodicity with the presence of diffracted spots, the structure of an amorphous alloy appears random (maze-like) and it is characterized by the presence of diffuse halos in the electron diffraction pattern. It should not surprise that fact that the first model which describes the structure of metallic glasses – the Bernal's model [12] – represents metallic glasses as a dense random packing of hard spheres. A complementary concept that is usually connected with a random packing is the *free* volume, which is defined as the atomic volume in excess with respect to the ideal densely packed structure (the crystalline phase) [5, 8]. Thus, a first naïf view of the structure of an amorphous alloy consists in a random distribution of atoms with the presence of distributed free volume arising from the rapid quenching of the melt which prevent crystallization.

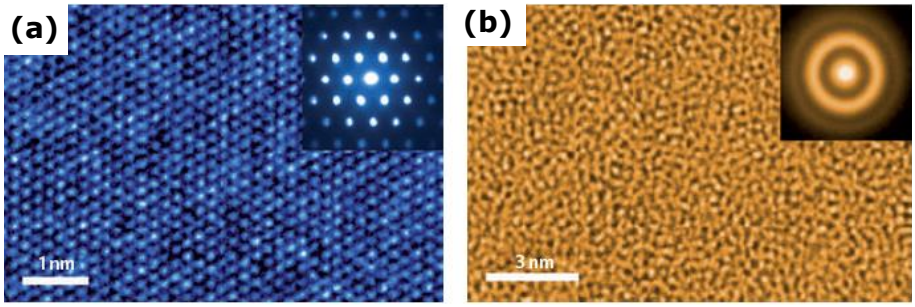

Figure 1.3 *– High resolution TEM images of a crystalline low-carbon steel (a) and a $Zr_{67}Ni_{33}$ metallic glass. In the inset the selected area electron diffraction [11].*

However, this model fails to describe many binary metallic glasses, where a short range order (SRO) is pronounced [5-8, 13-16]. This means that metallic glasses show an ordered structure at least within the first neighbor coordination shell from a selected atom (~0.5 nm). The evidence of a SRO is

intimately related to the output of diffraction experiments, which show the presence of a first intense diffuse halo followed by less intense and broad one (Figure 1.3b, inset) which carry significant information about the local order [5, 8, 16]. In fact, the Fourier inversion of diffraction data yields the radial distribution function (RDF) $4\pi^2\rho(r)$ where $\rho(r)$ is the microscopic density of atoms at a distance *r* from a reference atom (Figure 1.4). At low *r*, $\rho(r)$ shows an oscillating trend with two or more peaks. The first peak corresponds to the SRO (nearest-neighbor shell), while the structural features starting from the second peak corresponds to the medium range order (MRO, 1-2 nm) [5, 6, 8, 16]. The area under the curve peaks (green or orange in Figure 1.4) allows to calculate the average coordination number that is the average number of nearest neighbors of the reference atom. The second peak is consistently broader than the first one due to a progressively ill-defined atomic structure. At larger *r*, oscillations in $\rho(r)$ progressively damp down meaning that no long range order (LRO) exists, while $\rho(r)$ attains the values of the macroscopic density.

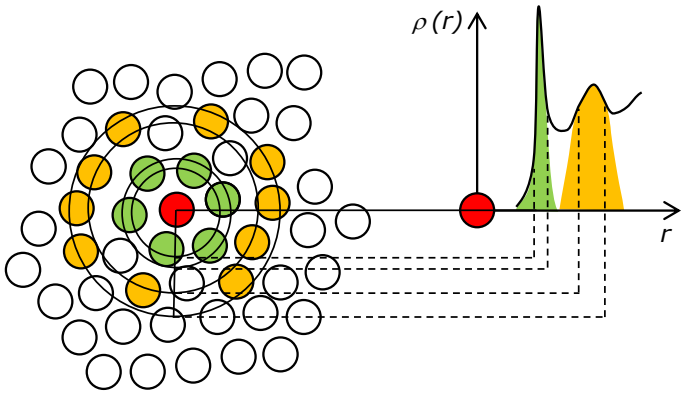

Figure 1.4 *– Microscopic density as a function of the distance (r) from a selected atom. Peaks at small r indicate the presence of a local order. Adapted from [5].*

It is important to underline that the RDF does not establish an unique set of coordinates of the atomic positions, but it represents only the positional dependence of the *average* atomic density. Even if it cannot be used to directly determine the SRO, it is possible to simulate the RDF for different models of atomic packing and then verify if they fit with the experimental RDF. These methods are at the basis of reverse Monte Carlo (RMC) and *ab initio* simulations [8, 13, 17]. The result is that the SRO in binary metallic glasses consists in packing of solute-centred clusters of Frank-Kasper polyhedra (Figure 1.5a) [8, 15, 18-21]. Each polyhedron is centered around the smaller atomic specie favoring unlike bonds which enhance chemical affinity. A peculiar characteristic of this local order is that it is constituted by tetrahedra only and it is characterized by an high packing efficiency. For instance, a tetrahedron have a packing efficiency of 78% with respect to a 74% of a face-centred cubic (FCC) or an hexagonal close packed (HCP) lattice. Nevertheless, this atomic structure does not allow long range order (LRO) to develop for steric reasons [5, 8]. As a matter of fact, the five-fold geometry made up of tetrahedra cannot be arranged in a simple and periodic manner to fill the space. This local order is called *frustrated* since there is the highest packing efficiency, but no compatibility with a LRO. FCC and HCP crystalline structures result from the combination of tetrahedral and octahedral units which reduce the packing efficiency, but enable LRO to develop thus reducing the overall energetic content [5, 8].

In the case of Frank-Kasper polyhedra in binary metallic glasses the different atomic radii between the two atomic species accommodate the steric effects and favor stability reducing the frustration arising from a tetrahedral packing [5, 8]. Moreover, SRO in metallic glasses is not

characterized only by the presence of a single type of Frank-Kasper polyhedron, but there is a distribution of solute-centered clusters which depends on the nature of the chemical elements and their relative proportion [8, 16, 19]. Metal-metalloid systems (e.g. NiB, NiP, FeB, CoP etc.) have a large difference of the atomic radii while the atomic bonds are characterized by a certain covalent (directional) content, whilst metal-metal systems (e.g. ZrNi, ZrCu, NiNb, CuTi etc.) are characterized by a reduced difference of atomic radius with a non-directional (metallic) bonds [8, 16, 19]. Lastly, the distribution of atomic cluster depends on the cooling rate which set the atomic arrangement and the packing efficiency of the system [8, 19].

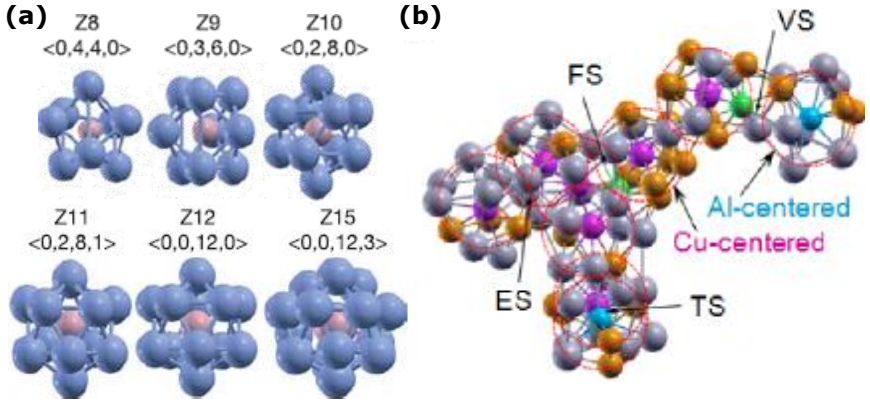

Figure 1.5 *– (a) Different Frank-Kasper polyhedra encountered in metal-metalloids glassy systems. The small solute atoms are surrounded by the larger solvent atoms [16]. (b) Connection of solute centered clusters to form MRO in a* $Cu_{46}Zr_{47}Al_7$ *metallic glass [22].*

The ploytetrahedral packing model discussed before provides a description of the SRO, but a picture of the MRO is not given. Even though the MRO is still object of scientific debate due to progressively ill-defined atomic structure in a metallic glass, a possible model of MRO considers the solute centred-clusters as a basic building blocks that connected each-other cerate the MRO (Figure 1.5b) [5, 8, 15, 16, 19, 21, 22]. Clusters can be connected by vertex, face, edge or tetrahedral sharing, respectively VS, FS, ES, and TS in Figure 1.5b. Since a LRO is not allowed, there will be some "*cavities*" associated with the cluster arrangement. These cavities justify the excess in free volume of a metallic glass with respect to a crystalline counterpart, while having a capital role to determine the macroscopic properties in terms of glass forming ability and localization of plastic flow [8, 16] (section 1.5.8).

The tetrahedral SRO in metallic glasses acts as a barrier to crystal nucleation in the supercooled liquid metals, because icosahedral clusters already exist and they are incompatible with the crystalline structure [8, 19]. This sizable barrier for the transition from the icosahedral packing to the long-range ordered crystal is the structural basis for the supercooling observed for metallic liquids (Figures 1.1 and 1.2) [8, 19]. Molecular-dynamics simulations show that icosahedral order increases sharply on cooling towards the glass transition (Figure 1.6). The ordering appears to be intimately associated with the increase in viscosity that leads to glass formation (Figure 1.1a). The alloys showing a large fraction of such clusters have improved glass-forming ability (GFA) preventing crystallization [8, 19].

We can conclude that a more precise model of the atomic structure of binary metallic glasses consists of a distribution of solute-centered clusters that can be connected with each other to produce a MRO. Clusters have an icosahedral structure that originated in the supercooled region and it is characterized by an high packing efficiency. This reflects ordering in the liquid (Figure 1.6), while limiting the increase in the thermodynamic driving force for crystallization yielding to a glass with an

entropic content barely higher than that of the crystal. This local order is incompatible with a LRO, thus leaving cavities (highly free volume zones) within the atomic structure. The distribution of clusters strongly depends on the characteristic atoms (their size and the character of bonds) and on the cooling rate. Slow cooling rate favors a denser structure with the presence of a significant percentage of fully icosahedra, while the result of a high cooling rate will be a structure having a higher free volume with the presence of fragmented icosahedra and non-Frank-Kasper polyhedra.

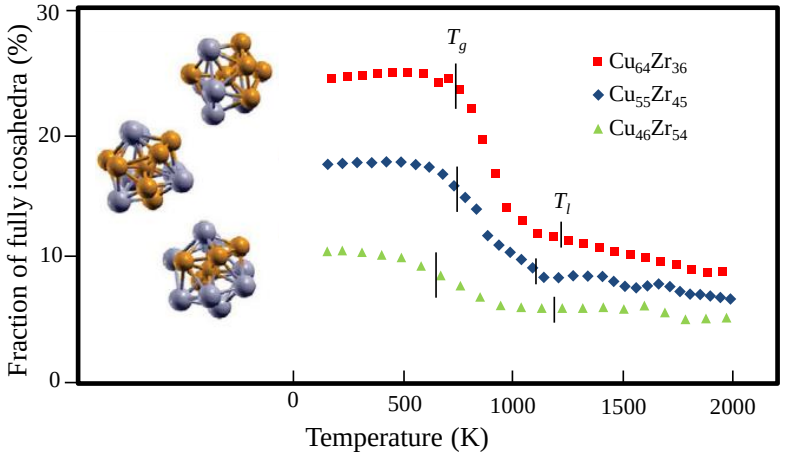

Figure 1.6 *– Evolution of Cu-centered icosahedral order with cooling for three compositions* Cu_xZr_{100-x}*. An increment of x favors the formation of icosahedra [19].*

The cluster-based model is appropriate only for binary systems. Other compositions which consist of four or more constituents have to be fully analyzed yet. Even though there are some evidences of local order for these multicomponent alloys (as reported from scattering data), SRO and MRO have not been fully understand yet. Fundamental questions about what determines the packing density and how the properties are affected by it are still partly unsolved.

1.3 Production of bulk metallic glasses (BMGs)

The first metallic glass has been discovered by Duwez and co-workers in 1960 [23] by a rapid quenching of $Au_{80}Si_{20}$ from the liquid state, Figure 1.7. The obtained glass was in the form of ribbon with an average thickness below 50 μm [23]. Afterwards, a big scientific effort have been devoted to increase the critical glass diameter to obtain the so-called bulk metallic glasses (BMGs) whose thickness can reach 10 cm which can be interesting for applications. In that respect, it is important to cite the work of Turnbull's group first [24] and of Inoue's group [25] which significantly improved the technical ability and the scientific knowledge to obtain larger and larger BMGs (Figure 1.7). The major challenges to obtain a large-diameter BMG was to avoid heterogeneous nucleation sites (oxides or impurities) which favor crystallization as well as to select an alloy which can become amorphous at relatively low cooling rate (large GFA) [1, 10, 26, 27]. Another crucial aspect is that the low heat conduction, so that the core of specimen could crystallize (slower cooling rate) [26, 27], explaining why the first metallic glasses were produced in a ribbon form.

We have already discussed that the amorphisation of metallic alloy requires a rapid cooling rates (up to 10^8 Ks^{-1}) to avoid crystallization. The composition can be tuned to favor the amorphisation with

the development of the icosahedral SRO in the supercooled phase (section 1.2). On this basis, some empirical criteria have been developed [8, 10, 27, 28].

In Figure 1.8 it is reported the influence of the internal structure (expressed in terms of configurational coordinate) on the system potential energy, namely the Gibbs free energy which can be related to the phase stability [8]. The crystalline phase lies in the deepest minimum which corresponds to the lowest energetic configuration [5, 8]. Glasses are metastable and occupy minima with an higher energy. While a single crystalline phase is usually present, different glassy phase can be obtained depending on the imposed cooling rate (Figure 1.1, lines 1 and 2) [5]. Glassy state minima can be extremely deep meaning that they can have a very high (meta)stability. Hence, a significant amount of energy (k_bT) is required to cross the energetic barrier and transform them into the crystalline phase. However, the glass atomic structure can undergo structural relaxation if a small amount of energy is provided to the system, as can be noticed by the presence of several oscillations within the same minimum. This corresponds to atomic re-organization favoring a compact structure with a reduction of free volume [5, 8].

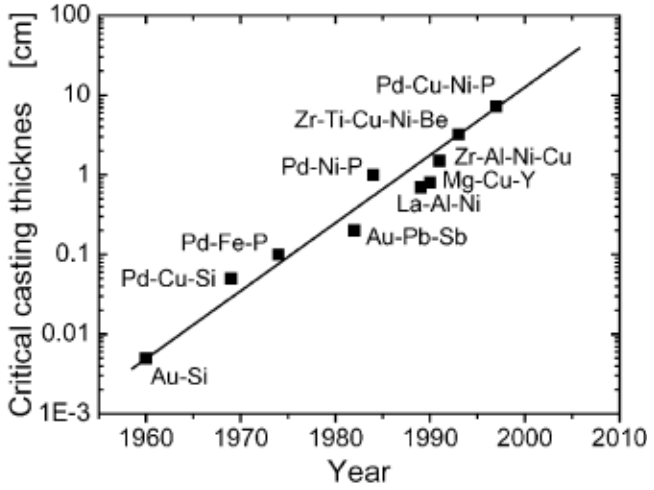

Figure 1.7 *– Historical evolution of BMGs with increasing critical casting thickness [26].*

The GFA can be enhanced by incrementing the barrier which separate the glassy phase from the crystalline one or by lowering the minima correspondent to the glassy phase (Figure 1.8). In case of binary systems (such as ZrNi and ZrCu) the efficient icosahedral packing and their strong chemical affinity stabilize the glassy phase (Figures 1.5 and 1.6). The high negative enthalpies of mixing stabilize the supercooled region and avoid phase segregation phenomena. The presence of deep eutectics in the equilibrium phase diagram provides a stable liquid phase even at low temperatures which is indicative of an atomic order even in the liquid state. Moreover, at the eutectic points the reduced glass transition temperature $T_{rg} = T_g / T_l$ (T_l is the liquidus temperature) approaches one meaning that the system tends to freeze immediately after cooling from the liquid state. The chemical confusion in a binary system is expressed by the difference of atomic radii of the constituent atoms which have to be higher than 12% favoring a disordered configuration. All these factors contribute to destabilize the crystalline phase, to increase the energetic barrier for crystallization and the GFA. We can anticipate that the glass forming interval for Zr_xNi_{100-x} alloys which has been studied in this PhD thesis is extremely large ranging over x values from 10 up to 80 (section 2.1).

Up to now we have presented some empirical rules to produce an amorphous alloy, Nagel and Tauc proposed an electronic criterion to predict the highest (meta)stability with respect to

crystallization as a function of the alloy composition [29]. This criterion has been developed especially for binary alloys and it has been validated in the case of AuP and AuSi metallic glasses and, partly, in the case of ZrNi and ZrCo amorphous ribbons [30, 31]. This criterion states that when Q_p – the scattering vector of the first sharp diffraction peak, FSPD – is equal to $2k_f$ (twice the Fermi wavevector), then an energy gap opens between the valence and conduction bands. This mechanism is associated with a stabilization of the glassy structure. Although this criterion is still somehow qualitative especially in the case for transition metals alloys such as ZrNi and ZrCu [32], we used it to predict the amorphous behavior of ZrNi thin film metallic glasses (TFMGs), providing also information about compositions with have an higher tendency to crystallize (section 3.5).

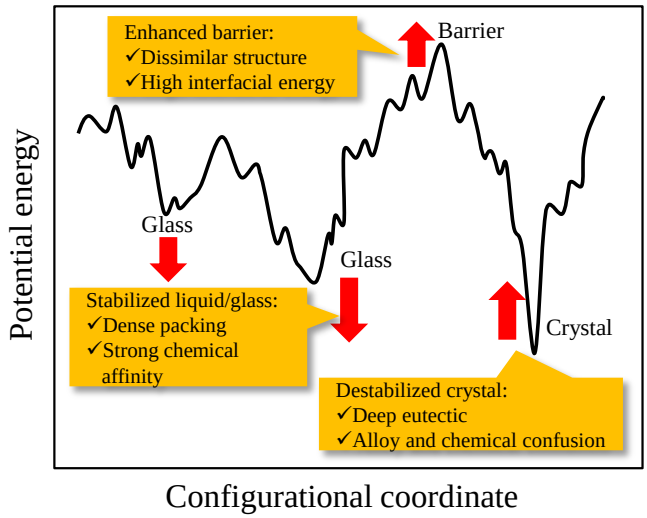

Figure 1.8 *– Schematic trend of the free energy for different atomic configurations of ZrCu. The mechanisms which improve the stability of the glassy phase are reported [8].*

It is important to mention the fact that most often BMGs are constituted by four or more atomic components (Figure 1.7) with a marked difference in atomic radius to avoid crystallization, reducing the required cooling rate, while enhancing the critical casting diameter [1, 26, 27]. One of the most studied BMGs $Zr_{41.2}Ti_{13.8}Cu_{12.5}Ni_{10}Be_{22.5}$ (Vitreloy1) can be obtained with a cooling rate below 10 K/s, meanwhile the technological progress allows the improvement of rapid cooling rate techniques thus expanding the alloy spectrum which can be transformed in the glassy state [1, 26, 27]. Vapor phase techniques can provide an extremely rapid cooling rate which can induce the formation of thin film metallic glasses (TFMGs) [33]. Among the various vapor phase techniques, sputtering plays a major role with the possibility to accurately tune the microstructure and the alloy composition (see sections 2.2 and 2.3).

1.4 Functional properties of bulk metallic glasses (BMGs)

The aim of this section is to review the main functional properties of BMGs. We first analyze the magnetic and the corrosion resistance properties of BMGs, then we will in-depth focus on electrical resistivity, which has been investigated in this PhD work in the case of ZrNi TFMGs.

One key aspect that has not been yet highlighted is that most often the physical, chemical and mechanical properties of BMGs are higher than the crystalline counterparts because of their disordered

atomic structure that can be considered completely homogeneous with the absence of defects such as dislocations, grain boundaries, and phase segregations [1, 27]. Contrary to crystalline materials, these properties are strongly dependent on the thermal history and the composition of the BMG (section 1.2) [8]. Furthermore, the presence of several atomic constituents (usually from three to five) and the lack of LRO leads to a difficulty in modeling and explain their physical properties. For these reasons, the physics behind a certain functional property has not be fully unraveled.

Most of the studies of magnetic properties of BMG deal with soft ferromagnetic materials, which can be easily magnetized, but do not tend to conserve magnetization. Fe- and Co-based BMGs have interesting soft magnetic characteristic which implies a low coercivity (< 5 A/m), a high saturation magnetization (> 1 T), and a high magnetic permeability with reduced hysteretic losses [1, 10, 26, 34]. These properties arise from the microstructural homogeneity and the absence of magneto-crystalline anisotropy. Moreover, annealing treatment leads to a material that has improved soft magnetic properties, as reported in Figure 1.9a where an annealing treatment of 600 seconds at the temperature of 723K has been applied to Fe-based BMGs [34]. The key point is that any crystalline phase which nucleates from a glass has a very fine and uniform-distributed microstructure since it is directly nucleated in the uniform glassy matrix without segregations. This the case of the alloy $Fe_{72.5}Si_{10}B_{12.5}Nb_4Cu_1$ (FINEMET) which shows a dispersion of α-Fe in an amorphous matrix conferring a relative magnetic permeability (> 200000), a very small coercivity of (0.53 A/m), and a saturation magnetization of 1.24 T [1].

The homogeneous structure is responsible also for the superior corrosion resistance of BMGs. Corrosion phenomena that most likely are enhanced in the presence of grain boundaries of discontinuities in the crystalline phase (pitting corrosion) are strongly limited. Thus BMGs can be employed in aggressive and harsh environments with high temperatures, oxidizing atmospheres, and corrosive media. The passive film developed in Fe- and Cr-based BMGs has been found to be around 20 to 25 nm, homogeneous and constituted in prevalence by Cr oxides which enhance corrosion resistance [1, 28, 34]. In the case of Mg-based BMGs, Gebert *et al.* [35] reported a superior corrosion behavior in aqueous environments compared to that of Mg and the conventional AZ31 alloys (Figure 1.9b) due to the combination of different superficial oxides formed by the several atomic constituent (Figure 1.9b). Other results reported by A. Inoue [34] have shown that the corrosion resistance of Zr-based BMGs in acid solutions (1M HCl) is higher than the pure Zr metal. As for magnetic properties, the corrosion resistance can be increased by tuning the composition and selecting heat treatments [1].

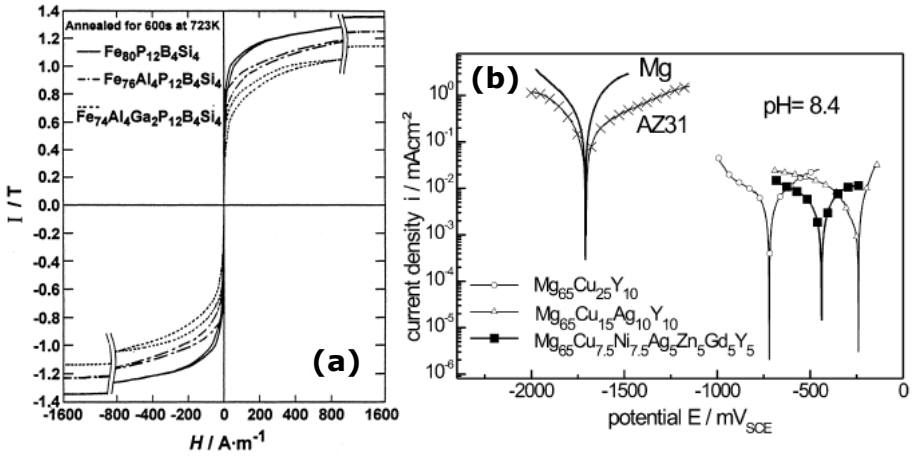

Figure 1.9 *– (a) Hysteresis curves of annealed Fe-based BMGs with soft magnetic properties [34]. (b) Current density vs. potential curves of Mg-based BMGs compared pure Mg and AZ31 alloy, experiments are recorded in alkaline solution with pH 8.4 (sr = 0.5 mV/s) [35].*

One of the first work on electrical resistivity of BMGs has been carried out in the late 70's by H.S. Chen [36] who study the electrical properties of Au-Ge-Si and Pd-Au-Si metallic glasses in a ribbon form. He found that BMGs have an electrical resistivity two orders of magnitude higher than their crystalline counterparts ($\rho_e \geq 100$ μΩ cm) even if the grain boundary scattering is completely avoided. The origin of the higher resistivity values come from their disordered structure which limits the electron mean free path. Furthermore, most of BMGs are characterized by having a small and negative temperature coefficient of resistivity (TCR), meaning that ρ_e decreases when increasing the temperature (Figure 1.10) [1, 36]. This is a significant difference with respect to crystalline metals in which electrical resistivity increases with temperature (enhanced electron-phonon scattering).

The analysis of electrical resistivity as function of the temperature allowed to obtain interesting information about the glass transition and the crystallization temperatures, respectively T_g and T_x [36, 37]. In Figure 1.10 is reported the trend of ρ_e/ρ_0 – where ρ_0 is the electrical resistivity at room temperature – as function of the temperature for a $Zr_{60}Al_{15}Ni_{25}$ BMGs. At the beginning, ρ_e/ρ_0 decreases with a negative TCR $(\alpha = d\ln\rho_e / dT)$, afterwards when the sample has reached the supercooled liquid state there is an inversion of slope leading to a positive TCR. The increment of ρ_e can be attribute to the enhancement of atomic mobility in the supercooled liquid state which enhance carriers scattering phenomena. Once the crystallization is completed, there is a drop of ρ_e as expected since crystalline materials have a reduced electrical resistivity. A further increment of the temperature beyond T_x leads to a positive TCR as found in most crystalline alloys. Even if T_x is always detectable the T_g can be more difficult to extract due to its second order nature. However, T_x can always be considered as the upper limit of T_g thus having important information about the stability of the glassy state [30]. The analysis of ρ_e has also a fundamental role to obtain T_g and T_x for thin film metallic glasses (TFMGs), in which the small amount of matter did not allow standard differential scanning calorimetry (DSC) measurements [30, 33].

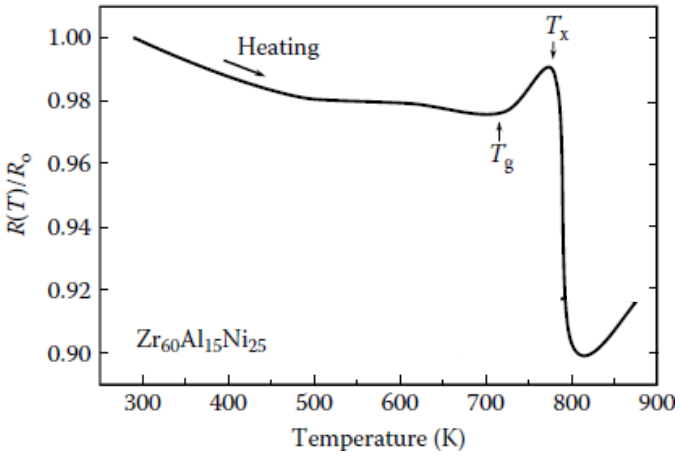

Figure 1.10 *– The electrical resistivity as a function of the temperature for $Zr_{60}Al_{15}Ni_{25}$ BMG [1].*

The first works on electrical resistivity as a function of composition in BMGs have been studied by H.S. Chen [36]. The case of binary ZrNi BMGs has been investigated by Morel *et al*. [38], Altounian *et al.* [39], and Pekala *et al.* [31]. ZrNi BMGs show a parabolic profile of resistivity and TCR (α) which have the maximum for average solute concentration around 50 (% at.). This trend can be roughly explained considering the entropy enhancement of the system reaching a more disordered configuration which favors electron scattering phenomena (Figure 1.11).

An interpretation of these trends can be inferred by the use of Nagel and Tauc criterion, which manages to provide information about the stability of the different glassy states. The Nagel and Tauc criterion [29] states that the maximum of electrical resistivity ρ_e is reached when Q_p – the XRD scattering vector corresponding to the first sharp diffraction peak (FSPD) – is equal to $2k_f$, twice the Fermi wavevector [30, 39]. This condition also implies that this composition will have the highest negative TCR as well. With this criterion, Buschow *et al.* [30], successfully predicted the maximum of resistivity and of the negative TCR for different compositions of ZrNi and ZrCo BMGs. This criterion allows also to predict the composition for which there will be a change in TCR from negative to positive. In fact, when $Q_p \ll 2k_f$ it is expected a positive TCR [30, 39]. While Q_p can be easily extracted from XRD data, k_f can be calculated as

$$k_f = \left(\frac{3\pi^2 \bar{Z}}{V_a} \right)^{1/3} \tag{1.2}$$

where $\bar{Z}$ is the average valence and V_a is the atomic volume defined for metallic glasses as

$$V_a = \frac{\bar{A}}{\rho N_a} \tag{1.3}$$

where N_a is the Avogadro's constant, $\bar{A}$ the averaged atomic weight and ρ the density [40].

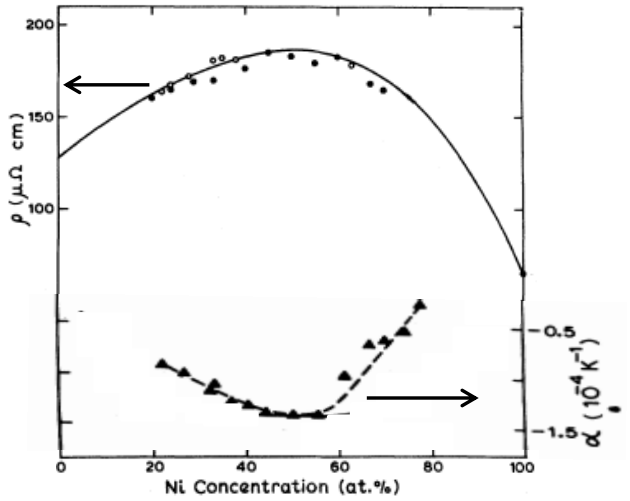

Figure 1.11 *– Electrical resistivity (ρ) and temperature coefficient of resistivity (α) as a function of the Ni concentration for ZrNi BMGs [39].*

1.5 Mechanical properties of bulk metallic glasses (BMGs)

The comprehension of mechanical properties of BMGs has a central role within this PhD thesis aiming to explore the mechanical properties for small-scale metallic glasses, i.e. thin film metallic glasses (TFMGs). In this section, we start to review the main deformation mode of BMGs with an in-depth analysis of inhomogeneous deformation occurring at room temperature. The relationship, atomic structure-mechanical properties will be fundamental to comprehend the deformation mechanisms related to the formation of shear bands. Furthermore, it will be analyzed the elastic constants, the indentation and scratch behavior as well as the fracture, with the idea to present the basis for the

understanding of the changes occurring at the small-scale, while also presenting the key elements for the interpretation of results.

1.5.1 Deformation modes

There are several reviews dealing with the mechanical properties of BMGs such as Schuh *et al.* [41], Greer *et al.* [3], Trexler *et al.* [42], M. Chen [43] as well as the book of Suryanarayana and Inoue [1]. Here, we aim to introduce the main aspects of the mechanical properties of BMGs, while refer readers to the previous cited reviews for an in-depth analysis.

Figure 1.12a shows the deformation map for a Zr-based BMGs [41]. The deformation maps were first developed by F. Spaepen in 1977 [44] and recently implemented by Schuh *et al.* [41]. Different deformation modes are present as a function of the normalized temperature (T/T_g). At $T/T_g < 0.8$ and low normalized shear stress (τ/μ), BMGs deforms elastically (with a negligible flow). For the same range of T, if the shear stress is increased BMGs undergo to a *inhomogeneous* flow that is characterized by intense localization within thin shear bands leading to a brittle-like fracture, Figure 1.12b [1, 3, 41-43]. On the other hand, for low τ/μ and high temperatures BMGs experience a *homogeneous* deformation where each volume element of the specimen contributes to the strain [1, 41, 42]. This deformation behavior can be thought as the viscous flow in the supercooled liquid (Figure 1.12a), and it is characterized by the possibility to obtain large deformations (Figure 1.12c). In this regime, the relationship shear stress-strain rate can be linear (Newtonian behavior) or not (non-Newtonian behavior) [41]. In the second case, the viscosity is not a constant showing a strain rate dependency. The inhomogeneous deformation can occur even at high T in the supercooled liquid regime if the shear stress is high enough. The deformation maps can also be drawn by plotting the strain rate as a function of the reduced temperature [41]. The low-temperature inhomogeneous deformation has a rate-independent strength response, but there is a strong influence of shear strain rate on shear banding spacing and serrated flow patterns (section 1.5.3) [41].

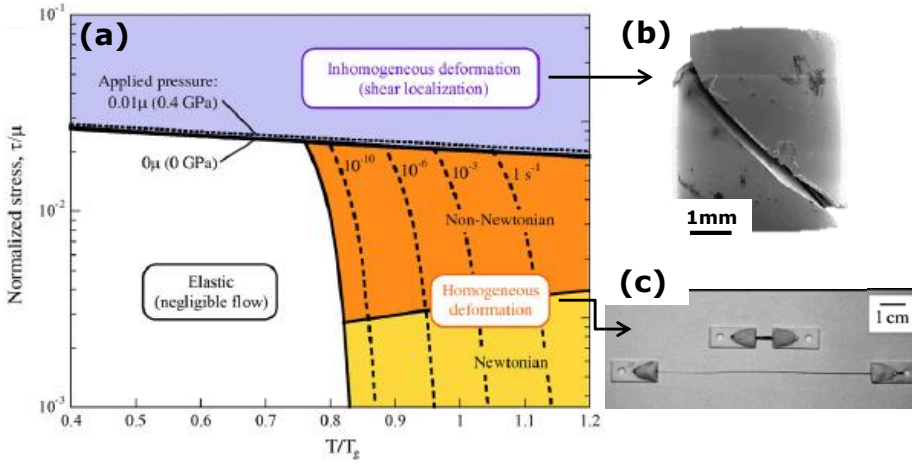

Figure 1.12 *– (a) Deformation map for metallic glasses, showing inhomogeneous (b) and homogeneous (c) deformation [41].*

It should be noted that these maps provide qualitative details of the flow mechanisms as a function of applied stress, strain rate, and temperature. Information regarding the evolution of the glass

structure during deformation and the fracture behavior is not captured. Notwithstanding, it can be observed that – since a metallic glasses are characterized by a structural homogeneity without crystalline defects – the elementary atomic mechanisms at the basis of each deformation mode will be the same [1, 41] and section 1.5.2.

Another important aspect is that homogeneous deformation is a characteristic of metallic glasses which is not experienced by crystalline materials and it is of a fundamental interest in shape-forming operations. This property allows the production of components with a very complicated shape, while avoiding the shrinkage effects since there is not an abrupt transition of the volume during cooling (Figure 1.1b) [27, 45]. On the other hand, the Achilles' heel of BMGs is the brittle-like behavior at low temperatures or high stresses with the localization of deformation within narrow shear bands undercutting structural applications [3].

1.5.2 Elementary mechanisms of deformation

The exact origin of the local atomic motion is not fully unraveled yet due to the "strange" nature of BMGs which are constituted of metallic elements while lacking LRO (section 1.2). Contrary to crystalline materials, an elementary description of local strain on the basis of the dislocation motion and local bond rupture is no more possible. Also the effects related to dislocations interaction with phase segregations or grain boundaries do not exist in BMGs. For these reasons, at the atomic scale, accommodation of shear strain in metallic glasses is believed to occur via local rearrangements of atoms around free volume-rich regions. Hence, the local strain in BMGs requires higher energy and stresses [1, 3, 41].

There are two main theories that describe the plastic flow and deformation behavior of metallic glasses. The first one proposed by F. Spaepen [44], referred as the "*free-volume*" model, theorizes that the deformation occurs through a series of diffusion-like atomic jumps into vacant sites within regions of large free volume (Figure 1.13a). The activation energy for strain accommodation is thus quite low. Local jumps are triggered by a shear stress and they can be considered as the diffusional flow in crystalline materials.

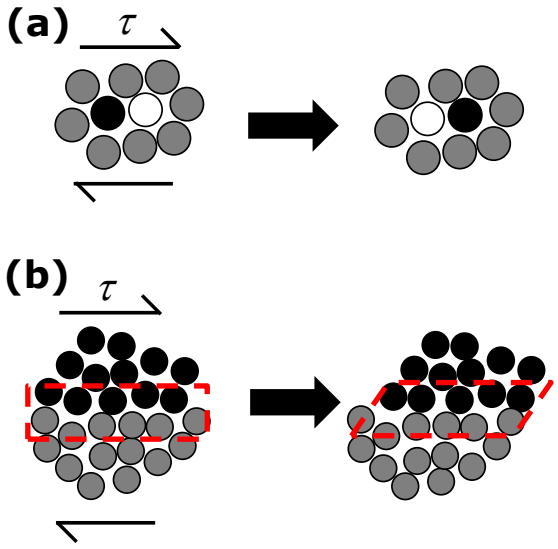

Figure 1.13 *– Schematic of atomic deformation mode in metallic glasses. (a) the local atomic jump after Spaepen [44] and (b) the shear transformation zone after Argon [46]. Modified from [41].*

The second model proposed by A.S. Argon [46] considers the presence of shear transformation zones (STZs) within the structure of a metallic glass (Figure 1.13b). STZs are essentially a group of atoms which easily undergo an inelastic deformation when a shear stress is applied, as shown in Figure 1.13b. On average, STZs have a size (diameter) of ~ 1 nm, containing a few tens to few hundreds of atoms [3, 43]. The density and size of STZs depends on the glass structure, indeed there is a marked effect of the thermal history and of the composition [41]. During a STZ operation there is a high local distortion from an initial to final equilibrium position through an intermediate activated state of high-energy (Figure 1.13b). In a metallic glass, subjected to an uniform tensile stress, STZs are activated among many potential sites which have a different energetic content. The activation of STZs depends on the applied stress level as well as on the local free volume content which in turn is determined by the glass atomic arrangement (section 1.2). Hence, contrary to the elements responsible for plasticity in crystalline materials (i.e. dislocations), STZs have a broad spectrum of energy distribution. Due to their small size STZs cannot be identified by using TEM nor it is possible to quantify them. However, at low temperatures, the continued propagation of the applied shear strain occurs when one STZ creates a localized distortion (dilatation) of the surrounding material, which triggers the planar coalescence of STZs, nucleating the so-called *"shear bands"* (see section 1.5.8).

The STZs model and the atomic-jump free volume model share some common features which, according to Schuh *et al.* [41], are:

- both mechanisms are characterized by atomic movement forward the stress direction involving the crossing of an energetic barrier,
- both mechanisms are thermally activated, even if the activation energy for STZs is higher than diffusion-like atomic jump, since a higher number of atoms is involved,
- both mechanisms are dilatational, which means that the local atomic structure is be dilated during the stress-induced local deformation.

While both theories can be adopted to the study of homogeneous deformation in BMGs, Falk and Langer [47] successfully implemented the model of STZs for the analysis of low-temperature shear deformation of metallic glasses. Several studies adopt STZs model to describe the process of nucleation of shear bands among which Refs. [3, 8, 48]. For these reasons, in the following analysis we will use the STZs model for the description of the elementary deformation mechanisms of metallic glasses at room temperature.

1.5.3 Mechanical properties at room temperature: a general overview

BMGs exhibit a unique set of mechanical properties [2, 10, 27, 28, 34]. The yield strength (σ_y) is usually in between 1000 and 3000 MPa (Figure 1.14a), depending on the alloy composition and the cooling rate [8]. An exception is represented by Co-based BMGs which have a σ_y around 5000 MPa [1]. Zr-based BMGs usually have a σ_y of around 2000 MPa. For comparison this strength value is ten time larger than the stainless steel (304L) one [27] and always higher than the crystalline counterparts (Figure 1.14a) [2, 27]. For most BMGs, σ_y approaches a significant fraction of the ideal elastic limit (the atomic cohesion force) because of their liquid-like atomic structure with the absence of low-energy activated dislocations. The elastic modulus (E) ranges between 70 and 150 GPa which gives a very large elastic deformation, usually equal to 1.9% for Zr-based BMGs. BMGs can be considered as isotropic materials with two independent elastic constants commonly taken to be the elastic modulus (E) and the Poisson ratio (ν) [41]. A BMG is less dense than its crystalline counterpart (due to a

disordered structure, section 1.2) thus giving a reduced value of elastic modulus with respect to the crystalline counterparts [1].

The elastic energy defined as $E_{el} = \sigma_y \varepsilon / 2$ (namely the area underneath the elastic region of the stress (σ) – strain (ε) curve, Figure 1.15) is very large allowing large-scale reversible deflection and elastic energy storage. Coupling together the high yield strength, the reduced density and elastic modulus, it is possible to identify BMGs as materials with the highest performance index of mechanical properties such as the specific strength σ_y / ρ and the high resilience per unit volume and mass, σ_y^2 / E [2]. The hardness (H) is higher than crystalline counterpart (Figure 1.14b) and could be related to the yield strength by using [41]

$$H \cong 3\sigma_y . \tag{1.4}$$

Note that this assumption is valid only if metallic glass yielding is described by a Von Mises criterion [41].

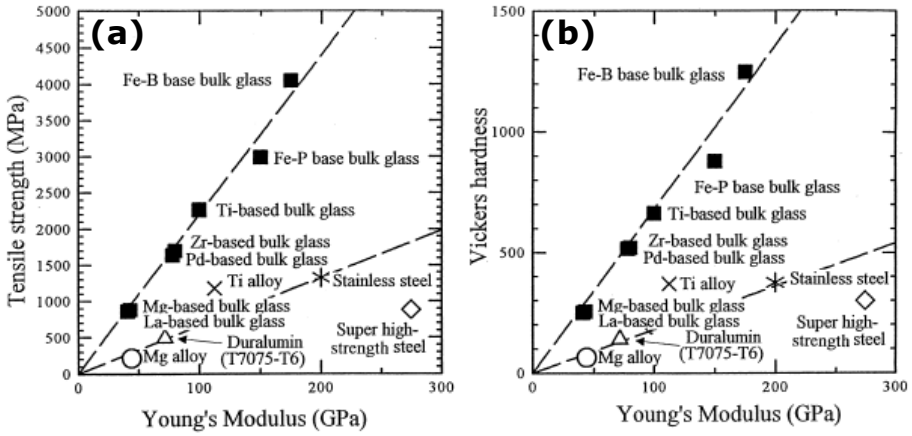

Figure 1.14 *– Comparison of tensile strength (a) and Vickers hardness (b) for amorphous and crystalline alloys [34].*

a) Stress-strain response

Figure 1.15a shows the stress-strain curve for Zr-based BMGs under compression [49]. BMGs display elastic-perfectly plastic behavior provided by the presence of constraints in this loading configuration. The plastic stress–strain zone is characterized by sections of elastic loading followed by load drops, which correspond to the formation and propagation of shear bands (Figure 1.15a inset). As the stress in a specimen increases to yielding (σ_y) a shear band is initiated and propagates across the specimen producing abrupt deformation and decreasing the stress. The specimen then reloads elastically and the process repeats, resulting in the characteristic serrated (pop-ins) flow pattern (Figure 1.15a inset). The *strain softening* represented by the load drop during plasticity is a characteristic fingerprint of BMGs [1, 41]. The formation of shear bands and shear localization has been considered a direct consequence of strain softening whose origin is attributed to a local drop in the viscosity.

Two connected reasons explain this phenomenon [1, 3, 41]. The first suggests that the viscosity in shear bands decreases during deformation due to the formation of free volume which reduces the resistance to deformation. Note the local dilatation phenomena occurs when a shear stress is applied

(Figure 1.13). A clear description of STZs dilatation is presented by Shimizu *et al.* [48] explaining the process of formation of shear bands (see also section 1.5.8). The second hypothesis suggests that local adiabatic heating occurs during shear bands propagation, which leads to a decrease of viscosity by several orders of magnitude, with local temperatures reaching T_g and even T_m. It has been proved that the extreme localization of deformation in narrow shear bands (~20 nm-thick), causes significant heat generation [50, 51]. BMGs can store an elastic energy several times higher than the crystalline counterparts and, when the external stress approaches yielding, the energy is not dissipated throughout the sample, but it is localized in thin shear bands [3]. Furthermore, the local strain in BMGs associated with STZs operations requires higher energies and stresses compared to crystalline materials leading to a significant heat generation [41, 42]. A classical fingerprint of heat generation during shear bands propagation is the vein pattern on the fracture surface (section 1.5.7) [3, 41, 52]. Both theories are connected since they originate from the high localization of deformation causing heat generation and free volume creation via local dilatation (Figure 1.13). The free volume within the shear band increases during deformation reducing the resistance to deformation and leading to strain softening.

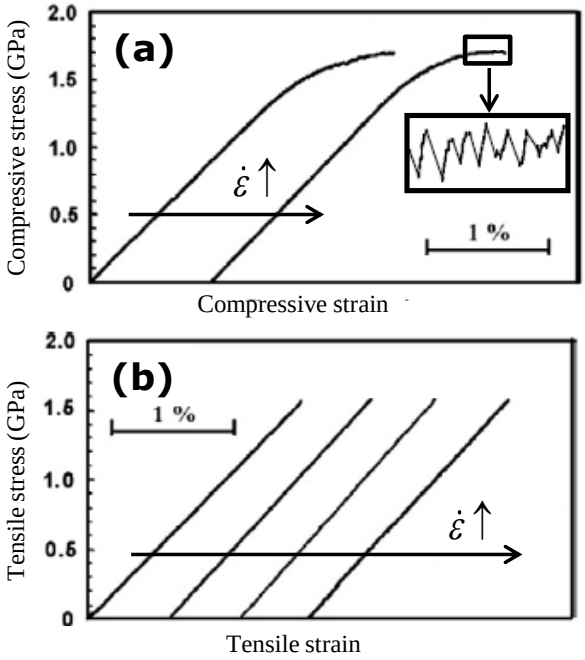

Figure 1.15 *– Compression (a) and tension (b) curves for Zr-based BMGs. Serration flow is highlighted in the inset in (a). Adapted from [49].*

In tension the deformation occurs within a single shear band with no plastic strain (Figure 1.15b) [42, 49]. Hence, the absence of flow defects (dislocations) leads to a macroscopic brittle-like mechanical behavior, characterized only by a large elastic period followed by a catastrophic failure. No strain rate ($\dot{\varepsilon}$) effects on both tension and compression curves (Figure 1.15) are present, even if the strain rate affects the serration flow (section 1.5.5).

b) Role of intrinsic and extrinsic parameters

Under a compression stress it has been demonstrated that a careful alloy selection can induce a large ductility. Das *et al*. [53] pointed out that the ductility of BMGs in compression is intimately related to

their specific microstructure at the atomic scale, which can enable easy and homogeneous nucleation of the shear bands and their continuous multiplication during deformation. They show that $Cu_{50}Zr_{50}$ has a limited ductility, while $Cu_{47.5}Zr_{47.5}Al_5$ experiences higher deformation (up to 18%) due to the presence of a more disordered atomic (enhanced confusion) which trigger STZs activation and multiplication of shear bands. Similar conclusions has been reported recently by Xu and Ma [54] that showed an enhancement of mechanical properties for highly disordered ZrCu metallic glasses, which have high propensity for shear transformation. Moreover, they show that a similar effect is reported for BMGs produced by a rapid quenching which favors a more disordered structure. Pan *et al.* [55] estimated the activation volume and the size of STZs of different class of BMGs by nanoindentation (section 1.5.5) and they found that BMGs which have higher plasticity are characterized by the presence of a large number of internal sites (STZs) prone to activation reinforcing the shear capability.

There are not only intrinsic effects (i.e. related to the sample atomic structure) that influence the BMGs mechanical behavior, but the external parameters are fundamental as well. It is the case of the formation of shear bands controlled by the specimen aspect ratio [3, 56] and the machine stiffness [3, 57, 58]. While high aspect ratio (height/diameter) samples involve the formation of a single shear band (Figure 1.16a), samples with smaller aspect ratio have a large part of their surface which is in the contact with machine cross-head, so that they are confined and cannot slide freely to generate the shear offset and leading to the formation of multiple shear bands (Figure 1.16b) [56]. Moreover, the lateral confining stress produced by the friction between the sample and the machine has more influence for specimens having a low aspect ratio again favoring the formation of multiple shear-band (Figure 1.16b), which enhance the ductility and strength of the specimen. This effect is similar to the previously reported example of highly-disorder BMGs, but here there is an external effect which affects mechanical properties.

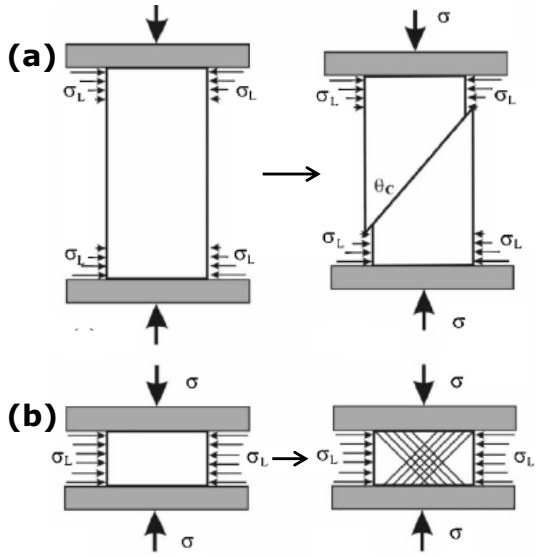

Figure 1.16 *– Effect of sample aspect ratio on shear bands formation in compression. A large aspect ratio favors the development of a single shear bands (a), while a small aspect ratio leads to multiple shear bands (b). Adapted from [56].*

The loading set-up plays a role in the mechanical response of the sample. We have already pointed out that the asymmetric behavior between the mechanical response in tension and compression derives from the constraint in the loading configuration in compression which induce a certain amount of plastic deformation. However, as quantitatively discussed by Han *et al.* [58], the stability of an

incipient shear band is affected by the elastic energy stored in the testing machine and related to the machine stiffness (k_M), which can dramatically influence the *apparent* mechanical behavior of BMGs (Figure 1.17a). An increment of k_m with respect to the sample stiffness (k_S) lowers the amount of elastic energy distributed into the machine, thereby reducing the machine effect on the shear band instability process. This enhances multiple shear bands formation (Figure 1.17b) instead of the development of a single shear band (Figure 1.17c). The machine stiffness can be increased by adding a frame parallel to the sample having a stiffness (k_F) which leads to an effective stiffness $k_{eff} = k_M + k_F$. Han *et al.* [58] derived a stability factor (S) for the formation of shear bands in the form of:

$$S_F = \frac{k_S}{k_M + k_F} = \frac{\pi E d^2}{4L(k_M + k_F)} \tag{1.5}$$

in which the sample stiffness (k_s) has been developed considering the BMG elastic modulus (E), the diameter (d) and the height (L). Both sample size and the machine stiffness play a role on the *apparent* mechanical behavior of a BMG. For a given machine stiffness, there is a transition from unstable to stable behavior when the sample size is reduced. Figure 1.18 shows that the maximum plastic strain before failure increases when the sample size is reduced from 4 to 1 mm with a stress–strain curve showing a positive slope at yielding (circle on the curves). Moreover, when the stiffness of the machine (k_M) increases, samples with the same size have a more stable behavior with enhanced plasticity and positive slope after yielding [3, 58]. For example, the 1 mm sample tested at a machine stiffness of 22800 N mm^{-1} shows no plasticity characterized by a macroscopic brittle-like behavior (Figure 1.18c), while the same diameter tested at k_M equal to 81200 N mm^{-1} behaves plastically achieving up to 20% of deformation (Figure 1.18a) [58]. A similar effect is reported in the case of an increment of frame stiffness leading to higher values of K_{eff} [3].

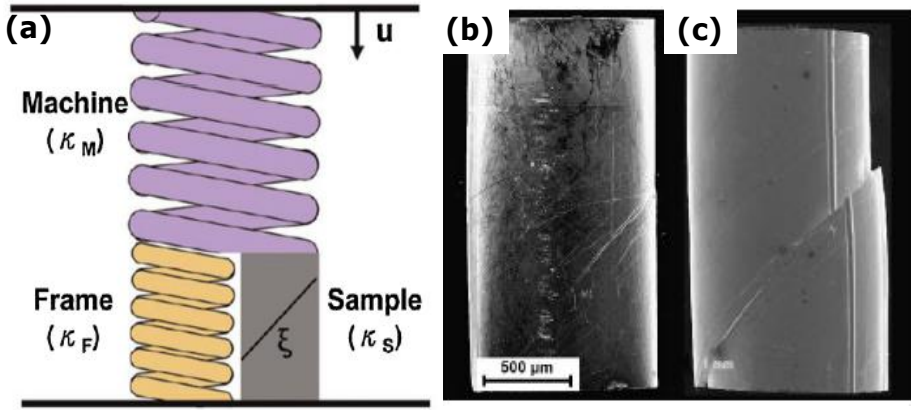

Figure 1.17 *– (a) Schematic showing the machine-sample-frame system and SEM micrographs of 1 mm 2:1 samples tested at a machine stiffness of 81.200 and 22.800 N mm^{-1}, respectively (b) and (c) [58]. A large machine stiffness involves a stable behavior with multiple shear bands throughout the sample (b), while an unstable behavior characterized by a single dominant shear band is found for low machine stiffness (c).*

The *extrinsic* parameters (the sample aspect ratio and the machine stiffness) have thus a capital importance when dealing with mechanical properties of BMGs. We showed that plastic deformation is enhanced for small aspect ratio specimens as well as for high machine stiffness, both acting to avoid strain localization and leading to multiple shear bands. The effect of sample size on mechanical properties is here only mentioned leaving the section 1.6 for an in-depth discussion of size-effects.

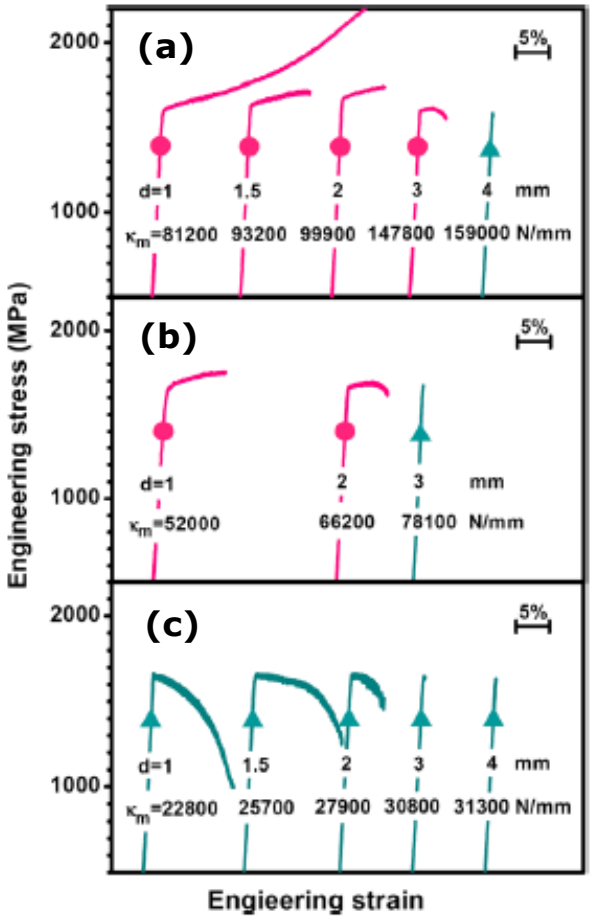

Figure 1.18 *– Stress–strain curves of 2:1 samples for different sample size (d) and machine stiffness(k_M). Plastic strain is enhanced for low samples diameters and high machine stiffness. Full circles and triangles represent the stable and unstable behavior, respectively [58].*

c) Fracture toughness

We conclude this section by analyzing fracture toughness and energy, respectively K_c and G_c. In principle, a low value of K_c and G_c should be expected because of their liquid-like atomic structure with absence of dislocations, likewise for ceramics or covalent glasses. While this is true for certain metallic glass types (i.e. Mg- and Fe-based), most BMGs (i.e. Zr and Pd-based) have K_c values of the same order as other crystalline materials and usually ranging from 70 to 100 MPa $m^{1/2}$ [2]. Therefore, the fracture energy $G_c = K_c^2 / E$ ranges from 100 to 1000 kJ/m^2 which is similar and even higher than the crystalline materials. Fracture toughness and energy is intimately related to the metallic glass atomic structure which in turn depends on the thermal history [59, 60]. The high fracture toughness and energy can be explained by combining the fact that plastic flow occurs at very large fractions of the theoretical strength with the capacity for develop extremely high local plastic deformation within shear bands [2, 3]. Figure 1.19 shows many shear bands initiating and propagating from the notch of a tough CuZr BMGs and crack blunting which is indicative of a ductile fracture mode [60]. As described for plasticity, the fracture toughness is dependent on the ease of shear bands formation which relies on the atomic structure (section 1.2). Even if the fracture toughness can be very high, the significant value of the yield strength leads to a reduction of the size of fracture process zone (FPZ, d_p) ahead of the crack tip which is defined as [2]

$$d_p = \frac{K_c^2}{\pi \sigma_y^2} \ . \qquad (1.6)$$

In the case of tough BMGs, d_p is usually smaller than 0.5 mm and even worse for brittle BMGs [2]. This again reflects the fact that no dissipation mechanisms are presented during shear bands propagation leading to extreme localization and to a macroscopically brittle behavior.

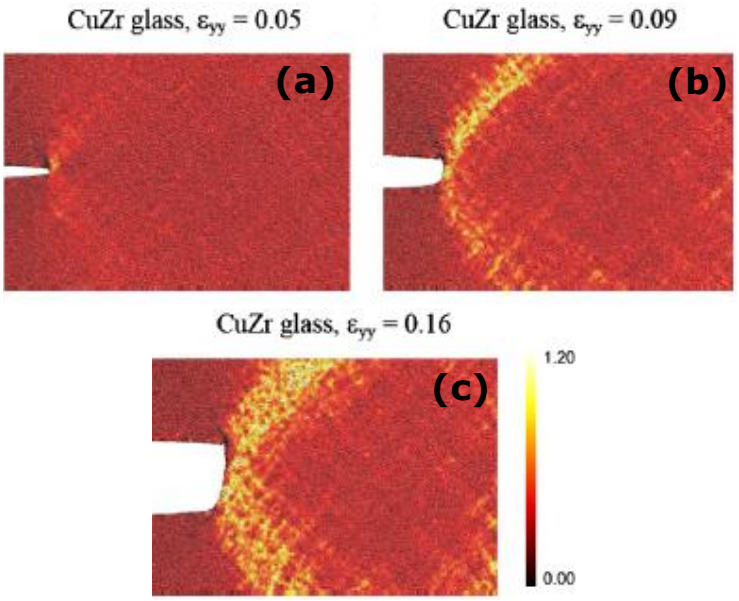

Figure 1.19 *– Simulations of crack propagation in a though CuZr BMG at different applied strains. Notice the crack blunting as well as the intense shear bands formation ahead of the crack tip. The colors indicate the local Von Mises strain [60].*

1.5.4 Elastic properties

The elastic properties directly reflect the atomic structure of BMG allowing a thorough understanding of the relationship structure-properties. In this section, it will be presented a general overview of the main elastic properties of BMGs emphasizing also their relationship with engineering quantities such as fracture toughness and energy, and ductility. More details can be found in a recent review of W.H. Wang [61].

We already mentioned the fact that BMGs can be considered as isotropic materials because of their liquid-like atomic structure. The two independent elastic constants characterize their behavior, namely the elastic modulus (E) and the Poisson ratio (ν) [26, 41, 61]. While the former is related to the atomic bond stiffness, the latter is rather linked to the compressibility of the material since it is defined as the ratio between the transversal and axial strain [61]. Hence, ν reflects the resistance that a material opposes to volume change with respect to shape change providing information about chemical bonding of atoms. Glassy materials exhibit a wide range of Poisson ratio from 0.1 to 0.45 [59, 61, 62]. The value of ν for BMGs is always higher than 0.28 and it can be influenced by the thermal history [59, 61, 62]. The Poisson ratio can be used to identify metallic glasses with respect to covalent glasses. In fact, a highly cross-linked network, a-SiO_2, involves a small values of ν ($\sim$ 0.15) with a significant content of free volume [5, 61, 63]. On the other hand, BMGs are constituted by metallic elements and

have a very compact structure favored by the presence of atoms of different atomic radius (sections 1.2 and 1.3).

In many cases the elastic properties of BMGs are reported in terms of μ and B, respectively the shear and the bulk modulus, which represent the resistance to an applied shear and to an hydrostatic stresses [41]. The density variation is in between 0.5 and 2% with respect to crystalline counterparts explains the difference in B which is about 6% less than crystalline counterpart [41]. However, BMGs exhibit μ and E values that are around 30% less than the corresponding crystalline phase, which cannot be explained only considered an enhancement of disorder coupled with an increment of bond distances. Schuh *et al.* [41] justify this change on the basis of the atomic rearrangement when a local stress is applied. As a matter of fact, in ordered crystals each atom is displaced by a fixed amount depending on the applied strain, while a BMG has a wider range of atomic environments and slightly less dense packing allowing local atomic displacements that differ from those prescribed by the macroscopic strain (distribution of STZs size), thus justifying the remarkable reduction of E and μ.

The relationship between the elastic constant and the fracture energy (or toughness) has been reported by Lewandowski *et al.* [59] for several class of glasses, showing that high values of Poisson ratio (ν) or low values μ/B involve an high fracture energy (Figure 1.20a and b). A transition brittle-to-tough occurs at ν higher than 0.31 or 0.32, or alternatively μ/B less than 0.4. These results has been more recently confirmed by Madge *et al*. [62].

The correlation between μ/B (or ν) and fracture energy is interpreted in terms of a competition between shear and dilatation. A low value of μ implies weak resistance to plastic deformation in shear, while a high value of B implies strong resistance to the dilatation required for crack propagation, which lead to the higher fracture energies (Figure 1.20b). A higher Poisson ratio represents a higher possibility for the material to shear under an applied stresses, indicating the presence of a large number of dispersed STZs which reinforce the shear capability of the metallic glass and promote the formation of multiple shear bands. The low ν (< 0.28) for a covalent glass is indicative of a limited movement of structural units constituted by long polymer-like chains with an high energy required for plastic flow. Moreover, a low Poisson ratio is related to the presence of large free volume zones which cause a low fracture toughness due to local intensification phenomena. On the other hand, a higher Poisson ratio is related to a more isotropic bonding behavior, so that plastic flow becomes easier favoring multiple shear bands formations and enhancing the fracture toughness and energy [59, 61].

Plummer *et al.* [63] related the elastic constants with the fragility index of metallic glasses (m_f), which has been already presented in section 1.1 (equation 1.1) and related with the thermodynamic stability of a glassy system. The lower is m_f the higher is the thermodynamic stability. Glasses can be grouped according to m_f in "strong" ($m_f \leq 29$), "intermediate" ($30 < m_f < 50$), and "fragile" ($m_f \geq 51$). A relationship between m_f and the ratio (B/μ) is in the form

$$m_f = 12(B/\mu + 0.67) \qquad (1.7)$$

A fragile glass is the more thermodynamically unstable and it will be characterized by the presence of a number of sites prone to undergo a local shear operation favoring the formation of multiple shear bands thus enhancing mechanical properties such as fracture toughness and energy and ductility. Hence, low values of μ/B lead to high thermodynamic fragility and enhance plasticity (Figure 1.21).

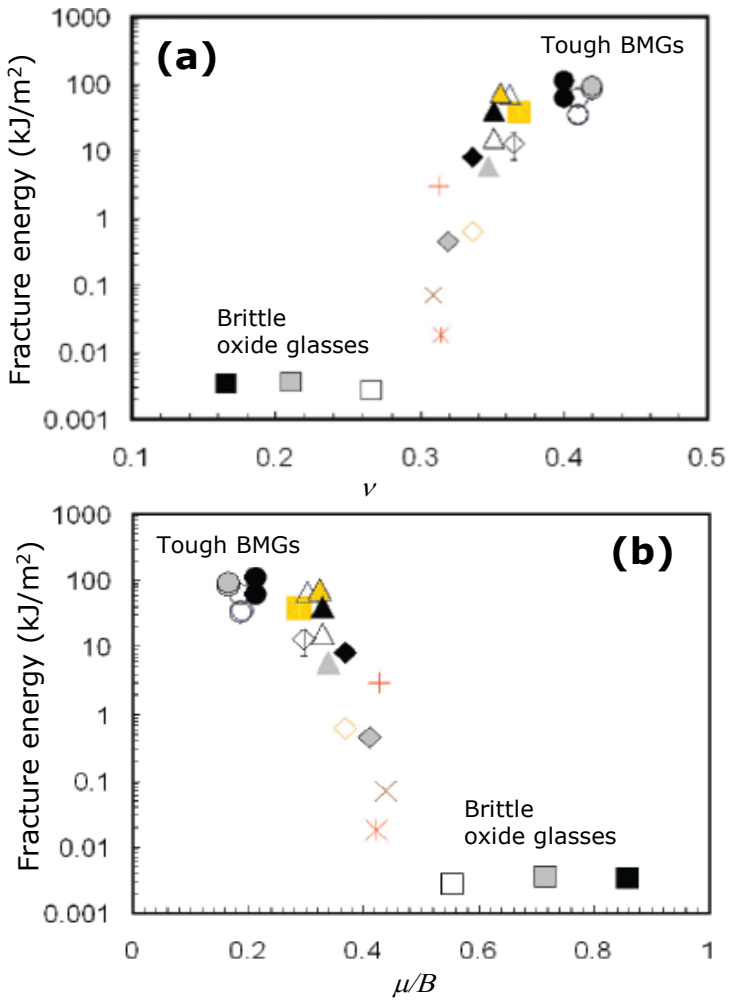

Figure 1.20 *– Correlation of fracture energy with Poisson ratio (a) and μ/B for several classes of oxide and metallic glasses. Adapted from [59].*

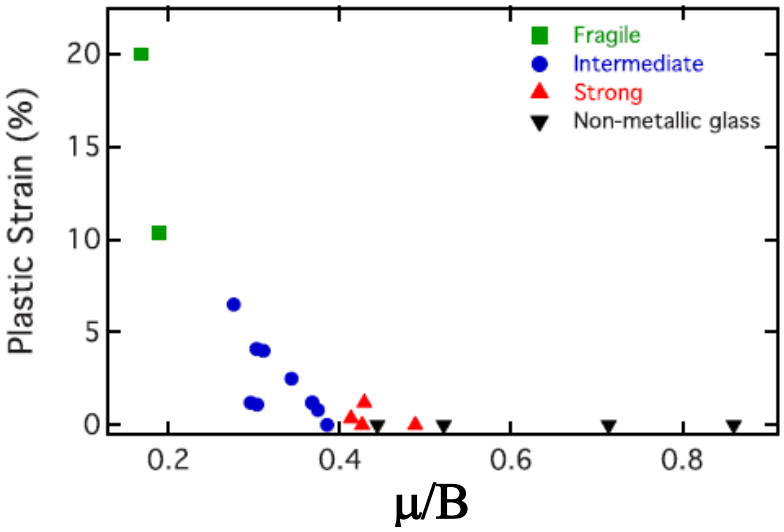

Figure 1.21 *– Plastic strain as a function of the ratio μ/B for different BMGs devised according to their fragility index [63].*

1.5.5 Viscoplastic behavior investigated by nanoindentation

Nanoindentation evolves from the microindentation test on bulk materials and has become a fundamental tool to extract the mechanical properties of small scale materials [64, 65]. The technique is based on the simple principle to indent a material with a tip of known geometry. The Berkovich tip, a three-sided pyramid with an centerline-to-face angle of 65.3°, is usually employed. The combined measurement of the penetration load and the indentation depth coupled with the estimation of the tip contact area allows to extract fundamental engineering quantities such as the elastic modulus and the hardness by using correlations presented in several models such as the Oliver and Pharr one [65]. Other advantages are represented by the possibility to induce severe local deformations avoiding specimen rupture, by the high spatiotemporal resolution of force and indent displacement, and by the possibility to carry out several tests achieving statistical data [64-66].

Nanoindentation has been widely employed for the characterization of BMGs owing to its ability to resolve individual shear events. Many authors [66-70] analyzed the load-displacement curve of several classes of BMGs under different loading rates exploring bursts (or *pop-ins*) formation and linking them to the activation of macroscopic shear band events. Figure 1.22 shows the load-displacement (*P-h*) curves for two types of Pd-based BMGs [67]. At low loading rates, the P-h curves are characterized by many discrete bursts of rapid displacement at constant load, similarly to the serrated flow observed in compression tests (Figure 1.15). In indentation experiments reported in Figure 1.22 the load is controlled, so the activation of a shear band gives rise to a burst of displacement. The effect of the loading rate on the bursts formation reflect the viscoplastic behavior of BMGs [55, 71]. A low loading rate allows local atomic rearrangements to accommodate the applied strain which favors a single shear bands formation.

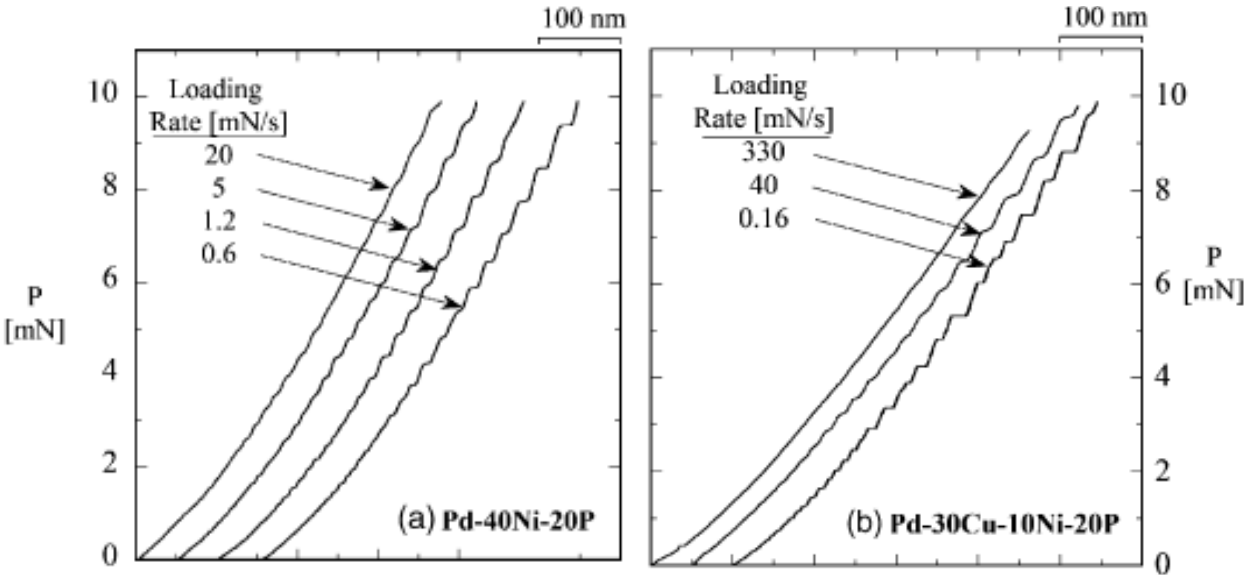

Figure 1.22 *– Load-displacement (P-h) curves for two Pd-based BMGs, the effect of the loading rate on burst formation is highlighted [67].*

On the contrary, an high load rate will not give sufficient time for atomic reorganization leading to an uniform load-displacement curve. In this case, the stress is not quickly relieved in the surrounding matrix and the yield condition remains satisfied in other locations under the indent which

favors multiple shear banding events which accommodate the applied strain. The nature of this effect is "*extrinsic*", namely related to the test conditions and can significantly enhance the mechanical properties, in the case of nanoindentation the hardness. This phenomenon can be used to extract the rate sensitivity coefficient and the activation volume [55, 72]. Figure 1.22 also shows that the depth increment within a single burst increases at higher loads (or indent penetrations). High load favors the large atomic displacements producing mature shear bands that can rapidly propagate [67, 69, 71].

Changes in local structure arising both from the cooling rate during casting or annealing and from the composition which cause a variation of free volume content and local order affecting the serrated flow which can be detected by nanoindentation (Figure 1.22a and b). Chou *et al.* [73] studied the effect of annealing treatments on a ZrCuTi thin film metallic glasses (TFMGs) showing structural relaxation phenomena during annealing which lead to an increment of nanoindentation hardness. Wang *et al.* [74] analyzed the effect of composition for different Zr_xCu_{100-x} thin film metallic glasses, suggesting a relationship between the highest (meta)stability and the largest values of hardness measured for specific film composition. Ristic *et al.* [75, 76] studied different composition of amorphous ribbons, with a special emphasis on ZrNi and ZrCu, linking the atomic structure with hardness and elastic modulus.

Most often the nanoindentation curves are reported in terms of strain rate ($\dot{\varepsilon}$) during nanoindentation that can be calculated as:

$$\dot{\varepsilon} = \frac{1}{h}\frac{dh}{dt} \tag{1.8}$$

where h is the indentation depth into the sample. This choice arises to best study the viscoplastic phenomena (serrations) occurring at different loading rate and indentation depths [67, 69] (Figure 1.23a-b). Moreover, according to Schuh *et al.* [41, 67] and Van Steenberge *et al.* [77] the indentation strain rate is directly proportional to the shear strain rate. The dependence of $\dot{\varepsilon}$ on h during loading is plotted in Figure 1.23a-b for as-cast and relaxed (obtained after annealing treatment) samples and for several values of maximum applied force (F_{max}) [77].

The strain rate during loading has similar values for both samples. Hence, the variation in hardness in Figure 1.23c depends on the amount of free volume produced in each sample during loading. Since the initial amount of free volume in the relaxed sample is reduced, the free volume production will be less pronounced [77]. After loading, the relaxed sample exhibits higher hardness than the as-cast one (Figure 1.23c). Figure 1.23a-b also shows that at fixed indentation depth (h), the strain rate is higher for larger F_{max}, meaning that the production of free volume under the indent is more pronounced for larger maximum applied loads, which in turn explains the enhanced serrations for the high load values (Figure 1.22). On this basis, it is also possible to describe the origin of the indentation size effect (ISE) reported in Figure 1.23c showing an increase of hardness for small indention depths, or low F_{max}. Similar results have also been reported by Fornell *et al.* [78] and Jang *et al.* [79].

The formation of shear bands during indentation can be observed by analyzing the indent image by atomic force microscopy (AFM) [66, 69, 70]. Figure 1.24 shows the formation of semicircular shear bands around the indent (a Berkovich tip has been used) at different loading strain rate of 1 (a) and 100 nm/s (b). Faster indentations produce a higher number density of more closely-spaced shear bands, while slower indentations favors the propagation of a single marked shear bands, as also shown in Figure 1.22.

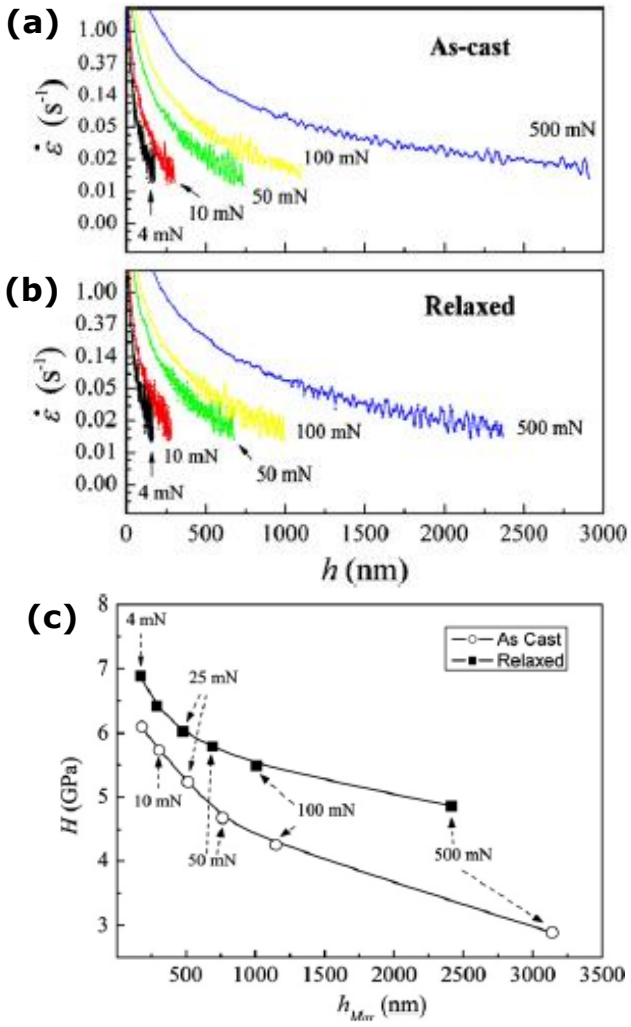

Figure 1.23 *– Strain rate as a function of the indentation depth (h) for an as-cast (a) and relaxed BMGs (b). (c)Dependence of hardness on the maximum indentation depth. Adapted from [77].*

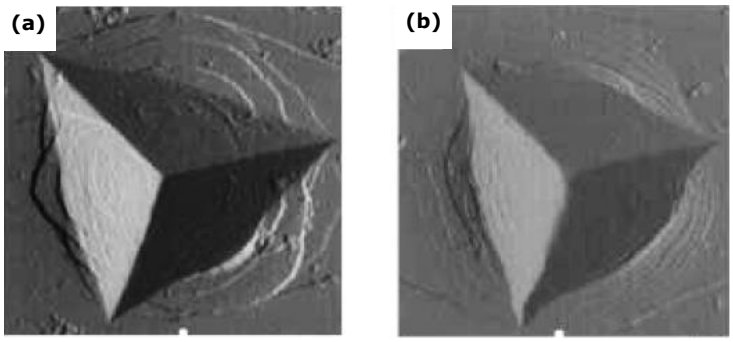

Figure 1.24 *– AFM images of indents in an Al-Fe-Gd BMG with an applied strain rate of 1 nm/s (a) and 100 nm/s (b) [70].*

1.5.6 Adhesion and tribological properties

The adhesion and tribological properties of a material can be investigated by scratch experiments. Most often they are conducted with a conical or Berkovich tip and different ramping-load schemes

with the normal load increasing linearly with the penetration. The scratches are then observed at the SEM analyzing the morphology evolution and relating it with the penetration curve or alternatively by analyzing the evolution of the coefficient of friction (COF), defined as the ratio between the measured lateral load with the imposed normal one. A review of nanoscratch and related failure mechanism can be found in Refs. [80, 81].

There are only few studies about the scratch behavior of metallic glasses, even if these materials involve a high yield strength and hardness, potentially providing an high scratch resistance [82-85]. Figure 1.25 shows the scratch morphology for a Zr-based BMG [82]. The indenter creates a groove that gets wider as the normal load increases (from left to right). A closer inspection reveals the presence of a large number of shear bands on the sides of the groove (inset 1 in Figure 1.25). These shear bands are oriented opposite to the scratching direction with an angle between 40° and 60°. With the increase in the normal load, this inclination is constant but their density increases (the distance between bands decreases). At higher loads a chip is formed (inset 2 in Figure 1.25), as shown also by an abrupt increase of the COF which then keeps constant due to tip glide.

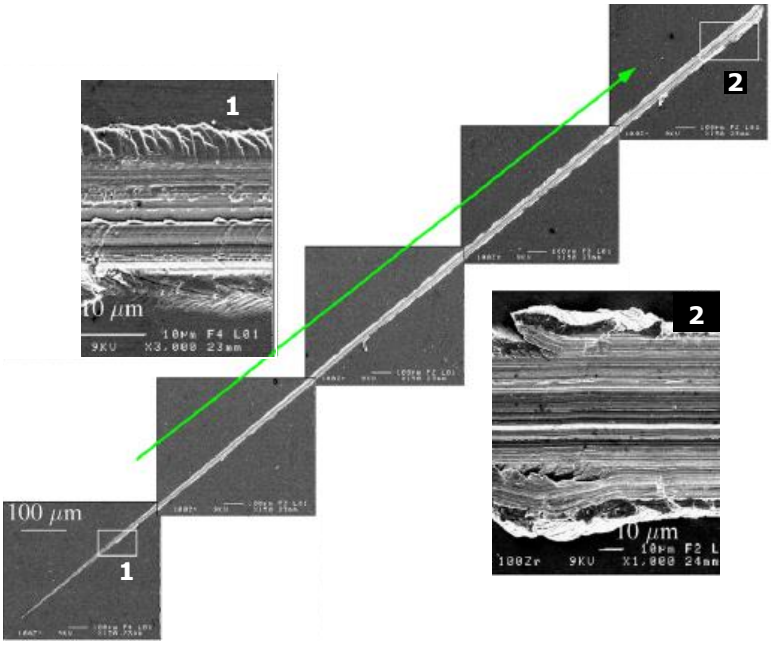

Figure 1.25 *– SEM images of a conical scratch in a Zr-based BMG. The shear bands and the chip formation during the scratch are highlighted in the inset 1 and 2, respectively. Adapted from [82].*

The nanoscratch has also been used to measure the adhesion and the wear resistance of coatings [33, 83-85]. Liu *et al.* [83] studied the coating of a $Zr_{47}Cu_{31}Al_{13}Ni_9$ TFMG deposited on 316L stainless, Figure 1.26. The penetration depth profile, the COF during the scratch test, and the corresponding scratch image with a loading ramp of 25–250 mN are shown. Once the penetration depth exceeds the film thickness (substrate scratching), the COF abruptly increases (vertical arrow in Figure 1.26). An abrupt decrement in the penetration depth and the residual depth curves is also present. As in Figure 1.25, some shear bands are formed parallel to the sliding direction (insets 1 and 2 in Figure 1.26). However, even if shear bands are formed, film debonding phenomena are not observed which indicates an high adhesion. With the further increase of the normal load, the film is squeezed out by the indenter leading to delamination with the formation of debris from the displaced substrate. The smoothness in the interior of the scratch groove and the small shear band spacing indicate a ductile deformation mode and good plasticity of the film.

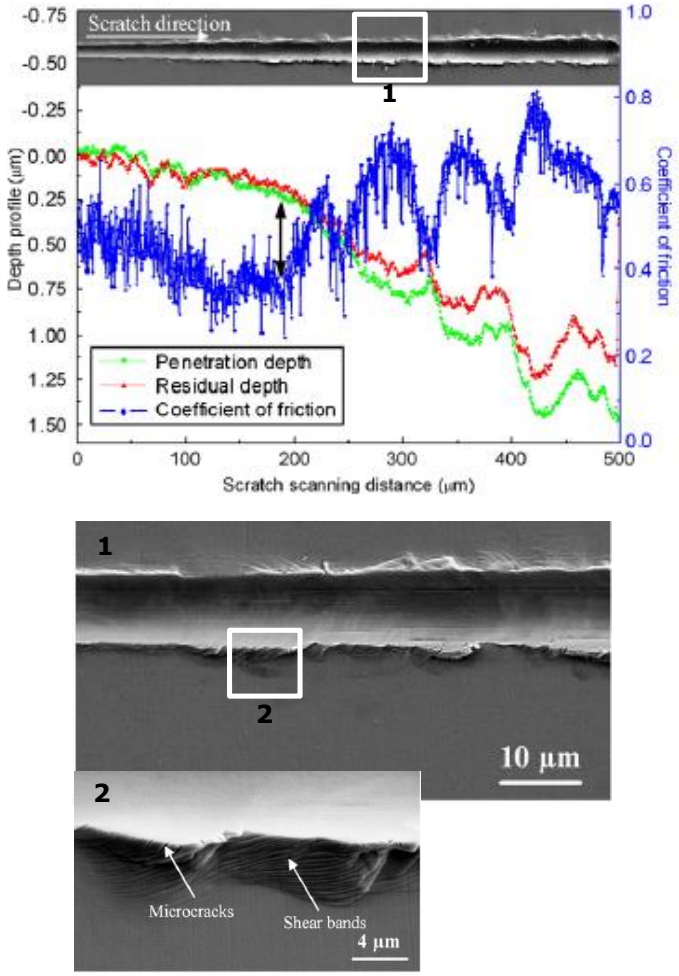

Figure 1.26 *– (b) COF and penetration depths versus the scratch distance for a ramping loading of 25–250 mN. In the inset the shear bands formations along the groove. Adapted from [83].*

1.5.7 Fracture behavior

The fracture behavior of BMGs at room temperatures is directly related to the formation and propagation of shear bands. We already mentioned in section 1.5.3a the fact that the extreme localization of deformation within thin shear bands (~ 20 nm) leads to a temperature rise provoking a viscosity drop and leading to shear softening phenomena. Lewandowski and Greer [50] performed fracture tests on a Zr-based BMG (Vitreloy 1) coated with a layer of tin (T_m = 207 °C). After fracture, the tin layer melts and beads up in the vicinity of the shear bands. The spatial-temporal temperature profile can thus be determined showing an increment of temperature in the vicinity of the shear bands up to thousands of degrees (>> T_g) in few hundreds of nanoseconds, while confirming that the temperature rise is a consequence of the shear band formation.

Such a substantial increase in temperature induces the formation of a fluid layer which leaves on the fracture surface *veins* and marked dimples as a characteristic fingerprint of BMGs fracture morphology [1, 86-89]. The vein pattern observed on fractured surfaces can be visualized as the structure formed when two glass slides are pulled apart with a thin layer of a viscous fluid such as Vaseline in between them [1]. To clarify this concept, Figure 1.27a shows the formation of the fluid layer during a compression highlighting the vein pattern on the fracture surface with the presence of spherical droplets, reminiscent of the local melting (Figure 1.27b-c) [90]. Note also the fact that the

fracture angle is inclined of about 45° with respect to the load direction which maximizes the shear stress. The fracture angle depends on the mechanical test. Under a compressive loading BMGs have a fracture angle in between 40° and 44° (Figure 1.27), while in tension is reported to be greater than 45° and usually ranging between 48° and 60° [41]. Furthermore, the fracture behavior of samples failed in tension is quite different from that on the compression [42]. In addition to the vein-like (dimples) structure, there are many round cores with different diameters on the tensile fracture surface. The veins radiate from these cores and propagate toward the outside, SEM micrographs can be found in Ref. [42]. Hence, it is suggested that the fracture of metallic glasses under tension should first originate from these cores induced by normal tensile stress on the plane.

Under tensile and compressive loading the fracture occurs by shear. Nonetheless – as we already pointed out in section 1.5.3a-b – the fracture in tension occurs within a major shear band, while in compression the density of shear bands is much higher, which can further justify the different origin of these two morphologies. Lastly, the vein pattern doesn't cover all the fracture surface, instead a *shear offset* (a smooth region) is present at the beginning and at the end of the fracture which is necessary for the shear bands activation (see section 1.5.8).

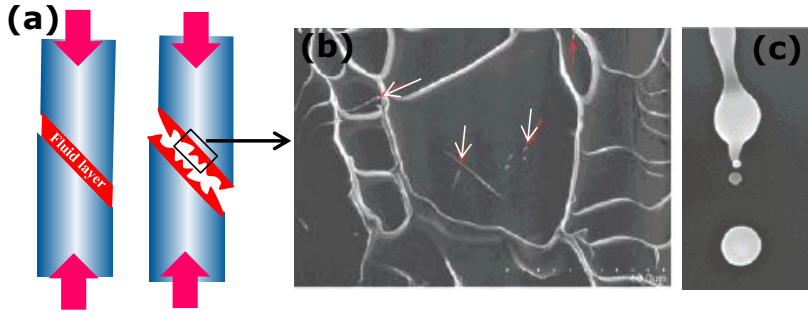

Figure 1.27 *– Formation of a liquid layer during compression test of BMG (a). SEM image of the vein pattern (b) and spherical droplets (c). Adapted from [90].*

The fracture surface relies on many other factors among which the intrinsic brittleness and ductility of metallic glasses [60, 86, 91, 92] and the curvature radius of the crack [92, 93]. Fracture is usually modeled by using the Taylor meniscus instability because of the formation of a liquid layer. The Taylor instability, is defined as an instability of an interface between two fluids of different densities that occurs when one of the fluids is accelerated into the other [94]. A common example is represented by a denser fluid such as water suspended above a lighter fluid such as oil in the Earth's gravitational field. The equilibrium between fluids is unstable to any perturbations or disturbances of the interface. If a parcel of heavier fluid is displaced downward with an equal volume of lighter fluid displaced upwards, the potential energy of the configuration is lower than the initial state. Thus the disturbance will grow and lead to a further release of potential energy, as the more dense material moves down and the less dense material is further displaced upwards [94].

The first description of crack propagation in BMGs using the Taylor meniscus instability has been made by Argon and Salama [95] and recently generalized by Wang *et al.* [92, 96] for brittle Mg-based BMGs and by Tandiya *et al.* [91] for ductile Zr-based BMGs. According to Argon and Salama model [95], the fluid meniscus advances due to a negative pressure gradient (suction, $d\sigma_N/dx$) zone ahead of the crack tip (Figure 1.28a). Driven by the negative pressure, the fluid meniscus is in an unstable state. An infinitesimal initial unstable perturbation with a wavelength of λ_I on the meniscus is activated and penetrates into the crack front on the X–Y plane, i.e. the fracture surface plane (Figure 1.28a). Once a critical value of a steady-state wavelength (λ_s) is reached, this negative pressure

induces the meniscus instability to penetrate as furrows within the fracture process zone, FPZ (Figure 1.28b). The perturbation cannot overcome the edge of the FPZ and it stops growing in the *x* direction, while expanding in the X-Y plane (Figure 1.28b). This mechanism when repeated generates large dimple (> 10 μm) and veins for a ductile BMG [91] (Figure 1.28d). On the contrary, a periodic corrugation pattern appears if the initial perturbation (λ_I) is *frustrated* and the fluid meniscus at the crack tip is kept stable ($\lambda_I < \lambda_s$). In this case, small damage cavities (< 100 nm) are formed in the FPZ ahead of the crack tip (Figure 1.28c and e). This mechanism has been described by Wang *et al.* for a brittle Mg-based BMGs [96], while the formation of cavities ahead of the crack tip has been clearly shown by Murali *et al.* [60] studying the brittle FeP BMGs with molecular dynamic simulations.

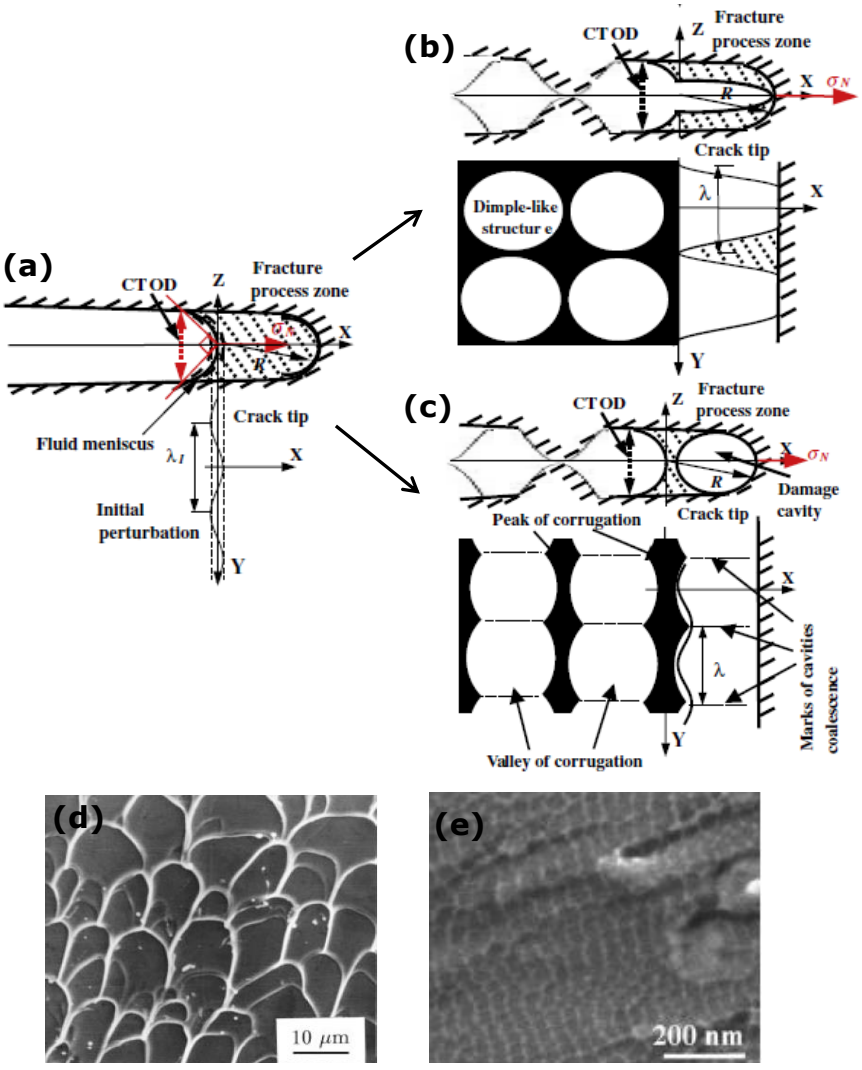

Figure 1.28 *– Sketch of the crack propagation. (a) The initial stage of the crack propagation. (b) Formation mechanism of dimples and veins. (c) Formation mechanism of corrugations. Adapted from [96].*

We will not enter in the conditions which lead to a specific fracture mode which will be discussed in the case of the fracture of thin film metallic glasses (section 5.2), we just point out that there exist criteria which can predict a specific morphology formation on a fracture surface which depends on the intrinsic brittleness or toughness of a BMG (section 1.5.3c). It is also important to underline that different morphologies vein-like and corrugation can appear for the same BMG, since

the corrugation formation depends on the crack curvature radius [93, 96]. The crack radius determines the size of fracture patterns. Therefore, even the same BMG can exhibit the ductile-to-brittle transition phenomenon. Jiang *et al.* [93] pointed out that a small curvature radius activate tensile transformations zones (TTZs) instead of shear transformation zone (STZs), leading to the formations of small cavitation even for ductile BMGs (Vit1). Through TTZ operations the stored energy is dissipated mainly by forming new surfaces, resulting in local quasi-cleavage zone ahead of the sharp crack tip. Similar results has also been reported by Wang *et al.* [92, 96] showing that large crack tip radius in a brittle Mg-based BMGs induces the formation of dimples. Xi *et al.* [86] related the fracture toughness (K_c) with corrugation or vein width (w) through:

$$K_c = \sigma_y \sqrt{40w} \tag{1.9}$$

where σ_y is the yield strength. Hence, the simple SEM observation of fracture surface can provide an accurate value of the fracture toughness.

1.5.8 Theories for shear bands nucleation and propagation

Some key elements to understand the physics of the formation of shear bands have already been presented in sections 1.5.2 and 1.5.3, where it has been introduced the concept of shear transformation zones (STZs) [3, 8, 41, 47]. STZs are preferred sites in which shear bands can nucleate whose origin is directly related to the structural inhomogeneity of BMGs (section 1.2). It has been demonstrated that the icosahedral order in Cu–Zr(–Al) corresponds to higher local stiffness (stability regions), while shear transformation preferentially nucleates from more disordered regions where the local stiffness and stability are low (Figure 1.29) [19, 20]. A rough picture of the atomic structure of metallic glasses is thus characterized by an elastic backbone (icosahedral) with unstable regions as embedded (STZs) which can be considered as "inclusions" [18]. Elasticity – discussed in section 1.5.4 – can thus be related to the bonds nature of the backbone, while plasticity is essentially related with STZ operations in free volume rich zones. At this point, three possible scenarios can describe the formation of shear bands [3, 48, 97].

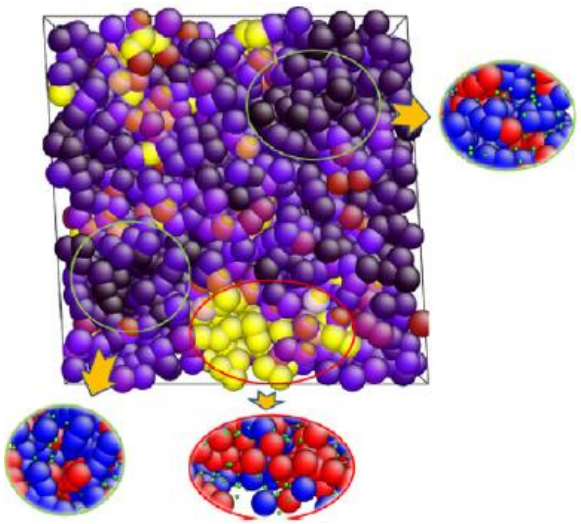

Figure 1.29 *– Activation of STZs in $Cu_{64}Zr_{36}$ BMG. The colors highlight the levels of atomic plastic strains. The highly packed dark purple regions are only elastically deformed (backbone), while the yellow ones (loosely packed) are involved in shear transformations [18].*

The first scenario consider the formation of shear bands as a result of the percolation of *homogeneously* activated STZs [3]. As long as the isolated STZs do not overcome the percolation limit, they can be reversed upon unloading. However, when the activation of a sufficiently large population of STZs exceeds the percolation limit a shear band is generated. STZs percolate along the maximum shear stress plane which is softened due to the activation of STZs (dilatation) and therefore would concentrate subsequent shear strains leading to a formation of a very thin shear band (section 1.5.3a). This scenario depicts a homogeneous nucleation of a shear bands, which means that the shear band nucleates from the structural fluctuations units inside the material itself, rather than extrinsic flaws that serve as heterogeneous nucleation sites.

The second scenario, which is more realistic for samples produced in laboratory, considers the presence of defects such as macroscopic porosity or surface notches which act as stress concentrators when a load is applied. Shimizu *et al.* [48] used simulations to study the yielding of metallic glasses in the presence of these defects (Figure 1.30a). They found that STZs preferentially nucleate from the more fertile sites and when a shear band reaches an critical embryonic size (~ 100 nm in length) propagates, thus developing a mature shear band. The effect of an imposed shear stress create a rejuvenated zone followed by and alienated softened region due to STZs dilatation (Figure 1.30b and section 1.5.2). The extreme localization and the atomic bonds rupture cause the formation of the liquid zone with heat generation (sections 1.5.3 and 1.5.6). The length scale effect on shear band nucleation has a capital importance in the study of size effects which will be analyzed in section 1.6. However, it has been demonstrated that the percolation of STZs causes the disruption of the icosahedral SRO and MRO during the formation of the shear band, leaving the formation of fragmented and highly unstable clusters, Figure 1.31c [8, 18-20, 97].

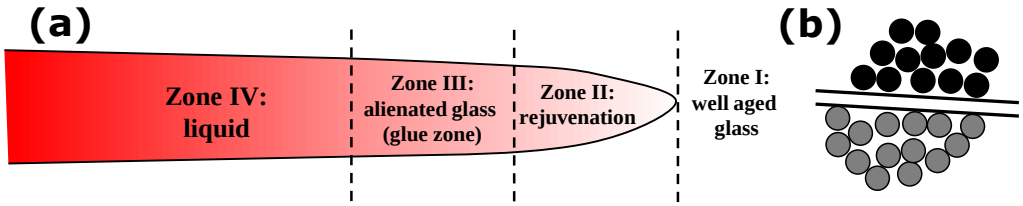

Figure 1.30 *– (a) The propagation front of a shear band. (b) An alienated STZ highlighting local dilatation. Adapted from [48].*

The third scenario describes the formation of shear bands as a two stage process [3, 97]. The first stage consists into the creation of a band for shearing by structural rejuvenation, which corresponds to the activation of STZs so that structure inside is disordered with the material being softened. The rejuvenation process is similar to the one described in the second scenario meaning that it is activated heterogeneously from stress concentrators, but the difference is that the shear strain throughout the band is small, and the temperature doesn't increase significantly. The rejuvenating front propagates as a shear wave (at the sound velocity), so that the local heating is limited (Figure 1.31a). Following the creation of the softened path, the second stage is activated with the synchronized sliding and shear along the rejuvenated plane (Figure 1.31b). As the shear offset is developed, the material involved in shear bands operations experiences large plastic strains with significant local heating and shear band thickens. During shear bands operation there is a marked reduction of icosahedral order (Figure 1.31b) [8, 18-20, 97]. A possible mechanism is identified in Figure 1.31c [8, 97]. This scenario is supported by the study of Han and Li [98] who analyzed the fracture surface of BMGs showing the presence of two shear offsets (smooth regions) with a vein pattern inside which arise from the material melt. This corresponds to the early stage of the sliding when the temperature

has not risen very high, followed by vein patterns where the band becomes hot. The presence of two smooth regions at both ends means the shear offset initiated almost simultaneously at the two tips and remained cold at the early stage of the shear-band sliding.

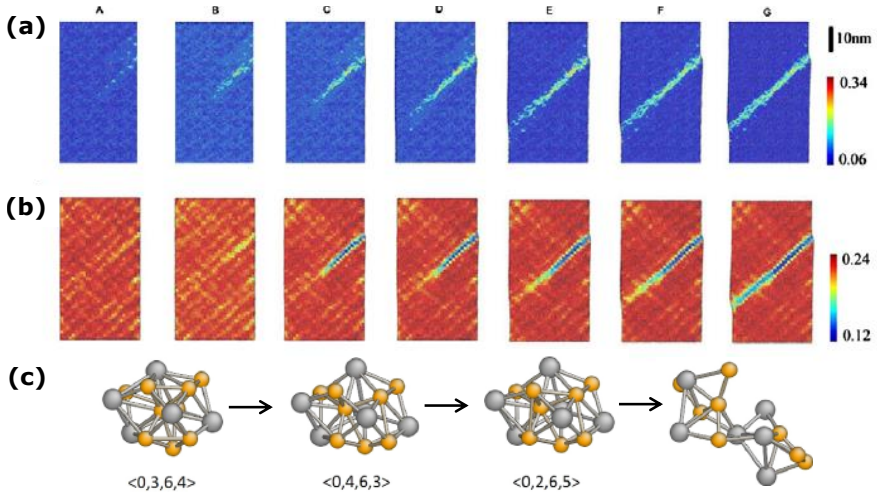

Figure 1.31 *– (a) Formation of the rejuvenated plane. (b) Fraction of icosahedra in the specimen showing a decrement inside the shear band (blue color). (c) Mechanism of the disruption of a solute-centered CuZr cluster. Adapted from [97].*

The described scenarios have a capital importance to understand mechanical size effects when moving toward a nanoscale sample (section 1.6). Here, we conclude this section by observing that the composition, the thermal history as well as the presence of heterogeneous defects can have a significant effect on shear bands formation and hence on the mechanical properties by promoting or not the formation of multiple shear bands (section 1.5.3). Specifically, by quenching at different cooling rates, different degree of structural ordering and percolation of the ordered clusters can be produced. For samples with higher degrees of SRO and percolation, the strength and shear modulus are higher, with more pronounced softening upon yielding, after which the strain tends to be more localized in the shear band (Figure 1.32a). On the other hand, a high cooling rate promotes the formation of a limited fraction of icosahedra (or Frank-Kasper polyhedra) leading to a more disordered structure which promotes the nucleation of multiple shear bands (Figure 1.32c).

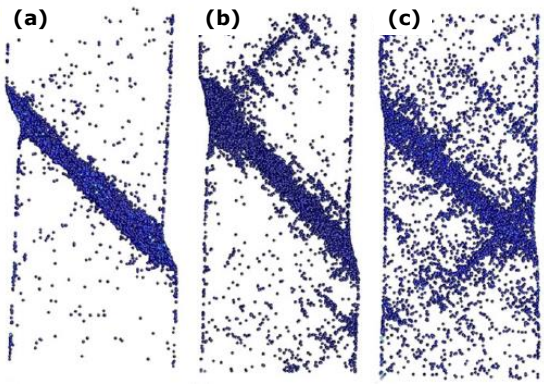

Figure 1.32 *– Comparison of the propensity for strain localization upon plastic deformation of $Cu_{64}Zr_{36}$ BMGs. Molecular dynamic simulations have been carried out at different cooling rates: (a) 10^{10} K/s, (b) 10^{11} K/s, and (c) 10^{12} K/s [20].*

A similar role is played by the composition as discussed in section 1.5.3b in the case of ZrCu and ZrCuAl BMGs. Lastly, the high defect sensitivity of BMGs can significantly degrade mechanical properties by concentrating the stress and leading to a sudden brittle fracture.

1.6 Mechanical size effects in metallic glasses

The main interest in studying the mechanical size effect in metallic glasses is related to the possibility to avoid the catastrophic failure of BMGs occurring at room temperature via shear bands formation as well as to better understand the deformation mechanisms (section 1.5.3). Furthermore, there is the possibility that at nanoscale metallic glasses behave in a different way with respect to the bulk counterparts [4], leading to an increment of the mechanical properties in terms of ductility and yield strength. These fascinating opportunities can have a capital importance for a number of application domains [33].

To emphasize how mechanical properties could change in the case of small scale metallic glasses, we can start highlighting the fact that the stress required to reach yielding in the case of the three scenarios reported in section 1.5.8 is not the same. As a matter of fact, while the first scenario involves a homogeneous nucleation of shear bands, the second and the third one consider the presence of flaws which can significantly reduce the amount of stress required for the shear band formation In the case of macroscopic samples, the presence of defects (porosity or notches) is inevitable, thus pinning the maximum strength to a value equal to the stress necessary to activate shear bands from these preexisting flaws. This is supported by simulations comparing deformation behavior of samples with and without pre-existing notches [99]. Figure 1.33 which shows the evolution of the strength (and elastic strain limit) as a function of the reduced temperature (T/T_g).

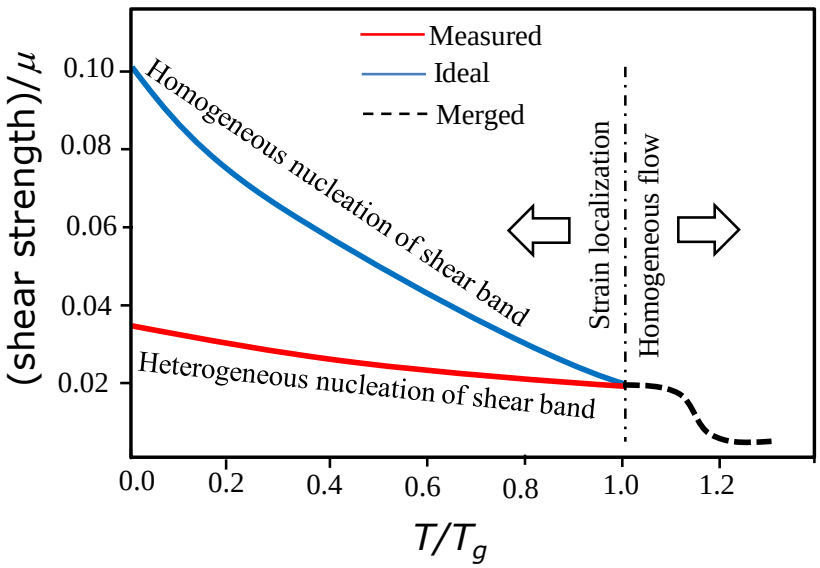

Figure 1.33 *– Schematic showing the merging of intrinsic strength and measured strength at T_g for a strain rate of 10^{-3} s^{-1}. The space between the two curves is the strength that can be reached by suppressing the heterogeneous nucleation of shear bands [100].*

The curve of ideal, upper bound elastic limit is derived from the analysis of Johnson and Samwer [101] which describes the temperature-dependent shear strain limit, in the form

$$\gamma_y = \gamma_{C0} - \gamma_{C1}(T / T_g)^{2/3} \quad (1.10)$$

where γ_y is the elastic strain limit in shear. This equation is valid for a typical strain rate around 10^{-3} s^{-1}. Recently, Ma and Cheng [100] validated the previous equation by setting the fitting parameters as γ_{C0} = 0.11 and γ_{C1} = 0.09. Since metallic glasses are isotropic, the equation 1.10 can be converted to obtain the ideal strain limit (ε_y) in uniaxial loading by knowing that $\varepsilon_y = \gamma_y / (1+\nu)$, where ν is the Poisson ratio. The result of the above model prediction is presented in Figure 1.33. At zero kelvin, the ideal elastic limit is predicted to be about three times the extrapolation of the measured elastic limit. At room temperature ($\sim 0.5\ T_g$), the ideal elastic strain limit is about twice that of the measured one, the latter being almost always close to 2% (section 1.5.3). Note that both curves converge at T_g when the deformation mode of BMGs changes to a continuous viscous flow.

The previous analysis is fundamental for size effects because the stress required for homogeneous nucleation of shear bands may be reached in sufficiently small metallic-glass samples, where flaws are absent (namely, they cannot overcome the external dimension of the specimen) such that shear-band nucleation becomes strength-controlling. Cheng and Ma [100], by using quantitative simulations, have shown that for a BMG with a uniform atomic structure and no extrinsic flaws or imperfections there is a limited probability for STZ percolation. This allows to attain very high strength values close to the ideal (ceiling) one with an elastic strain limit which can reach the values of equation 1.10.

In the recent review of Greer and co-workers [3], the possible mechanisms involved when reducing the size of the sample are clearly summarized. The first consideration is that the strength of the samples depends on presence and size of macroscopic flaws which can act stress concentrators. An analysis based on Weibull statistics is thus developed in which the likelihood of finding macroscopic flaws is significantly reduced when moving toward small scale sample. Specifically, if the sample size is lower than the critical size threshold necessary for the activation of heterogeneous shear bands, there will prevail the nucleation of homogeneous shear bands which involve an higher stress (regime I, in Figure 1.34a). If the sample has no defects, the stress would reach the ideal homogeneous stress determined from equation 1.10 (σ_{homo} in Figure 1.34a). For large size (and large flow defects), the strength behavior will be dependent on the diameter of the fracture plastic zone (FPZ, d_p) ahead of the crack tip, reported also in equation 1.6 as $d_p = K_c^2 / \pi\sigma_y^2$. A large FPZ can blunt the crack tip and limit the macroscopic brittle behavior, via multiple shear bands formation (Figure 1.19) [60, 91]. If d_p is greater than the size of the sample under test, brittle failure is not expected, thus making the metallic glass less sensitive to defects, plateau of regime II in Figure 1.34a.

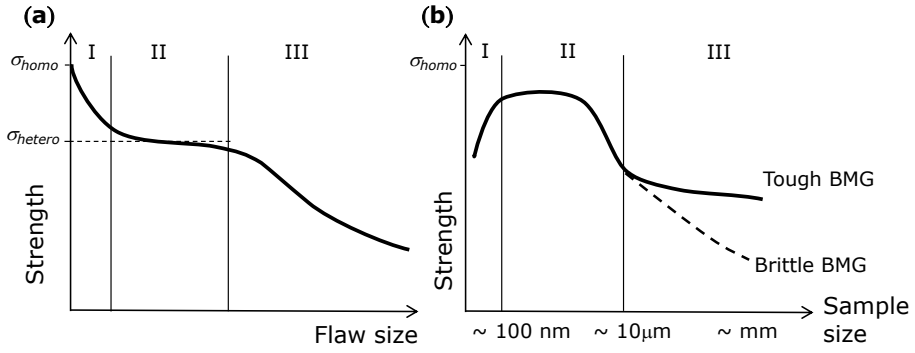

Figure 1.34 *– Schematic showing the strength as a function of the flaw and sample size, respectively (a) and (b). Different regimes are highlighted showing the difference between though and brittle BMG.*

Lastly, if the sample size still increases, there will be also the possibility of the presence of large defects greater than the plastic zone, thus leading to an abrupt reduction of strength (regime III in Figure 1.34a). The effect of composition will mainly play a role in the regime III by setting the length scale involved in the transition from zone III to II, see also the work of Yang *et al.* [57]. Tough BMGs (section 1.5.3), will have a larger d_p meaning that the region II (defect-insensitive) will be expanded even for macroscopic samples (~mm), regime III in Figure 1.34b. Brittle BMGs (small FPZ and cavitation) will show a sudden reduction of strength in regime III (Figure 1.34b). If the size of the sample is below 100 nm, surface effects will be dominant thus leaving a reduction of the attainable strength, regime I in Figure 1.34b.

1.6.1 Experimental observations of mechanical size effects

The previous reported analysis represents a general trend or the ideal case which is mostly deduced from molecular dynamic simulations and by knowing the mechanical behavior of BMGs. Other fundamental issues arise when the mechanical properties of small scale metallic glasses have to be tested. Obviously, one central point is represented by the manipulation and mechanical testing of specimens which should have a dimension of the order of few hundreds of nanometers. In the literature, there are two main categories of test used to investigate mechanical size effects: compression (or tension) of micro-nano pillars (which covers most of the studies) and tension tests of free standing film.

Micropillars are produced by using the focus ion beam (FIB) technique, in which an ionized gas (usually Ga^+) bombards the surface of a BMGs or of thick metallic glass coating. The result of a circular surface erosion is the production of a micropillar (Figure 1.35). The FIB-milling is well consolidate technique due to the ease of sample production with a possibility to accurately tune the diameter and taper angle of the pillar. Micropillars are then tested in compression by using the tip mounted on a nanoindenter. The stress-strain curve is thus recorded. The deformation can be observed directly during the compression (*in-situ* TEM) or after the load *ex-situ* usually in a SEM.

One of the first studies on compression test of $Pd_{77}Si_{23}$ micropillars has been reported by Volkert *et al.* [102]. Figure 1.35 shows the effect of compression for different pillars diameters ranging from 3.61 μm (Figure 1.35a) down to 140 nm (Figure 1.35d). There is a transition in deformation behavior from inhomogeneous, shear bands-mediated, deformation for large diameters (Figure 1.35a-b), to a homogeneous deformation for the thinnest one (Figure 1.35c-d). We discuss later a possible origin of this transition, but we can note that for a diameter very close to the critical length scale proposed by Shimizu *et al.* [48] (∼ 100 nm), the nucleation of a mature shear band is more difficult, thus activating different deformation mechanisms.

Figure 1.36 shows the stress-strain curve as a function of the pillar diameter. Large diameters pillars show an elastic-plastic behavior which also show a slightly increment of the yield strength, while small pillars are characterized by a "rounded" stress-strain curve. There is a large scattering of data especially for small diameters (as reported in the error bars). This trend does not correspond to the analysis proposed by Greer *et al.* [3] and Ma et Cheng [100], in which it is expected an increment of the yield strength for the highly confinement geometry. An explication could arise from the conical shape enhanced for thinner micropillars leading to a non-constant applied stress as well as from the contribution of the top rounded surface and FIB surface damage.

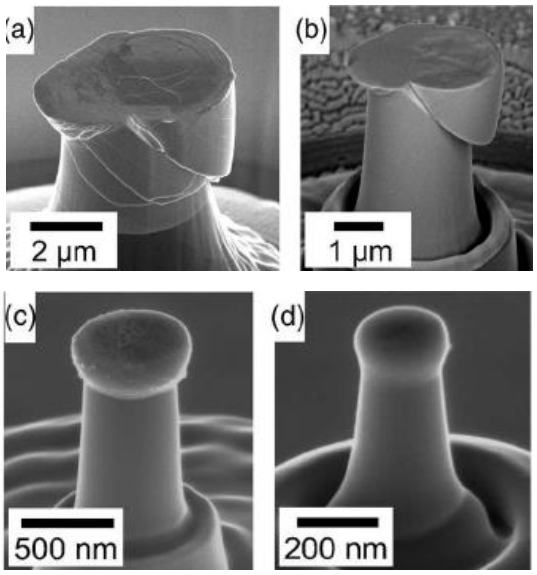

Figure 1.35 *– SEM images of deformed 3.61 µm (a),1.84µm (b),440 nm (a) and 140 nm (d) diameter pillars. The deformation mechanism changes from shear band formation to homogeneous deformation with decreasing column diameter [102].*

More recently Volkert's research group [103] confirmed the trend presented in Figure 1.36 for $Pd_{77}Si_{23}$ pillars, showing that the mechanical behavior for sample sizes larger than 500 nm involves an elastic-plastic flow regime very close to what observed for BMGs deformed in compression, but extended plasticity (Figure 1.15a). In this size-regime, displacement jumps during plastic deformation are detected and related to the intermittent kinetics of shear-banding during serrated flow (section 1.5.3).

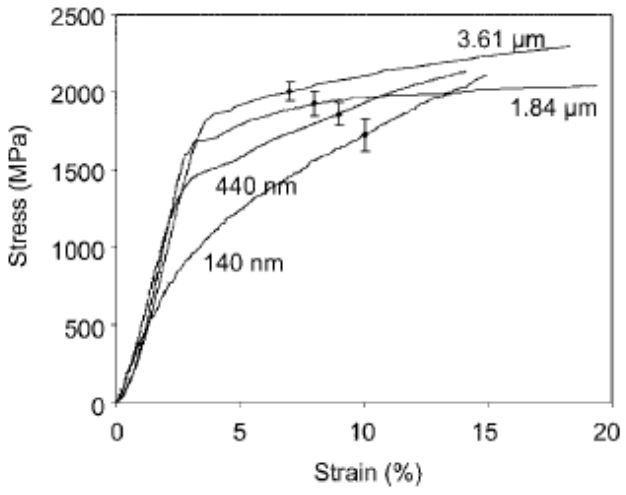

Figure 1.36 *– Stress-strain curves for different diameter micropillars reported in Figure 1.35 [102].*

Samples smaller than 300 nm in diameter exhibit a distinctly different stress-strain response without strain-jumps and a transition to plastic flow sets in at much lower stresses. Furthermore, they have shown that for diameters less than 500 nm the shear-band spacing becomes roughly twice the shear-band thickness itself, which potentially leads to an interaction with neighboring shear bands as also reported for BMGs [57, 58]. With decreasing the diameter the shear-band affected volumes

overlap, imparting deformation into the entire sample volume (homogeneous deformation). More interesting, they used this phenomenon to show that a transition in pillar mechanical behavior can be found at different loading rate even for thicker pillars (Figure 1.37). A low deformation rate allows smooth flow of pillars as big as 1 μm in diameter (Figure 1.37a-f) which leads to reduction of the shear band spacing approaching the internal length scale of the shear-band thickness. Obviously, the load rate required for a transition in small diameter pillars will be higher due to the enhanced confinement effect (Figure 1.37g-k).

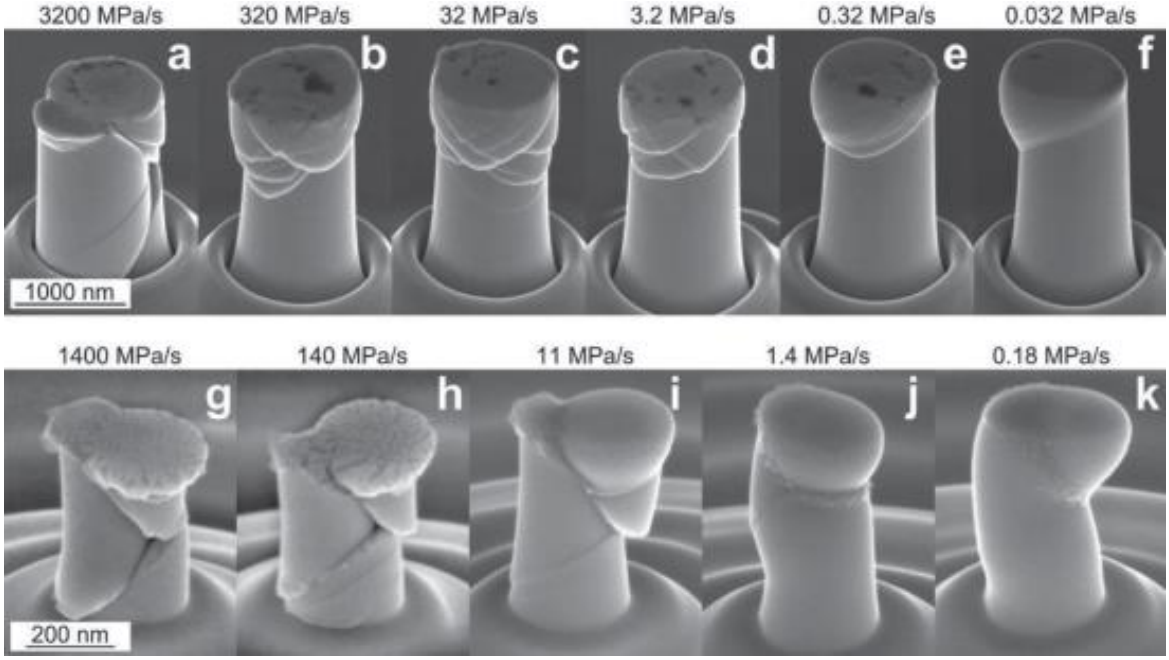

Figure 1.37 *– Compression of micropillars with a diameter of 1000 and 200 nm, respectively from (a-f) and (g-k). Reducing the loading rate pillars deform homogeneously [103].*

Other studies of Lee *et al.* [104] and Lai *et al.* [105], respectively on Mg- and Zr-based micropillars showed that the deformation mode even for small micropillars is dominated by visible shear bands (Figure 1.38a-c). More interesting, they found an increment of the yield stress which is higher than 80% over the value of the same alloy in the bulk form. Furthermore, this values increases if the diameter of the pillar is reduced, while a serration flow is visible for all the thicknesses (Figure 1.38d). Both authors modeled this increment in mechanical properties by using the Weibull statistics which show a reduction of the likelihood of defect formation when reducing the sample size, a concept in agreement with the general trend previously reported by Greer *et al.* [3]. Other results reported by Dubach *et al.* [106] on Zr-based micropillars indicate shear bands as the dominant mechanism even for small diameters (200 nm). Nonetheless, they did not observe any change in the yield stress, which is kept constant. Moreover, they also observe that the annealing treatment which reduce the free volume content do not affect the elastic limit. Similar results are confirmed in the case of Cu- and Zr-based micropillars Chen *et al.* [107] and Kuzmin *et al.* [108].

A better understanding of the elastic limit is critical for applications in the field of microscale components. A possibility is thus to carry out *in-situ* TEM compression test of micropillars allowing a direct observation of the microstructural evolution even for diameters below 100 nm. Nevertheless, there are not many studies dealing with this process due to the difficulty to realize precise samples without a taper angle and very small diameter [4, 107-109].

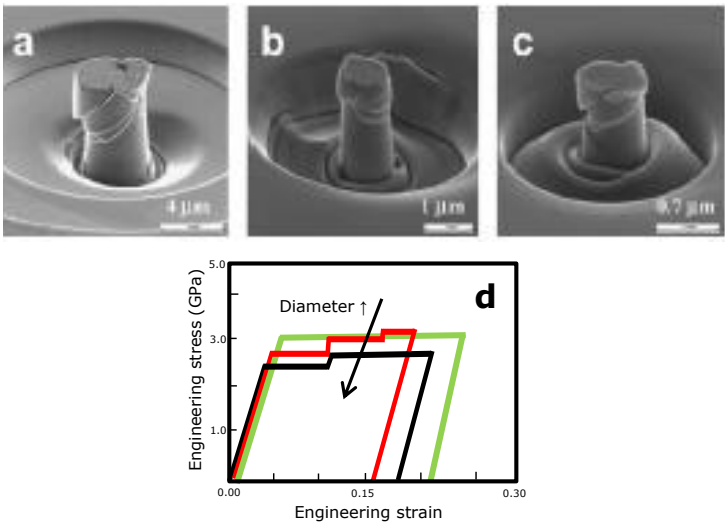

Figure 1.38 *– (a)-(c)Compression test of micropillars with a diameter of 3.8 μm, 1 μm and 700 nm, showing a shear band deformation mode. (d), The stress-strain curves [105].*

One of the most interesting work has been carried out by Chen *et al*. [109] as shown in Figure 1.39 reporting the case of two taper-free pillars with a diameter of 200 and 70 nm, respectively (a) and (b). While the 200 nm deforms via shear bands (note the white arrows and the presence of burst in the stress-strain curve), the 70 nm deforms homogeneously showing a rounded stress strain curve which resembles as in Figure 1.36. Pillars with a 200 nm of diameter have an elastic limit close to 1.8 GPa with no variation with respect to the bulk values for Cu- or Zr-based BMGs. Barreling phenomena are enhanced for the 70 nm diameter showing also a distortion of the pillar axis for large deformations. They explain the sample size effect considering the formation of shear bands as the only deformation mechanism even for small diameters. In fact, large pillar diameters plastically deform through the STZs operation which percolate creating a mature shear band. Decreasing the diameter the incipient shear band becomes slower in shear speed and with a small offset giving STZs elsewhere opportunities to activate. Indeed, they observed that with decreasing diameter the serrations become less visible and more uniform in the stress-strain curves. This leads to a morphologically homogeneous deformation, though still accommodated by intrinsically inhomogeneous local events which have no chance to develop into a global shear band.

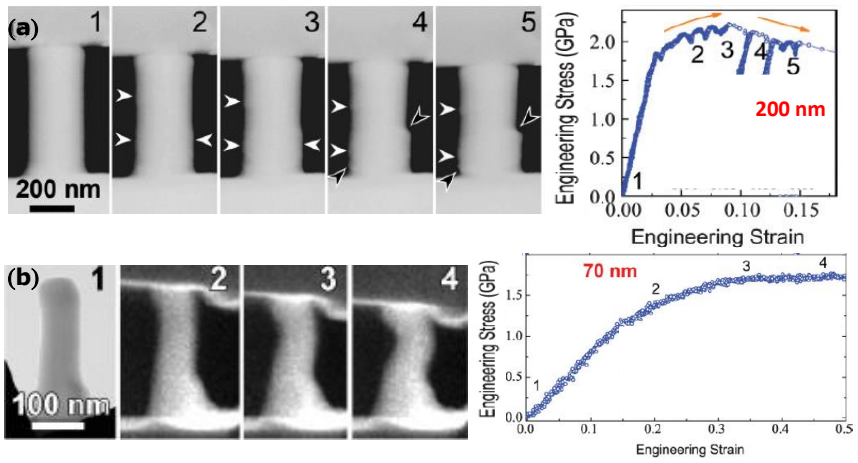

Figure 1.39 *– In-situ TEM compression test of 200 and 70-nm-diametr pillars, respectively (a) and (b). The corresponding stress-strain curves are reported as well. Adapted from [109].*

Jang and Greer [110] investigated through scanning electron microscopy the tensile behavior of Zr-based metallic glass fabricated in non-tapered, free-standing specimens (Figure 1.40). They show that the tensile yield strength increases of 50% upon reducing the specimen diameter to 0.5 μm, remaining at a constant value with subsequent diameter reduction. Moreover, when the diameter approaches 0.1 μm homogeneous plastic deformation was observed (Figure 1.40). They explain the transition, following the analysis of Volkert *et al.* [102, 103] and Chen *et al.* [107], attributing their observations to a competition between two processes: crack-like shear-band propagation and "homogeneous-like flow" (Figure 1.41). Analogous to Griffith's criterion, the critical stress needed to propagate a pre-existing crack-like shear band scales inversely with the sample diameter (Figure 1.41). In large samples, this critical stress is always much lower than the stress needed to drive room temperature distributed flow, leading to localization. In very small samples (∼100 nm in diameter), the competition favors the activation of STZs throughout the sample at a high stress level (σ_{homo}), resulting in homogeneously distributed deformation of the specimen. A threshold pillar diameter (d^*) indicate the transition from inhomogeneous ($d > d^*$) to homogeneous deformation ($d < d^*$), while the corresponding maximum stress level will be dictated by σ_{homo} if $d < d^*$, and by the Griffith's criterion if $d > d^*$ (Figure 1.41). To confirm this hypothesis J. Greer's research group [111] analyze the tensile behavior of pillar with notches. With the help of numerical simulations, they found that the notches significantly reduced the amount of stress required for shear banding formation, leading to abrupt failure without homogeneous deformation.

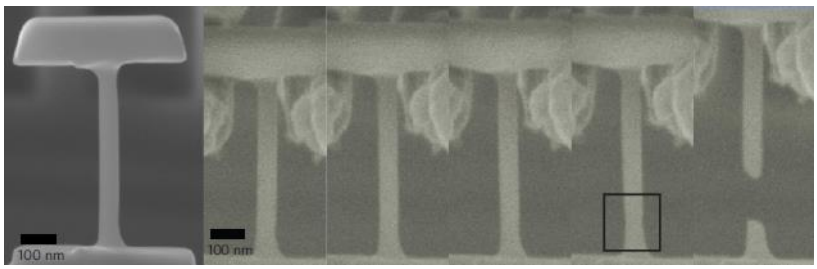

Figure 1.40 *– Tension test for 100-nm-diameter pillars, showing homogeneous elongation [110].*

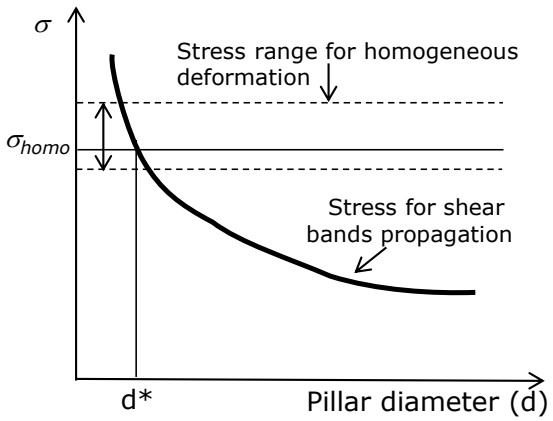

Figure 1.41 *– Evolution of the strength (σ) required for homogeneous and shear bands-mediated deformation. Below a critical pillar diameter (d^*) homogeneous deformation prevails.*

The mechanical properties of small scale materials can be probed also by *in-situ* TEM tensile test [112-117]. The technique consists in producing (via FIB-milling) samples with a rectangular or dogbone shape and then to apply a tension. This technique allows to test films below 100 nm in

thickness direction and to directly observe the deformation. Nonetheless, it does not allow to accurately extract the stress values, thus giving only partial information. The general results in testing thin film metallic glasses (TFMGs) is the large homogeneous deformation. For instance a first work of Guo *et al.* [116] for Zr-based TFMGs with a 250 nm of thickness has shown a large and uniform tensile ductility in the range of 23-45% including extensive necking. They explain this behavior by the reduced dimension of the specimen (100 nm x 100 nm x 250 nm), which does not allow the development of a mature shear band. Deng *et al.* [117] for a $Cu_{49}Zr_{51}$ TFMG with a thickness of 50 nm reported an elastic behavior up to 4.4% followed by a plastic deformation up to 12.3% (Figure 1.42). They observe that the testing condition such as machine stiffness could play a capital role especially for small specimens, with potentially enhancing the ductility such as reported in section 1.5.3. However, they recognized the impossibility to develop shear bands for the smallest specimens. Other studies of Jiang *et al.* [112, 113] on $Ni_{60}Nb_{40}$ TFMGs with a thickness of 50 nm have shown a giant elastic deformation up to 6.6% coupled with a plasticity which can attain a value close 40%. They also found that elastic deformation decreases if the thickness increases from 6.6% down to 3.5%, respectively for a 50 and a 200 nm-thick film. They relate this change with a reduced density of the thinnest film which promotes multiple shear bending operations due to the large number of STZs (section 1.5.3).

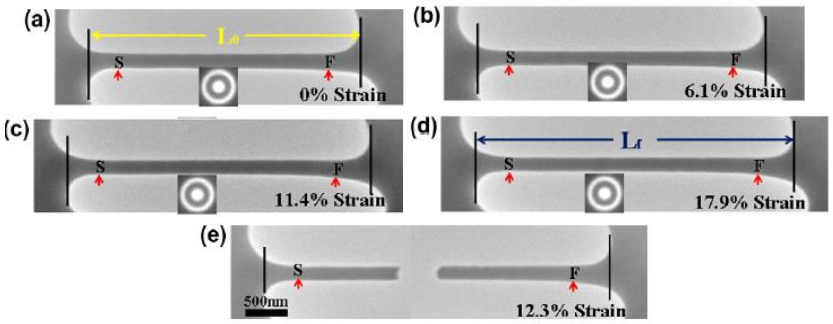

Figure 1.42 *– Bright-field TEM images at different total strains, showing large uniform elongation. The selected-area diffraction patterns of the deformed samples are given in the insets [117].*

Tian *et al.* [114] analyzed the tensile mechanical behavior of $Cu_{49}Zr_{51}$ TFMGs *in-situ* TEM. Samples have dogbone shape (inset in Figure 1.43a) allowing the extraction of the stress during the deformation. Figure 1.43a shows the stress-strain curve for a 220 nm-thick specimen. It can be noted that films deform elastically up to a deformation of around 4%, while exhibiting strain hardening and reaching a fracture deformation up to 5.5%. Furthermore, the elastic limit is close to 2.5 GPa, while the fracture one can reach 3.5 GPa. These impressive values are much more than the values of CuZr BMGs (Figure 1.43b), with the fracture strain that is close to the theoretical limit estimated using equation 1.10. They explain this transition considering that free-standing TFMG require a certain length scale (∼100 nm [48]) to develop into single shear banding process.

Samples of 200 nm thus may not undergo shear banding immediately after the onset of STZ activities from softer local regions or surface defects. Hence, the sample is still dominated by harder and confined backbone regions that continue to deform elastically (section 1.5.8) up to very high values 4%. Increasing the stress, the likelihood of activation of STZs is enhanced justifying the change of slope after the yielding and due to dilatation and local irreversible deformation (Figure 1.43a). The increasing stress (strain hardening) is indicative of the enhancement of the stress required for the activation of less favored (highly packed) STZs. A further increment of stress allows the activation of shear bands and finally the rupture.

In another work for 70 and 80-nm thick TFMG with a composition $Cu_{49}Zr_{51}$ Tian *et al.* [115], have also shown a large elastic behavior up to 4.6% coupled with a large plasticity (up to 6%). Furthermore, they observed that the mechanical behavior is strongly dependent on the applied strain rate. Low loading strain rates favor ductile necking, while high ones induce a brittle-like behavior with rupture at 45° with respect to the loading direction and hence a lowering of plasticity. This resulting is very similar to what reported in Figure 1.37 for compression test of micropillars, even if the length scales involved are different.

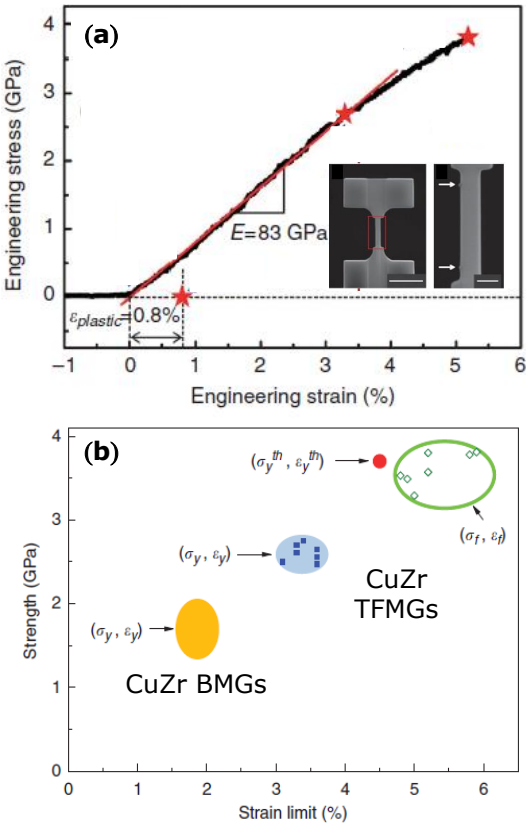

Figure 1.43 *– (a) Stress-strain response for a 220 nm-thick sample. (b) Strength and strain limit of Cu-Zr BMGs and TFMGs. Adapted from [114].*

1.6.2 Discussion

In the previous section it has been reviewed size effects on the mechanical properties of metallic glasses. It can be noted that there is no a general consensus about the deformation mode of micropillars as well as on the evolution of the elastic limit (see Table 1.1). Nevertheless, all studies agree with the observation of a large plastic behavior which can be more than 20% (Figure 1.36 and 1.38d) and as well as on the relationship serration flow-shear band operations. More important, all studies identify the shear bands formation as the only mechanism which dictate the mechanical properties even at the smallest scales. This is also valid if a transition inhomogeneous-to-homogeneous is observed.

Scatter in the data as well as the presence or not of a transition arise mainly from the difficulty to produce and manipulate small scale specimen. There is a strong debate about the effect of FIB to produce nanoscale specimens. In fact, Ga^+ implantation and ion beam damage has been recognized to

have an effect on the deformation behavior of sub-micrometer samples introducing free volume, chemical softening, and surface ion implantation [118]. The impact of this heavily disordered glass structure in the FIB-affected surface layer increases as the sample size decreases and facilitates the process of shear bands nucleation, and altering the mechanical properties. Furthermore, testing of tiny samples is non-trivial and may involve discrepancies from sample to sample, especially in the case of compression test of micropillars. Care should be taken about the effect of the aspect ratio, which can lead to buckling and bending phenomena instead of pure compression. Other issues arise from presence of taper angle which may deform preferentially and facilitate shear-band nucleation as well as for the non-uniform contact between the punch and the pillars, which can lead stress localization. The effect of the applied loading rate must also be considered.

Ref.	**Composition**	**Minimum size + (loading)**	**Transition inhomogeneous - homogeneous**	**Strength size dependence**
Volkert *et al.* [102]	$Pd_{77}Si_{23}$	140 nm pillar with taper (compression)	Yes (Figure 1.35)	Slight decrease
Tonnies *et al.* [103]	$Pd_{77}Si_{23}$	200 nm pillar with taper (compression)	Yes (Figure 1.37)	Slight decrease
Lee *et al.* [104]	Mg-based	1 μm pillar with taper (compression)	No	Strong increase
Lai *et al.* [105]	Zr-based	700 nm pillar with taper (compression)	No (Figure 1.38)	Strong increase
Dubach *et al.* [106]	Zr-based	300 nm pillar with taper (compression)	No	No change
Chen *et al.* [107]	Cu- and Zr-based	100 nm pillar with taper (compression)	No	No change
Kuzmin *et al.* [108]	Zr- Cu- and Au-based	90 nm pillar taper free (compression)	Yes	No change
Chen *et al.* [109]	Cu-based	70 nm pillar taper free (compression)	Yes (Figure 1.39)	Slight decrease
Jang and Greer [110]	Zr-based	100 nm pillar freestanding (tension)	Yes (Figure 1.40)	Slight increase

Table 1.1 *– Literature overview of size effects in metallic glasses.*

In the case of *in-situ* TEM tensile test, the issue of the FIB damage is still present coupled with the more complicated setup for sample production and testing (which justify the less number of studies). Furthermore, the main drawbacks is represented by the lack of information about the stress (the only exception is the work of Tian *et al.* [114, 115]). However, all the studies have shown that TFMGs can sustain an extremely large plastic behavior together with a high yield strength [114], indicating the shear bands formation as the only deformation mechanism even at very small scales.

The common evidences obtained both from compression (or tension) test of micropillars and from *in-situ* TEM tensile test are somehow in agreement with the model proposed by Greer *et al.* [3], indicating a distribute plastic deformation in sub-micron specimens. Stress concentrators are absent or impotent and homogeneous nucleation of shear bands from structural fluctuation becomes more and more important decreasing the sample size. The required stress can increase towards the ideal strength (σ_{homo}), promoting seemingly homogeneous plastic deformations in the form of distributed STZs. For a specimen of around ~100 nm the distributed shear transformation can survive longer and contribute to larger plastic strain.

This model is in agreement with the numerical simulations for shear bands formation (presented in section 1.5.8) which point towards the existence of a critical length scale required to create "mature" shear bands. Shimizu *et al.* [48] indicated this critical length of the order of 100 nm a value reported recently by Cheng and Ma [8, 100]. However, care should be taken when comparing simulations with real experiments. For instance, the metallic glasses made in simulations suffer from the very high cooling rate used in their "preparation". The surface condition of the simulated samples may also be very far from the realistic ones and, more importantly, the loading rate in simulation is orders of magnitude higher than the typical values in experiments, while the strain localization is expected to be very sensitive to the loading rate.

Even if the model of Greer *et al.* [3] sheds light on the possible mechanisms to explain mechanical properties of small scale metallic glasses, the scatter of data presented in the literature due to specimen production and manipulation (Table 1.1) leads to open questions which are not fully unraveled yet. The origin of size effects can be *intrinsic* (change in atomic structure) or *extrinsic* (effect of external parameters during the test), while the corresponding threshold size for a transition from inhomogeneous-to-homogeneous flow is still matter of debate. In section 1.5.3b it has been discussed the effect of atomic structure as well as sample geometry and testing conditions on the mechanical properties of BMGs. Yang *et al.* [57] and Kuzmin *et al.* [108] studying compression test of micropillars have shown that ductile metallic glasses (high Poisson ratio) have a transition in deformation mode at higher length scales. On the other hand, the effect of external parameters are discussed by Wu *et al.* [119] which demonstrate the high sensitivity in the mechanical response and shear banding, pointing out that specimens with are chemically and structurally identical but have different sizes, can have a significantly different behavior even for bulk samples. They explained their observations by considering the energy density dissipated on the fracture surface and the shear offset, both of which scale with sample size, and eventually determine the stability of the plastic deformation.

Intrinsic and extrinsic effects make not directly comparable even the results obtained for BMGs, thus leading to an even more confusion when studying the mechanical properties of micrometer size metallic glasses. However, it is evident that there is noy an unique mechanical behavior of metallic and both extrinsic and intrinsic (composition, quenching rate etc.) parameters play a central role affecting the mechanism for shear bands nucleation and propagation.

1.7 Conclusion

In this chapter we presented the functional and mechanical properties of metallic glasses starting from the analysis of their disordered atomic structure resulting from a rapid solidification process. Among the functional properties, we focused on the electrical resistivity which has been investigated for thin film metallic glasses (TFMGs) in Chapter III. The electrical resistivity of a metallic glass is higher than the crystalline counterparts because of the disordered atomic structure. Moreover, we pointed out that the glass transition and the crystallization temperatures can be detected by probing electrical resistivity as a function of the temperature. Lastly, we show that for binary metallic glasses it is possible to predict the composition with the highest value of electrical resistivity by using the Nagel and Tauc criterion.

The analysis of mechanical properties of bulk metallic glasses (BMGs) covers most of this chapter. The absence of crystalline defects (i.e. dislocations and grain boundaries) makes the mechanical behavior of BMGs unique and characterized by large elastic deformation (up to 2%), coupled with a yield strength close to the theoretical limit ($\sim$2000 MPa for Zr-based BMGs). Nevertheless, the macroscopic brittle-like mechanical behavior via shear bands formation limits their applications. In this contest, the mechanical properties of BMGs at room temperature have been thoroughly reviewed analyzing the elementary mechanisms of deformation (i.e. STZs operations) which are responsible for the mechanical behavior controlling the formation of shear bands. Moreover, all the mechanical properties have been described involving elasticity, plasticity, fracture as well as the viscoplastic behavior obtained performing nanoindentation tests. The adhesion and tribological properties studied by scratching tests has been discussed as well.

A special emphasis has been attributed to the structure-properties relationship. It has been shown that BMGs with a high Poisson ratio have higher toughness and ductility due to the formation and interaction of multiple shear bands. The effect of extrinsic parameters has been considered as well, highlighting how mechanical properties can be altered by changing the specimen aspect ratio or by modifying the machine stiffness. We show that both intrinsic and extrinsic effects play a similar role on shear bands nucleation a propagation affecting BMGs mechanical behavior.

The previous analysis, coupled with a thorough description of the theories for shear bands nucleation and propagation, is fundamental to understand mechanical *size effects* in small scale metallic glasses. At first, we analyze the theoretical trend on mechanical properties when reducing the dimension up to few hundreds of nanometers. Afterwards, the main literature results have been presented. We showed that the total strain of a small-scale metallic glass can reach the 20%, even if shear bands have been identified as the only possible deformation mechanism. However, the activation of the shear banding process is hindered due to the smaller number of defects leading to extended homogeneous plasticity with an increment of the yield strength up to the ideal one.

Nevertheless, we have shown that there is not a general consensus about the evolution of mechanical properties and possible artifacts can originate by sample manipulation and FIB damaging especially in the case of compression test of micropillars. We highlighted the fact that there are a number of open questions such as the origin of size effects and the length scales involved depending both on intrinsic and extrinsic effects. These questions are not fully unraveled yet, leading to fascinating scientific research.

Chapter II – Processing and characterization methods

In this chapter we review the deposition and the characterization techniques employed to study ZrNi thin film metallic glasses (TFMGs). We start explaining the reasons of the choice of TFMGs with ZrNi composition (section 2.1), followed by an introduction to vapor phase deposition techniques, emphasizing the mechanisms of film growth and the role of the deposition parameters (pressure and temperature) to obtain a TFMG (section 2.2).

After this background, we present the specific sputtering parameters used to deposit ZrNi TFMGs with the development of a composite sputtering target to accurately tune the composition (section 2.3). An analysis of film composition, growth rate and thickness profile along the substrate will be presented showing that we succeed to obtain TFMGs with the desired thickness and composition (section 2.3).

Afterwards, the characterization techniques to study the atomic structure will be presented (section 2.4). Then, we review the mechanical characterization techniques starting from the analysis of elasticity by surface Brillouin spectroscopy (SBS) and picosecond ultrasonics (PU) followed by the nanoindentation, nanoscratch and fracture (sections 2.5-7). The procedure to estimate the activation volume using nanoindentation at different loading rates will be presented as well.

The mechanical properties of TFMGs have been extracted by uniaxial tensile test on freestanding film as well, using the so-called lab-on-chip technique (section 2.8). This technique will be thoroughly described introducing the concept and how to extract mechanical properties, followed by the analysis of the specific fabrication steps.

Lastly, the electrical resistivity technique and the specific parameters to test TFMGs will be presented (section 2.9).

2.1 The alloy selection: properties of ZrNi metallic glasses

ZrNi amorphous alloys are among the most studied binary metallic glasses because of their high glass forming ability (GFA, sections 1.2 and 1.3). The early works of Buschow *et al.* [30] and Dong *et al.* [120] have shown that ZrNi metallic glasses in ribbon form (thickness $\sim$20 μm) have a large amorphisation range from 10 up to 80 % at. of Zr, which make these materials natural glass formers, the Ni-Zr phase diagram is reported in Figure 2.1. The large GFA (section 1.4) can be explained considering the difference in the atomic radius higher than 12% (155 pm and 135 pm, respectively for Zr and Ni), the negative enthalpy of mixing which reach a maximum for the composition close to $Zr_{40}Ni_{60}$ [121] as well as by the presence of three deep eutectic points within the amorphisation range in the equilibrium phase diagram for Ni-Zr binary alloys, respectively at 36, 64, and 76% at. of Zr

(Figure 2.1) [122]. However, even if ZrNi alloys easily undergo amorphisation, it is always required a high quenching rate. Ribbons are produced by melt-spinning which have a typical cooling rates about 10^5-10^6 Ks^{-1} [1]. The Nagel and Tauc criterion [29] (presented in sections 1.3 and 1.4) allows to comprehend the thermodynamic stability of different ZrNi glassy phases in terms of their electronic properties and to justify crystallization phenomena. Recently, Turnow *et al*. confirmed the amorphisation range for 500-nm thick ZrNi thin film metallic glasses (TFMGs) deposited by sputtering (Figure 2.2) [123].

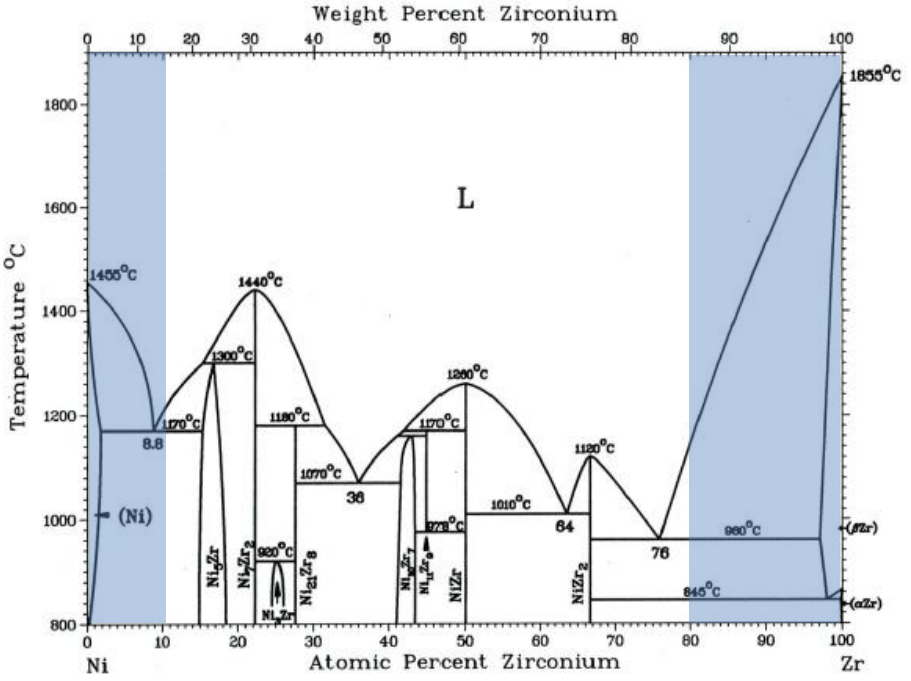

***Figure 2.1** – Phase diagram of the Ni–Zr system [122]. In white the amorphisation range.*

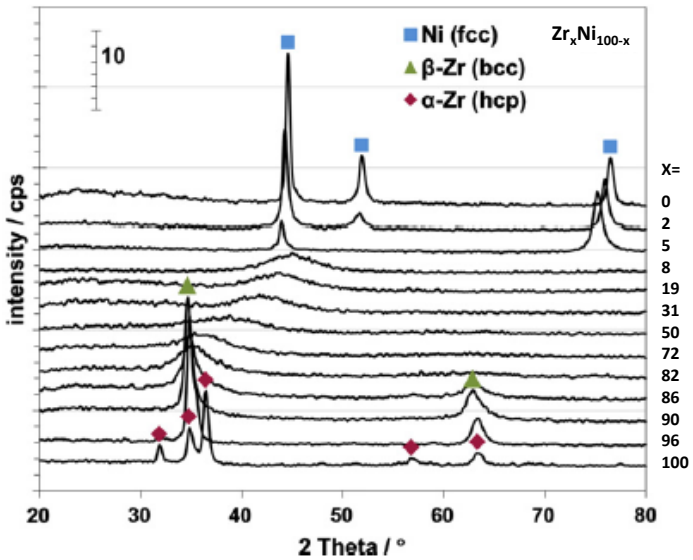

***Figure 2.2** – X-ray diffractograms of Zr_xNi_{100-x} TFMGs showing an amorphisation range between 8 and 82 % at. of Zr; note the presence of a broad halo. The crystalline phases have been identified. Adapted from [123].*

The origin of the large GFA is related to the presence of a strong short and medium range order (SRO and MRO), which enhance the stability of the glassy phase (section 1.2). Liu *et al.* [124] investigated the local atomic structure in ZrNi metallic glasses ribbons by extended X-ray absorption fine structure (EXAFS) technique. They found that the average bond length of unlike atomic pair is constant and equal to 2.62 Å for all the investigated compositions Zr_xNi_{100-x} (x = 66.7, 64, and 50 % at.). This value is shorter than the sum of Ni and Zr atomic radii, indicating a strong chemical interaction. Their model of SRO is constituted by tetragonal elements favoring hetero-bonds deduced by distortion of chemical bonds of the crystalline counterparts. The presence of SRO have been also found by Fukunaga *et al.*[125], Yang *et al.* [126], combing high resolution diffraction techniques and reverse Monte Carlo simulations for the composition $Zr_{66.7}Ni_{33.3}$. However, although they recognize a strong chemical affinity between Zr and Ni, they describe SRO as a distribution of icosahedral polyhedra. A definitive evidence of SRO in $Zr_{66.7}Ni_{33.3}$ amorphous ribbons have been found by Hirata *et al.* [127], by using nanobeam electron diffraction on 3-5 nm-thick specimens. They were able to detect the diffraction signal of the single clusters and to model it by using *ab initio* molecular dynamic simulations. An atomic structure based on a solute-centered icosahedral SRO has been found. MRO has also been deduced by combining the elementary atomic clusters which form the SRO (section 1.2).

The high local order leads to an high thermodynamic stability with high values of crystallization and glass transition temperatures, respectively T_x and T_g [30, 75, 120, 124]. The T_g is not easily detectible in a differential scanning calorimetry (DSC) experiment [125], however it is possible to consider the T_x as the upper value for T_g . Figure 2.3 shows the T_x values reported by different authors. Note that the crystallization temperature increases for Ni-rich specimen due to the higher melting point of Ni and the formation of ZrNi bonds. The high values of T_x also guarantees that ZrNi metallic glasses maintain their amorphous structure even if a heat treatment is applied. For instance, the process to obtain freestanding $Zr_{65}Ni_{35}$ thin film metallic glasses (section 2.8.2) involves an etching phase at 358 K (85°C), which is significantly below the T_x (and possibly T_g) expected at 725 K (425°C), Figure 2.3.

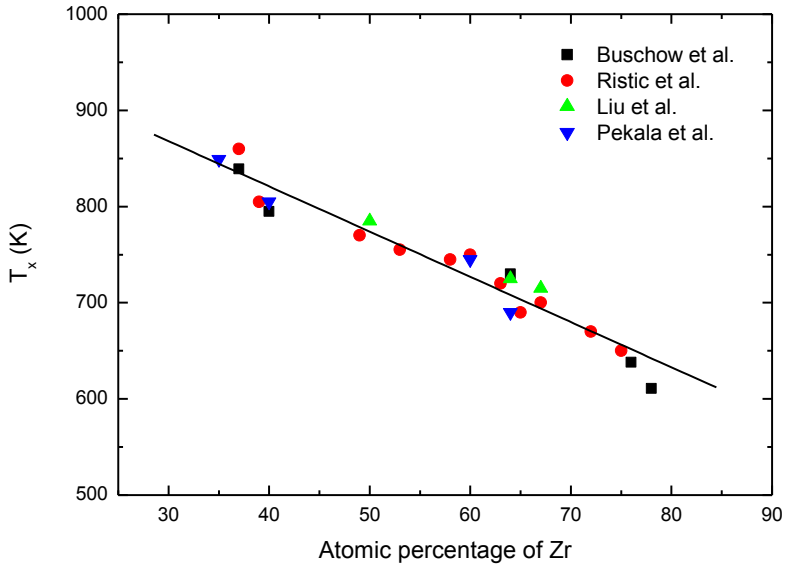

***Figure 2.3** – Evolution of the crystallization temperature for Zr_xNi_{100-x} ribbons as reported by several authors. Buschow et al.[30], Ristić et al.[75], Liu et al.[124], Pekala et al.[31].*

Ristić *et al.* [75, 76] analyze the evolution of elastic modulus (*E*) and Vickers hardness as a function of the composition for ZrNi amorphous ribbons (Figure 2.4). The increment in elastic

modulus and hardness for Ni-rich samples is related to the higher (meta)stability (Figure 2.3) favored by the highly packed atomic structure with the formation of strong Zr-Ni bonds. Note that the elastic modulus of pure Zr (α-phase HCP lattice) and Ni (FCC) are respectively of 88 GPa and 200 GPa [76]. A mixing rule cannot be used to predict the elastic modulus of the amorphous ZrNi which is significantly lower (Figure 2.4) and roughly obtained after a reduction of 30-40% of the value calculated using the mixing rule from pure crystalline Ni and Zr, (see section 1.5.4). The formation of ZrNi bonds can also be deduced from the position of the first sharp diffraction peak (FSDP) in XRD experiments, which can be related to the average position of neighbor atoms [30, 120, 123] as well as by the analysis of the atomic volume [40], which is inversely proportional to the density (equation 1.3). Lastly, Ristić *et al.* [75, 76] reported a composition-independent value of the Poisson ratio equal to 0.375.

Functional properties of ZrNi mainly focus on the electrical resistivity as a function of the composition and of the temperature [30, 31, 38, 39]. The main results have been already presented in section 1.4, showing that it is possible to predict the composition with the highest electrical resistivity and the maximum negative TCR (temperature coefficient of resistivity), by using the Nagel and Tauc criterion.

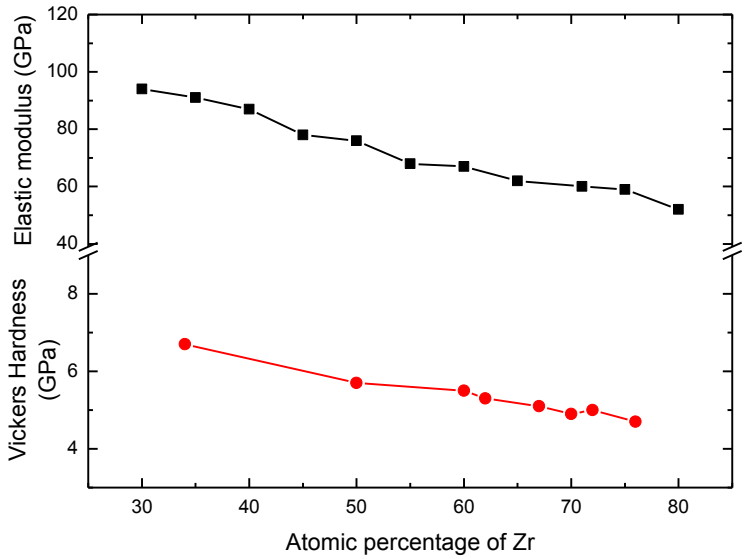

Figure 2.4 *– Evolution of elastic modulus and Vickers hardness for ZrNi ribbons. Adapted from [76].*

The choice of ZrNi metallic glasses is also dictated by the high resistance to oxidation as well. This property is fundamental for realizing freestanding films for mechanical testing. As a matter of fact, the presence of a thick oxide layer can cause a surface stress which can result in folding phenomena for free-standing films. In Antoine Volland's PhD thesis which focused on the mechanical properties of $Zr_{70}Ni_{30}$ TFMGs [128] it has been shown that it is possible to release free-standing cantilevers with a length of 10 μm, avoiding folding phenomena due to the enhanced oxidation resistance. Furthermore, electron probe microanalysis (EPMA) reported in section 2.3 in the case of TFMGs deposited in this PhD thesis work has shown a negligible oxygen content, even several days after the deposition. Lastly, another reason to select ZrNi as the ideal candidate for mechanical testing is the resistance to Tetramethylammonium hydroxide (TMAH) which has been used to selective etching the Si substrate and to release freestanding beams. These evidences has been firstly reported in the Antoine Volland's PhD thesis [128], while detailed results will be shown in section 2.8.2.

2.2 Basic notions of deposition of thin films and growth mechanisms

The principal domain in which small-scale materials are involved is microelectronics and coating industry [129, 130]. Both applications lie on thin film deposition technology which follows a *bottom-up* approach, namely films are deposited starting from the elementary atoms or clusters level, while increasing in thickness. There are several methods to deposit a thin film, but the microelectronics domain involves especially vapor phase techniques divided in CVD and PVD (Chemical and Physical Vapor Deposition), respectively if a chemical reaction in the vapor phase occurs or not [129, 130].

There are three modes of film growth: 2D, 3D or mixed, Figure 2.5 [129]. The 2D growth is also known as *layer-by-layer* growth. The whole surface of the substrate is covered by a homogeneous layer in which the deposited atoms are more strongly bond to the substrate than each other avoiding to form clusters (Figure 2.5a). This mode is favored during epitaxial depositions where a crystalline layer grows on a crystalline substrate. Films can grow in the *island* mode, where the atomic bonds of deposited species are stronger than the interactions with the substrate, leading to a 3D growth (Figure 2.5b) as in the case of metals deposited onto a semiconductor. A third mode, is a mixture between 2D and 3D where early stage monolayers are followed by an island growth (Figure 2.5c). Islands usually merge after the first 10-20 nm of thickness creating a continuous film.

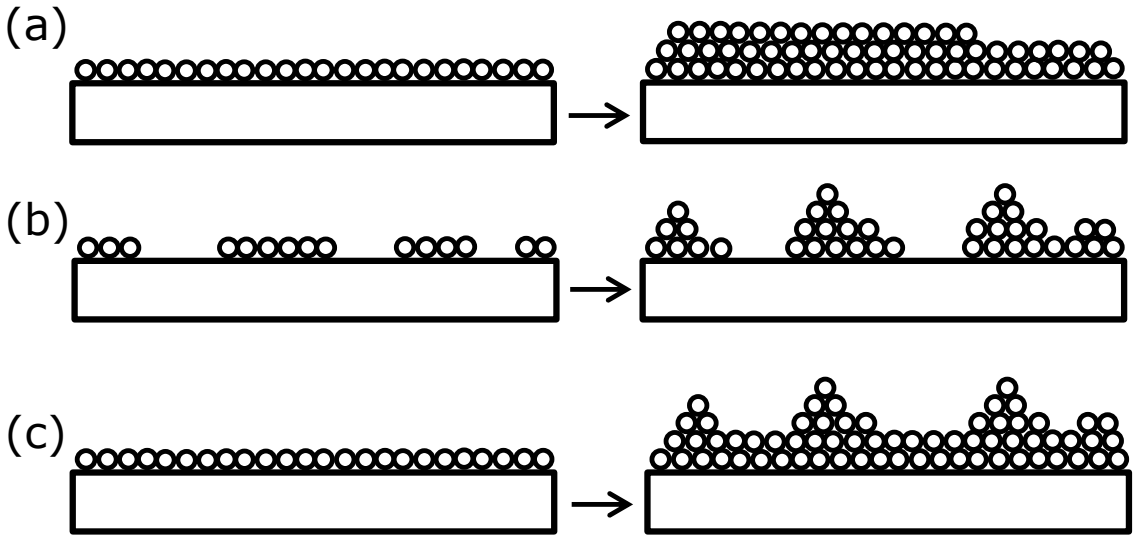

Figure 2.5 *– Basic mode of thin film growth. (a),(b),(c) respectively, layer-by-layer, island and mixed growth mode.*

In Figure 2.6 are represented the elementary mechanisms of film growth in a PVD/CVD reactor [129, 131]. After chemical reactions in the gas phase (only for CVD) such as precursor decomposition or compound formation, there is a convective and diffusive flow that allows the deposition of gas species onto the substrate. These species are then adsorbed and, through surface diffusion, they can coalesce to form clusters with a limited surface mobility (island growth) or they can fit in the energetically favorable positions (*kinks*) leading to the layer-by-layer growth [130]. Eventually, there could be desorption of species with high energy. The choice between island or the layer-by-layer growth depends on several parameters among which the nature of substrate-film as well as by the external temperature and pressure.

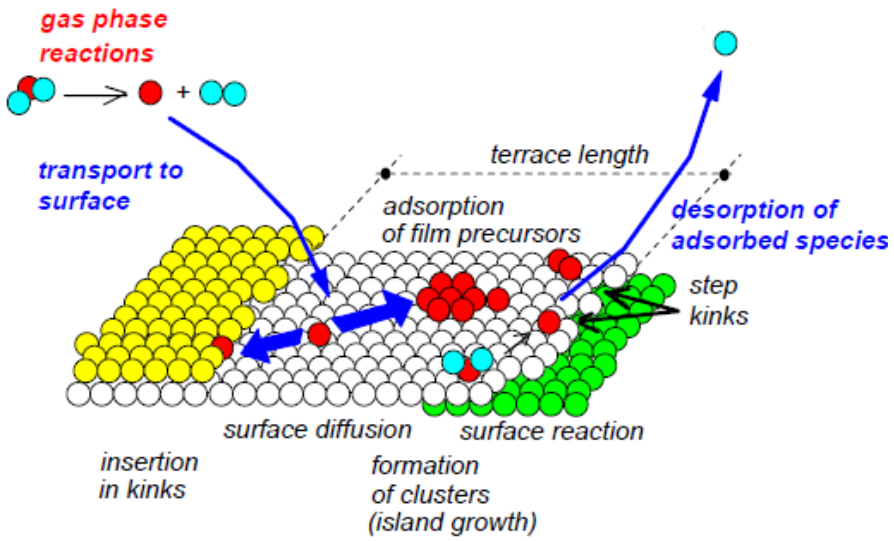

Figure 2.6 *– Key steps of film growth in a PVD/CVD reactor. Adapted from [131].*

A qualitative analysis which can describe different film growth modes can be derived by evaluating the characteristic times of superficial diffusion (τ_D) and reaction (τ_R) [131]. τ_D is related to the surface diffusion coefficient (D_S) by

$$\tau_D = \frac{l^2}{16 D_S} \tag{2.1}$$

where l represent the terrace length for the superficial diffusion (Figure 2.6), while τ_R is linked with the constants of surface reaction and of gas flow rate which are grouped together in k^*, through

$$\tau_R = \frac{1}{k^* a} \tag{2.2}$$

where a is the adsorption surface per unit volume. The film morphology depends on the longest characteristic time. If $\tau_D \gg \tau_R$ then the surface reactions are favored with respect to the surface diffusion, which in turn leads to the island growth where the gas species are "frozen" and they cluster together very close to the surface landing point. This case is favored at low temperatures and pressures. In fact, D_s follows an Arrhenius kinetic law and it can be expressed as

$$D_s = D_0 \exp(-E_D / RT) \tag{2.3}$$

where D_0, E_D and R are respectively the surface diffusion constant, the activation energy for surface diffusion, and the gas constant [130]. Low temperatures reduce D_s while increasing the characteristic diffusion time τ_D (equation 2.1). Moreover, low pressures imply that there are no resistances in the gas flow and rapid kinetic of adsorption which lower τ_R. These conditions correspond to a formation of an amorphous film, in which there is no crystalline order because of the limited diffusion necessary for the formation of a periodic crystal (section 1.2). If $\tau_D \ll \tau_R$ the surface diffusive phenomena will become dominant thus favoring a layer-by-layer growth. The high temperatures promote the surface motion increasing D_S, while increasing τ_R. Hence, it is favored the formation of crystalline layer. Lastly, when $\tau_D \approx \tau_R$ surface diffusion and reaction kinetics will have the same importance allowing the formation of a poly-crystalline film, in which surface clusters grow generating crystalline grains.

The effect of pressure and temperature on film microstructure – deposited by means of PVD techniques such as sputtering (section 2.3) can be described by using a 3D Thornton diagram, where the background pressure is plotted against the reduced temperature, i.e. the ratio between the substrate temperature and material melting temperature, Figure 2.7 [132]. Films deposited at low temperatures and high pressures (zone 1, top) have a porous structure due to the low energy of deposited species, which experience also clustering phenomena in the gas phase (island growth). If the pressure is reduced, highly energetic species impinge the substrate (enhanced mean free path in gas phase) which leads to densification of pores and development of internal stresses. This condition corresponds to the formation of amorphous thin films with a compact structure. If the temperature increases, the contribution of surface diffusion will become relevant favoring porosity reduction, crystallization phenomena, stress relaxation, and grain growth as can be observed moving from zone 1 to zone T (Thornton) and then to zone 3.

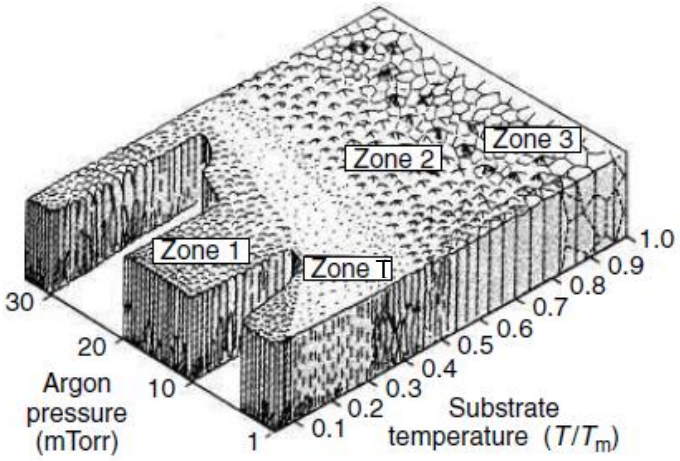

Figure 2.7 *– Different microstructures of sputtered thin-film [132].*

2.3 Deposition and characterization of ZrNi thin film metallic glasses (TFMGs)

ZrNi thin film metallic glasses (TFMGs) have been deposited by DC-magnetron sputtering (Alliance Concept AC450) within a clean room (class 1,000) to limit sample contamination. We exploited the deposition facilities of the Plateforme Technologique Amont (PTA) within the Centre Energie Atomique (CEA) in Grenoble. The choice of the sputtering deposition was dictated by a background experience (Antoine Volland's PhD thesis [128]). Moreover, sputtering enables to obtain hard compact films playing with parameters such as the temperature and the gas pressure (Figure 2.7).

Without entering in the details of sputtering physics (which is well explained in [129]), a naïf view of sputtering consists of a plasma – in our case Ar^+ ions – which bombards a target due to the presence of an applied bias which accelerates the Ar^+ ions (Figure 2.8). As the ions collide with the cathode (the target), secondary electrons are emitted. An electrical discharge is then initiated and sustained. The result is a strong erosion of the target whose atomic species (atoms or clusters) are then deposited onto a substrate (Si) leading to film growth (section 2.2). In the magnetron configuration there is application of a magnetic field at the cathode which confines the plasma above the surface (Figure 2.8). The advantages of this configuration are represented by the high film growth rate, by the possibility to reduce the background gas pressure (enhanced number of ion-target collisions), and by

the lower heating (less power is needed for plasma activation). However, a cooling system is always present allowing a reduction of thermal stresses and dilatation of the target which is subjected to intense ion bombardment (Figure 2.8). The limitations of this configuration are represented by the preferential target erosion along a specific circumference. However, this inconvenience is favorable when designing a composite target constituted by two distinct components, instead of a monolithic one with a fixed composition.

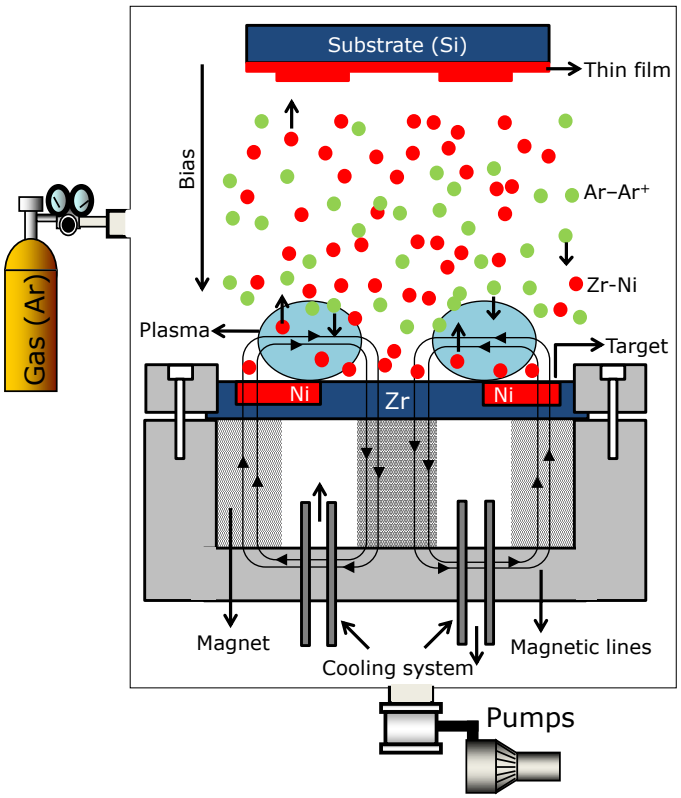

Figure 2.8 *– Schematic of a DC-magnetron sputtering machine.*

The target we designed consist of pure grade (> 99.995%) Ni rectangular slices inserted into a high purity (> 99.95%) Zr matrix (Figure 2.9). Firstly, 12 groves separated by an angle of 30° have been created by milling the Zr plate. The groove depth is equal to 3 mm (half the thickness) with rounded lateral edges that allow an easy insertion and removal of Ni slices (Figure 2.9a). Secondly, 12 Ni rectangular slices have been prepared by wired erosion which provide an accurate size control, especially when dealing with a very small dimensions. Their thickness of 3 mm enables to fit them in the grooves of the Zr matrix. Furthermore, we selected a length of 30.6 mm assuring the intersection with the maximum erosion circumference (dashed line in Figure 2.9a). The resulting target with the addition of 6 Ni slices is showing in Figure 2.9b.

With this configuration, the Ni concentration in the film (C_{Ni}) which is a function of the number and width (l_{Ni}) of Ni slices inserted into the Zr matrix can be estimated considering the Zr and Ni sputtering yields (Y) and the maximum erosion circumference length (l_{tot}), using

$$\begin{cases} C_{Ni} = \dfrac{Y_{Ni} l_{Ni}}{Y_{Zr} l_{Zr} + Y_{Ni} l_{Ni}} \\ l_{tot} = l_{Ni} + l_{Zr} \end{cases} . \qquad (2.4)$$

The Ni and Zr sputtering yields have been determined for Ar^+ energy range between 400 and 1000 eV (corresponding to the imposed voltage), considering an incidence angle of 90° and neglecting any target topological effects. For the selected Ar^+ energies, the ratio Y_{Ni}/Y_{Zr} is constant and is equal to 2. A data set of the sputtering yield for different materials as a function of the Ar^+ energies can be found in [133]. Although several efforts have been made to conceive the best target design as well as to machine the single components, this configuration have several advantages:

- there are no flaws or casting defects in contrast with monolithic targets with a custom-made composition produced by solidification of the melt. The thermal and atomic peening stresses during the sputtering process can provoke a cleavage fracture, especially if the target has an intermetallic composition and if the deposition conditions are more severe (high power and long deposition time),

- the Zr and Ni are highly pure, meaning that no impurities will be present in the film. This condition is very important in the study of mechanical properties of metallic glasses which can be significantly affected by impurities even at very low percentages (section 1.5). A monolithic target with a custom composition can have a significant content of impurities arising from casting phase [128],

- the design easily allows to change the composition of the film by adding or removing Ni slices. By using equation 2.4, it is possible to estimate the range of the compositions in the film from 100% of Zr (0 slices of Ni) to a composition $Zr_{48}Ni_{52}$ (% at.) if 12 Ni slices are added. Hence, it is possible to study the effect of composition for different alloys within the amorphisation domain as well as to investigate crystallization phenomena for Zr-rich specimens (section 2.1).

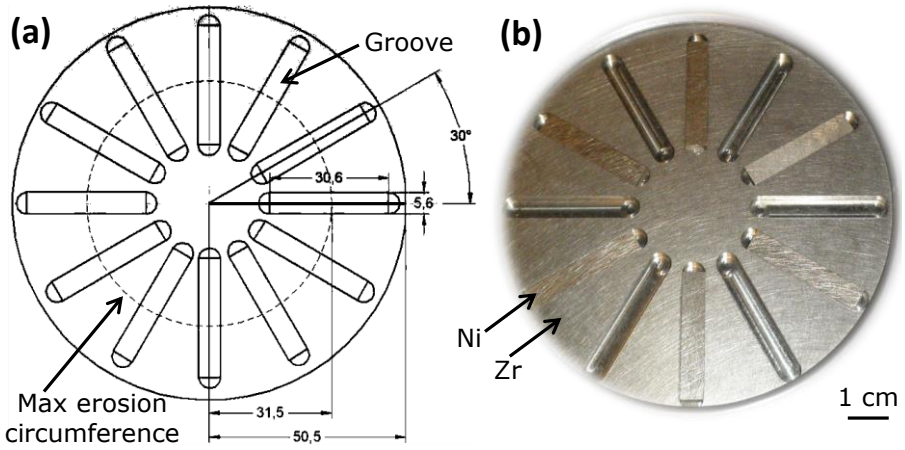

***Figure 2.9** – (a) Sketch of the composite target highlighting the presence of grooves in the Zr matrix. (b) The target with 6 Ni slices inserted in the Zr matrix.*

In Table 2.1 are summarized the experimental conditions adopted during the deposition. The substrate is silicon (100) with a diameter of 3 inches (7.62 cm). The distance target-substrate ($d_{t\text{-}s}$) was fixed at 7 cm, allowing the best thickness uniformity. Shorter distances produce a bimodal thickness profile, with a maximum thickness correspondent to the maximum erosion circumference, while higher distances lead to a Gaussian profile with a significant curvature profile between the center and the edges [129]. Note that in the AC450 there is no the possibility to rotate the substrate which can enhance the thickness uniformity. Hence, the $d_{t\text{-}s}$ is a fundamental parameter to assure a best thickness

control, a fundamental parameter for the study of size effects. The deposition time is variable and depends on the thickness.The power has been set at 300 W a condition already studied in [128], while the limit pressure (the vacuum pressure before each deposition) is always below $4 \cdot 10^{-5}$ Pa guaranteeing the absence of contamination prior the deposition. The working (Ar) pressure and the temperature of the substrate (T_s) are set at 0.3 Pa and room temperature, respectively. This condition leads to the formation of compact amorphous films (section 2.2). Lastly, each deposition is preceded by at least 6 minutes of pre-deposition time, aiming to warm up and clean the target. During this period, the plasma changes color from red (possible oxidation phenomena of the target and presence of C contaminants) to light blue, even if this transition depends on the number of Ni slices in the target.

Substrate	**$d_{t\text{-}s}$ (cm)**	**Time (s)**	**Power (W)**	**Limit pressure (Pa)**	**Working pressure (Pa)**	**T_s**
Si (100)	7	variable	300	$\leq 4 \cdot 10^{-5}$	0.3	room

***Table 2.1** – The deposition parameters.*

The characterization of the film composition as a function of the Ni slices in the target is a fundamental to verify the predicted values using equation 2.4. Furthermore, the composition has to be checked at different points on the substrate since the composite target geometry can lead to a non-uniform composition of the film. Energy dispersive X-ray spectroscopy (EDX) and electron probe micro analysis (EPMA) measurements have been carried out in different substrate points, exploiting the target symmetry (black dots in Figure 2.10). The composition was found constant with a very small scatter of data within the measured points, indicating an efficient plasma mixing and the absence of effects related to the target geometry [134]. Note that we do not observe any compositional variation even if only two Ni slices, separated of 180°, are inserted in the Zr target. The composition along the thickness has been analyzed by transmission electron microscopy (TEM) with EDX and found to be constant without Si diffusion phenomena at the film interface.

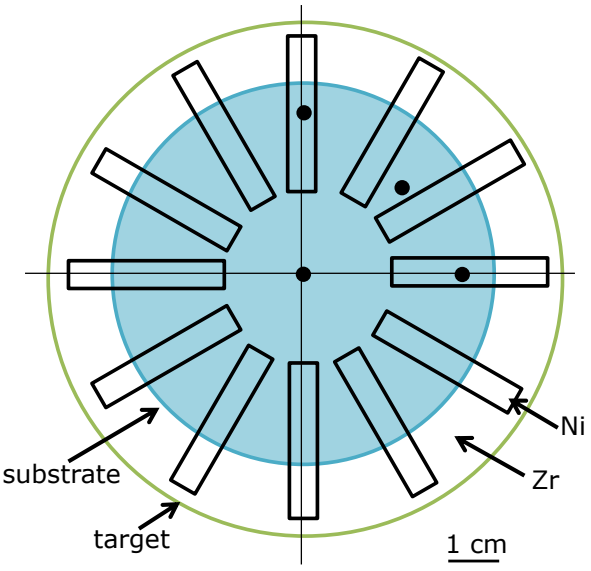

***Figure 2.10** – Schematic representing the target and the substrate. Black dots indicate the points where a EDX and EPMA analysis has been carried out.*

Table 2.2 reports the compositions as a function of the number of Ni slices in the target. The measured compositions are very close to the expected one (equation 2.4), while there is a very small scatter of data between each techniques. The compositions obtained by EPMA are the most accurate since a calibration procedure has been carried out with specimens of known composition. In this case, measurements have been carried out overnight to achieve the maximum accuracy. For this reason, hereafter we refer to the EPMA values when describing different film compositions. The small discrepancy between the predicted values and the EPMA ones has been attributed to sputtering events outside the maximum erosion circumference not considered by the model underlying equation 2.4. Films show a negligible (< 1%) amount of C and O and absence of metallic impurities.

Number of Ni slices in the target	**Expected composition (% at.)**	**EPMA composition (% at.)**	**EDX composition (% at.)**	**EDX composition (TEM) (% at.)**
12	$Zr_{48}Ni_{52}$	$Zr_{42}Ni_{58}$	$Zr_{44}Ni_{56}$	$Zr_{45}Ni_{55}$
6	$Zr_{70}Ni_{30}$	$Zr_{65}Ni_{35}$	$Zr_{68}Ni_{32}$	$Zr_{67}Ni_{33}$
4	$Zr_{80}Ni_{20}$	$Zr_{75}Ni_{25}$	$Zr_{75}Ni_{25}$	$Zr_{75}Ni_{25}$
2	$Zr_{90}Ni_{10}$	$Zr_{85}Ni_{15}$	$Zr_{86}Ni_{14}$	$Zr_{86}Ni_{14}$

***Table 2.2** – TFMGs composition as a function of the number of Ni slices in the target. The expected composition and the measured ones using EPMA, EDX and EDX in TEM (cross-sectional view). The most accurate value estimated with EPMA is highlighted in a red box [134].*

The film growth rate is determined by thickness profilometry and through measurements of field emission scanning electron microscopy (FE-SEM) in cross-section view after cleavage of the substrate. A linear growth rate for the composition $Zr_{65}Ni_{35}$ is found equal to 1.1 nm/s, as determined by thickness profilometry (Figure 2.11a). This result is consistent with the 1.08 nm/s obtained by using FE-SEM. The film growth rate is directly related to the number of Ni slices in the target, and increases for Ni-rich compositions due to the enhanced sputtering yield of Ni. For the same sputtering parameters (Table 2.1), the growth rate evolves from 1.2 nm/s for $Zr_{42}Ni_{58}$ down to 1.00 nm/s for $Zr_{85}Ni_{15}$. The thickness profile along the substrate shows a parabolic profile (Figure 2.11). The thickness curvature increases for thicker films, while is almost negligible for thicknesses below 300 nm. However, all the specimens are analyzed within an interval of ± 20 mm from the substrate center (dashed lines in Figure 2.11b) with show a limited thickness variation. Moreover, before each test the thickness has been accurately measured because it represents a fundamental quantity when investigating size effects.

Lastly, it is worth noting that the average roughness measured by XRR (section 2.4) is in between 0.4 and 0.6 nm, indicating a very smooth surface related to the absence of crystalline defects such as grain boundaries and phase segregations (section 1.5.3). The evidence of high surface smoothness can also be inferred when looking at the specimens after the sputtering deposition showing a perfect mirror-like surface.

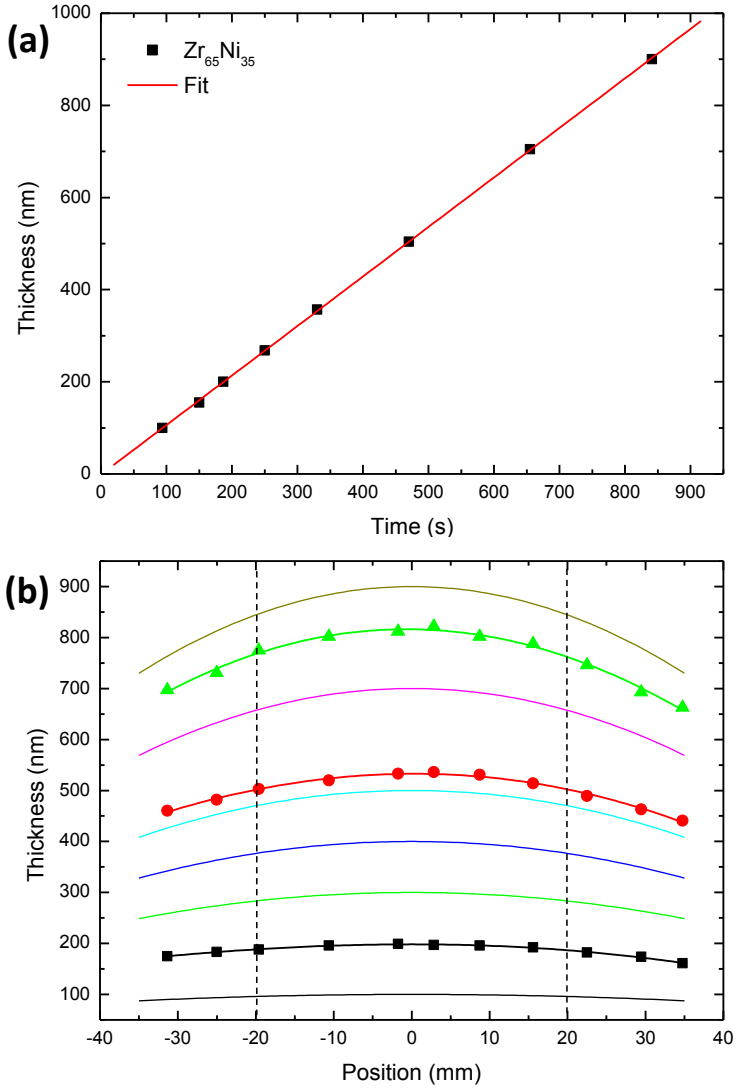

***Figure 2.11** – (a) Linear growth rate (1.1 nm/s) for $Zr_{65}Ni_{35}$ TFMGs (b) Thickness profile along the substrate diameter. Continuous lines are estimated profiles, while symbols indicate the measured values. The profile curvature increases for thicker films, while this effect is negligible for thinner films and partly mitigated if samples are extracted in a region of ± 20 mm from the center (dashed vertical lines).*

In this PhD thesis we investigated different compositions and thicknesses to analyze, respectively, the evolution of the microstructure and the size effects on mechanical properties. The former effect has been studied for 4 alloys $Zr_{42}Ni_{58}$, $Zr_{65}Ni_{35}$, $Zr_{75}Ni_{25}$, and $Zr_{85}Ni_{15}$ (% at), reported in Table 2.2 with a constant thickness of 800 nm (900 for the $Zr_{65}Ni_{35}$). The latter effect has been investigated for the composition $Zr_{65}Ni_{35}$ with a thickness range from 900 nm down to 200 nm.

2.4 Structural characterization

In this section we detail about the experimental conditions for the structural characterization of ZrNi TFMGs. Three techniques have been employed X-ray diffraction (XRD) and transmission electron microscopy (TEM) for the analysis of the microstructure, while X-ray reflectivity (XRR) has been used to measure the mass density.

a) X-ray diffraction (XRD)

The XRD measurements have been carried out using a standard Cu Kα radiation (λ = 0.15418 nm) provided by a PANalytical X'Pert PRO MPD instrument. In order to avoid the silicon (100) substrate signal, the XRD measurements have been performed in grazing incidence geometry, with the incident angle fixed at 0.75° for the thinnest film (≤ 400 nm), and at 0.95° for the thickest one (≥500 nm). The measurements were conducted overnight with an accumulation time of 30 seconds for every 0.14° of scan, in order to maximize the TFMG signal. The acquisition range was varied from 20° up to 100°. Further experimental details are presented in [134-136], while the diffractograms for different compositions and thicknesses are reported in Chapter III section 3.1.

b) Transmission electron microscopy (TEM)

TEM experiments have been carried out by Frédéric Mompiou at the CEMES laboratory at the University of Toulouse. The specimens were analyzed in cross-section and glued together with an epoxy resin (Figure 2.12). The specimens have then been polished by mechanical grinding and ion bombardment using GATAN PIPS system to obtain a thin layer adapted for TEM analysis. Low voltage was used to avoid excessive heating. TEM observations have been carried on a CM20 FEG operated at 200 kV. The electron microdiffraction has been extracted in different areas of the film (inset in Figure 2.12).

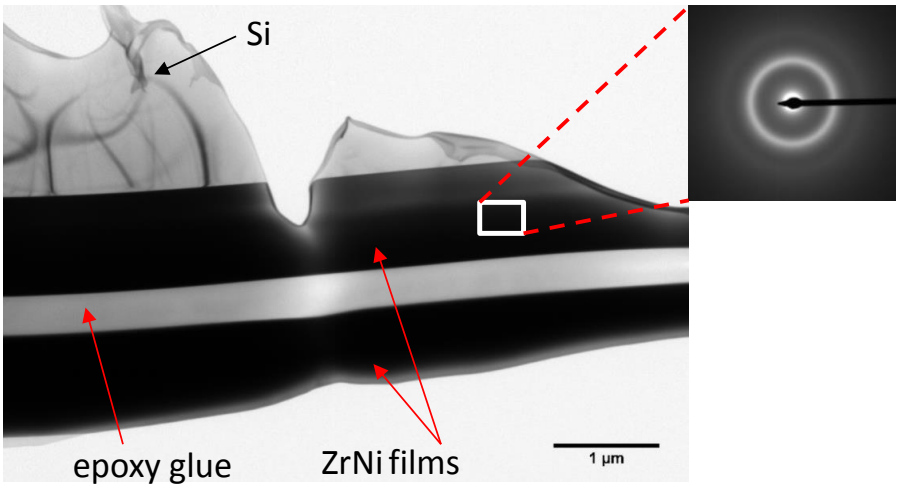

***Figure 2.12** – Specimen preparation for TEM analysis. Two ZrNi TFMGs are glued together using an epoxy resin. A microdiffraction pattern is extracted from a selected zone.*

c) X-ray reflectivity (XRR)

The XRR experiments have been carried out by Grégory Abadias at the PPrime laboratory at the University of Poitiers. The XRR technique involves the reflection at very small angles (< 1.5°) of an X-ray radiation (we used the standard Cu Kα), while analyzing the reflected spectrum. A setup schematic is reported in the inset of Figure 2.13, while more details about the technique can be found

in [129]. An optical model based on Parrat's formalism considering a top surface layer, the ZrNi film, and the interfacial layer between the film and the Si substrate was used to fit the experimental data (Figure 2.13). The fitting procedure enables an accurate determination of the mass density (ρ) estimated from the critical angle (Figure 2.13). Furthermore, XRR allows to measure the thickness (from $\Delta\theta$) as well as to achieve information about the surface roughness from the intensity decay at higher θ (see section 2.3). Figure 2.13 reports the XRR scans for the $Zr_{65}Ni_{35}$ compositions (black line), with the corresponding best-fit simulation (red solid line).

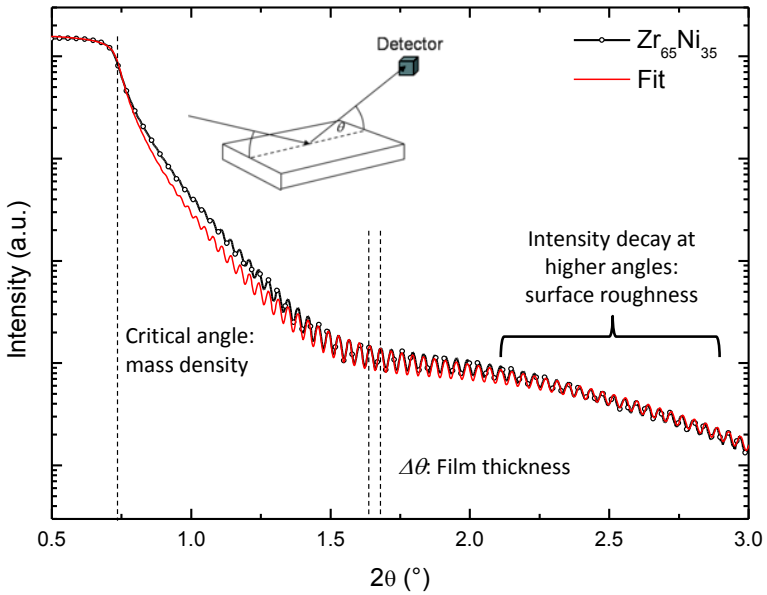

***Figure 2.13** – X-ray reflectivity (XRR) scans for $Zr_{65}Ni_{35}$ TFMGs. The red solid lines correspond to the best-fit curves.*

2.5 Elastic constants extraction

The film elastic constants have been extracted by surface Brillouin spectroscopy (SBS) and picosecond ultrasonics (PU). These experiments have been carried out respectively by Philippe Djemia (LSPM, University of Paris XIII), and Laurent Belliard (INSP, University of Paris VI).

a) Surface Brillouin spectroscopy (SBS)

SBS measurements have been carried out with a monochromatic laser (λ_L = 532 nm) to probe the thermally excited acoustic waves generated inside the sample (details in Refs. [137, 138]). The scattered light has been collected using a backscattering geometry. The SBS spectra were obtained at room temperature in air using a naturally p-polarized light, with typical acquisition times of 2 hours and 200-300 mW power. For nearly opaque layers – such as ZrNi films – the scattering mechanism is restricted to the scattering of light by acoustic waves traveling parallel to the film plane with a wave vector modulus $Q = 4\pi / \lambda_L \sin(\theta)$ [137, 139]. For films with thicknesses around the acoustic wavelength (~ 0.3 μm) and deposited on a substrate with higher acoustic phase velocity ("slow" film on "fast" substrate), the surface acoustic waves consist of the Rayleigh wave (R) and the so-called

Sezawa guided waves (S) at higher frequencies [139] (Figure 2.14). In the case of thicker films (900 nm) the Sezawa waves are merged into a continuum delimited by the transverse threshold frequency $(\omega_T = Qv_T)$ and the longitudinal threshold (LT) frequency ($\omega_l = Qv_l$), Figure 2.14b and [139]. The velocity of the Rayleigh surface wave (v_R) is mainly dependent on the transverse velocity (v_T) [140] through the relation $v_R = \beta v_T$ where β is slightly varying function of the elastic constants that remains closed to 0.94. It should be noticed that v_R does not depend on the film thickness if higher that 300 nm, while a correction is applied for thinner films.

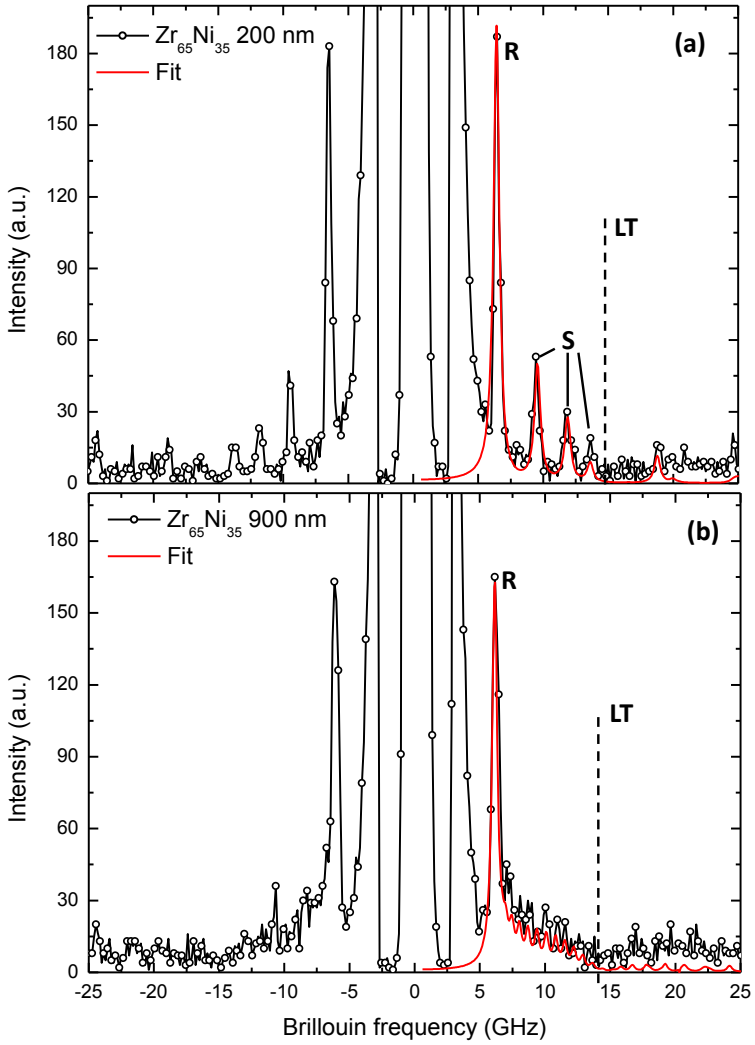

Figure 2.14 *– Surface Brillouin spectra (SBS) for (a) a 200 nm thin film and (b) a 900 nm-thicker film. The best fit (continuous line) allows to extract the Rayleigh (R) and of the longitudinal threshold position (LT) provides the C_{44} and C_{11} elastic constants. Note that Sezawa (S) peaks merge in a continuum spectrum for the 900 nm-thick film (b).*

b) Picosecond ultrasonics (PU)

Picosecond ultrasonics has been used to confirm the values obtained for the longitudinal wave velocity (v_l) by SBS. A femtosecond laser pulse (the pump beam) is absorbed at the sample surface. This

absorption generates by thermal-expansion acoustic waves which propagate in the film normal direction (longitudinal wave). After reflection at the substrate/film interface, the acoustic wave is then probed at the free surface by a time-delayed laser pulse (the probe beam).

The changes in the surface reflectivity (Δr) have been recorded by reflectivity measurements [141]. In the experimental set-up, a mode-locked Ti:sapphire laser source is used, operating at 800 nm with a repetition rate around 79.3 MHz. The pump beam is modulated at 1.8 MHz to improve the signal-to-noise ratio. The longitudinal wave velocity (v_l) is calculated by knowing the film thickness (t) and the time of flight (TOF) as $v_l = 2t / TOF$, where the TOF is the temporal interval between two echoes of the sound wave at the surface (Figure 2.15).

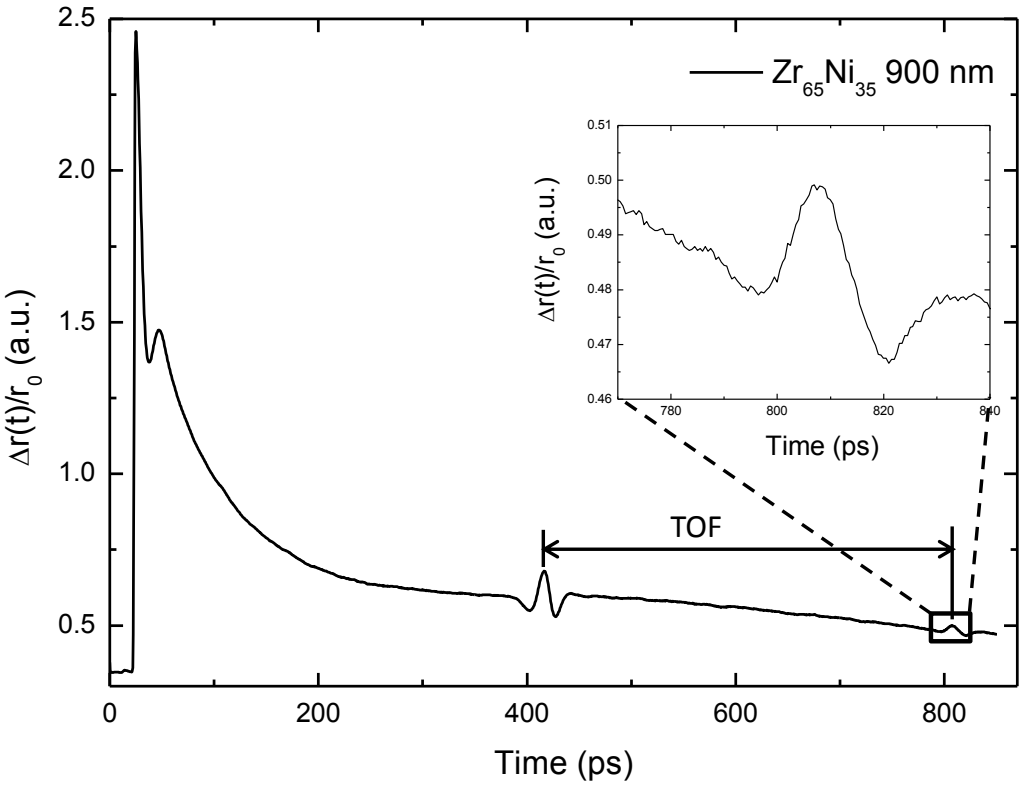

***Figure 2.15** – Variation of the surface reflectivity as a function of time for a 900 nm-thick film. The time of flight (TOF) is calculated as the interval between two echoes of the sound wave at the surface.*

After the extraction of longitudinal (SBP + PU) and transversal (SBS) acoustic waves velocities, the elastic constants can be calculated, considering TFMGs isotropic with two independent elastic constants longitudinal C_{11} and transverse C_{44} (section 1.5.4). The elastic constants $C_{11} = v_l^2 \rho$ and $C_{44} = v_T^2 \rho$ have been obtained from SBS and PU spectra which enable the calculation of the longitudinal (v_l) and transverse (v_T) sound velocities after measuring the mass density (ρ) by XRR. The elastic constants are then combined to determine the elastic modulus (E) and the Poisson ratio (ν) through

$$E = \frac{C_{44}(3C_{11} - 4C_{44})}{C_{11} - C_{44}} \text{ and } \nu = \frac{C_{11} - 2C_{44}}{2(C_{11} - C_{44})} \qquad (2.5)$$

2.6 Nanoindentation and nanoscratch

a) Nanoindentation

Indentation tests were made with a diamond Berkovich tip mounted on an Agilent G200 Nanoindenter DCM II head. Prior to testing, the tip area function was calibrated using a fused silica reference. The nanoindentation measurements were performed under load-control mode at room temperature using the continuous stiffness measurements (CSM) method providing the current value of hardness with increasing indentation depth. The allowable thermal drift rate has been limited at 0.05 nm s^{-1}. Sixteen indents were performed in each sample. The maximum indentation depth was fixed at 500 nm for film thickness larger than 500 nm. The load rate ($\dot{P}/P$) was imposed equal to 0.05 s^{-1}. The hardness was calculated using the Oliver and Pharr method [65]. The film elastic modulus has been extracted to after subtracting the Si (100) substrate contribution.

The activation volume of ZrNi TFMGs can be estimated using nanoindentation data based on the method proposed by Pan *et al.* [55] (see also section 1.5.5, which describes the viscoplastic properties of BMGs under indentation). In BMGs, the constitutive law that controls the viscoplastic deformation is assumed to follow an Arrhenius kinetics of the form $\dot{\gamma} = \dot{\gamma}_s \exp(-\Delta G / kT)$ where $\dot{\gamma}$ is the strain rate, $\dot{\gamma}_s$ is a constant, ΔG is the activation free energy for the elementary deformation mechanism, k is the Boltzmann constant, and T is the temperature [41]. ΔG is related to the applied shear stress (τ) and temperature as

$$d\Delta G = (\frac{\partial \Delta G}{\partial \tau})_T d\tau + (\frac{\partial \Delta G}{\partial T})_\tau dT = -\Delta V d\tau - \Delta S dT . \quad (2.6)$$

Neglecting the entropy variation (ΔS), the so called (apparent) activation volume (ΔV) is given by

$$\Delta V = -(\frac{\partial \Delta G}{\partial \tau})_T = \frac{kT}{\tau}(\frac{\partial \ln \dot{\gamma}}{\partial \ln \tau})_T . \quad (2.7)$$

The strain rate sensitivity is defined as $m_H = (\partial \ln \tau / \partial \ln \dot{\gamma})_T$, hence $\Delta V = kT / m_H \tau$. Moreover, the hardness $H \approx 3\sigma_y \approx 3\sqrt{3}\tau_y$ [41, 55, 77], thus

$$\Delta V \approx \frac{3\sqrt{3}kT}{m_H H} . \quad (2.8)$$

Therefore, the activation volume can be extracted by knowing the strain rate sensitivity (m_H) and hardness (H). The rate sensitivity can be calculated considering that $\dot{\gamma} \approx \dot{\varepsilon}$, (with $\dot{\varepsilon}$ being the representative indentation strain rate) [41, 55, 77]. Hence, m_H could be re-written as $\partial \ln H / \partial \ln \dot{\varepsilon}$, and it can be extracted from the slope of a logarithmic plot of H versus $\dot{\varepsilon}$. The indentation strain rate can be easily calculated since the loading rate ($\dot{P}/P$) is kept constant in a CSM configuration and $\dot{\varepsilon}$ can be estimated as $\dot{P}/2P$ [55]. Three different loading rates equal to 0.02, 0.05, and 0.1 s^{-1} have been used.

Other nanoindentation measurements have been conducted by Jean-Pierre Guin and Mariette Nivard (LARMAUR, university of Rennes I). Measurements have been conducted with a diamond

Berkowich tip mounted on a Hysitron nanoindenter using a standard indentation mode. A constant normalized indentation depth (ratio between the indenter penetration and the film thickness) equal to 25% has been applied for all investigated thicknesses. Indents have then analyzed by scanning probe microscopy (SPM).

b) Nanoscratch

Nanoscratch experiments have been conducted with a diamond conico-spherical tip mounted on a Agilent G200 instrument (used also for nanoindentation). The tip opening angle is 90° ± 5°, while the tip curvature radius is of 5.0 ± 5 μm. The choice of a conico-spherical tip is dictated by the symmetric configuration maintained during scratch. The opening angle and the tip curvature radius have been selected to produce a well-defined scratch similarly to studies reported in the literature [82, 83]. Different loading ramp were studied with the normal load increasing linearly from minimum to maximum up to substrate scratching. Films with thickness equal to 300 nm were tested with a loading rate from 0 to 60 mN over a scratch length of 180 and 360 μm, while for 700 nm-thick films a loading ramp from 0 to 80 mN and from 0 to 60 mN has been applied over a scratch length of 240 and 360 μm, respectively. This leads to a constant values of force increment, respectively of 0.33 and 0.17 mN/μm. For each condition, two scratch velocities have been investigated respectively of 3 and 30 μm/s. Before the scratch, the surface is scanned by the tip to acquire the surface profile. The same procedure is effectuated also at the end of the test to measure the elastic recovery. The applied normal force, the tangential force, and the penetration depth during the scratching test were recorded by the system, and the coefficient of friction (COF) was calculated as the ratio of the tangential force to the normal force. FE-SEM was used to examine the morphologies of the scratches.

2.7 Fracture test

The fracture analysis has been performed by cracking Si wafers using cleaving pliers from a shallow notch induced by a diamond tip on the back face, with the crack finally propagating into the film (Figure 2.16). The loading configuration resembles a standard three-point bending test. The fracture surfaces are then observed by FE-SEM [142].

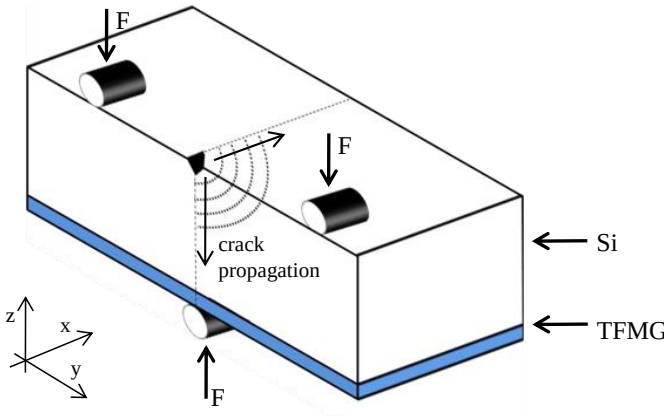

***Figure 2.16** – Schematic representation of the crack propagation configuration for a TFMG deposited onto a Si wafer [142].*

2.8 Uniaxial tensile test: lab-on-chip concept

In this section we describe the lab-on-chip technique which allows to produce ZrNi freestanding films and to extract the mechanical properties from microtensile tests. We will not enter in the specific details of each step that constitute the process, while refer readers to the following references [143-145] and the PhD thesis of the Michael Coulombier at the Université catholique de Louvain (UCL) [146] to achieve in-depth information.

The lab-on-chip concept aims to extract the mechanical behavior of thin film from the elastic deformation up to plasticity and fracture. This concept differs from the majority of techniques presented in the literature (see for instance section 1.6 for testing of small scale metallic glasses) through essentially two aspects:

- the idea to test a thin film by using an internal stress presented in one material (Si_3N_4), the so called "actuator" layer, while avoiding external loading,
- the use of microfabrication technology which allows to reproduce different elementary patterns. Connected to this advantage, there is the possibility to develop thousands of elementary testing concept on a single Si wafer.

In the case of mechanical testing of ZrNi TFMGs, a single structure often referred as "micromachine" involves two layers deposited on top of a silicon substrate, Figure 2.17. The first layer is the "actuator layer" (Si_3N_4) and provides the actuation force coming from the high tensile internal stress (σ_{int}) generated inside the layer during deposition. This layer is patterned by means of lithography technique to have a rectangular shape. The second layer called "specimen layer" is the film material to be tested (ZrNi). This layer partly overlaps with the actuator layer and it is patterned in a dogbone shape. After release by selective etching the substrate, the specimen beam is strained owing to the contraction of the actuator beam. The resulting freestanding structure reaches a stable position governed by force equilibrium. Knowing the displacement of the system actuator-specimen, direct application of force equilibrium gives access to the strain and stress in the specimen beam assuming that the actuator deforms elastically. Different states of stress can be generated from small strain elastic behavior up to fracture of the specimen beam by modifying the geometry of the beams (section 2.8.1).

2.8.1 Extraction of film mechanical properties

This section aims to analyze the mechanics of a single micromachine in order to determine the relationship that allows extraction of the strain and stress inside the specimen beam [143-145].

In the case of uniaxial tension, the stress (σ) and mechanical strain (ε^{mech}) in the specimen can be directly inferred from the displacement (u) measured between a moving and a fixed cursor (Figures 2.16 and 2.18) and from the knowledge of the mismatch strain of both the actuator (ε_a^{mis}) and test specimen (ε^{mis}). These mismatch strains result from the fabrication process and the deposition steps. The mechanical strain in the specimen and actuator is given by the difference between the total and mismatch strain respectively as

$$\varepsilon^{mech} = \ln\left(\frac{l_0 + u}{l_0}\right) - \varepsilon^{mis}, \tag{2.9}$$

$$\varepsilon_a^{mech} = \ln\left(\frac{l_{0a} - u}{l_{0a}}\right) - \varepsilon_a^{mis}, \tag{2.10}$$

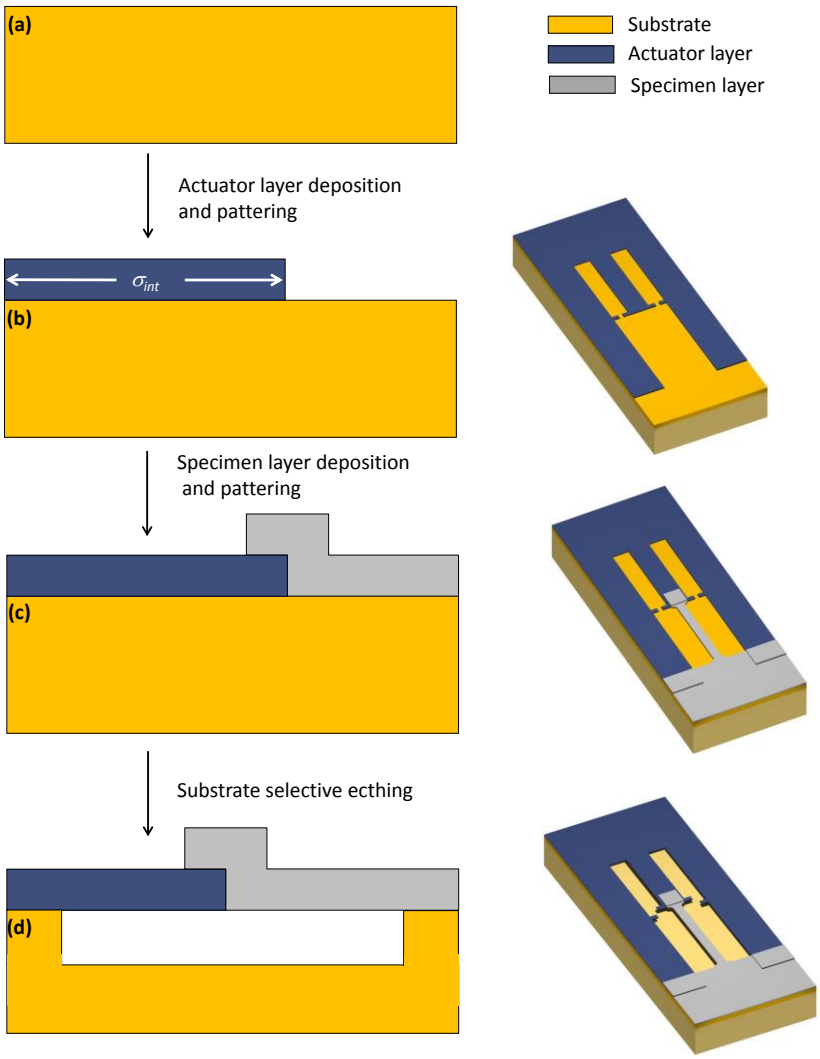

Figure 2.17 *– Schematic of the lab-on-chip concept. Starting from the bare substrate (a). The fabrication process involves the deposition of the actuator layer (Si_3N_4) and the specimen layer, respectively (b) and (c). The selective etching of the substrate leads to releasing the internal stresses in the actuator and to generate a strain in the specimen beam (d).*

where l_0 is the initial length of the specimen and l_{0a} is the initial length of the actuator beam. Assuming the actuator material remains elastic and knowing its Young's modulus (E_a), the stress is given by

$$\sigma_a = E_a \varepsilon_a^{mech} . \tag{2.11}$$

This assumption is justified by the choice for a low pressure chemical vapor deposition (LPCVD) Si_3N_4 layer as the actuator beam. Si_3N_4 is a stiff, brittle material which deforms in a linear elastic way and which can be deposited with large tensile internal stresses (around 1GPa). The stress in the sample can be calculated using

$$\sigma = \sigma_a \frac{S_a}{S}, \tag{2.12}$$

where S_a and S are the actuator and test sample sections, respectively. The equation 2.9 and the combination of equations 2.10, 2.11, and 2.12 provide the general expression for the stress generated by the actuator layer and for the corresponding deformation of the specimen beam as:

$$\begin{cases} \varepsilon^{mech} = \ln(\frac{l_0 + u}{l_0}) - \varepsilon^{mis} \\ \sigma = E_a \frac{S_a}{S} (\ln(\frac{l_{0a} - u}{l_{0a}}) - \varepsilon_a^{mis}) \end{cases} . \quad (2.13)$$

Hence, it is possible to evaluate the stress and strain in the specimen by knowing the mismatch strain of the actuator and the specimen beam, and the cursor displacement (u). Different strains can be imposed by changing the length (l), the width (w), and the thickness (t) of the actuator and/or of the test specimen, allowing the determination of a full stress strain curve. As a consequence, the design includes a series of test structures with varying dimensions (Figure 2.18). Specifically, short actuators and long specimen beams provide small stresses thus deforming only elastically the specimen, while long actuator and short specimen involve higher stress reaching plasticity (Figure 2.18). The effect of the width and thickness of the film and actuator play a similar role, with higher stresses and deformations achieved for a large ratio w_a / w and t_a / t.

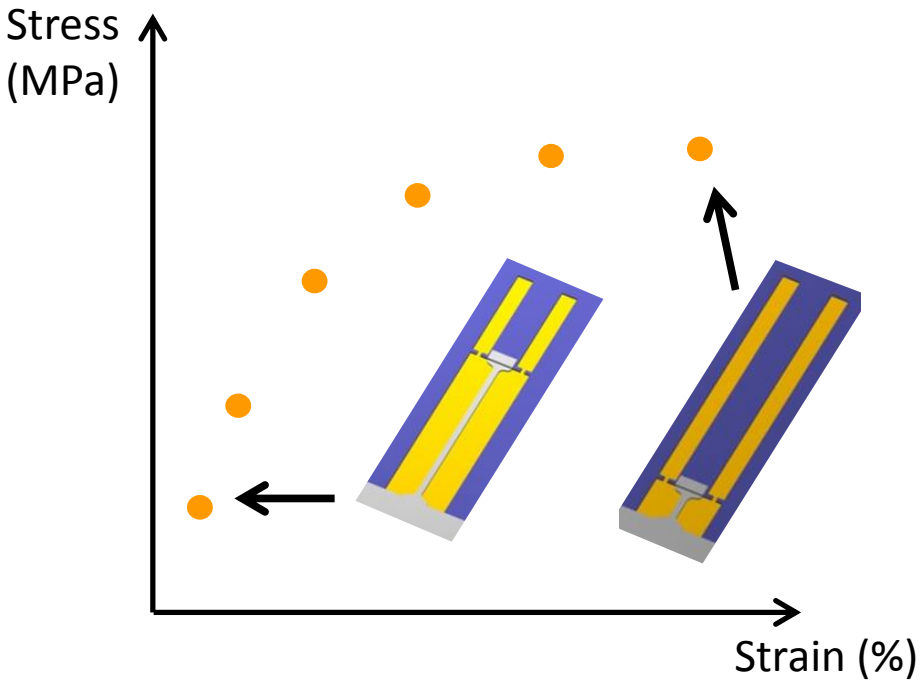

Figure 2.18 *– The stress strain curve obtained for different actuator-specimen lengths.*

While u is measured by direct SEM observation of cursors displacement for different micromachine lengths (Figure 2.19), the mismatch strain of the actuator and the specimen beams have been calculated from the analysis of auto-actuated structures and by the measurement of internal stresses, respectively.

In the former case, ε_a^{mis} is derived from the cursor displacement measured on a double clamped beam involving two parts (i.e. the actuator and the specimen) constituted of the same material (Si_3N_4) [145, 146]. The larger one acts as the actuator, while the smaller acts as the specimen. After release and development of tensile internal stress, the wider beam will contract and pull on the smaller one. Under the condition that all the parts of the structure stay in the elastic regime, the structure reaches a stable equilibrium with a deformation value ε_a^{mis} in the form of [145, 146]:

$$\varepsilon_a^{mis} = \frac{S\ln(\frac{l_0+u}{l_0}) - S_a\frac{-u}{l_{0a}}}{S - S_a}. \qquad (2.14)$$

Note that all the geometrical parameters are known, while *u* is easily measured at the SEM. Multiple structures are designed with varying dimensions in order to optimize the parameters that will give the most accurate value for mismatch strain. We found a constant value of ε_a^{mis} equal to -0.0028, where the minus indicates the development of tensile stress on the specimen beam.

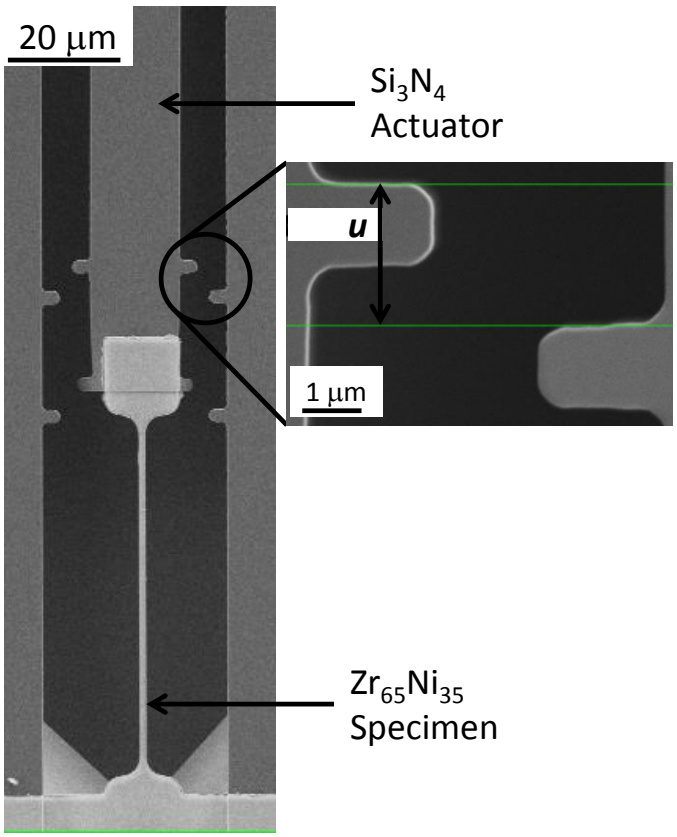

Figure 2.19 *– SEM micrograph of a "micromachine" after release. The measure of the cursor displacement provides the deformation in the specimen beam.*

However, this method cannot be applied for the measure of mismatch strain of the specimen beam, ε^{mis}. As a matter of fact, the specimen film is subjected to internal compressive stress during the deposition, leading to out-of-plane bending for the longest beams which elongate in the same direction of the tensile deformation imposed by the actuator (Figure 2.20). Since the auto-actuated structures have a length of about 1 mm involving out-of-plane-bending, the specimen mismatch has been calculated starting from the measure of internal stresses in the film (σ), using the Stoney's equation [143, 145, 146]:

$$\sigma = \frac{1}{6}\frac{E_s}{1-\nu_s}\frac{t_s^2}{t_f}\left(\frac{1}{R_{post}} - \frac{1}{R_{pre}}\right) \qquad (2.15)$$

where $E_s/(1\text{-}\nu_s)$ is the biaxial modulus of the substrate (Si) equal to 180 GPa, t_s is the substrate thickness equal to 380 μm, t_f the film thickness and R_{pre} and R_{post} the initial and the final curvature of

the substrate, respectively. Specifically, the measure of specimen internal stresses has been calculated by measuring the substrate curvature with a mechanical profilometer before and after the deposition of the ZrNi specimen layer. The corresponding deformation (ε^{mis}) is calculated as:

$$\varepsilon^{mis} = \frac{\sigma(1-\nu)}{E} \tag{2.16}$$

where E and ν are the ZrNi elastic modulus and Poisson ratio measured by surface Brillouin spectroscopy and picosecond ultrasonics (section 2.5). The internal stress has a value of 240 MPa (in compression) with a small scatter as a function of film thickness. By knowing E and ν (respectively 72000 MPa and 0.39), ε^{mis} is equal to +0.0017, where the positive sign indicate the development of a compressive stress.

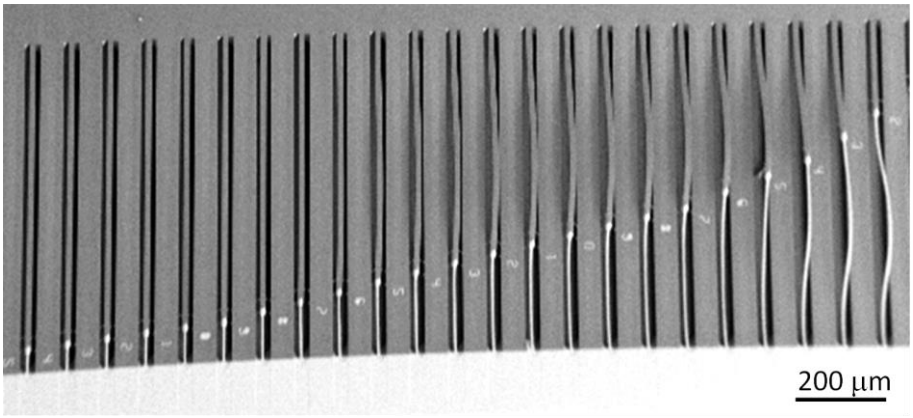

Figure 2.20 *– Out-of-plane bending of longer specimen beams (white) due to internal compressive stresses. Note also a severe deformation of the actuator beam (gray).*

Although the presence of compressive internal stresses causes a significant bending and distortion of the specimen beam, there are no evidences of fracture at the overlap between the specimen and the actuator, which is always the most delicate part of each micromachine. Figure 2.21 shows the case of highly bent and twisted specimens which do not separate for the actuator beam. This means that ZrNi specimens are ideal materials for the lab-on-chip technique. A possible explanation of the high adhesion between actuator and specimen beams is the high energy of ZrNi atomic species deposited by magnetron sputtering, as well as the isotropic film growth providing the formation of a compact ZrNi film strongly anchored to the actuator layer.

However, the presence of an out-of-plane bending can significantly alter the measure of cursors displacement (u), and also the value of the stress (equation 2.13). To sort out this problem, we investigate only the lab-on-chip within the so-called B series, where B indicates special micromachines designed for brittle materials. Here, the specimens have a fixed length, while varying the length of the actuator thus leading to different deformation and stress level of the specimen.

Furthermore, the specimens investigated have a very short length of 25, 50 and 100 μm which does not lead to any out-of-plane deformation, even if compressive external stresses are present (Figure 2.22). Other advantages of the B series consist in having the largest actuator width (15 μm), thus reaching the highest stress values. In addition, it has been analyzed also the series BT, where T indicate the tapered shape of the actuator. This series provides a more delicate release internal stresses of the actuator leading to a uniform deformation rate. However, both series (B and BT) involve the same length of actuator and specimen, thus leading to the same stress and strain levels.

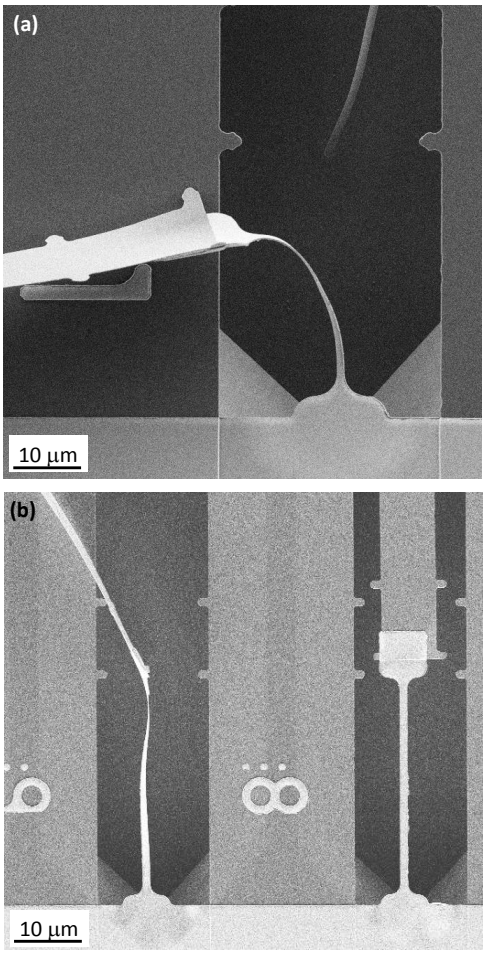

Figure 2.21 *– Examples of bent and twisted specimens which do not separate from the actuator beam. (a) and (b), respectively a 360 nm-thick film deposited on a 160 nm-thick actuator and a 200 nm-thick film deposited on a 100 nm-thick actuator. A non-bent specimen for comparison is reported in (b).*

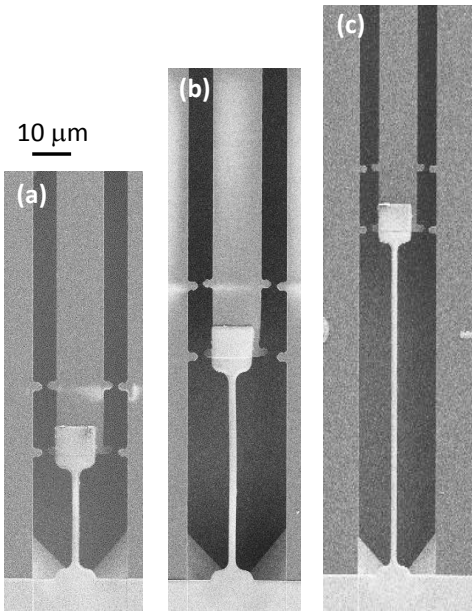

Figure 2.22 *–Absence of out-of-plane bending for 25, 50 and 100 μm-long specimen beams within the B series, respectively (a), (b), and (c).*

2.8.2 Fabrication steps

In Figure 2.17 it has been described the process involved in the production of the lab-on-chip. Here, we make in-depth analysis, while focusing on the characteristic steps for testing ZrNi specimen. The whole process have been conducted exploiting the WINFAB facilities at the UCL (a clean room class 1,000), with the exception of the deposition of the ZrNi TFMGs which has been done at the PTA in Grenoble. A simplified scheme of whole process consists of the following phases:

1. wafer selection,
2. deposition and patterning of the actuator layer,
3. deposition and patterning of specimen layer ("lift-off" process),
4. release of freestanding films.

1) Wafer selection

The substrates used for processing are Si wafers with a diameter of 3 inches and a thickness equal to 380 μm polished on the front face. The wafers are made of pure monocrystalline Si (100). The orientation is given in Figure 2.23a. Note that <100> directions are oriented at 45° with respect to the Si flat. The measure of the internal stress of the actuator and specimen to extract, respectively, the internal stress and the mismatch strain requires a monotonic curvature (equation 2.15, Figure 2.23b). Indeed, wafer curvature method is used for stress measurement (equation 2.15) and monotonic curved substrate is a first requirement in order to produce accurate measurement. The curvature is determined by running a profilometer tip along one axis of the wafer.

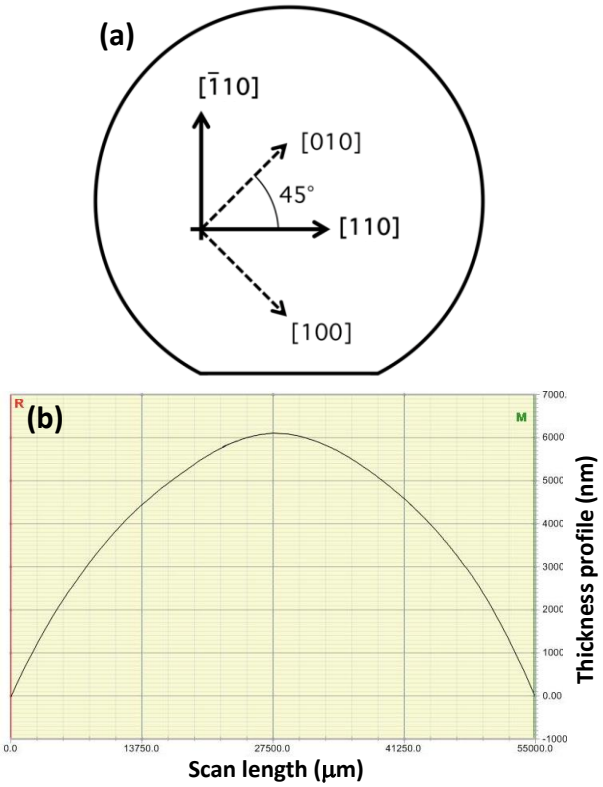

Figure 2.23 *– (a) Si substrate orientation and (b) an example of positive curvature profile.*

2) Deposition and pattering of the actuator layer

The actuator dimensions and its mechanical properties are essential in order to extract accurate stress values of deformation and stress in the specimen beam. Hence, this layer should be uniform over the entire wafer. Furthermore, it should have a very high resistance to the TMAH solution used in the releasing phase.

LPCVD (low pressure chemical vapor deposition) silicon nitride (Si_3N_4) is used as the actuator layer. It is deposited at 790°C in a vertical Koyo VF-1000LP furnace. The internal stresses (measured with equation 2.15) are thickness independent and about 1GPa in tension. The thickness uniformity is very good as it varies by approximately 1-3 nm over a 3-inches wafer. The internal stress inside the Si_3N_4 layer comes from the difference of thermal expansion coefficient (α) between the silicon nitride ($\alpha = 6.06\ 10^{-6}\ °C^{-1}$) and the silicon substrate ($\alpha = 2.3\ 10^{-6}\ °C^{-1}$). LPCVD Si_3N_4 is amorphous and transparent to visible light, hence its thickness can thus be measured using ellipsometry. Moreover, It is an isotropic brittle material meaning that its mechanical behavior is entirely described by its elastic modulus (250 GPa) and its fracture strength.

Si_3N_4 is deposited on both faces of the silicon substrate. No change of curvature is observed after deposition. Internal stress inside the upper layer can only be determined after etching of the silicon nitride deposited on the back side. This is performed by dry etching with SF_6 plasma. Then, a wafer curvature measurement can be performed to extract internal stress in the Si_3N_4 upper layer.

The patterning of the actuator layer is made by photolithography (an example of the process can be found in Refs. [130, 146]). A positive photoresist (AZ6612) is deposited on the active face of the wafer. After prebaking of 90 seconds at 110°C, the photoresist is exposed to a pattern of UV light using the “actuator mask”. Note that in order to have a complete release of freestanding film with TMAH (Tetramethyl-ammonium hydroxide) etching, the mask pattern must be rotated of approximately 45° with respect to the flat on the Si in order to be aligned to the (100) directions (Figure 2.23). The exposed positive photoresist is then dissolved in a TMAH-based solution called "developer". A post-exposure bake allows the densification of the remaining photoresist. At this step, the pattern has been transferred from the mask to the photoresist. The next step consists in a pattern transfer from the photoresist to the Si_3N_4 layer. Dry etching is used for that purpose. A two steps SF_6 and CHF_3 plasma etches the unprotected part of the Si_3N_4 layer. This choice is motivated by the low selectivity of SF_6 with the Si substrate. Hence, the last 25 nm of Si_3N_4 are etched with CHF_3 assuring the etch stop at the interface with the silicon and limiting underetching. The remaining photoresist is then removed using acetone. Using UV light for the photolithography process offers a resolution of 0.6 μm meaning that the smallest shape that can be transferred is 0.6 μm large.

3) Deposition and patterning of the specimen layer (“lift-off” process)

The deposition of the specimen and pattering has been made by using the lift-off method (Figure 2.24). Contrary to the actuator patterning involving a positive lithography step, here the idea is to deposit a negative photoresist (AZ5214) on the wafer *before* the specimen deposition (Figure 2.24b). After pre-baking of 110 seconds at 110 °C, the photoresist is exposed to a pattern of UV light through the “specimen mask” (Figure 2.24c). Note that the specimen mask must be perfectly aligned with respect to the actuator pattern. This is a very delicate part of the process because an error of more than 1 μm did not allow a correct overlap the specimen beam onto the actuator beam. The rotation of the

wafer at 45° with respect to the pattern on the mask increases the difficulty of the process as well. A post-baking of 40 seconds at 118 °C is then performed followed by another exposure to UV light under an all-transparent mask. The negative photoresist which was masked during the first exposure is then dissolved in the "developer" (Figure 2.24d). At this point, the wafers have been packed and sealed under a protective N_2 atmosphere and transported to the PTA in Grenoble for the specimen (ZrNi) deposition (section 2.3). The deposition covers the whole wafer (Figure 2.24d). Afterwards, wafers are packed and sealed again in a protective N_2 atmosphere and transported to the WINFAB at the UCL, where the lift-off process is completed dissolving the photoresist in acetone within a ultrasonic bath. The specimen material located on the photoresist disappears with the acetone solution, while specimen material deposited directly on the wafer remains intact (Figure 2.24f).

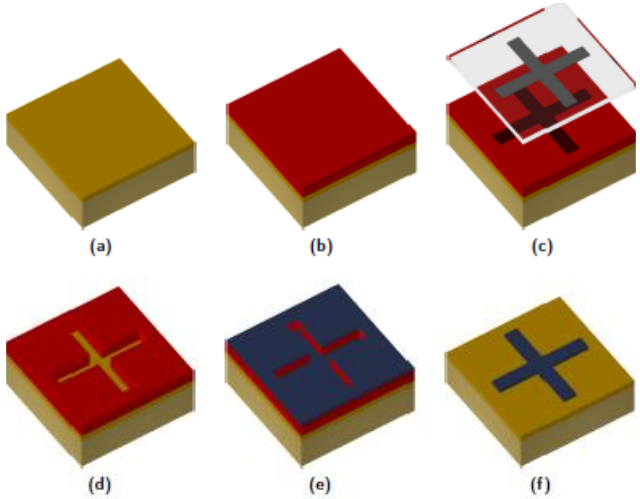

Figure 2.24 *– Lift off process (negative photoresist): (a) initial configuration, (b) photoresist deposition, (c) mask contact and exposure, (d) dissolution of the exposed photoresist, (e) thin film deposition, (f) photoresist removal (lift-off) [146].*

4) Release of freestanding films

All the previous steps aimed at creating the micromachines. However, in order to load and deform the test material, the Si substrate must be etched enabling actuator to contract.

Before the etching phase, the 3-inches wafer must be cut in small dies correspondent to the structures (i.e. the B series) that we want to investigate. Nevertheless, because the 45° orientation of the pattern with respect to the Si flat (Figure 2.23), a hand-made cleavage is not possible. Therefore, wafer is cleaved by mechanical dicing. During dicing, wafers are mounted on a specific tape and then cut along precise directions designed in the mask. Once a wafer has been diced, the dies stay on the dicing tape until they are extracted. A photoresist (a blue resist) deposited onto the wafer patterned surface protects the structure from debris produced during the dicing process. The photoresist is then removed by using acetone.

Now the small dies are ready for the selective etching (referred to release phase). The release has been conducted in a TMAH (Tetramethylammonium hydroxide) solution (10% vol. in deionized water) at a fixed temperature of 85°C. The choice of TMAH etching arises from the Antoine Volland's PhD thesis [128], which has shown a very high selectivity with respect to the ZrNi TFMGs. As a

matter of fact, the TMAH solution dissolves selectively the Si substrate without any effect on the ZrNi and the actuator layer, even if the etching phase can last several minutes (see also Ref. [130]). For the reported conditions, the etching rate for the <100> direction is of 1μm/min, this means that to fully release the widest actuator (15 μm) the die should stay in the TMAH solution for at least 7.5 minutes. However, the Si dissolution process requires more time due to activation kinetics. Hence, the selected time was optimized to be around 17 minutes assuring a complete release of the micromachines.

Here, it is important to note that the TMAH etching is an anisotropic etching, meaning that the etching rate depends on Si crystalline planes, which have different atomic densities [130]. As a matter of fact, the etching rate of the denser (111) plane is about 0.12 μm/min, while the (100) planes can be etched at a velocity of 1 μm/min or more [130]. Hence, the (111) planes act a etch stop planes. This means that freestanding beams can be obtained only if they are oriented along the (100) plane which is at 45° with respect to the flat (Figure 2.25). As a matter of fact, if the beams are oriented toward the <110> direction (Figure 2.25a), the (111) planes stop the etching creating a characteristic angle of 54.74° with respect to the (100) planes. On the other hand, if the pattern is oriented toward the <100> direction, the Si does not expose the (111) planes, with the possibility to fully release freestanding beams (Figure 2.25b). However, the absence of etch stop plane leads to an underetching in the region between two neighbor micromachines (see Figure 2.25b and the brighter zones in Figure 2.21b). This does not represent a real problem, however it is suggested that the underetching should not overcome the distance of 40 μm between two neighbor micromachines. Hence, the etching time must never exceed 20 minutes.

Once the etching in TMAH solution is concluded, the die is immersed for 10 minutes in a deionized H_2O at 40°C to stop the etching and to reduce the thermal stresses gradient. Afterwards, the die is placed in two deionized H_2O bakers at room temperature for 10 minutes each to complete the etching stop process.

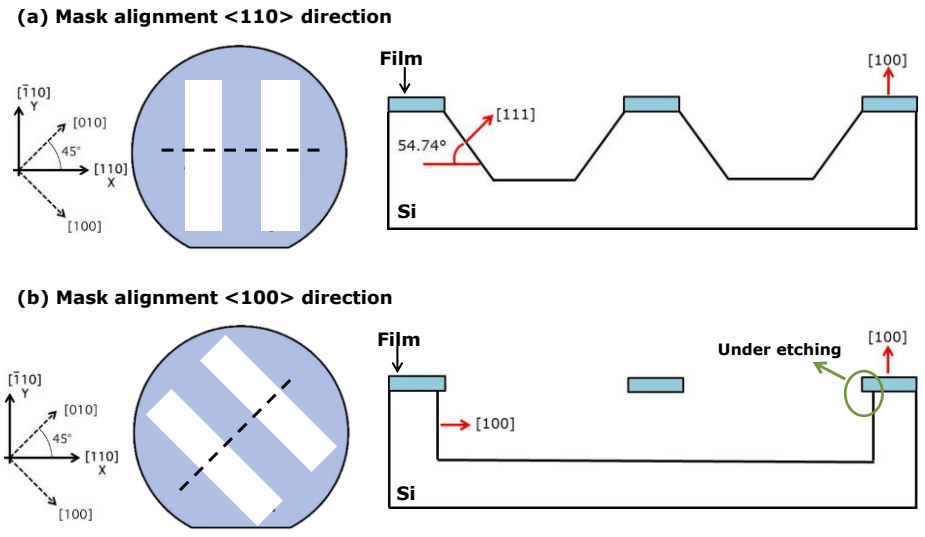

Figure 2.25 *– TMAH etching as a function of the beam orientation. Only beams oriented along Si (100) planes can be released (b).*

The measurements of cursors displacements (*u*) have to be performed in a SEM environment, involving very low pressure and no liquid can remain on the wafer. Hence, the structures must be carefully dried. Air drying can damage the structures. Indeed, capillary forces would cause the stiction of the structures on the underneath substrate (even if the TMAH etches up to a depth of about 17 μm).

The solution is to avoid the phase transformation from liquid to vapor by using a critical point dryer (CPD). Basically, a CPD consists in a chamber in which the temperature and the pressure can be controlled. CPD raises the pressure and the temperature of the liquid solution till reaching its critical point where there is no interface between liquid and vapor phases. Pressure in the chamber is then decreased to atmospheric pressure. The CPD machine is a Tousimis 915B and uses CO_2 for drying. The critical point of CO_2 is 31.3 °C and 7.38 MPa. After the drying, the sample is ready for SEM observation. Note that a whole cycle in the CPD lasts for about one hour.

2.8.3 Samples investigated

The samples investigated with the lab-on-chip technique have been reported in Table 2.3. The actuator (Si_3N_4) has a fixed width of 15 μm and a variable length to provide different stress and deformation in the specimen (Figure 2.18). The specimens have a composition $Zr_{65}Ni_{35}$ with different thicknesses (110, 200 and 360 nm), lengths (25, 50, and 100 μm) and widths (1, 2, 4 μm), aiming to investigate size effects on thickness as well as the effect of different geometries on the mechanical behavior. All the samples have been observed at the SEM at different time interval after release to study the relaxation behavior and to extract the activation volume.

Actuator thickness (nm)	**Specimen thickness (nm)**	**Specimen length (μm)**	**Specimen width (μm)**
80	110	25-50-100	1-2-4
100	200	25-50-100	1-2-4
160	360	25-50-100	1-2-4

Table 2.3 *– Geometries of specimens and actuators analyzed in this thesis.*

2.9 Electrical resistivity

Electrical resistivity have been measured using a four-points collinear probe (K2400) to avoid contact resistances between the tips and the sample surface. The current (I) is injected from the external tips, while the voltage (V) is measured by the central ones. Accurate data are collected at a voltage of 20 mV and placing the probes at a distance of at least 1 cm from the specimen edge. Data are averaged between five measurements to have statistical consistency. The sheet resistance (R_s, Ω/□) can be calculated as

$$R_s = \frac{\pi}{\ln(2)} \frac{V}{I} \tag{2.17}$$

while electrical resistivity (ρ_e, μΩ cm) can be determined as $\rho_e = R_S t$, where t is the thickness.

The measurement of electrical resistivity as a function of the temperature have been carried out by Jerzy Antonowicz (department of physics, technical University of Warsaw). A DC four-probe

collinear method with electrodes separated of 10 mm has been used. The sample is placed on a cold finger sitting inside a furnace and the electrodes press the sample from above against the cold finger. The whole setup is located in a secondary vacuum chamber created by a diffusion pump. The heating rate is fixed at 10 K/min, while measuring the voltage. The maximum temperature limit is fixed at 900K. Measurements have been collected before and after the test on the recrystallized sample. To avoid Si effect on electrical resistivity (enhanced at high temperatures), the ZrNi TFMGs has been deposited on Si substrate coated by a SiO_2 insulating layer.

2.10 Conclusion

In this chapter we review the deposition and the characterization techniques used to study ZrNi TFMGs with the objectives to summarize all the key elements necessary for the understanding of the results reported in Chapters III, IV, and V.

After a brief introduction justifying the choice of the ZrNi composition followed by the vapor phase deposition techniques and growth mechanisms, the deposition of ZrNi TFMGs has been presented. We have shown that the selected sputtering parameters as well as the development of a composite target enable to deposit TFMGs accurately controlling the composition, the growth rate and the thickness profile.

The structural characterization techniques (XRD, TEM and XRR) has been presented reporting the experimental condition used to analyze TFMGs.

The mechanical characterization techniques involve surface Brillouin spectroscopy, picosecond ultrasonic, nanoindentation, nanoscratch, and fracture. These techniques have been reviewed summarizing the adopted experimental parameters. In the case of surface Brillouin spectroscopy and Picosecond ultrasonics, the procedure to extract the elastic constants on the basis the measured velocity of longitudinal and transversal phonon waves has been discussed. The method to calculate the atomic volume on the basis of nanoindentation experiments at different loading rate has been presented as well.

The mechanical characterization using the lab-on-chip concept occupied a large part of this chapter. The concept has been presented from a theoretic view highlighting how to obtain the mechanical properties as a function of different geometries of actuator and specimen. Moreover, emphasis has been dedicated to the methodology used to extract the actuator and specimen mismatch strain. We reported the presence of out-of-plane bending for long specimen beams anchored to short actuator, while showing a very good adhesion and no debonding at the overlap. The problem of out-of-plane bending has been sorted out by considering only shorter specimen beams (up to 100 μm) which are not affected by this phenomenon. Lastly, the entire lab-on-chip fabrication process has been summarized.

The analysis of the experimental setup for the measure of electrical resistivity closed the chapter.

Chapter III – Structural and elastic properties of ZrNi thin film metallic glasses

The objectives of this chapter are to analyze the atomic structure of ZrNi thin film metallic glasses (TFMGs) with respect to the thickness and composition, providing the basis for the understanding of other experimental results involving plasticity and fracture, respectively in Chapters IV and V.

As reported in section 2.3, the investigation on mechanical size effects has been carried out for the composition $Zr_{65}Ni_{35}$ with a thickness range from 900 down to 200 nm. The mechanical properties of a 110 nm-thick freestanding films have also been investigated (Chapter IV, section 4.2.3). On the other hand, the effect of the composition has been addressed at constant thickness only (800 nm). Four compositions have been studied $Zr_{42}Ni_{58}$, $Zr_{65}Ni_{35}$, $Zr_{75}Ni_{25}$, and $Zr_{85}Ni_{15}$.

We start this chapter investigating the structure of different thicknesses and compositions, followed by an analysis of the mass density and the elastic constants obtained, respectively by X-ray reflectivity and by surface Brillouin spectroscopy and picosecond ultrasonics. The fragility index will be calculated and used to predict the mechanical behavior in terms of plastic strain as reported in sections 1.5.4 and 3.3. Afterwards, we analyze the electrical resistivity, while ending the chapter with the Nagel and Tauc criterion used to model both the structural evolution, with crystallization phenomena for Zr-rich specimens, and the change in electrical resistivity as a function of the composition.

3.1 Microstructural analysis

The analysis of the microstructure has been carried out using grazing incidence X-ray diffraction (XRD) and transmission electron microscopy (TEM), see section 2.4 for the description of the methods. At first, we focus on the effect of thickness for the composition $Zr_{65}Ni_{35}$, followed by the effect of the composition at constant thickness.

a) Effect of thickness

The XRD diffractograms for $Zr_{65}Ni_{35}$ TFMGs are reported in Figure 3.1a for different thicknesses. All the specimens involve a fully amorphous structure indicated by the presence of an asymmetric first sharp diffraction peak (FSDP) followed by a broader halo at higher angles (section 1.2). This is confirmed by the absence of crystalline spots for a 900 nm-thick specimen analyzed by TEM microdiffraction (inset of Figure 3.1a). Note that the investigated alloy has a composition within the

amorphisation range of ZrNi (10 < %at. Zr < 80, section 2.1). The position of the FSDP (Q_p) and the full width at half maximum (FWHM) – obtained after fitting with a Lorentzian function – are constant and equal to 36.7° and 5.5°, respectively (Figure 3.1b).

If the diffractograms in Figure 3.1a are converted into scattering vector (Q, Å^{-1}) coordinates by means of $Q = 4\pi \sin\theta / \lambda$, where λ is the X-ray wavelength (1.5418 Å), the FWHM is equal to 0.39 Å^{-1} slightly below the literature values for multicomponents BMGs (~0.5 Å^{-1}) [147]. The average atomic distance, calculated using the Bragg law, is close to 2.4 Å. Note that this value is smaller than the sum of the atomic radius of Zr (1.55 Å) and Ni (1.35Å), meaning that there exist strong chemical interaction between Zr and Ni [123, 124]. The thickness independent values of both Q_p and FWHM indicate that specimens have a similar atomic structure (or the same free volume content). Moreover, they show the same strong Zr-Ni atomic correlations – as expected for the compositions close to $Zr_{65}Ni_{35}$ (section 2.1 and Refs. [124, 127, 134]) – with the FWHM below the literature values reported for multicomponent highly disordered BMGs [147].

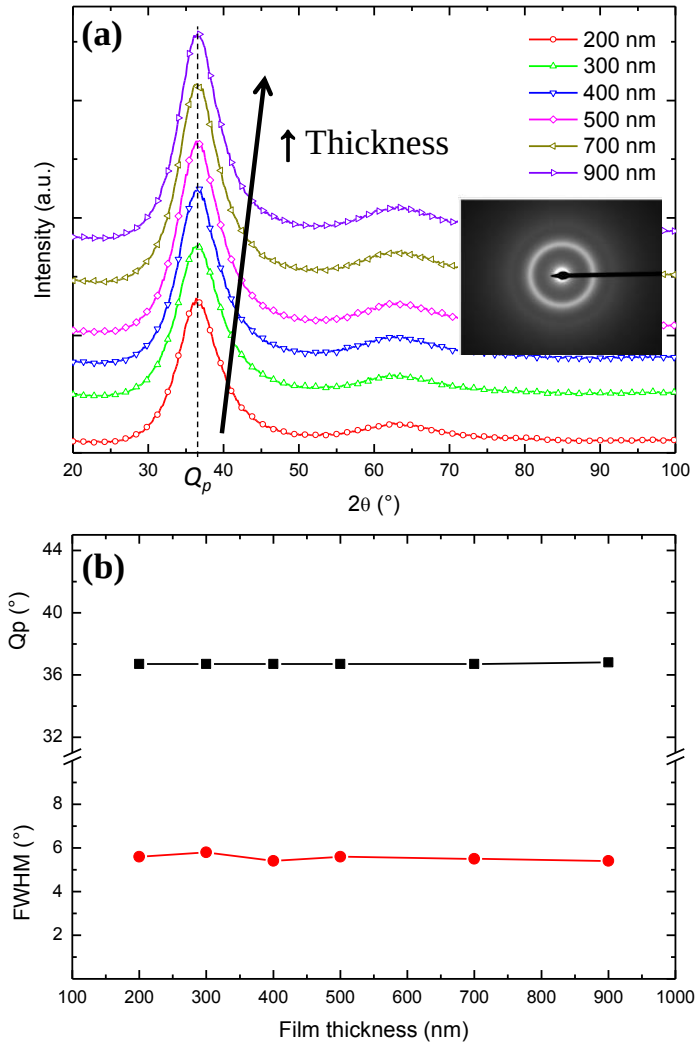

Figure 3.1 *– X-Ray diffractograms for $Zr_{65}Ni_{35}$ TFMGs with different thicknesses. (a) A first sharp diffraction peak (FSDP) and a second broader halos are observed, diffractograms are vertical shifted for sake of clarity. In the inset, TEM microdiffraction pattern for the 900 nm-thick film showing two diffuse halos, further proving the amorphous structure. (b) FSDP position (Q_p) and FWHM extracted from diffractograms in (a). Both quantities are thickness independent and respectively around 36.7° and 5.5°.*

b) Effect of composition

Cross-section TEM images reported in Figure 3.2 show the microstructural evolution in ZrNi TFMGs when changing the percentage of Zr. Specifically, small nanocrystals (~ 3 nm) can be observed for $Zr_{75}Ni_{25}$ (Figure 3.2b, red arrow), while intense crystallization occurs for $Zr_{85}Ni_{15}$ in which 60-70 nm-long crystallites are embedded in an amorphous matrix (Figure 3.2c, red arrow) [134]. These observations agree also with the microdiffraction pattern reported in the inset, which shows a speckle (white arrow) for $Zr_{75}Ni_{25}$ and the presence crystalline spots for $Zr_{85}Ni_{15}$. On the other hand, the structure of $Zr_{42}Ni_{58}$ (and $Zr_{65}Ni_{35}$, Figure 3.1) are fully amorphous as proven by the absence of spots in the microdiffraction pattern (Figure 3.2a). Crystallization phenomena are expected for Zr-rich compositions which are close to the edge of amorphisation range (section 2.1) and it can be justified in terms of a reduced mixing enthalpy [121].

The XRD diffractograms of Zr_xNi_{100-x} TFMGs in Figure 3.3a are provided for the compositions lying within the amorphisation range, namely $Zr_{42}Ni_{58}$, $Zr_{65}Ni_{35}$, and $Zr_{75}Ni_{25}$. Similarly to what is reported in Figure 3.1, an asymmetric FSDP centered between 35° and 40° is observed followed by a second broader halo around 60°, indicating the presence of a fully amorphous structure. Note also that no crystalline peaks are detected for the $Zr_{75}Ni_{25}$ due to the lower spatial resolution of XRD with respect to TEM, which shows the presence of a speckle in the electron microdiffraction (Figure 3.2b). It has not been possible to determine the exact composition of the small nanocrystals in $Zr_{75}Ni_{25}$ due to their small size (∼3 nm). Probably, they are constituted of a Zr-rich phase (α–Zr or Zr_2Ni) as expected from the Zr–Ni equilibrium phase diagram [122].

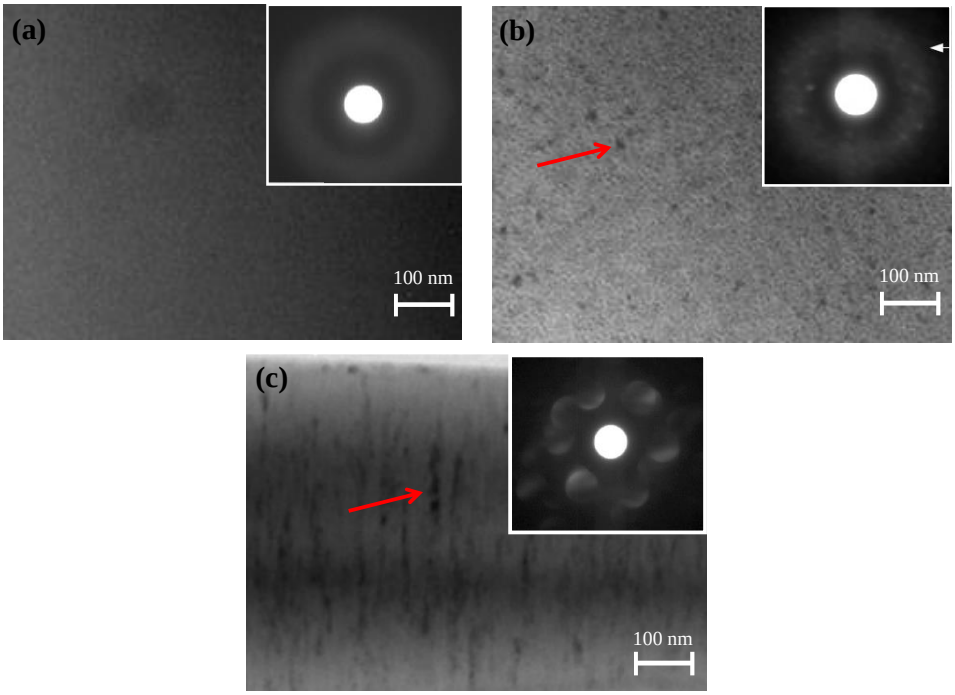

Figure 3.2 *– Cross-section TEM images of Zr_xNi_{100-x} TFMGs with a thickness equal to 800 nm. In the inset, the microdiffraction pattern. From (a) to (c) the composition $Zr_{42}Ni_{58}$, $Zr_{75}Ni_{25}$, and $Zr_{85}Ni_{15}$, respectively. The red arrows indicate dispersed nanocrystals of around 3 nm and 60 nm-long, respectively for $Zr_{75}Ni_{25}$ and $Zr_{85}Ni_{15}$ [136].*

The FWHM (Figure 3.3b) varies from 4.3° to 6.5° (0.30 $Å^{-1}$ and 0.41 $Å^{-1}$) increasing with the Ni content in the film. These values are slightly below the literature results for amorphous bulk alloys (0.5 $Å^{-1}$) [147]. According to Chou *et al.* [73], an increment of the FWHM with Ni content is an indication of an increase of structural disorder (i.e. the so-called "confusion principle", section 1.3). Nevertheless, a strong atomic correlation clearly exists since the obtained values are lower than the literature data in the case of multi-components BMGs.

Furthermore, the position of the FSDP (Q_p) is shifted toward lower scattering angles (θ) when increasing the amount of Zr and, specifically, from 36° up to 40° for $Zr_{75}Ni_{25}$ and $Zr_{42}Ni_{58}$, respectively (Figure 3.3a-b). These results are in a good agreement with the Q_p variation reported by Buschow *et al.* [30] for ZrNi amorphous ribbons, for which the Q_p linearly decreases for Zr-rich specimens (see Fig. 3.3).

These trends can be easily related to the favored formation of strong hetero Zr–Ni bonds when the content of Ni increases leading to an increment of the cohesive energy and a reduction of the average atomic distances (Figure 3.3b). Note also that Ni atomic radius is smaller than the Zr one, respectively of 135 and 155 pm.

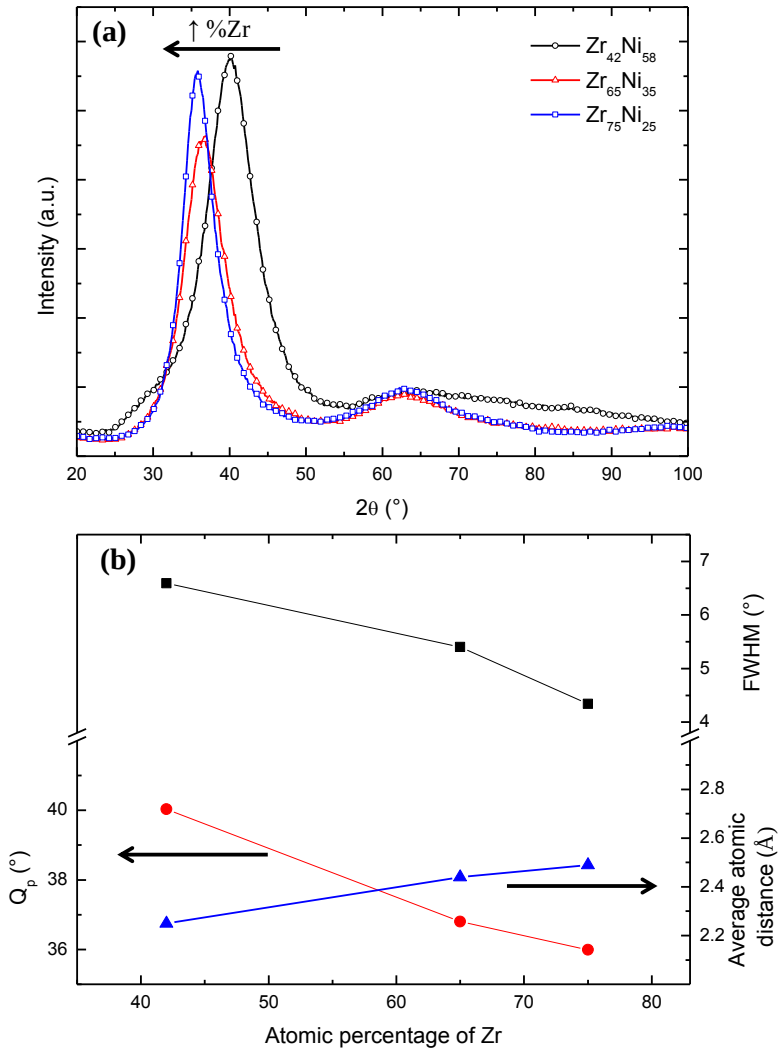

Figure 3.3 *– (a) X-ray diffractograms for amorphous Zr_xNi_{100-x} TFMGs. (b) Position and FWHM of the first sharp diffraction peak (FSDP, Qp) as function of the Zr content. The average atomic spacing decreases when increasing Zr content, indicating the formation of hetero Zr-Ni bonds [136].*

The X-ray diffractogram of $Zr_{85}Ni_{15}$ TFMGs is reported in Figure 3.4a-b. Figure 3.4a shows the results obtained in a standard Bragg–Brentano configuration. An offset equal to 2° between the X-ray source and the detector has been imposed to limit the Si (100) substrate signal. This configuration makes possible the detection of the crystalline phase without the formation of shifted Bragg peaks arising from a grazing angle geometry (crystalline peaks in Figure 3.4b). Nevertheless, a Si signal is still detected at around 69°, and it is not possible to detect any amorphous phase whose scattering intensity is significantly lower than the crystalline one which covers its signal. The crystalline peak at 34.5° in Figure 3.4a corresponds to the family plane (0001) of the crystalline hexagonal α-Zr phase. The absence of other diffraction peaks in Figure 3.4a indicates that the vertical *c* axis of the hexagonal lattice is oriented normal to the Si surface (inset of Figure 3.4a). A further proof of this crystalline structure is the presence of the (0002) fringe around 72°. If a grazing angle configuration is adopted to analyze this composition (Figure 3.4b) amorphous (A) and crystalline peaks (C) are observed. Therefore, a composite structure in which a crystalline phase is embedded within an amorphous matrix is found. This analysis is consistent with TEM observations (Figure 3.2c) showing long nanocrystals oriented normally to the Si surface within an amorphous matrix.

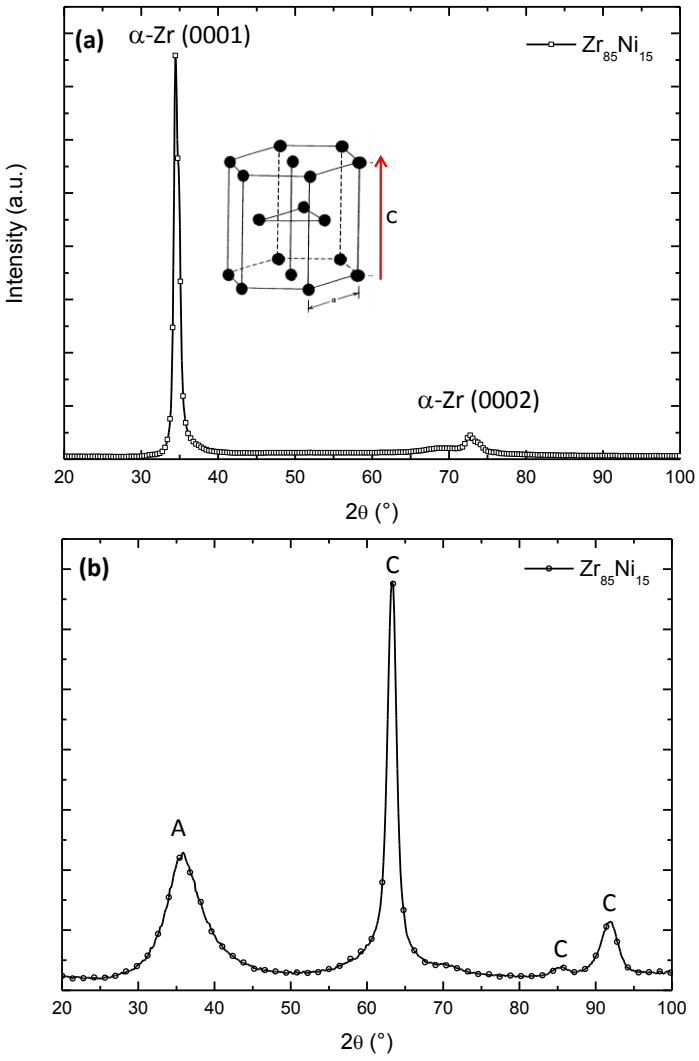

Figure 3.4 *– (a) X-ray diffractograms of $Zr_{85}Ni_{15}$ TFMG in a standard Bragg-Brentano configuration showing the presence of crystalline α–Zr (0001) planes at 34.5°. (b) Grazing incidence XRD for $Zr_{85}Ni_{15}$ TFMG showing amorphous (A) and crystalline (C) peaks. Note that the crystalline peaks are shifted with respect to the position in (a).*

3.2 Mass density evolution

The analysis of mass density is fundamental for the extraction of the elastic constants by means of surface Brillouin spectroscopy (SBS) and picoseconds ultrasonics (PU). The mass density has been measured by X-ray reflectivity (XRR), which also provide information about the surface roughness and thickness (section 2.4). An example of a XRR spectrum has been reported in Figure 2.13, showing the very good quality of the fit (red solid line) which enables the extraction of an accurate value of the mass density and surface roughness.

Figure 3.5 shows the variation of the mass density (ρ) and of the atomic volume as a function of Zr concentration for the fully amorphous compositions[1]. The atomic volume for amorphous alloys is defined as $V_a = \bar{A} / \rho N_a$, where $\bar{A}$ is the weighted atomic mass and N_a is Avogadro's number (section 1.4, and Refs. [40, 147]). The mass density decreases when increasing the amount of Zr, while the opposite trend is reported for the atomic volume. Specifically, the density changes from 7.25 g/cm^3 of $Zr_{75}Ni_{25}$ up to 7.65 g/cm^3 for $Zr_{42}Ni_{58}$. These trends indicate a favored formation of strong Zr-Ni bonds for Ni-rich specimens in agreement with the evolution of Q_p reported in Figure 3.3. The mass density and the atomic volume follow a mixing rule (dashed lines in Figure 3.5) obtained from crystalline Zr and Ni. The Ni density is higher than Zr, respectively equal to 8.91 and 6.50 g/cm^3 leading to a reduced atomic volume respectively of 10.93 Å^3 and of 23.28 Å^3 as reported in Ref. [40]. Note that it is possible to estimate the mass density of a binary amorphous alloy starting from the pure crystalline components since only a very low mass density reduction (0.5-2%) is expected for the amorphous alloy with respect to the crystalline one (section 1.5.4). All the specimens have an atomic volume comparable with ZrNi ribbons with similar composition [40, 147].

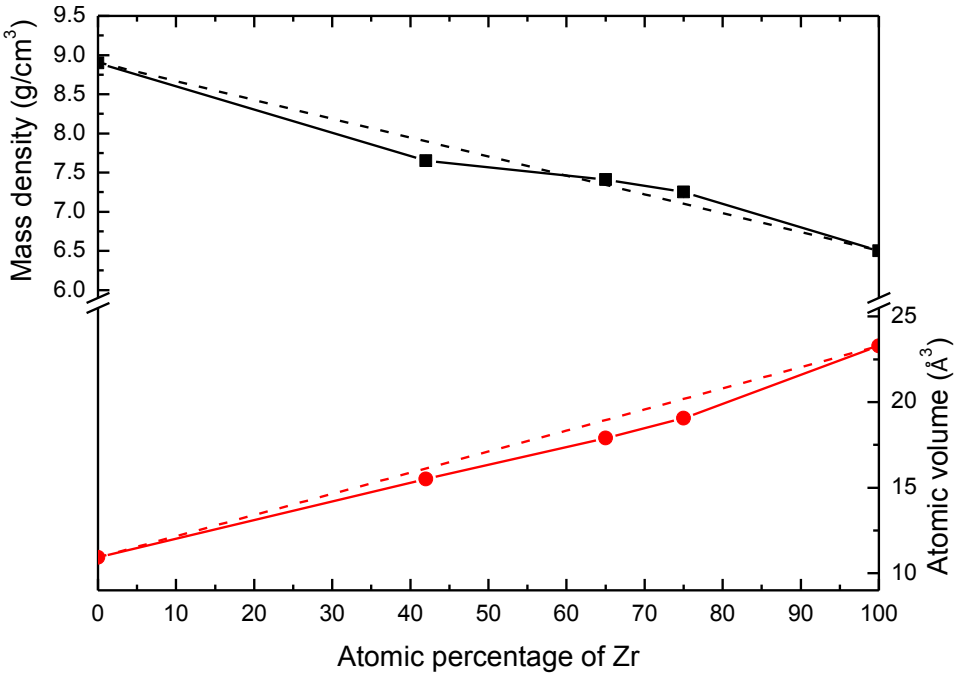

Figure 3.5 *– Mass density measured by X-ray reflectivity (XRR) and atomic volume as a function of the Zr concentration. The values follow a mixing rule obtained from crystalline Zr and Ni (dashed lines). An error bar of ± 0.04 g/cm^3 is added, but it cannot be distinguished from the data set [136].*

[1]The composition $Zr_{75}Ni_{25}$ is considered amorphous due to the low percentage and size of crystallites which are not detectable with the X-ray diffraction.

No change of the mass density has been detected for different $Zr_{65}Ni_{35}$ thickness (100, 200, and 300 nm), with a constant value of 7.4 g/cm^3, again indicating that film has the same atomic structure (section 3.1). Note also that the thickness value measured by XRR is in agreement with the values obtained by FE-SEM in cross-sectional view and by mechanical profilometer (section 2.3).

Lastly, the partially crystallized $Zr_{85}Ni_{15}$ composition has a mass density of 7 g/cm^3 due to the high percentage of Zr which have a density of 6.51 g/cm^3.

3.3 Elastic constants analysis

In this section, we analyze the effect of thickness and composition on the elastic constants obtained by surface Brillouin spectroscopy (SBS) and picosecond ultrasonics (PU). Details about the experimental techniques are reported in section 2.5. The analysis of the elastic constants allows to shed additional light on the atomic structure and its evolution as well as to calculate the fragility index (section 1.5.4) enabling to predict macroscopic properties such as plasticity.

a) Effect of thickness

Figure 3.6a shows the evolution of the elastic constants for different thicknesses for the composition $Zr_{65}Ni_{35}$. Both C_{11} and C_{44} are thickness independent and, respectively, around 150 and 26 GPa [136]. There are no differences between the C_{11} calculated by SBS and PU, indicating the high accuracy of the techniques and further proving the quality of the results.

The elastic modulus (E) and Poisson ratio ν are calculated by using equation (2.5) after combining the elastic constants C_{11} and C_{44} (Figure 3.6b). The values of E and ν are respectively around 72 GPa and 0.39 (Figure 3.6b), slightly above the literature values reported for ribbons in Refs. [76, 120]. The thickness independence of the values of E and ν further confirms that the films have a similar atomic structure (see the trend of Q_p in Figure 3.1).

Furthermore, the values of the shear (μ) and bulk (B) modulus as well as the fragility index (m_f) can be deduced from the elastic constants. Specifically, they can be derived using the following expression:

$$\mu = C_{44} \tag{3.1}$$

$$B = C_{11} - (4C_{44})/3 \tag{3.2}$$

$$m_f = 12(B/\mu + 0.67). \tag{3.3}$$

Since C_{11} and C_{44} are thickness independent, the corresponding values of μ, B, m_f are equal to 26 GPa, 113 GPa and 60, respectively. The ratio μ/B which is related to the fracture toughness (section 1.5.4 and Ref. [59]) is constant and equal to 0.23. Hence, a high fracture energy higher than 70 kJ/m^2 is expected. Similar results can also be deduced from the Poisson ratio equal to 0.39. The high fragility index indicates a low thermodynamic stability of this composition which is constituted only of two components (sections 1.1 and 1.2). Following the classification of Plummer *et al.* [63], when m_f is greater than 51 a metallic glass can be defined as "fragile". Hence, extended plasticity can be expected

due to the activation of a number of dispersed shear transformation zones (STZs) that favors the activation of multiple shear bands (see sections 1.5.4 and 1.5.8).

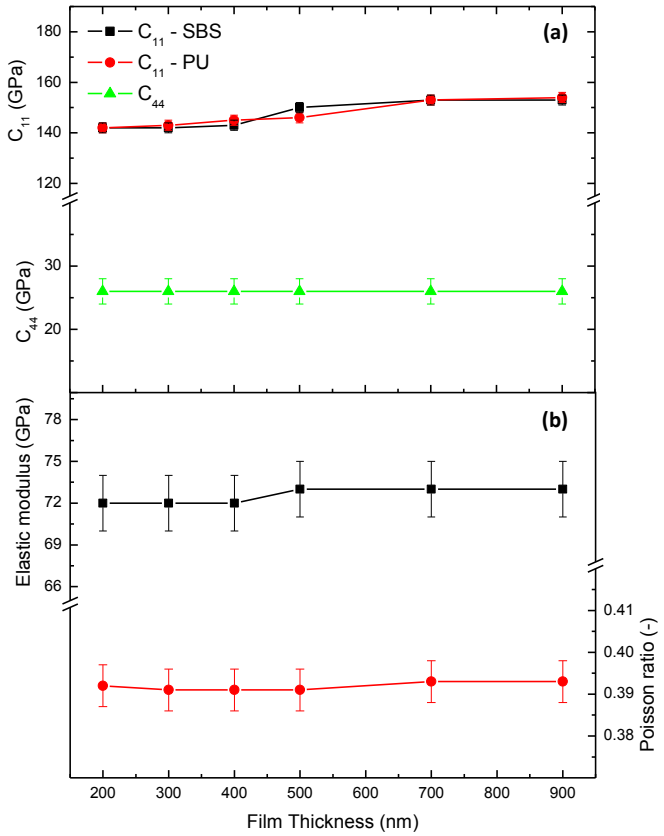

Figure 3.6 *– (a) Evolution of the elastic constants obtained by surface Brillouin spectroscopy (SBS) and picosecond ultrasonics (PU). (b) The corresponding trend of the elastic modulus and the Poisson ratio.*

b) Effect of composition

Figure 3.7a displays the effect of composition on the elastic constants for the ZrNi alloys exhibiting a fully amorphous structure. Both C_{11} and C_{44} decrease when increasing the Zr concentration, respectively from 138 up to 188 GPa and from 23 up to 32 GPa for $Zr_{75}Ni_{25}$ and $Zr_{42}Ni_{58}$. No differences are detected within the values of C_{11} obtained by SBS and PU, confirming the high accuracy of the results.

The corresponding values of elastic modulus (E) and Poisson ratio (ν) are shown in Figure 3.7b. There is a marked effect on E which increases from 65 GPa up to 91 GPa when decreasing the Zr content, while ν slightly increases, reaching the value of 0.4 for $Zr_{42}Ni_{58}$. The values of E and ν are slightly above the literature values reported for ribbons in Refs. [76, 120]. The changes in E and ν carry useful information about the evolution of local order, with the enhanced formation of Zr-Ni bonds and cohesive energy for Ni-rich specimens [136]. This trend is consistent with the reported evolution of Q_p and atomic volume reported in Figures 3.3b and 3.5.

The evolution of the shear (μ) and bulk (B) modulus are reported in Figure 3.8 showing, respectively, an increment from 24 to 32 GPa and from 104 up to 146 GPa for Ni-rich specimen. This

trend leads to an increment of the fragility index (m_f) from 58.5 up to 63.5, respectively for $Zr_{75}Ni_{25}$ and $Zr_{42}Ni_{58}$.

While the trends for μ and B justify the formation of ZrNi bonds favored for Ni-rich specimens, the higher thermodynamic fragility of $Zr_{42}Ni_{58}$ can be related to the size of free volume defects, namely the STZs (see also sections 4.1.1c and 4.1.2). In fact, the composition $Zr_{42}Ni_{58}$ maximizes the entropic content (see Ref. [121]), leading to a more disordered glass. Note, for instance, that the FWHM (Figure 3.3b) reaches the highest values for this composition, indicating a higher degree of disorder within the first neighbor shell from a selected atom (see Figure 1.4 which reports the trend of the microscopic density).

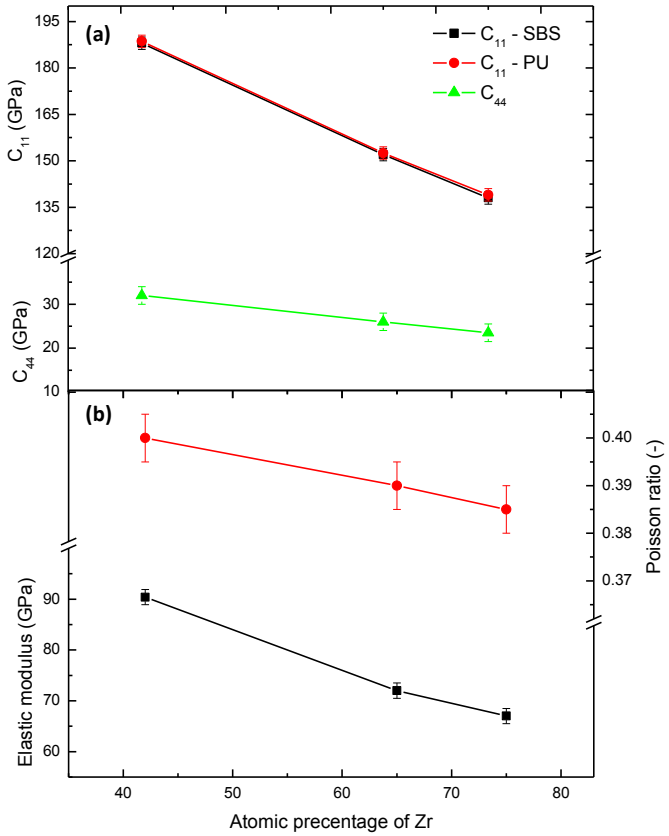

Figure 3.7 *– (a) Evolution of the elastic constants as a function of composition. (b) The corresponding values of elastic modulus and Poisson ratio.*

Ni-rich specimens are thus expected to exhibit an enhanced plasticity due to the presence of large STZs favoring the formation of multiple shear banding events (section 1.5.4). However, a ductile-like behavior is expected for all the compositions due to the large thermodynamic fragility (m_f is larger than 51). Figure 3.9 shows the expected plastic strain in compression for different families of glasses [63]. Strong glasses (a-SiO_2) are characterized by directional bonds (high ratio μ/B) do not show any plasticity, while fragile systems such as metallic glasses (with non-directional atomic bonds and thus a low ratio μ/B) can exhibit a large plastic deformation up to 20% in compression at T_{room} [63] (section 1.5.3). Zr-based BMGs have a ratio μ/B in between 0.3 and 0.35 [59], with a limited plastic behavior. On the contrary, ZrNi TFMGs have a ratio μ/B is in between 0.21 and 0.24 thus it can be expected a larger plasticity up to 10%. For the same reasons, a very large fracture toughness should be expected in the bulk form (section 1.5.3).

Lastly, the composition $Zr_{85}Ni_{15}$ which shows an intense crystallization (Figures 3.2 and 3.4) involves an elastic modulus of 73 GPa, a Poisson ratio of 0.38 and a fragility index around 52. While the first two values cannot be compared with the results presented for the other compositions due to the effect of large α–Zr nanocrystals dispersed in an amorphous matrix, the lower value of fragility index suggests a reduction of the mixing entropy contribution with the formation of Zr-Zr bonds, which in turns leads to crystallization phenomena (sections 3.1 and 3.5).

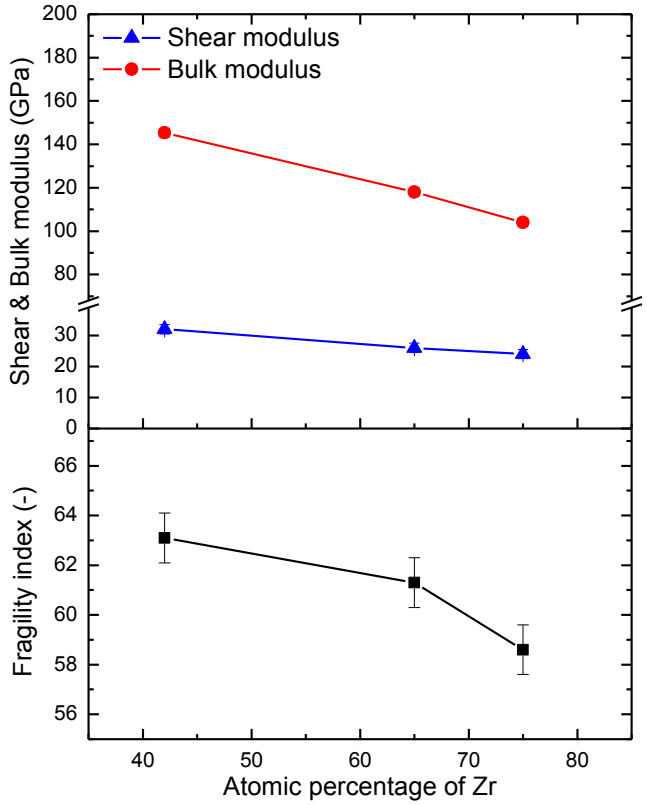

Figure 3.8 *– (a) Evolution of the shear and bulk modulus as a function of composition; (b) the corresponding values of fragility index.*

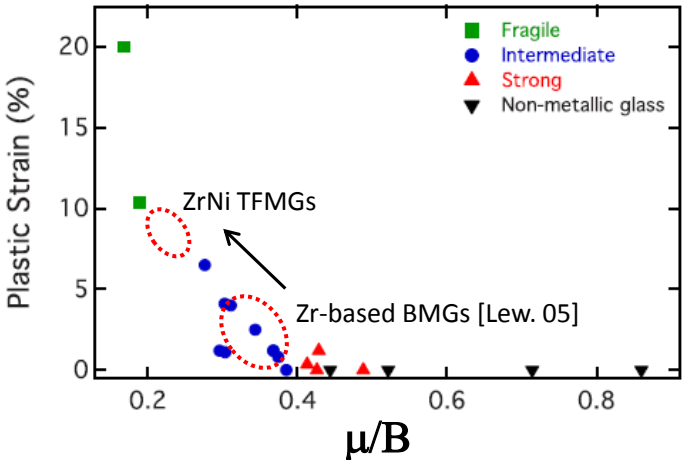

Figure 3.9 *– Variation of the plastic strain in compression for different families of glasses as a function of μ/B (adapted from [63]). ZrNi TFMGs show a lower μ/B with respect to Zr-based BMGs reported in Lewandowski et al. [59].*

3.4 Electrical resistivity analysis

The analysis of electrical resistivity of BMGs glasses received a lot of attention since the first works published in the late 70's (section 1.4). However, only few studies deal with thin films. Here, we present an overview of the electrical resistivity as a function of thickness and composition, in order to achieve a thorough understanding of the atomic structure of ZrNi TFMGs. Moreover, the analysis of electrical resistivity as a function of the temperature enables to extract fundamental quantities such as the glass transition temperature (T_g) and the crystallization temperature (T_x), which are very difficult to obtain using the differential scanning calorimetry (DSC) due to the very low quantity of material present in thin films. Details about the experimental setup we used for the measurement of electrical resistivity of TFMGs are provided in section 2.9.

Figure 3.10a shows the evolution of the electrical resistivity (ρ_e) measured at room temperature for different $Zr_{65}Ni_{35}$ thicknesses. The electrical resistivity is constant with a value equal to 186 ± μΩ cm, in agreement with literature results for ZrNi films and ribbons [30, 31, 38, 39]. The thickness independent values of the electrical resistivity can be related to the liquid-like atomic structure of metallic glasses, without crystalline defects (such as grain boundaries or phase segregations) which maintain the same ill-defined structure even at very small scales. This fact implies that there are no changes in the electron mean free path, indicating that the materials opposes the same resistance to the electron flow or, in other words, that it has the same atomic structure (section 3.3).

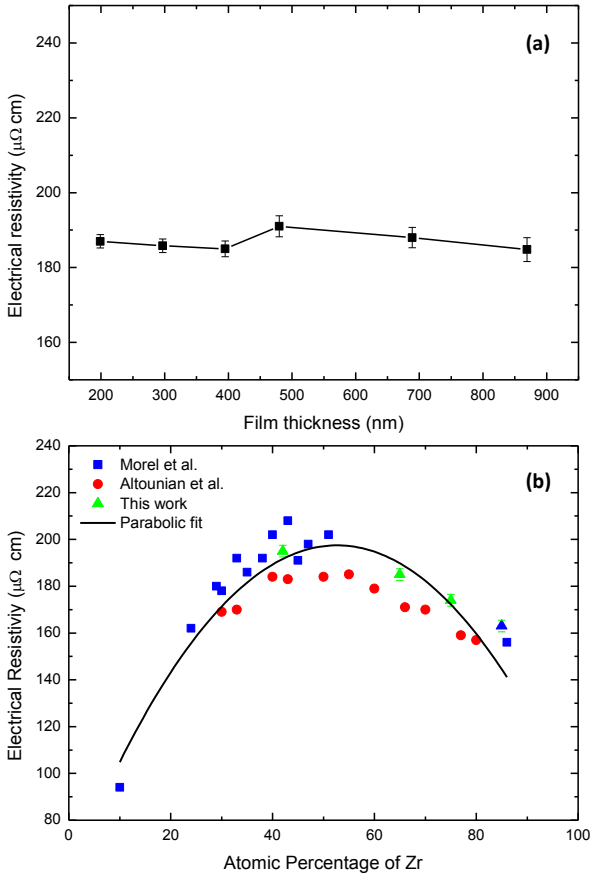

Figure 3.10 *– (a) Electrical resistivity as a function of film thickness for $Zr_{65}Ni_{35}$ TFMGs.(b) Electrical resistivity as a function of film composition (green triangles). Red circles and blue squares represent the literature works of Morel et al.[38] and Altounian et al. [39], respectively for ZrNi films and ribbons.*

Figure 3.10b shows the variation of electrical resistivity as a function of Zr percentage for films within the amorphisation range (green triangles). The results are in good agreement with the literature data for ZrNi ribbons and thin films [38, 39], which report a parabolic trend of electrical resistivity with a maximum around the composition $Zr_{50}Ni_{50}$. For instance, the ρ_e of $Zr_{42}Ni_{58}$ and $Zr_{75}Ni_{25}$ is respectively equal to 194 and 174 μΩ cm. The resistivity of thin films is slightly higher than of thick ribbon probably due to surface scattering effects, see Ref. [38]. Note also that the electrical resistivity of pure Ni (6.93 μΩ cm) is lower than the pure α-Zr (42.1 μΩ cm), while the overall ρ_e for an amorphous system increases for Ni-rich compositions close to $Zr_{50}Ni_{50}$ [39].

The origin of the parabolic trend in Figure 3.10b can be explained on the basis of the structural disorder (alloy entropic content) which is enhanced for compositions close to $Zr_{50}Ni_{50}$, leading to a more disordered atomic structure which enhanced electrical resistivity [121]. In this regard, it is reasonable to expect an higher ρ_e for the composition $Zr_{42}Ni_{58}$ which also has the largest FWHM (Figure 3.3b). The result of a parabolic fit reported in Figure 3.10b shows that the maximum of resistivity (198 μΩ cm) is reached for the composition $Zr_{53}Ni_{47}$.

Lastly, the electrical resistivity of $Zr_{85}Ni_{15}$ is equal to 163 ± 3 μΩ cm due to the presence of an α−Zr crystalline phase which is supposed to have an higher electrical conductivity (42.1 μΩ cm).

The electrical resistivity has also been studied as a function of the temperature for the composition $Zr_{65}Ni_{35}$. The measurement setup has been described in section 2.8. Here, we point out that in order to achieve accurate results, $Zr_{65}Ni_{35}$ TFMGs have been deposited on a Si substrate coated with and SiO_2 layer. As a matter of fact, when the temperature increases there is a increment of conductivity of Si substrate (which is a semiconductor) significantly altering the signal of the TFMGs. Hence, a highly insulating SiO_2 layer prevents this effect, by confining all the electron flow within the ZrNi TFMGs. Moreover, the investigated thickness is equal to 800 nm further limiting substrate effects. The electrical resistivity has been probed for the as-deposited specimen as well as for the annealed one obtained after completing the heating process. Moreover, in order to capture all thermodynamic transitions, the TFMGs have been heated up to 900 K (∼627 °C) with a constant heating rate of 10 K/min (section 2.9).

Figure 3.11 shows the variation of ρ_e/ρ_{e0} (namely the ratio between the measured electrical resistivity and the electrical resistivity at T_{room}) as a function of temperature. Following the heating curve on the as-prepared specimen (black squares), it can be noted that:

- at low temperatures, the electrical resistivity (ρ_e/ρ_{e0}) decreases linearly when increasing the temperature. A negative temperature coefficient of resistivity (TCR, α) can be calculated as $\alpha = d\ln(\rho_e)/dT$ and is found equal to -1.2 10^{-4} K^{-1} [39]. This result is in line with the values for ZrNi ribbons with the same composition [39] (Figure 1.11). More recently, a value of -1.4·10^{-4} K^{-1} has been obtained for $Zr_{65}Cu_{35}$ ribbons [32]. Note that the negative TCR is a peculiar characteristic of amorphous alloys, which is not expected for crystalline materials (section 1.4). The absolute value of ρ_{e0} (namely at T_{room}) is equal to 190μΩ cm in agreement with the results reported in Figure 3.10a,
- at T = 694 K (∼421 °C), the ratio ρ_e/ρ_{e0} has an abrupt increment which indicate the glass transition temperature (T_g, section 1.4). The glass enters in the supercooled region (section 1.1), characterized by an increment of electrical resistivity due to the enhanced electron scattering phenomena within this viscous phase [1, 31, 33]. The system reaches

the crystallization temperature (T_x) which is located at 745 K (∼472 °C). The value of the crystallization temperature is higher than the values reported for ribbons which usually exhibit a T_x around 700 K (section 2.1). This means that ZrNi TFMGs are highly (meta)stable due to a more packed structure and to the formation of ZrNi bonds. Note for instance that the Poisson ratio which is a rough measure of the packing efficiency – since it is defined as the ratio of transverse contraction strain to longitudinal strain during the elastic loading – is higher in ZrNi TFMGs compared to ribbons, respectively 0.39 and 0.375 (section 3.3). However, the obtained values of T_g and T_x indicate that the TFMG will be stable even several months after the deposition , while ensuring a fully amorphous structure even after the release phase to obtain freestanding TFMGs which involve an immersion in a TMAH bath at a temperature of 85 °C (see section 2.8),

- once crystallization sets in, the ratio ρ_e/ρ_{e0} drops rapidly since the crystalline phase involves a reduced electrical resistivity (see section 1.4).

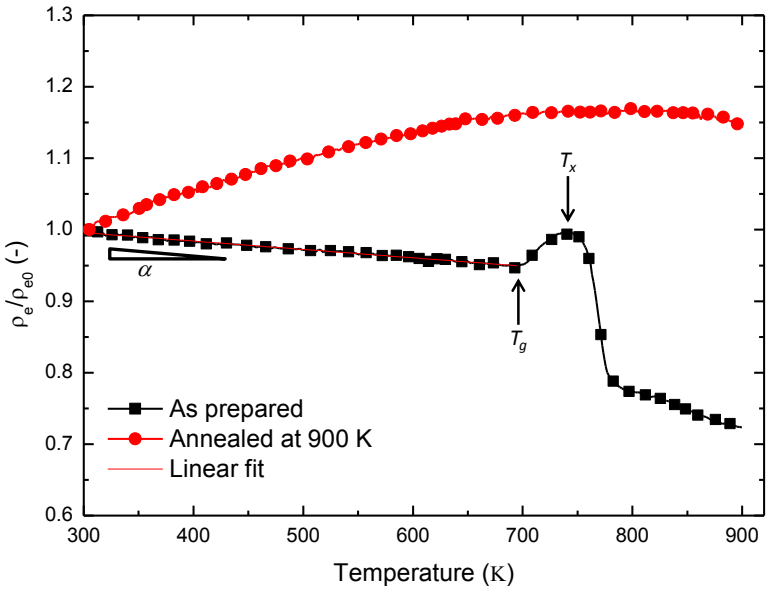

Figure 3.11 *– Electrical resistivity (ρ_e/ρ_{e0}) as a function of the temperature. Black squares indicate the as prepared specimen showing a negative TCR (α) and the T_x peak, while red circles indicate the electrical resistivity of the crystalline phase (positive TCR) obtained after the previous annealing treatment.*

The evolution of ρ_e/ρ_{e0} has been measured after crystallization (red circles) in Figure 3.11. The annealed film has a positive TCR which is characteristic of crystalline alloys (section 1.4). The electrical resistivity at room temperature is equal to 53 μΩ cm, a value significantly lower than the measured one for $Zr_{65}Ni_{35}$ TFMG (∼186 μΩ cm) indicating the reduced electron scattering phenomena in the crystalline phase (section 1.4).

Lastly, it is worth noting that the value of T_g and T_x are fundamental to estimate the ideal yield strength (atomic bonding rupture), especially in the case of thin films. As a matter of fact, the upper bound yield strength can be derived by using the Johnson and Samwer model [101], recently modified by Cheng and Ma [100] (section 1.6, equation 1.10). More details will be presented in Chapter IV.

3.5 Overall analysis of compositional changes

A convenient way to wrap up all the compositional effects is the Nagel and Tauc criterion [29] presented in sections 1.3 and 1.4.

The Nagel and Tauc criterion [29] states that when Q_p – the scattering vector of the FSPD – is equal to $2k_f$ (twice the Fermi wavevector), an energy gap opens between the valence and conduction bands. This mechanism is associated with a stabilization of the glassy structure. While Q_p can be easily extracted from XRD data (after conversion in scattering vector coordinates), k_f can be calculated as

$$k_f = \left(\frac{3\pi^2 \bar{Z}}{V_a} \right)^{1/3} \tag{3.4}$$

where $\bar{Z}$ is the average valence and V_a is the atomic volume calculated from the film density (section 3.2). Buschow *et al.* [30] adopted an average atomic valence of 0.6 and 2 for Ni and Zr, respectively.

The criterion is applied in Figure 3.12. At first, it is interesting to note that the Q_p values of ZrNi TFMGs are similar with ribbons reported by Buschow *et al*. [30]. Decreasing the percentage of Zr in the film Q_p increases (see Figure 3.3b), clearly indicating a reduction of the average atomic distances (the atomic radius of Ni and Zr are respectively equal to 135 and 155 pm). The Q_p values of pure Ni and Zr are deduced by XRD analysis of the corresponding liquids [148]. The intersection between Q_p and $2k_f$ is found for the composition $Zr_{52}Ni_{48}$ [134], in agreement with the maximum negative mixing enthalpy ZrNi binary systems [121]. For compositions close to $Zr_{52}Ni_{48}$ there is the maximum formation of Zr-Ni hetero bonds which enhance the (meta)stability, favoring confusion in the system. In fact, we show that $Zr_{42}Ni_{58}$ and $Zr_{65}Ni_{35}$ are fully amorphous (sections 3.1, 3.2 and 3.3). Even if both compositions involve Zr-Ni bonds formation, hetero bonds are favored for the composition $Zr_{42}Ni_{58}$, as demonstrated the analysis of the average atomic distances, the density and the elastic constants. On the other hand, $Zr_{75}Ni_{25}$ and $Zr_{85}Ni_{15}$ have $Q_p \ll 2k_f$ justifying the occurrence of crystallization phenomena (section 3.1) due to the reduced system confusion characterized by the formation of Zr-Zr bonds. The formation of Zr-Zr bonds explains the reduced values of elastic constants and density for $Zr_{75}Ni_{25}$ as well. Lastly, all the amorphous compositions have a large fragility index indicating a high tendency in shear banding process. $Zr_{42}Ni_{58}$ has the largest fragility index due to the more disordered structure as also proved by the trend of the FWHM, in agreement with the largest system confusion.

It is worth noting that the Nagel and Tauc criterion for the analysis of stability of an amorphous alloy is still qualitative especially in the case of transition metal alloys such as ZrNi and ZrCu [32]. In this regard, we can observe the formation of fully amorphous alloys even for compositions close to $Zr_{10}Ni_{90}$ (Figure 2.2[123]), for which it is expected $Q_p \gg 2k_f$.

Nevertheless, the Nagel and Tauc criterion can be quantitatively used to accurately predict the composition with the highest electrical resistivity and negative temperature coefficient of resistivity (TCR), which again correspond to the condition $Q_p = 2k_f$ (section 1.4). The parabolic fit of the electrical resistivity (Figure 3.10) indicates the maximum electrical resistivity for a composition $Zr_{53}Ni_{47}$, very close to $Zr_{52}Ni_{48}$ obtained using the Nagel and Tauc criterion. For this composition, it is expected also the highest negative TCR as reported in Ref. [39] and Figure 1.11 with a value around $-1.5\ 10^{-4}\ K^{-1}$. For compositions richer in Zr or Ni, the TCR increases following a parabolic profile, reaching positive values outside the amorphisation domain. This trend can be also inferred for composition $Zr_{65}Ni_{35}$ (Figure 3.11) which has a negative TCR equal to $-1.2\ 10^{-4}\ K^{-1}$.

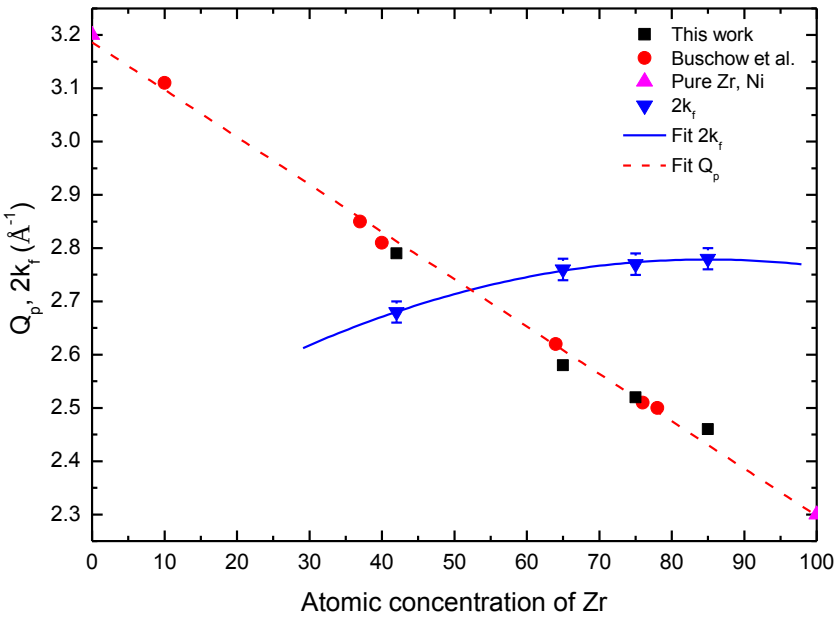

Figure 3.12 *– Variation of the position of the first sharp diffraction peak (FSDP, Q_p) and of the Fermi wavevector ($2k_f$) as function of film composition [134]. Black squares and red circles indicate, respectively, the position of the FSDP measured for TFMGs and the values obtained by Buschow et al.[30] for amorphous ZrNi ribbons. A maximum of (meta)stability is found around 52% of Zr ($Q_p = 2k_f$).*

3.6 Conclusion

In this chapter, we analyzed the structure of ZrNi TFMGs for different thicknesses and compositions.

For the composition $Zr_{65}Ni_{35}$ – which has been used to investigate mechanical size effects – no thickness effects has been observed on the atomic structure. Specifically, $Zr_{65}Ni_{35}$ is fully amorphous with no change of the position of the first sharp diffraction peak (FSDP) and the corresponding full width at half maximum (FWHM). This result is supported by the thickness independent values of the mass density, the elastic constants, the fragility index, and the electrical resistivity. Hence, the possible origin of mechanical size effect should not be related to a change of the atomic structure. Furthermore, the high fragility index and the low ratio μ/B (shear over bulk modulus) indicate a large plasticity due to the large size of dispersed shear transformation zones (STZs) that promote the formation of multiple shear bands, thus increasing the overall plasticity.

On the other hand, for a fixed thickness – equal to 800 nm – a compositional change involves crystallization phenomena for Zr-rich specimens as well as a significant variation of the position of the FSDP and the corresponding FWHM. Moreover, the mass density, the elastic constants, the fragility index, and the electrical resistivity evolve as well. These variations are explained in terms of the formation of strong Zr-Ni bonds and of a more disordered structure (enhanced entropic confusion) for Ni-rich specimens. The Nagel and Tauc criterion has been used to qualitatively analyze these trends providing information about the thermal stability and the crystallization phenomena for Zr-rich specimens, while enabling quantitatively to predict the composition with the highest electrical resistivity and negative TCR.

Chapter IV – Viscoplastic properties of ZrNi thin film metallic glasses

In this chapter, the viscoplastic properties of ZrNi thin film metallic glasses (TFMGs) are addressed through an analysis of the mechanical behavior by means of nanoindentation and of tension tests on freestanding films using the lab-on-chip technique (section 2.8). Key elements to understand the main results of this chapter have been presented in section 1.5.5 for the nanoindentation, and in sections 1.5.8 and 1.6 for the analysis of size effects. Furthermore, the in-depth understanding of these results is intimately related to the structural analysis presented in Chapter III.

Here, we first focus on the results of nanoindentation by exploring both the effect of thickness (for the composition $Zr_{65}Ni_{35}$) and of composition (at fixed thickness of 800 nm). This study will consider the viscoplastic effects involving the extraction of the activation volume. Second, we look at the mechanical properties of freestanding $Zr_{65}Ni_{35}$ TFMGs by investigating the effect of thickness on the stress strain curve and on the related quantities such as the yield stress and elastic modulus, while leaving to Chapter V the analysis of the fracture behavior in tension. Moreover, viscoplastic effects will be investigated as well by studying the stress relaxation phenomena providing a second estimate of the activation volume as well.

The objectives of this chapter are thus to present an overview of the mechanical size effects by exploring the origins and by modeling the changes in mechanical properties when reducing the thickness. The investigation of the composition effect (explored only by nanoindentation) will be fundamental to strengthen the results presented in Chapter III and to get further insight in the atomic structure of ZrNi TFMGs.

4.1 Nanoindentation behavior of ZrNi TFMGs

The description of nanoindentation experimental setup has been provided in section 2.6. Two methods have been used to extract the mechanical properties.

The first one is the continuous stiffness measurement (CSM) in which the nanoindenter system applies a load to the indenter tip to force the tip into the surface, while simultaneously superimposing an oscillating force with an amplitude generally several orders of magnitude smaller than the nominal load. This configuration provides a very accurate measure of the contact stiffness (and hence of the hardness) as a function of the indentation depth or, alternatively, of the normalized indentation depth defined as the ratio between the indentation depth and film thickness. Note that in a CSM test, the loading rate $(\dot{P}/P)$ is kept constant as a function of the indentation depth, leading to a constant value of the indentation strain rate $\dot{\varepsilon}$. An analysis of the effect of the different loading rates (viscoplastic

behavior) will be presented, allowing the calculation of the activation volume. More details about this technique can be found in Ref. [65].

The second method is the standard indentation mode [65, 71, 77] (section 2.6) in which a progressive load is applied up to a normalized indentation depth of 25%, recording the stiffness only at this precise depth. In this case, $\dot{P}/P$ it is not constant leading to progressive decrease of $\dot{\varepsilon}$ (see Figure 1.23 in section 1.5.5). The obtained results will be compared to the CSM mode, analyzing by scanning probe microscopy (SPM) the formation of shear bands around the indent as well.

4.1.1 Effect of thickness

a) CSM hardness and elastic modulus

The effect of thickness on the mechanical properties has been investigated for the fully amorphous composition $Zr_{65}Ni_{35}$. At first, we consider the results obtained with a CSM method using a standard loading rate equal to 0.05 s^{-1}.

The variation of hardness (*H*) as a function of indentation depth and normalized indentation depth is reported in Figure 4.1a-b. In general, the hardness of a film is considered independent from the underlying substrate as long as the penetration depth is shallow enough, namely when the normalized indentation depth is smaller than a critical value. This critical value is mainly dependent on the stiffness and strength ratio between the film and the substrate [65, 149]. For films deposited on a stiff and hard substrate, the "10% of film thickness" rule of thumb is generally valid for the critical penetration, even though it is supposed that there are no substrate influence up to 20% of normalized indentation depth [65, 149].

Figure 4.1a shows that after an initial jump at very low indentation depth, presumably due to the surface-tip interaction as well as tip surface roughness, the hardness slightly increases when decreasing film thickness irrespective of the selected indentation, indicating the absence of substrate effects. A similar trend is found if *H* is plotted against the normalized indentation depth, see Figure 4.1b. If an average value of hardness is extracted from the normalized indentation depth between 10 and 20%, the hardness increases from 6.3 GPa for a 900 nm-thick film up to 7.3 GPa for a 200 nm-thick film, Figure 4.1c. The only comparison with the literature is the work of Ristić *et al.* [76] reporting a micro-hardness value of 5.2 GPa for $Zr_{65}Ni_{35}$ ribbons, although this measurement is not directly comparable with our nanoindentation results.

The yield strength σ_y taken equal to *H/3* (Ref. [41] and section 1.5.3), increases from 2.1 up to 2.4 GPa for thicknesses varying from 900 to 200 nm, which is consistent with Zr-based BMGs values reported in the literature [62]. The corresponding elastic deformation (equal to *H/3E*) is around 3% slightly increasing when the thickness decreases from 900 down to 200 nm (Figure 4.1c) [136]. Note that this value is higher than the elastic deformation of Zr-based BMGs usually around 1.9% (section 1.5.3 and Ref. [2]).

The moderate increase of hardness with decreasing film thickness irrespective of the indentation depth and of the normalized indentation depth as well cannot be explained considering a substrate effect nor on the basis of a change in atomic arrangement (see Chapter III), thus it should have an *extrinsic* origin in terms of thickness confinement affecting the shear bands development (section 1.5.3 and Ref. [136]). This phenomenon is quite similar to a compression test on an amorphous bulk specimen having a low aspect ratio (height to diameter). In this case, shear bands are often generated

at the contact interface between the sample and the machine cross-head, and the confinement effect prevent them to freely glide to create the shear offset [3]. A low aspect ratio also favors multiple shear bands formation, *apparently* enhancing the measured strength of the sample [3]. Even if the exact load conditions under the indent tip are different with respect to a compression test, the confinement effect can be enhanced for small thicknesses, thus potentially affecting the nucleation processes of shear bands. The local constraint would thus favors shear bands nucleation to accommodate the deformation induced by the indent.

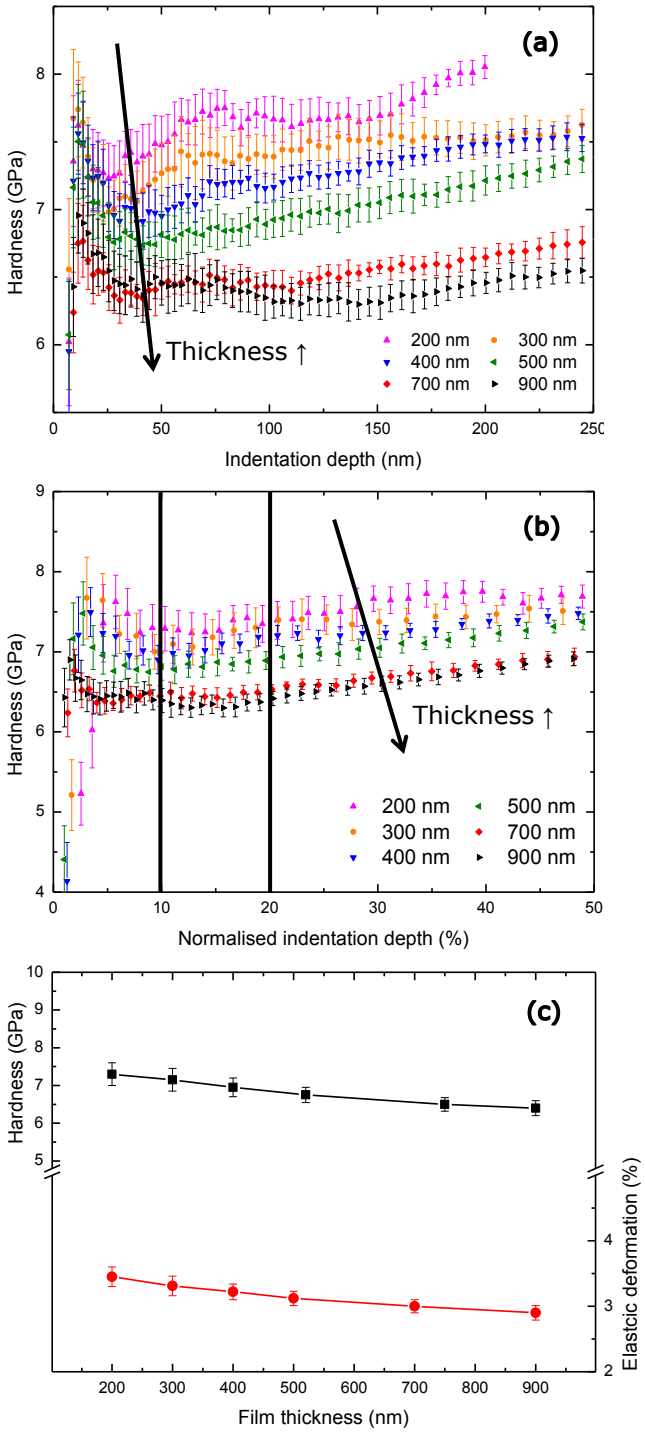

***Figure 4.1** – CSM hardness as function of the indentation depth and normalized indentation depth, respectively (a) and (b). (c) Average hardness and elastic deformation as a function of film thickness determined for a normalized indentation depth between 10 and 20% (black vertical lines).*

The nanoindentation can be used also to extract the film elastic modulus (E), with correction for the effect of substrate [149, 150]. As a matter of fact – while the extraction of hardness is connected to the development of plastic zone ahead of the indent which leads to a substrate influence starting at large normalized penetration depth – the elastic stress field ahead of the indenter is affected even at small penetration depths involving possibly surface effect phenomena [149, 150]. To obtain substrate independent values of E, several models can be used to correct the rough data set [149, 150]. The Agilent nanoindenter (section 2.6) provides an automatic correction of the elastic modulus data by using the model of Hay *et al.* [149]. Chu *et al.* [33] suggest the use of the so-called King's model to extract the elastic modulus of TFMGs which relates the reduced elastic modulus (film + substrate, E_r) with the penetration depth (h) in the following form:

$$\frac{1}{E_r} = \frac{1-\nu_i^2}{E_i} + \frac{1-\nu_f^2}{E_f}\left(1-e^{\frac{-\gamma(t_f-h)}{a}}\right) + \frac{1-\nu_s^2}{E_s}\left(e^{\frac{-\gamma(t_f-h)}{a}}\right) \qquad (4.1)$$

where E_i, E_f, E_s and ν_i, ν_f, ν_s are the elastic modulus and the Poisson ratio of the diamond indenter, film, and Si (100) substrate, respectively. Note that all these quantities are known. The effective contact radius (a) is approximated as $2.8h$ for a Berkovich nanoindenter, while γ is a weighting factor that accounts for the continuously changing contribution of the film and substrate to the overall stiffness. The rough experimental data (E_r) are fitted with equation 4.1 considering E_f and γ as free fitting parameters.

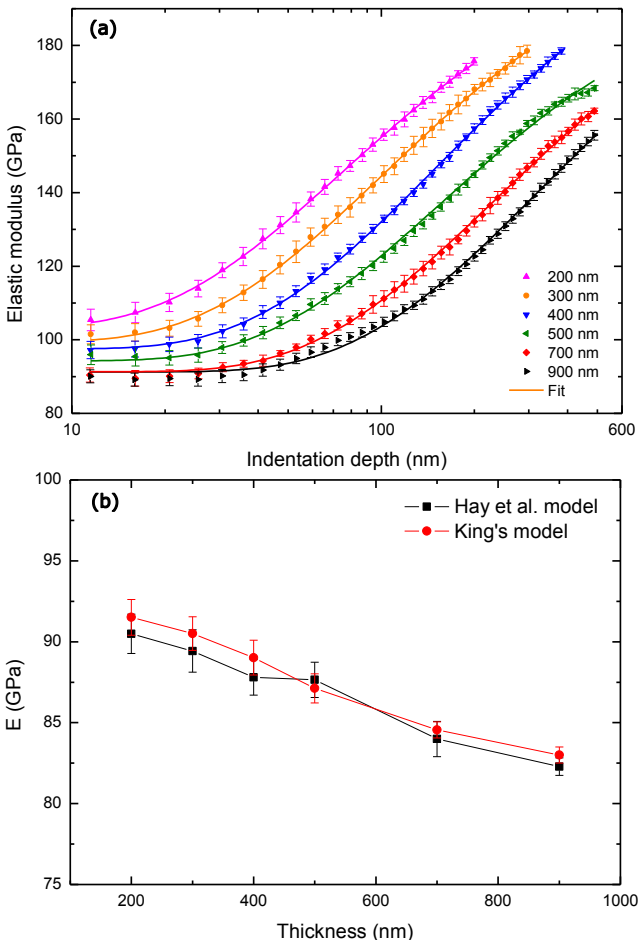

Figure 4.2 *– (a) Reduced elastic modulus as a function of the indentation depth. The data are fitted with the King's model. (b) Comparison between the elastic modulus calculated using the Hay's and King's models.*

Figure 4.2a reports the variation of the apparent elastic modulus (E_r) as function of the logarithmic of indentation depth. Equation 4.1 successfully fits the data set allowing an estimation of the film elastic modulus, Figure 4.2b. Moreover, Figure 4.2a shows that E_r significantly increases even for very low indentation depths, indicating a clear substrate effect which is not found in the case of hardness (Figure 4.1a-b). The comparison with the elastic modulus derived with King's model and the Hay's one is displayed in Figure 4.2b. Both results are in agreement, showing a small decrease of the elastic modulus with increasing thickness. Specifically, E decreases from 91 to 83 GPa. This trend clearly reflects the effect of Si substrate having an elastic modulus of 183 GPa affecting the measurements especially for the thinnest film, which might not have been perfectly corrected by the Hay or King models.

Note also that the lowest absolute value of E is more than 10% higher than the surface Brillouin spectroscopy (SBS) and picosecond ultrasonics (PU) results presented in section 3.3a, which show a constant value of E equal to 72 GPa. Obviously, the SBS and PU technique are more accurate and their results are not affected by the substrate since both measurements involve the probing the velocity of the acoustic waves. Hence, in the following analysis we will refer to elastic properties presented in Chapter III, while exploiting nanoindentation only for the analysis of hardness. Nevertheless, the nanoindentation analysis of E provides useful information to verify the accuracy and the limits of the technique especially for small thicknesses as well as to validate the models to fit the experimental results.

b) Standard nanoindentation

The effect of thickness has also been investigated by means of a standard nanoindentation (section 2.6). Figure 4.3a shows the indentation curves at fixed normalized indentation depth of 25%. The loading curves have the expected parabolic profile with a loading curvature (C) which can be extracted from:

$$P = Ch^2 \tag{4.2}$$

where P is the load and h the indentation depth. The loading curvature (C) increases from 130 GPa up to 142 GPa respectively for a 200 and a 900 nm-thick TFMGs, indicating an increment of film hardness for the thinnest film, as reported in Figure 4.3b.

Specifically, the hardness trend confirms the evolution obtained using the CSM method (Figure 4.1c), showing an increment from 6.3 up to 7.3 GPa with decreasing film thickness from 900 down to 200 nm. Figure 4.3a also shows the presence of bursts on the loading curve as indicated by black arrows for the 900 and 700 nm-thick films. The origin of these bursts has been explained in section 1.5.5 and related to the activation and a propagation of a single shear band around the indent. These bursts are more visible at large indentation depths for thicker films (Figure 4.3b).

An analysis of the indents by means of scanning probe microscopy (SPM) has been carried out to thoroughly investigate the formation of shear bands, Figure 4.4. Obviously, since tests have been conducted at fixed normalized indentation depths of 25% to limit substrate effect, thicker film will undergo deeper indentation (225 nm for the 900 nm-thick film), while thinnest film will be subjected to shallower indentation (50 nm for the 200 nm-thick film), see Figure 4.3a. Figure 4.4 shows the formation of annular shear bands developing outside and inside the indent involving also a pile-up around the indent, a phenomenon expected for metallic glasses [41, 66, 70], showing no strain hardening [65].

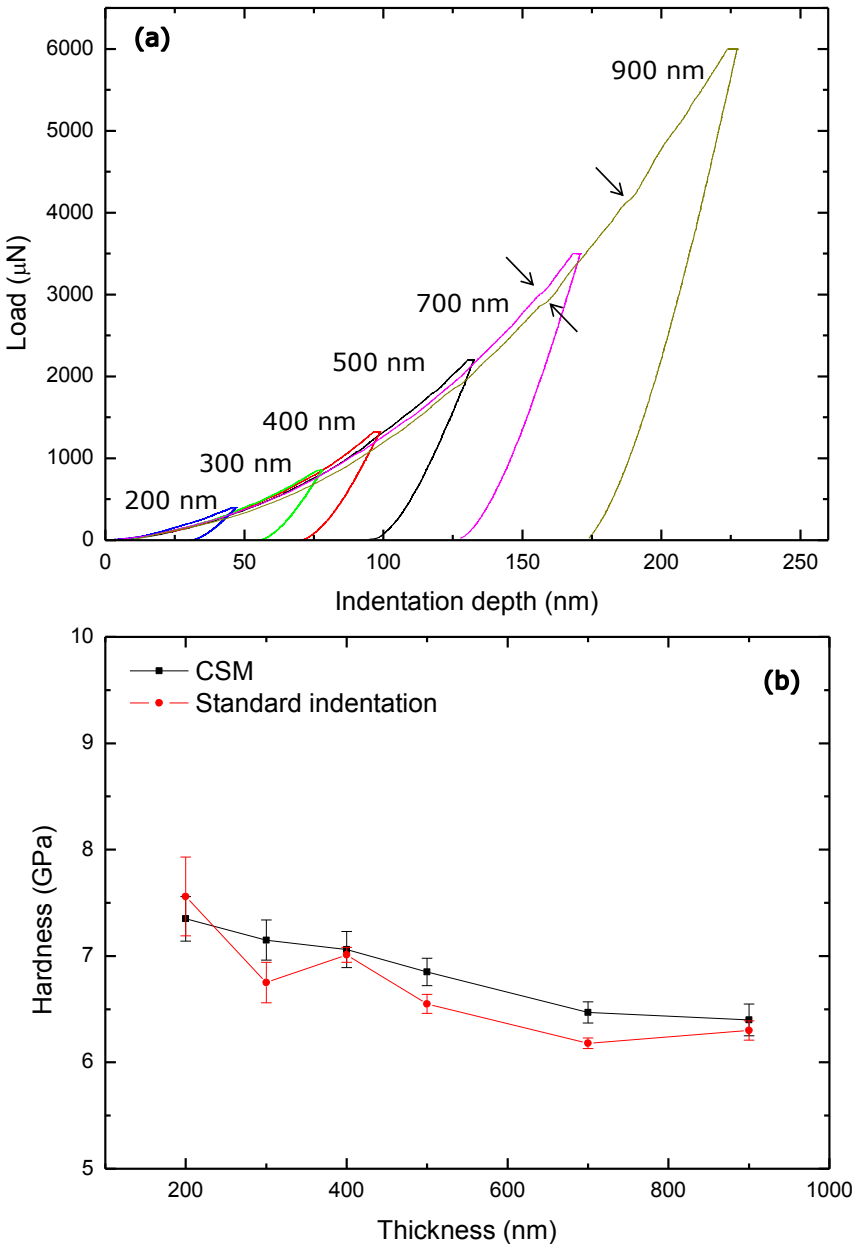

Figure 4.3 *– (a) Standard indentation curves for $Zr_{65}Ni_{35}$ TFMGs obtained at a normalized indentation depth of 25%. The formation of bursts is highlighted by arrows. (b) Variation of hardness as a function of film thickness in standard and CSM mode.*

More interesting, the development of annular shear bands is reduced if the thickness of the film decreases. In fact, 200 and 300 nm-thick film do not show any annular shear bands, while a small crack propagates from one side of the indent proceeded by a remarkable pile up phenomena (black arrows). This effect can be related to the lower indentation depth applied for thinnest film which probably does not allow sufficient percolation of STZs necessary for the formation of shear bands (sections 1.5.5 and 1.5.8). Moreover, since the indents have been made at the same normalized indentation depth, the formation or the absence of annular shear bands does not depend on the substrate confinement effect, but is rather related to the shallower penetration applied for the thinnest films.

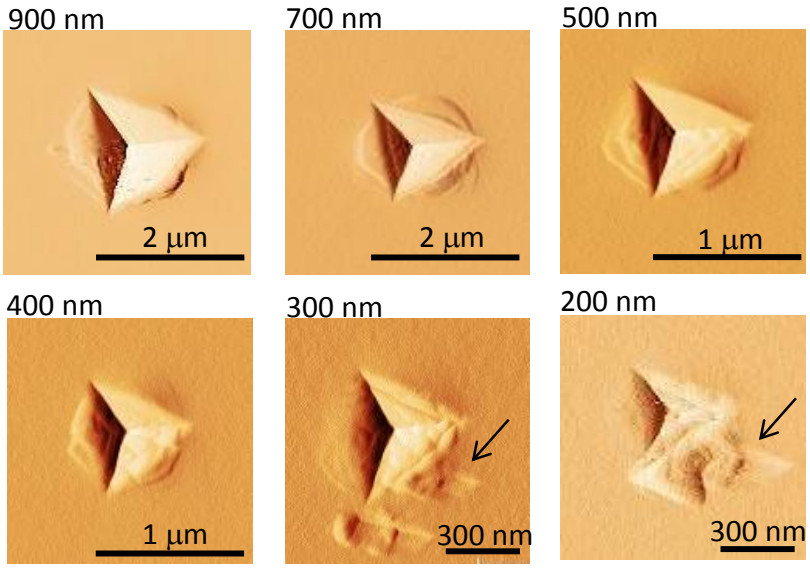

Figure 4.4 *– SPM images of indents made at a fixed normalized indentation depth of 25%. The thickness of the film is indicated on the top of the SPM images.*

The formation and the number of the annular shear bands can be investigated by analyzing the load displacement curve (Figure 4.3a), comparing the number of bursts with the SPM images (Figure 4.4). However, as reported in section 1.5.5, a more convenient way to analyze the data is to consider the evolution of the strain rate ($\dot{\varepsilon}$) as a function of indentation depth which shows a monotonic decrease when increasing the depth, if standard indentation experiments are conducted. The strain rate can be defined as:

$$\dot{\varepsilon} = \frac{\dot{P}}{2P} \tag{4.3}$$

or

$$\dot{\varepsilon} = \frac{\dot{h}}{h}. \tag{4.4}$$

Since the loading rate $\dot{P}$ is constant, equation 4.1 cannot be used for the analysis of strain bursts corresponding to the formation of shear bands. On the other hand, equation 4.4 considers directly the penetration depth (h) and the local indentation velocity ($\dot{h}$) providing thus more accurate analysis of the strain bursts. Figure 4.5a displays an example of the strain rate calculated using equations 4.3 and 4.4 as a function of the indentation depth for a 900 nm-thick film. While equation 4.3 provides a smooth hyperbolic profile, the strain rate calculated with equation 4.4 shows the presence of two peaks at around 150 and 180 nm corresponding to the formation of strain bursts also indicated in Figure 4.3a by arrows on the 900 nm-thick film. Other peaks at small indentation depths in Figure 4.5a are rather related to the noise during the derivation procedure enhanced at small indentation depths. The origin of these peaks is related to the abrupt propagation of annular shear bands which trigger an sudden increment of the strain rate (i.e. the indenter penetrates faster in the film). The number of bursts on the $\dot{\varepsilon}$ curve can be related also with the topological profile extracted from the SPM images (Figure 4.5b). As a matter of fact, the two discrete bumps on the surface profile correspond to the formation of two annular shear bands, shown in the inset of Figure 4.5b (see section 1.5.5).

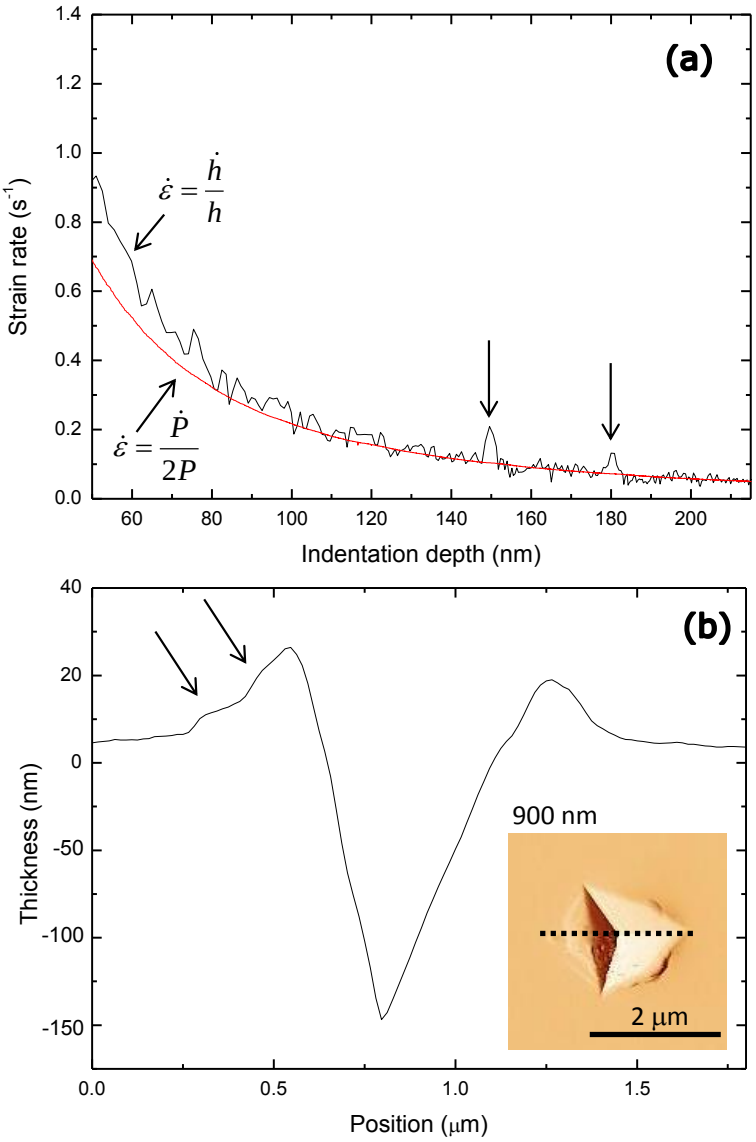

Figure 4.5 *– (a) Strain rate as a function of indentation depth for a 900 nm-thick film. Peaks corresponding to the formation of shear bands are indicated by vertical arrows. (b) The corresponding indentation profile confirming the presence two discrete bursts (diagonal arrows).*

c) Viscoplastic behavior in CSM mode

The nanoindentation in the CSM configuration has also been used to analyze the viscoplastic properties by investigating the effect of different loading rates (section 1.5.5). Specifically, the experiments have been carried out at three different loading rates $(\dot{P}/P)$ equal to 0.02, 0.05, and 0.1 s^{-1}. Note that since the ratio $\dot{P}/P$ is fixed, the corresponding indentation strain rate $(\dot{\varepsilon})$ can be easily calculated with equation 4.3. Figure 4.6 shows the effect of the loading rate for a 900 nm-thick TFMGs on the load-indentation depth curves. For the sake of clarity, the curves corresponding to the 0.05 and 0.1 s^{-1} are horizontally shifted. The presence of strain bursts can be noticed at lower loading rate (black arrows in the inset), while for higher loading rates the curves are smooth. This effect has been already described in section 1.5.5 and related to the enhanced possibility of atomic rearrangements to accommodate the applied strain which promote the formation of shear bands if a

lower strain rate is imposed. On the contrary, a high load rate will not give sufficient time for atomic reorganization leading to an uniform load-indentation depth curve. Moreover, no discrete bursts have been observed on the indentation curve for small thicknesses (i.e. 200 nm), even at lower loading rate, indicating the favored formation of shear bands for large penetrations on thicker films.

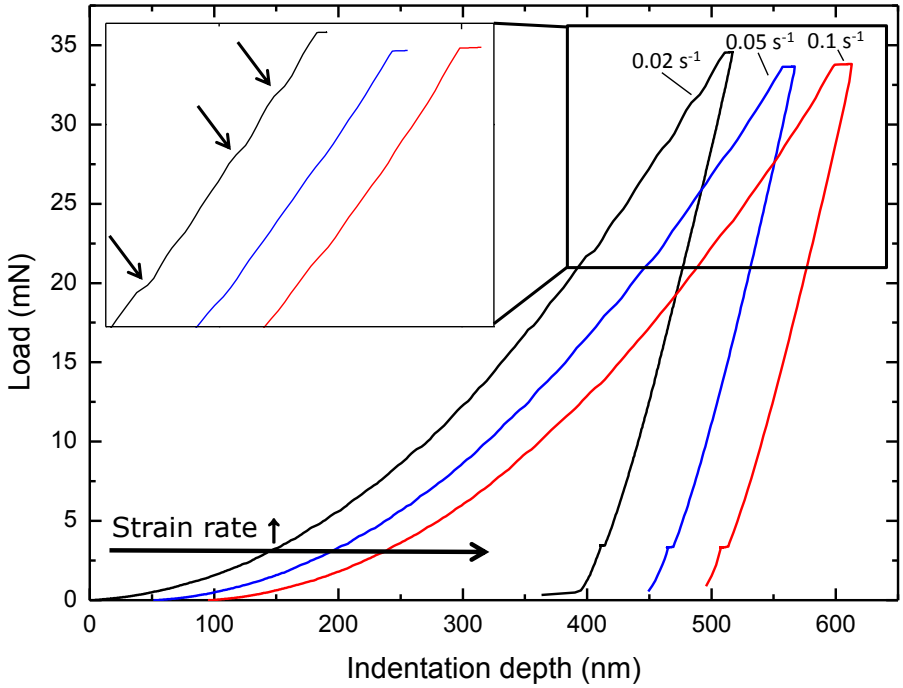

Figure 4.6 *– Evidence of strain bursts formation for a 900 nm-thick film subjected to different loading rates of 0.02, 0,05 and 0.1 s^{-1}. The strain bursts are indicated by black arrows in the inset.*

The change of mechanical properties due to a different loading configuration has a capital importance for the analysis of the rate sensitivity of hardness and the calculation of the activation volume (section 2.6). Figure 4.7 shows a logarithmic plot the variation of H with the strain rate for different film thicknesses [136]. The variation of H as a function of the normalized indentation depth for different strain rates and thicknesses are reported in the Appendix A, showing a constant value of hardness as in Figure 4.1b (absence of substrate effects). In Figure 4.7 it can be noted that the hardness clearly increases with decreasing film thickness at all strain rates, thus confirming the results of Figure 4.1c. Moreover, the hardness increases when increasing the imposed strain rate (viscoplasticity). This phenomenon is described also for BMGs and it is mainly related to the thermally activated nature of shear events (see section 1.5.5 and Refs. [41, 67]) favored at low strain rates leading to a reduced hardness. The extracted strain rate sensitivity coefficient (m_H) is thickness independent and approximately equal to 0.026 [136]. Therefore, by using the procedure described in section 2.6, it is possible to calculate the activation volume which has a value around 120 $Å^3$, if calculated for a 700 and 900 nm-thick specimens having very close hardness values. The values of m_H are comparable with the literature values for Zr-based BMGs having m_H equal to 0.021 for a $Zr_{44}Cu_{44}Al_6Ag_6$ [55]. Other families of BMGs usually show m_H values around 0.01 [55]. However, a direct comparison with our films is not easily to perform since BMGs are composed by several atoms with different sizes and they are produced from liquid phase techniques (sections 1.2 and 1.3), thus leading to different atomic organizations affecting the barrier for triggering shear bands [55, 61]. An overall discussion of the values of the activation volume as a function of composition is presented in section 4.1.2.

Here, it is important to observe that, in agreement with the results presented in the case of microstructure and elastic properties (sections 3.1 and 3.3), the thickness independent value of the rate sensitivity and the activation volume for $Zr_{65}Ni_{35}$ TFMGs indicates that films have the same atomic structure. Once again, the hardness evolution (Figure 4.1c) should be considered in terms of *extrinsic* effects due to thickness confinement.

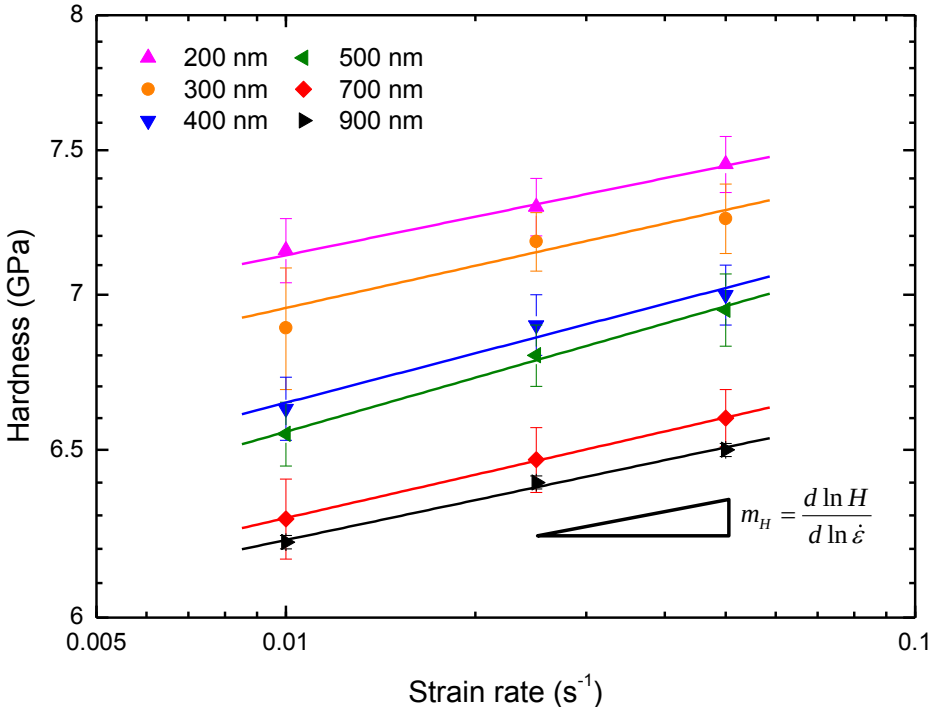

Figure 4.7 *– Determination of the rate sensitivity of hardness (m_H) for $Zr_{65}Ni_{35}$ TFMGs with different thicknesses. The m_H values are constant whatever the thickness and equal to 0.026.*

4.1.2 Effect of composition

The nanoindentation study in the CSM configuration has been used to investigate the effect of composition at fixed thickness (800 nm), aiming to strengthen the results reported in sections 3.1 and 3.3 as well as to the understanding of the effect of composition.

Figure 4.8 shows the variation of the load displacement curve obtained at a constant loading rate of 0.05 s^{-1} for different compositions within the amorphisation range, namely $Zr_{42}Ni_{58}$, $Zr_{65}Ni_{35}$, and $Zr_{75}Ni_{15}$ (section 3.1). The different maximum of load reflect the trend of hardness (Figure 4.9a) and the elastic modulus (Figure 3.7) both increasing for Ni-rich specimen. Moreover, it can be noted that the formation of bursts is enhanced when increasing the percentage of Zr in the film (black arrows), while the indentation curve for the composition $Zr_{42}Ni_{58}$ is completely smooth. A possible explanation for this behavior relies on the change of the atomic structure as a function of composition. In section 3.3, we have shown that Zr-rich TFMGs have a lower fragility index and the reduced formation of strong Zr-Ni bonds. This, in turns, leads to an enhanced tendency to localize plastic deformation within shear band, promoting the formation of strain bursts on the curve. However, the presence of small crystallites (∼3 nm) in the microstructure of $Zr_{75}Ni_{35}$ (section 3.1) can play a role on the activation of strain bursts as well. On the other hand, the increment of the number and the size of fertile sites of shear bands formation for the composition $Zr_{42}Ni_{58}$, leads to production of multiple

shear bands whose interactions give rise to a smooth indentation curve. Figure 4.8 exhibits also a change of the loading curvature, closely related to the hardness variation increasing for Ni-rich compositions (Figure 4.9a).

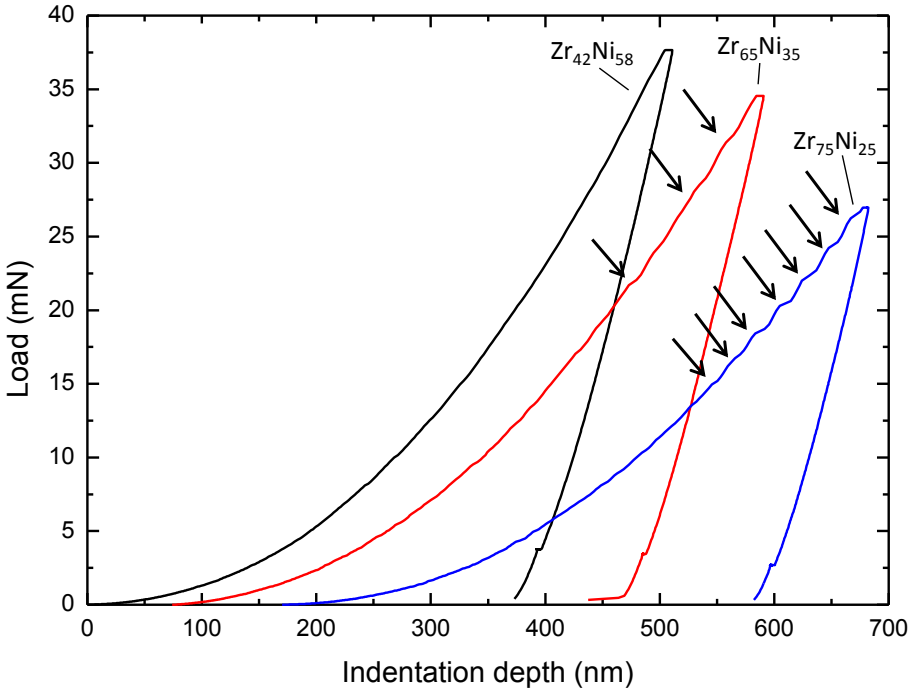

Figure 4.8 *– Load-indentation depth curves for different compositions of TFMGs. Strain bursts are indicated with black arrows. The curves corresponding to $Zr_{65}Ni_{35}$ and $Zr_{75}Ni_{25}$ are horizontally shifted.*

Figure 4.9a shows the trend of hardness (*H*) as function of normalized indentation depth for different compositions. As reported in Figure 4.1b, after a first jump related to the surface-tip interaction, the hardness reaches a plateau (absence of substrate effects). The average hardness values extracted from the interval of normalized indentation depth between 10 and 20% show an increment of *H* with decreasing the Zr content from 5.6 GPa for $Zr_{75}Ni_{25}$ up to 7.8 GPa for $Zr_{42}Ni_{58}$ (Figure 4.9b). Contrary to what appears in Figure 4.1, this trend is attributed to a change of local order due to the presence of strong Zr-Ni bonds when reducing the Zr content (section 3.3b). We further note that these values are in agreement with the literature results for BMGs when converted in terms of yield strength $\sigma_y = H/3$ (section 1.5.3). Moreover, using the values of elastic modulus reported in section 3.3b, it can be estimated the elastic deformation as $H/3E$ which is almost constant and around 2.9% (Figure 4.9b and Ref. [136]). This value is larger than the literature results for Zr-based ribbons or BMGs (1.9%) reported in Refs. [62, 76] and section 1.5.3.

Lastly, the composition $Zr_{85}Ni_{15}$, characterized by the presence of large α–Zr crystals embedded in an amorphous matrix, has an average hardness equal to 7.1 GPa. Tacking *E* equal to 73 GPa (section 3.3b) we obtain an elastic deformation around 3.2%.

The effect of the rate sensitivity of hardness has been studied in Figure 4.10a. showing an hardness increment for higher strain rates (a viscoplastic effect described in section 4.1.1c). The corresponding variation of the activation volume as a function of film composition is shown in Figure 4.10b. There is a large effect when reducing the Zr content which leads to an increase of the activation

volume up to 180 Å^3 for $Zr_{42}Ni_{58}$, while $Zr_{75}Ni_{25}$ exhibits a very small value of about 60 Å^3. This evolution reflects into the strain rate sensitivity coefficient (m_H) which is equal to 0.016 and 0.058, respectively for $Zr_{42}Ni_{58}$ and $Zr_{75}Ni_{25}$ (Figure 4.10a) and, in the case of $Zr_{42}Ni_{58}$, in agreement with results reported in [55].

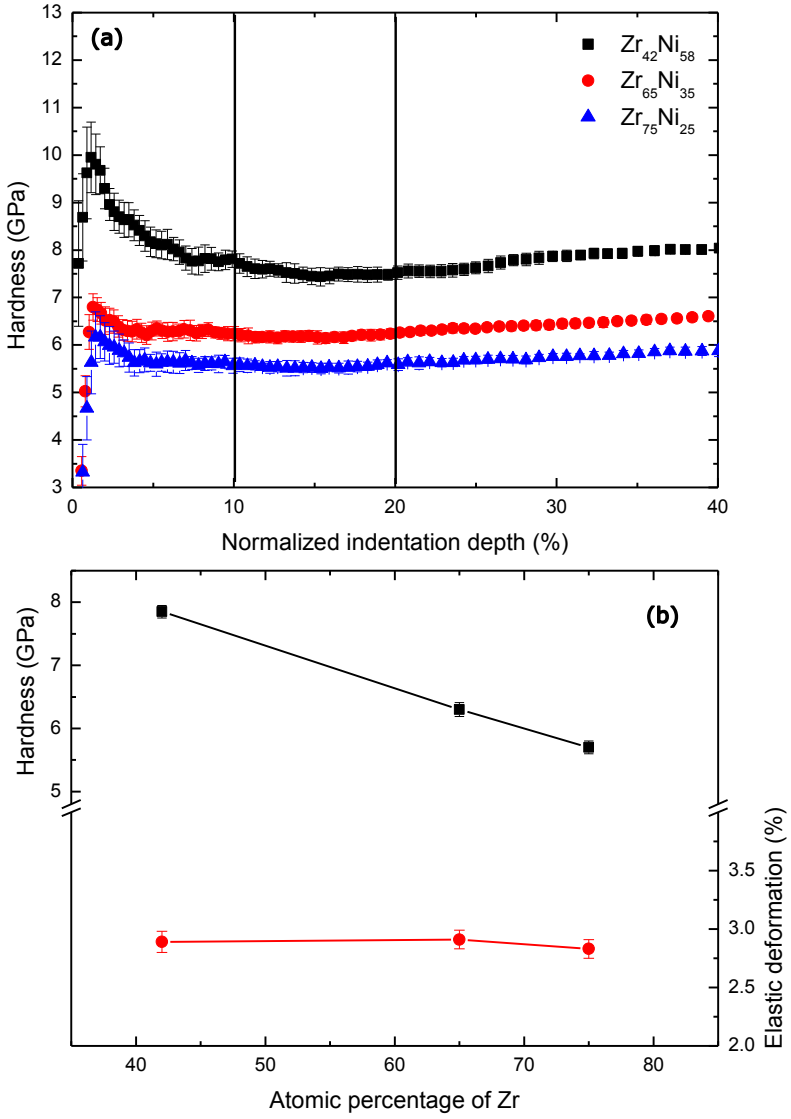

Figure 4.9 *–(a) Variation of the hardness as a function of the normalized indentation depth. (b) Average hardness and elastic deformation as function of Zr content in the film.*

Reducing the Zr percentage, Zr-Ni bonds are favored as shown by the increase of mass density, elastic constants and the reduction of average atomic distances (Chapter III and Ref. [136]). This trend is confirmed by the increase of hardness reported in Figure 4.9b. On the other hand, the increase of the apparent activation volume seems to be indicative of a structural heterogeneity characterized by large loosely packed regions (STZs) – due to the enhanced mixed entropy (section 3.3b and Ref. [136]). This result is intimately related with the enhanced FWHM for $Zr_{42}Ni_{58}$ (section 3.1b). A better plasticity should be expected for Ni-rich specimens showing a lower rate sensitivity and a higher activation volume promoting the nucleation and formation of multiple shear bands, thus might enhancing mechanical properties [55, 61].

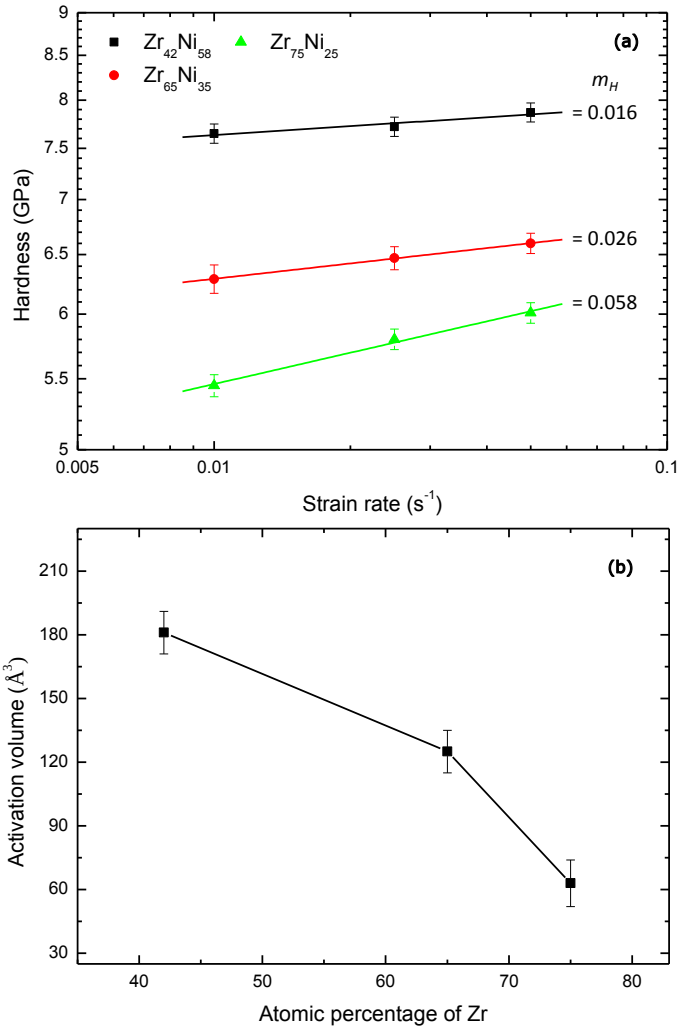

Figure 4.10 *–(a) Determination of the rate sensitivity of hardness (m_H) for ZrNi TFMGs with different composition. (b) The corresponding value of the activation volume increasing for Ni-rich specimens.*

4.1.3 Conclusion about nanoindentation test campaign

In sections 4.1.1 and 4.1.2 we have analyzed the effect of the thickness and the composition on the nanoindentation behavior of TFMGs.

For the amorphous composition $Zr_{65}Ni_{35}$, a reduction of the film thickness leads to an increase of the hardness (both with the CSM method and the standard indentation), combined with the enhanced formation of strain bursts and annular shear bands around the indent for large indentations on thicker film. On the other hand, TFMGs have the same rate sensitivity and, consequently, the same activation volume, in agreement with the results presented in Chapter III in terms of local order, density, and elastic constants. For these reasons, size effects observed on hardness probably have an *extrinsic* origin related to a confinement effect on the shear bands formations.

A compositional variation involves changes in hardness, rate sensitivity, and activation volume, increasing also the formation of strain bursts for Zr-rich specimen. These trends are related to the variation of local order with the formation of Zr-Ni bonds favored for Ni-rich specimens, which also exhibit a large size of STZs in agreement with the enhanced thermodynamic fragility and FWHM reported in Chapter III.

4.2 Mechanical properties of freestanding $Zr_{65}Ni_{35}$

In this section we present the main results on the elastoplastic properties of freestanding $Zr_{65}Ni_{35}$ TFMGs using the lab-on-chip method described in section 2.8. As a short reminder, the method consists in depositing the $Zr_{65}Ni_{35}$ film which overlaps an actuator layer (Si_3N_4) characterized by the presence of an high internal tensile stress (∼1 GPa). The actuator layer is patterned by means of lithography to generate a long rectangular shape. The specimen layer ($Zr_{65}Ni_{35}$) is patterned with a dogbone shape. After release by selective etching of the substrate (Si), the specimen beam is deformed owing to the contraction of the actuator beam. The resulting freestanding structure reaches a stable position governed by force equilibrium. The deformation of the specimen beams is calculated after SEM measurement of displacement of cursors specifically designed on the actuator, while the stress is deduced by direct application of force equilibrium assuming that the actuator deforms elastically. Different geometries of specimen and actuator generate different stress levels in the specimen which can deform elastically or plastically up to fracture in the case of short beams anchored to long actuators (section 2.8.1).

Table 4.1 summarized the geometries of actuator and specimen beams investigated in this work. As mentioned in section 2.8.1, we studied the "B" series whose main characteristic is represented by the different length of the actuator beams, while fixing the length of the specimen (25, 50 and 100 μm). Moreover, while the width of the actuator is fixed (15 μm), the width of the specimen is varied and equal to 1, 2 and 4 μm. The thickness of the specimen is equal to 110, 200 and 360 nm and it is deposited on an actuator layer having a thickness of 80, 100 and 160 nm, respectively. Table 4.1 reports all the combinations investigated. For example, considering a specimen of 200 nm deposited on a 100 nm-thick actuator, we studied the mechanical properties of 3 specimen lengths (25, 50 and 100 μm), each of which having a width of 1, 2 and 4 μm leading to a total of 9 combinations. Concerning the 110 nm-thick specimen with beam length of 25 and 50 μm, 1 μm-wide beams have not been studied because the photolithography did not work properly, probably because of the small size. A single series (namely with fixed specimen length and width) is composed of 40 test structures characterized by a different actuator length to generate different stress in the beam (section 2.8.1).

The choice to analyze with the lab-on-chip technique a 110 nm-thick specimen, which instead it has not been studied by nanoindentation, has been dictated by the possibility to further enhance size effects for freestanding films, while avoiding the effect of the substrate which can affect the results during nanoindentation (section 4.1.1).

As can be noted in Table 4.1, the ratio actuator/specimen thickness is not constant and it increases for the 110 nm-thick specimens up to 0.73. This choice can be explained by the expectation that more severe stress levels could be attained for thinnest specimens involving size effects and possibly increasing mechanical properties such as the yield strength (σ_y), section 1.6. Equation 4.5 provides the general expression for the extraction of the strain and stress in the specimen layer. Specifically, it can be noted that higher stress levels are reached for ratio actuator/specimen thickness (t_a/t_s) close to unity and when reducing the width of the specimen beam (w_s).

$$\begin{cases} \varepsilon^{mech} = \ln\left(\dfrac{l_0 + u}{l_0}\right) - \varepsilon^{mis} \\ \sigma = E_a \dfrac{w_a t_a}{w_s t_s}\left(\ln\left(\dfrac{l_{0a} - u}{l_{0a}}\right) - \varepsilon_a^{mis}\right) \end{cases} \tag{4.5}$$

Actuator thickness (nm)	Specimen thickness (nm)	Specimen length (μm)	Specimen width (μm)
80	110	25	2-4
		50	2-4
		100	1-2-4
100	200	25	1-2-4
		50	1-2-4
		100	1-2-4
160	360	25	1-2-4
		50	1-2-4
		100	1-2-4

Table 4.1 *– Geometries of specimen and actuator beams investigated in this thesis.*

From equation 4.5 it can be estimated the stress value for different actuator and specimen geometries, evaluating if fracture can occurs or not (Table 4.2). It is worth noting that in all cases it has been considered the more severe stress condition, namely with the actuator length equal to 1500 μm. A thorough analysis of Table 4.2 reveals that for an actuator geometry of 1500 μm x 15 μm x 80 nm produces a very high stress level on both a 25 μm x 1 μm x 110 nm and on a 25 μm x 2 μm x 110 nm specimens. This stress level is higher than the ideal limit (sections 1.5.8 and 4.2.4), thus possibly induce fracture for these specimens.

On the other hand, the ratio actuator/specimen thickness selected to investigate the mechanical properties of 200 and 360 nm-thick specimen is less severe overcoming the threshold of 3000 MPa only for 1 μm-wide beams (Table 4.2). An actuator with geometries given by 1500 μm x 15 μm x 100 nm will generate a stress of 2300 MPa on a 25 μm x 2μm x 200 nm specimen, which might not be enough for fracture. For instance the yield strength calculated as *H/3* (section 4.1.1) is equal to 2400 MPa. An actuator with the same geometry, but 160 nm-thick will produce a stress equal to 2100 MPa onto a specimen beam of 25 μm x 2μm x 360 nm (Table 4.2), a value below the result obtained from *H/3* (section 4.1.1) and slightly above the yield strength of BMGs counterparts which may not be sufficient to produce rupture of the film. Obviously, a lower stress level will be reached for a 4 μm-wide specimen beams for which we expect a limited plastic deformation without rupture.

From the analysis of Table 4.1, it is also possible to comment about the specimen length scales investigated with respect to the literature dealing with mechanical size effects (section 1.6). In the case of compression test of micropillars, Volkert *et al.* [102] studied pillars with a diameter from 140 nm up to 3.6 μm (cross-sectional area ranging from 0.015 to 10.2 μm^2) and heights from 350 nm up to 9 μm (aspect ratio equal to 2.5). Similarly, Lee *et al.* [104] studied micropillars with a diameter of 1 and 3.8 μm (cross-sectional area ranging from 0.8 to 11.3 μm^2) and heights of respectively of 2.5 and 9.5 μm (aspect ratio equal to 2.5). Other authors [4, 103, 105] reports similar values for pillars having a diameter in between 100 nm and 5 μm, with an aspect ratio (height/diameter) usually ranging from

1.5 to 3. Jang and Greer [110] studied tension test on micropillars with a diameter from 140 nm up to 1 μm (cross-sectional area ranging from 0.015 to 0.8 μm^2) and a fixed aspect ratio of 8, leading to heights in between 1.1 μm and 8 μm. All the studies involving *in-situ* TEM use even smaller samples with a thickness around 50 nm (or less) and a length usually up to 5 μm [113, 116, 117]. Tian *et al.* [115] using *in-situ* TEM investigated samples with a thickness in between 200 and 300 nm and a width of 300 nm (cross-sectional area ranging from 0.04 to 0.09 μm^2). The length is equal to 1 μm.

Actuator geometry	**Film geometry**	**Applied stress (MPa)**
1500 μm x 15 μm x 80 nm	25 μm x 1 μm x 110 nm	> 4000
1500 μm x 15 μm x 80 nm	25 μm x 2 μm x 110 nm	3500
1500 μm x 15 μm x 100 nm	25 μm x 1 μm x 200 nm	3700
1500 μm x 15 μm x 100 nm	25 μm x 2 μm x 200 nm	2300
1500 μm x 15 μm x 160 nm	25 μm x 1 μm x 360 nm	3600
1500 μm x 15 μm x 160 nm	25 μm x 2 μm x 360 nm	2100

Table 4.2 *– Effect of the actuator and specimen geometries on the maximum applied stress.*

The smallest dimensions of our specimens are equal to 25 μm x 1 μm x 200 nm (a volume of 5 μm^3 and a free surface of 60 μm^2), while the largest specimens have a dimension of 100 μm x 4 μm x 360 nm (a volume of 144 μm^3 and a surface area of 872 μm^2). Therefore, even though the thickness range is comparable with the previously reported studies, the width and especially the length are much larger, reaching the values of 4 μm and 100 μm, respectively. As a consequence, the volume and the free surface of our specimens are in between 2 and 10 times larger than the literature ones. Moreover, it worth noting that the lab-on-chip testing avoid FIB-milling operations and provide taper-free specimens with a perfect dogbone shape (section 2.8). Hence, the analyzed samples allow expanding the investigation of mechanical size effect for larger dimensions, while avoiding FIB damage. Another advantage of this technique is the enforcement of a purely uniaxial tensile loading, avoiding all the problems usually present in compression test of micropillars and related to the contact between the punch and the pillars surface (section 1.6). Lastly, most of *in-situ* TEM experiments do not allow the extraction of the stress-strain curve, providing only the deformations. Here, we can reconstruct the entire stress-strain curve with great accuracy.

In the next section we start the analysis of the stress-strain curves obtained for the different specimen thickness and geometries. For the sake of clarity, different specimen geometries are named as "B15_*x*_*y*", where B indicates the "B" series, 15 is the width of the actuator (15 μm), while *x* and *y* represent the width and the length of the specimen beam (Table 4.1). The thickness of the specimen will be indicated at the beginning of each subparagraph as well as in the Figure caption. The letter "B" can be followed by a "T" indicating that the actuator have a tapered shape. As reported in [146], the tapered geometry does not alter the stress and deformation levels reached in the specimen beam with respect to the standard "B" specimen, while leading to a more gradual release. This actuator geometry

has been preferred for the study of mechanical properties of thinner specimen, namely 200 and 110 nm-thick.

4.2.1 Stress-strain response of 360 nm-thick film

Figure 4.11 shows the stress-strain curves obtained for 360nm-thick specimens with a width of 1, 2, and 4 μm, respectively (a), (b), and (c). The specimen length is indicated in the legend, while the actuator mismatch strain is equal to -0.0028 (section 2.8.1). The curves have the following common characteristics:

- an elasto-plastic behavior, somehow similar to the behavior reported in the literature for compression test of BMGs (section 1.5.3),
- an elastic modulus (E) very close to the predicted one (72 GPa) obtained by surface Brillouin spectroscopy and picosecond ultrasonics (section 3.3a) and indicated by the straight black line,
- the presence of strain hardening here especially visible for the 1 and 2 μm-wide beams.

Moreover, it can be noted that:

- the yields strength (σ_y) – taken equal to the point that deviates from the elastic behavior (black line in Figure 4.11) – is dependent on the width, while it is only slightly dependent on the beam length. Specifically, it changes from 2850 MPa down to 1786 and 1582 MPa, respectively for the 1, 2 and 4 μm-wide specimens. The corresponding elastic strain evolves too and, taking E equals to72 GPa, it decreases from 4.0% down to 2.2%,
- the 1 μm-wide specimens experience large ductility (up to 14.1%) and fracture due to the higher stress involved (section 4.2). Black arrows in Figure 4.11a indicate the stress and strain corresponding to the last unbroken specimen. Large deformations (up to 10.7%) are shown also for the 2 μm-wide specimen, although fracture is not reached. The 4μm-wide specimen has a reduced plastic strain due to the smaller stress and strain levels attainable,
- the fracture strain is dependent on the beam length, decreasing for longer beams (Figure 4.11a). An in-depth analysis of the fracture behavior will be described in Chapter V.

A preliminary understanding of these results involves the analysis of the elastic modulus (E), the yield strength (σ_y), and the plastic deformation. Specifically, E is agreement with the results obtained by surface Brillouin spectroscopy (section 3.3a), this means that the lab-on-chip technique, involving uniaxial tension of freestanding films, provides a very accurate values of the elastic behavior. Furthermore, the fact that E is constant indicates that the confinement effect imposed by the beam geometry does not alter the atomic structure especially in terms of Zr-Ni bonds and free volume content (section 3.3a). Similar results will be shown for other investigated specimens as well.

The yield stress (σ_y) increases when reducing specimen width. The overall trend as a function of the cross-sectional area will be discussed in section 4.2.4. Nevertheless, it can be observed that this trend is analogous to what has been presented by some authors in the case of compression or traction test of micropillars decreasing the pillar diameter [104, 110] (section 1.6). Moreover, it agrees also with the general trend reported in the review of Greer *et al.* [3] (Figure 1.34), showing the increment of yield strength when the sample size is below few micrometers. However, it is worth to remark again that in our case there is a trend as a function of the cross-sectional area which strongly depends on the width of the specimen and not only on its thickness. The yield strength approaches the ideal

homogeneous stress (σ_{homo}) which we estimated equal to 3170 MPa (section 4.2.4). Hence, it can be pointed out that no changes in terms of beam structure (i.e. shear bands formation) are observed even for the highly deformed beams. An example of SEM micrographs is reported for a 110 nm-thick specimen in Figure 4.15. The deformation develops *homogeneously* throughout the specimen, a result presented in several studies dealing with compression test of micropillars [102, 103, 110] and *in-situ* TEM tensile test [113-117] (section 1.6).

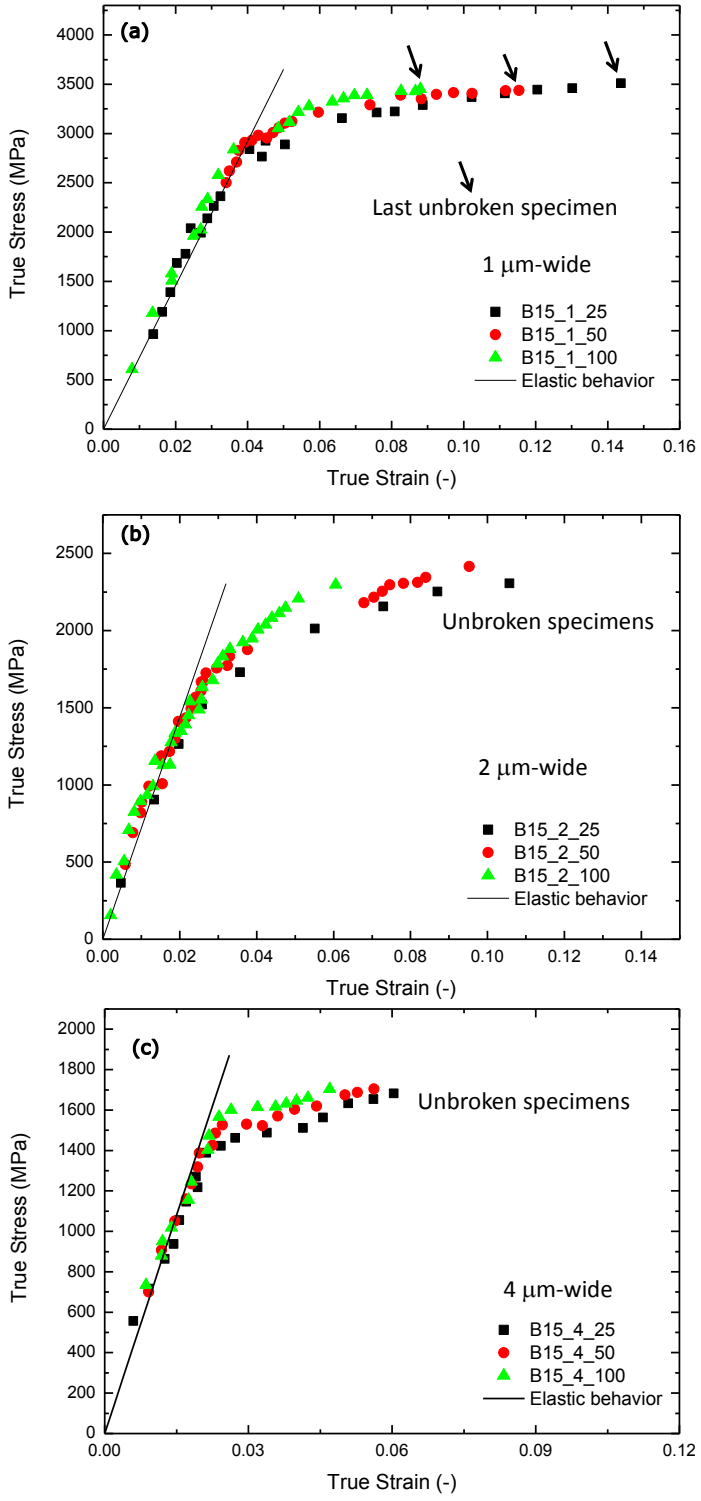

Figure 4.11 *– The stress-strain curves of a 360 nm-thick specimens with different widths equal to 1, 2, and 4 µm, respectively (a), (b) and (c).*

The total strain reaches very high values (14.1%) before fracture (Figure 4.11a). This result is in agreement with the prediction on the basis of μ/B ratio and the fragility index (section 3.3a), while being compatible with the development of a homogeneous deformation (up to 20%) occurring for specimen with confined geometry as reported by many in-situ TEM studies [113, 116, 117] (section 1.6).

The analysis of Figure 4.11 reveals the presence of strain hardening. At first, it can be noted that the strain hardening behavior is an unusual phenomenon for BMGs which instead exhibit strain softening related to the viscosity drop caused by shear bands propagations (section 1.5.3). However, in the case of compression test of a 2 mm-large and 4 mm-high cylindrical BMG, Das et *al.* [53] reported strain hardening related to the activation of dispersed shear transformation zones (STZ) leading to the development of multiple shear bands whose interaction produce strain hardening and enhance plasticity (section 1.5.3). This phenomenon is favored for BMGs having a large free volume content. In the case of TFMGs Tian *et al.* [114] observed strain hardening during *in-situ* TEM tensile tests (section 1.6) for samples with a thickness in between 200 and 300 nm, having a width and a length around 300 nm and 1 μm, respectively

The analysis of strain hardening has been conducted on 1 a 2 μm-wide beams involving larger plastic strain. A Hollomon fit has been used to relate the stress (σ) with the plastic deformation (ε_p) as

$$\sigma = K\varepsilon_p^n \tag{4.6}$$

where K is a constant and n the strain hardening coefficient. The plastic strain has been obtained by subtracting the elastic strain $(\varepsilon_{el} = \sigma_y / E)$ from the total strain. The results of the fit with equation 4.6 are reported in Figure 4.12.

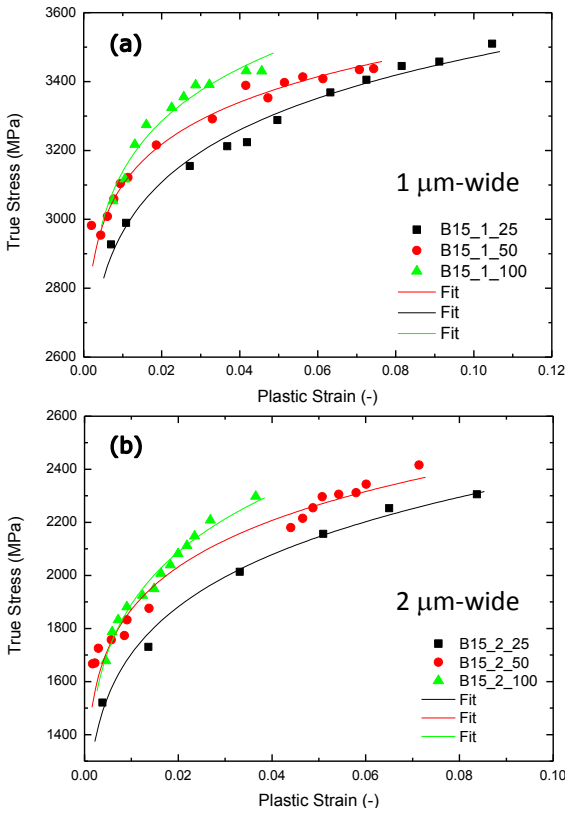

Figure 4.12 *– Strain hardening analysis of 360 nm-thick specimens. The fit has been carried out with equation 4.6.*

Specifically, the power law fit is well suited. The *n* value increases for wider specimen, while is almost independent of beam length. In particular, *n* changes from 0.065 to 0.14, respectively for 1 μm and 2 μm-wide beam. An overall trend of *n* will be reported in section 4.2.4. Here, we point out that the strain hardening behavior is related to homogeneous deformation mechanisms with the simultaneous activation of STZs. Furthermore, this result represents a quite original achievement since it has never been observed in the case of compression test of micropillars or in most on *in-situ* TEM tension studies, while being of capital importance to understand the physics underlying the deformation mechanisms for TFMGs.

4.2.2 Stress-strain response of 200 nm-thick film

Figure 4.13 shows the stress-strain curve for a 200 nm-thick specimen with a width of 1, 2 and 4 μm, respectively (a), (b) and (c). The actuator mismatch strain is still equal to -0.0028 (section 2.8.1). There are several aspects that are closely related to the analysis of Figure 4.11, among which:

- the films exhibit again an elastic-plastic behavior characterized by large ductility,
- the elastic modulus (slope of the black line) is independent with respect to the beam width and equal to 72 GPa,
- the curves involve strain hardening phenomena which is marked for the 2 μm-wide specimen,
- the yield strength increasing from 1780 MPa (4 μm-wide beam) up to 2150 MPa and 3280 MPa, respectively for 2 and 1 μm-wide beams (Figure 4.13). Taking *E* equal to 72 GPa, the corresponding elastic deformation increases from 2.5% up to 4.6%. The trend of σ_y is slightly dependent on the specimen length,
- the fracture is reached only for 1 μm-wide beams with a total deformation of 14.3% in the case of 25-μm long beams (black arrows). Moreover, large ductility is found also for 2 μm-wide beams showing a total deformation reaching 10.7%. However, in this case, the lower stress and strain generated by the actuator is not sufficient to lead to fracture. Note also that the fracture strain is dependent on the length of the specimen (Figure 4.13a).

As discussed in section 4.2.1, the elastic modulus does not depends on beam geometry and it is in agreement with the Brillouin spectroscopy and the picosecond ultrasonics results (section 3.3a). This further validates the lab-on-chip technique to investigate mechanical properties of thin films, while also carrying significant information related to the film atomic structure. Since no changes in *E* are observed, we might assume that the specimen maintains its atomic structure (and free volume content) even if there is an high confinement effect in terms of specimen width and thickness.

The evolution of the yield strength is similar to what was reported in section 4.2.1. Specifically, small widths favor an increment of the yield strength which can reach 3280 MPa, a value very close to the ideal elastic limit estimated to be equal to 3170 MPa (section 4.2.4). The materials deforms homogeneously and no shear bands or necking events are visible using the SEM. Hence, film properties are strongly affected by its geometry which plays a role on the nucleation and development of macroscopic shear bands events. An thorough analysis will be presented in section 4.2.4.

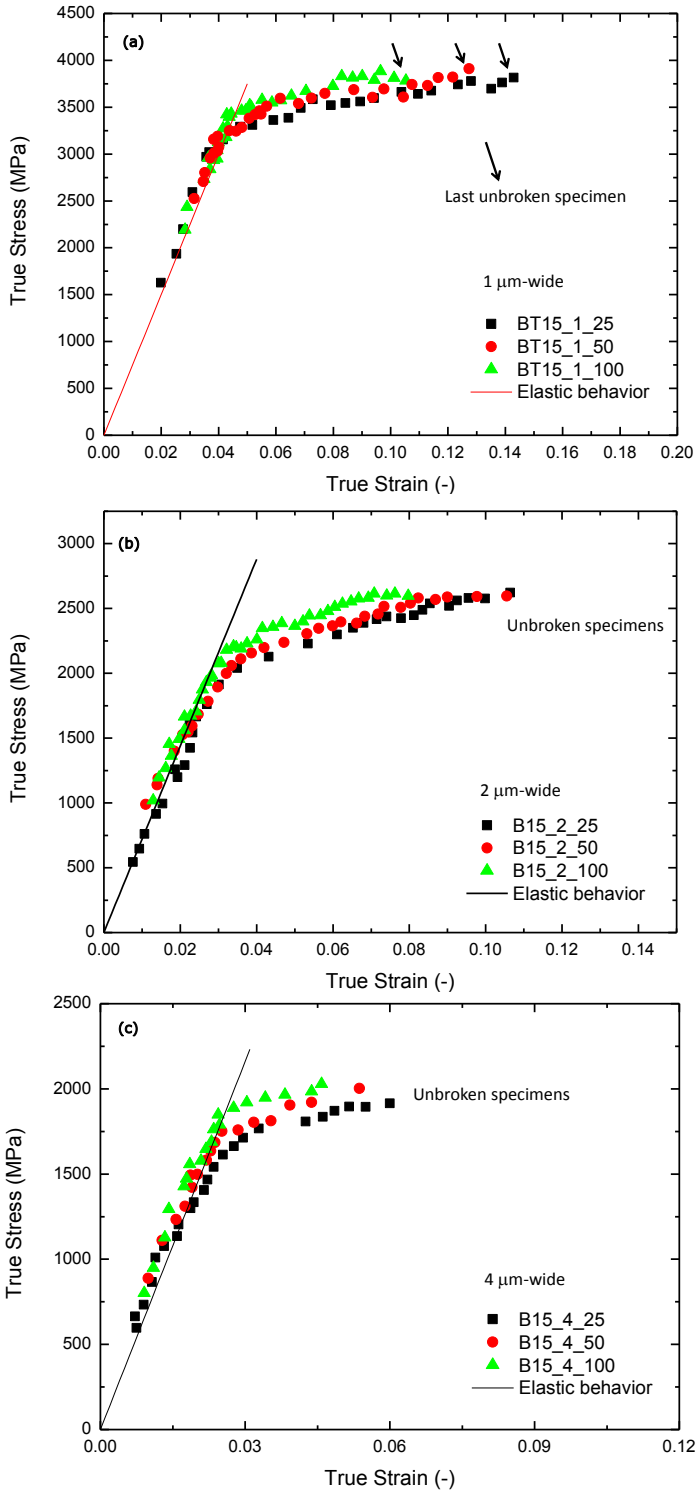

Figure 4.13 *– The stress-strain curves of a 200 nm-thick specimens with different widths equal to 1, 2 and 4 μm, respectively (a), (b) and (c).*

In agreement with the high fragility index (section 3.3a), TFMGs exhibit a significant plastic deformation related to the interaction of local deformation mechanisms (STZ operations). In this view, it can be pointed out that the strain hardening coefficient (*n*) calculated with equation 4.6 changes from 0.045 up to 0.08 increasing the width of the beam (the results of the fit are reported in the Appendix B). Note that these values are almost independent of specimen length. This means that the occurrence of localized STZ operation is favored by wider beams, which in turn can justify the lower yield strength.

4.2.3 Stress-strain response of 110 nm-thick film

Figure 4.14 shows the stress-strain curve of 110 nm-thick specimens with different widths of 1, 2 and 4 μm, respectively (a), (b), and (c). As for the other thickness, the actuator mismatch strain is equal to -0.0028. Moreover, it can be noted that:

- films exhibit an elasto-plastic behavior characterized by large ductility. The curve of the 1-μm wide beam is quite anomalous, showing a marked strain hardening (Figure 4.14a). This dissimilar behavior can be attributed to the less defined beam geometry for low thicknesses and widths during photolithography. Furthermore, SEM observation reveals a slight out-of-plane bending of the specimen related to the very high stress imposed by the actuator (section 4.2). For instance, an 80 nm-thick actuator can generate a stress of 4300 MPa on a beam of 100 μm x 1 μm x 110 nm. Hence, we will not consider this trend as quantitative. However, it can be used to qualitative understand the accuracy limit which can be obtained with the lab-on-chip technique,
- the elastic modulus (slope of the black line) is not dependent on the beam width with a constant value of 72 GPa.
- 2 and 4 μm-wide beams show strain hardening, which is marked for the 4 μm-wide beam,
- the yield strength increases reducing the beam width from 2050 MPa up to 3500 MPa, respectively for 4 and 2 μm-wide beams. Taking E equal to 72 GPa, the corresponding elastic deformation increases from 2.8% up to 4.9%. The trend of σ_y is slightly dependent on the specimen length,
- the film exhibits a large amount of plastic deformation reaching fracture for both 1 and 2 μm-wide beams. Black arrows indicate the last unbroken specimen. This result is in agreement with the prediction made in section 4.2. The total deformation reaches 11.8% in the case of 2 μm-wide beams 25-μm long, while it is equal to 10.2% for a 4 μm-wide beam even if the imposed stress does not produce rupture. As for the trends presented in the sections 4.2.1 and 4.2.2, the fracture strain is dependent on the specimen length.

The analysis of Figure 4.14 shows some common points with the discussion of sections 4.2.1 and 4.2.2. The elastic modulus is in agreement with the Brillouin spectroscopy and picosecond ultrasonics results (section 3.3a). Furthermore, since E is equal to 72 GPa independently of film geometry, we might assume that there are no effect of specimen geometry on the atomic structure (and free volume content). This result agrees with the analysis made in section 3.3a.

On the other hand, the yield strength increases for lower widths reaching the value of 3500 MPa slightly above the ideal limit involving homogeneous deformations (3170 MPa, section 4.2.4). Note that this is the largest value of σ_y measured, above the 3280 MPa for 1 μm-wide and 200 nm-thick specimen (Figure 4.13).

The deformation is homogeneous throughout the specimen beam (as also discussed in section 4.2.1 and 4.2.2). Figure 4.15 shows a 2 μm-wide and 25 μm-long beam deformed in the elastic domain (a) and after experiencing a large plastic deformation (b). Specifically, Figure 4.15a corresponds to the first point in the elastic domain of Figure 4.14b (black squares), while Figure 4.15b shows the last unbroken specimen in Figure 4.14b (black squares) which undergoes a total deformation of 11.8%. The deformation in Figure 4.15b is homogeneous and no obvious events of localization with shear bands are observed even at higher magnification. Again, the presence of a homogeneous deformation

can be justified on the basis of the literature of small scale metallic glasses (section 1.6) [3, 102, 103, 110].

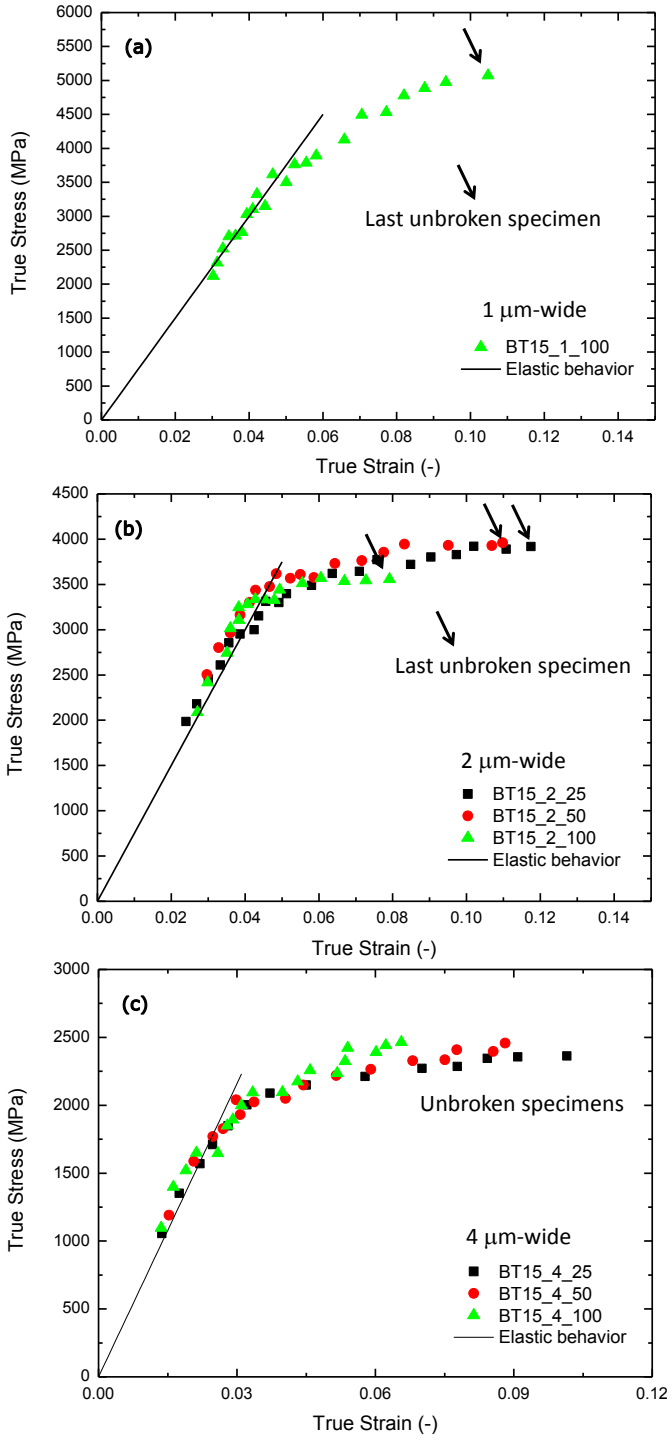

Figure 4.14 *– The stress-strain curves of a 110 nm-thick specimens with different widths equal to 1, 2 and 4 µm, respectively (a), (b), and (c).*

A homogeneous deformation implies large plastic strain (Figure 4.14a-b) due to the activation of dispersed STZs which irreversibly deforms under the application of an external load (sections 1.5.1 and 1.5.8). This observation can be related with the high fragility index (section 3.3), meaning that the atomic structure is more prone to activate local shear transformation events due to the number and size

of dispersed STZs which in turn are responsible for the large plastic strain (section 1.5.3). A detailed view of the physical phenomena which explain the plastic deformation and the evolution of the yield strength will be presented in section 4.2.4.

We conclude this section by observing that specimen experience strain hardening, with a coefficient (n) that increases for wider beams. Specifically, n changes from 0.043 up to 0.075 without a significant effect of the specimen length (the results of the fit are reported in the Appendix B).

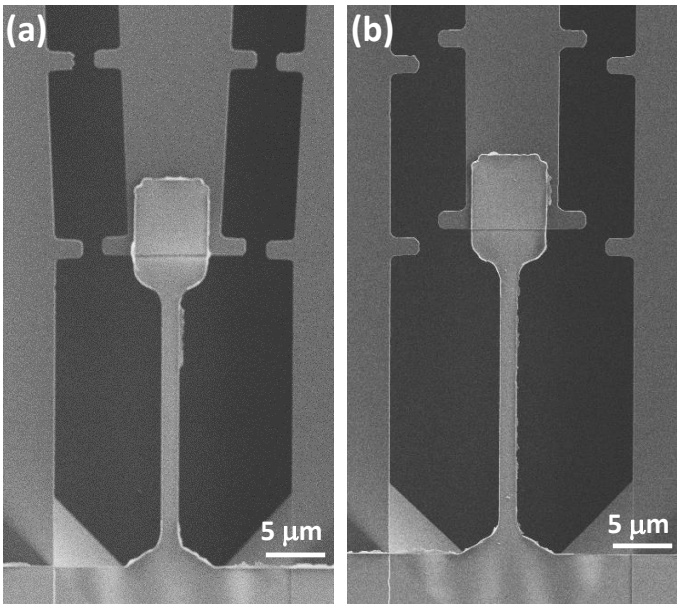

Figure 4.15 *– SEM micrographs of specimen (25 μm x 2 μm x 110 nm) subjected to different stresses and deformations. (a) The small deformation in the elastic regime. (b) The specimen after a total deformation of 11.8% showing that deformation occurs homogeneously throughout the specimen.*

4.2.4 Overall trends of the elastoplastic properties

Here, we analyze the overall trends regarding the elastic modulus (E), yield strength (σ_y) and strain hardening as a function of the specimen geometry summarized in Table 4.1, with the aim to better understand the physics underlying the experimental results arising from the analysis of stress-strain curves reported in sections 4.2.1-3. The analysis of fracture in tension will be left for the Chapter V, where the mechanisms of fracture in TFMGs are addressed.

Figure 4.16 shows the comparison of the stress-strain curves for a 25 μm-long beams. The 1 μm-wide beams are selected for the thickness of 360 and 200 nm, while a 2 μm-wide beam is considered for the 110 nm-thick film. This choice is dictated by the idea to show the entire stress-strain curve up to fracture. However, for the same widths, similar graphs can be drawn for 50 and 100 μm-long specimen as well. In Figure 4.16 it can be noted that:

- the elastic modulus (slope of the black line) is independent of the beam geometry and equal to 72 GPa,
- the yield strength increases when decreasing the film thickness even if this effect is less marked with respect to the reduction of the width presented in sections 4.2.1-3. Specifically, it changes from 2850 MPa up to 3282 MPa and 3300 MPa, respectively from 360, 200 and 110 nm thick specimens. Note that there is no a significant change

from 1 μm-wide and 200 nm-thick beams and 2 μm-wide and 110 nm-thick beams which have almost the same cross-sectional area, respectively equal to 0.2 and 0.22 μm^2,

- all the geometries exhibit a large ductility with plastic deformation reaching the maximum of 14.3% for the 200 nm-thick beams. A very close value (14.1%) is obtained for the 360 nm-thick specimen, while the maximum deformation for the 110 nm-thick beam is equal to 11.8%,
- strain hardening is present for all geometries.

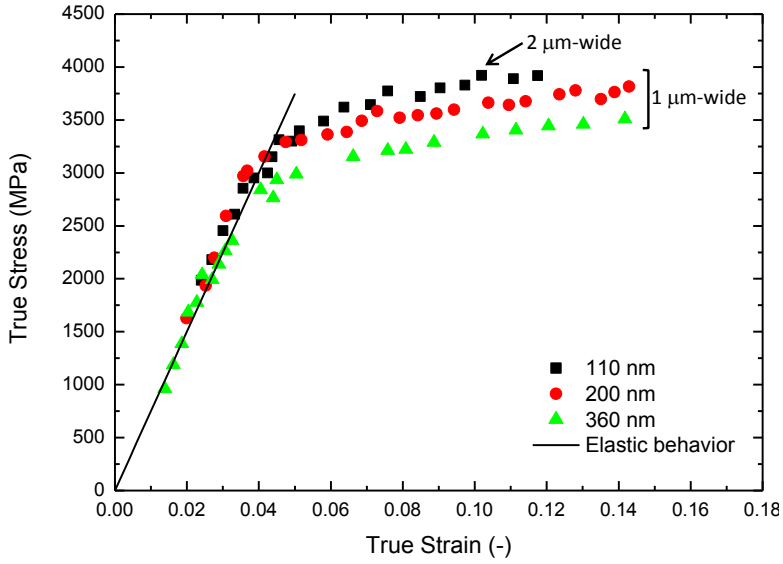

Figure 4.16 *– Overall stress-strain curves for 110, 200 and 360 nm-thick specimens until fracture. The beam width is indicated in the graphs, while the beam length is equal to 25 μm.*

As already been discussed, a preliminary analysis of Figure 4.16 can be drawn by considering the trend of elastic modulus. As a matter of fact, *E* does not depends on the specimen geometry (width, thickness and length) while being constant and equal to 72 GPa. This results is perfectly in agreement with the measurements conducted by Brillouin spectroscopy and picosecond ultrasonics (section 3.3a). Once again, the fact that *E* is constant might indicate that there is no effect of film geometry on the atomic structure in terms of Zr-Ni bonds and free volume content (section 3.3). Moreover, this is also verified for the 110 nm-thick films which have not been investigated by Brillouin spectroscopy and picosecond ultrasonics. Furthermore, in section 4.1.1 we have shown that $Zr_{65}Ni_{35}$ films with different thicknesses have the same activation volume which is strongly related to the STZ size (loosely packed regions) [55], further justifying the claim that there are no geometrical effect on the atomic structure.

a) Size effects on yield strength

Figure 4.17 reports the evolution of the yield strength (σ_y) as a function of the cross-sectional area. It can be noted that σ_y increases when reducing the cross-sectional area following an "hyperbolic" trend (dotted line). Specifically, σ_y evolves from values very close to the Zr-based BMGs (1700-1800 MPa) for a specimen of 360 nm-thick and 4 μm-wide (1.44 μm^2) up to values slightly above the ideal yield strength (cross-section of 0.2 μm^2) whose range is in between 3050 and 3250 MPa (dash-dotted line) [110]. An ideal yield strength of 3170 MPa (solid line) has been calculated using the Johnson and

Samwer model [101], recently implemented by Cheng and Ma [100]. Specifically, using equation 1.10 in section 1.6 and considering a crystallization temperature (T_x) equal to 745 K (section 3.4), we obtain an ideal elastic deformation of 4.4% which gives an ideal yield strength of 3170 MPa.

As already discussed in the previous sections, a thorough analysis of σ_y reveals that it is not determined by the single dimension (width or thickness), but it is dependent on the cross-sectional area (Figure 4.17). Note for instance that different beam geometries produce the same σ_y. This is the case of 0.2 and 0.22 μm^2 beams described in Figure 4.16, but also for 0.4 and 0.44 μm^2 beams (2 μm x 200 nm and 4 μm x 110 nm) as well as of 0.72 and 0.8 μm^2 (2 μm x 360 nm and 4 μm x 200 nm). The effect of the length is represented by the scatter of the data at fixed cross-sectional area, justifying the claim that σ_y is length-independent. Hence, it can be deduced that the real parameter which dictate the yield strength is the cross-sectional area. However, our results differ from the literature since our beams deform *homogeneously* even if large cross-sections and lengths are involved. For instance, a 2 μm-wide beam with a thickness equal to 360 nm (cross-sectional area equal to 0.72 μm^2) and a length of 50 μm reaches a total deformation of 9.5% (2.4% elastic + 7.1% plastic strain, Figure 4.11b red circles). In the case of a 4 μm wide beam with a thickness of 110 nm (cross-sectional area equal to 0.44 μm^2) and a length of 50 μm, the total deformation is equal to 9.7% (2.8% elastic + 6.9 plastic deformation, Figure 4.14c red circles). In both cases, larger fracture strains should be expected since the actuator geometry does not allow to reach fracture. Considering Figures 4.11, 4.13, and 4.14 several other examples can be made. Remarkably, in all cases, the deformation occurs homogeneously with no detectable formation of shear bands or necking (Figure 4.15).

These results are new with respect to the literature. As pointed out in section 4.2, the investigated specimens have a much larger volume with respect to the data reported in literature involving size effects (i.e. compression test of micropillars and for *in-situ* TEM tensile tests). Furthermore, it is surprising that a micrometer-scale TFMG has a yield strength equivalent to a BMG (1700-1800 MPa), but exhibiting plasticity without inhomogeneous failure via shear bands formation. This fact is remarkable considering also that the applied stress is pure uniaxial tension.

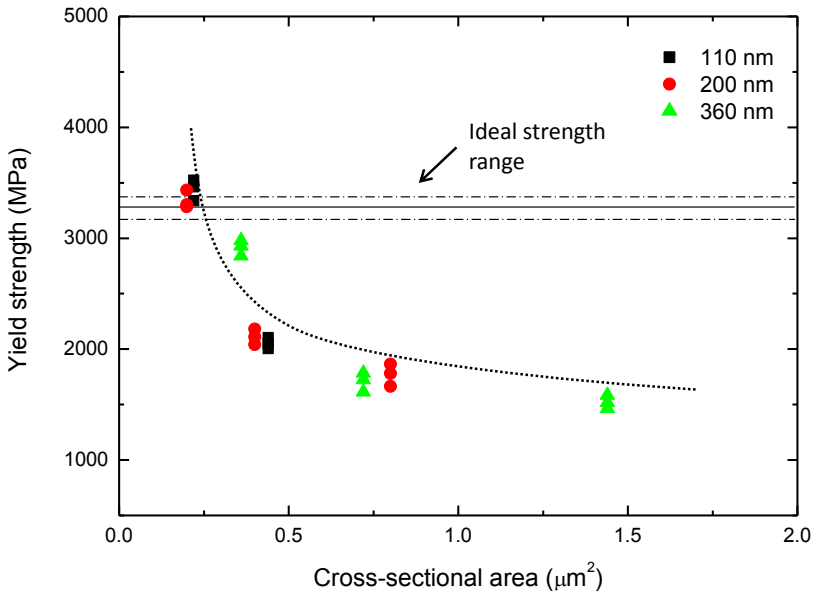

Figure 4.17 *– Evolution of the yield strength as a function of the cross-sectional area of the beam. Small cross-section exhibit an elastic limit close to the ideal one (indicated by dash dotted lines), while large cross-section have value very close to Zr-based BMGs. The dotted line is a guide to the eyes.*

Jang and Greer [110] explain the evolution of the yield strength in the case of tension test on micropillars by showing a trend similar to Figure 4.17. They suggest that plastic deformation occurs if the diameter of the pillars is below a critical threshold (≤ 100 nm) which corresponds to a homogeneous deformation with an ideal strength close to the ideal one (see the schematic reported in Figure 1.41). When the sample size is below this thickness threshold, STZs cannot percolate to produce a mature shear bands, leading to a homogeneous deformation involving local dilatation with the generation of free volume in the entire specimen (section 1.6 and Shimizu *et al.* [48]). On the other hand, they claim that pillars having a diameter above the critical threshold require less stress for the activation of shear bands (percolation of STZs) leading to an inhomogeneous deformation characterized by the development of shear bands. However, while they show a homogeneous deformation for small diameter pillars, they report only a very low decrease of σ_y with increasing the size and no evidence of inhomogeneous shear bands-mediated fracture are reported. In our case, we found a homogeneous deformation under tensile stress even for large specimen cross-sections (up to 1.44 μm^2) and lengths (up to 100 μm), but with a clear drop in the yield strength (Figure 4.17). This means that the geometrical confinement effect influences the plastic behavior of TFMGs even at larger length scales.

A more in-depth analysis of the reported phenomena in Figure 4.17 can be understood by fitting the data with the Griffith's crack propagation criterion which has been used to model the evolution of the yield strength in the case of compression or traction test of micropillars [3, 4, 102, 110]. Volkert *et al.* [102] and Jang and Greer [110] plot σ_y as a function of the pillar height (i.e. the pillar diameter multiplied by the aspect ratio). For our beams which do not have a cylindrical symmetry and with a σ_y independent with the length, we plot σ_y versus the square root of the cross-sectional area, which can be considered as an "average" characteristic length (Figure 4.18). In this context the application of Griffith's criterion states that the stress required to propagate a pre-existing shear band is:

$$\sigma = \sqrt{\frac{2^{3/2}\Gamma E}{\sqrt{A}}} \tag{4.7}$$

where Γ is the shear band energy (J/m^2), E is the elastic modulus [3, 4, 102, 110]. Figure 4.18 shows a good fit with of the experimental data. Moreover, by fixing the elastic modulus equal to 72 GPa, Γ is found equal to 16.5 J/m^2, a value very close to the 11 J/m^2 reported for the shear band energy [102, 110]. This means that Griffith's crack propagation model explains the decrement of the yield strength for larger cross-sections in terms of the ease of activation and percolation of STZs, which are more numerous for larger cross-sections. However, for the investigated beam geometries, we do not observe any evidence of inhomogeneous deformation for large cross-sections and a ductile-to-brittle transition does not occur. Notwithstanding, since Zr-based BMGs have a brittle-like macroscopic behavior in tension (section 1.5.3) a threshold transition should be expected, but at much larger length scales with respect to the investigated ones. Moreover, it is worth noting that for our specimens, the presence of a critical threshold which dictate the macroscopic deformation behaviors $(\sqrt{A})^*$ is meaningless. However, this threshold can be used to predict the critical length scale below which the ideal yield strength is reached (Figure 4.18). For low cross-sectional areas the reduced number of STZs limit their percolation to activate macroscopic yielding and thus reaching the ideal strength which also implies a homogeneous deformation with large plastic strain.

Hence, on the basis of the presented results, a clearer explanation of the physics behind the reported size effects can be drawn. First, we might assume that TFMGs have the same atomic structure in terms of Zr-Ni bonds as indicated by the constant elastic modulus (72 GPa), the density and the all the elastic constants (section 3.3a). Moreover, in section 4.2.5 we will show that films have the same activation volume which possibly indicate that size of the elementary units which carry plasticity in

metallic glasses (STZs) is constant as well. This observation can be supported by the constant value of the fragility index (section 3.3a). Hence, we might assume that the specimens have roughly the same atomic structure and the same size distribution of STZs size.

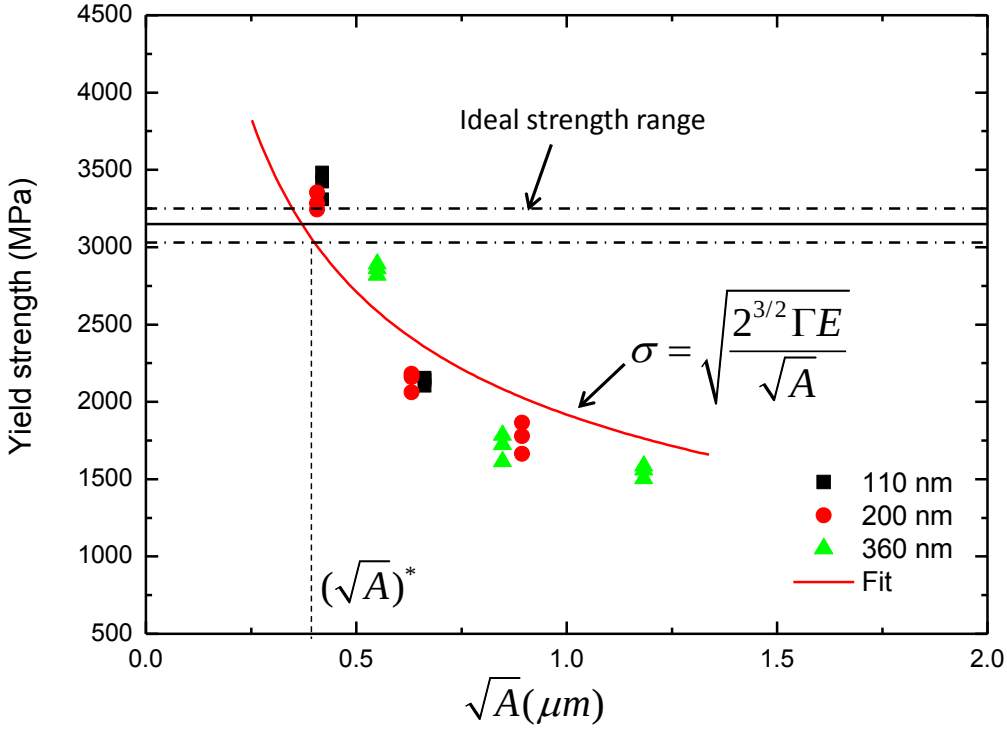

Figure 4.18 *– Evolution of the yield strength as a function of* $\sqrt{A}$*. The Griffith's model (solid red line) accurately fits the data, describing the decrement of the yield strength for large cross-sections.*

For these reasons, the observed changes in the yield stress as a function of the cross-sectional area should be considered in terms of the number of potentially activated STZ which is reduced for small cross-sections. This leads to an enhancement of the yield strength (close to the ideal one) since an higher stress is required for their percolation to form a mature shear band which explain the large plasticity and the homogeneous deformation. Larger cross-section required a reduced stress for yielding due to the ease of percolation of numerous STZs. However, the presence of multiple events of local shearing (STZ operations) leads to plasticity and homogeneous deformation as well. This fact can be sustained by the large fragility index (section 3.3a). Note also that the investigated specimens do not have macroscopic defects such as voids that act as stress concentrators and potential sites for the nucleation of shear bands and they can be considered as a nearly perfect metallic glasses, thus explaining the large plasticity encountered in large cross-section as well.

b) Size effects on strain hardening

To sustain the previous conclusion we analyzed the evolution of the strain hardening coefficient (*n*) as a function of the cross-sectional area (Figure 4.19). This coefficient has been extracted by fitting the trend of the plastic deformation with a Hollomon equation, section 4.2.1. Clearly, Figure 4.19 shows that *n* increases from values close to 0.05 up to 0.14, respectively for small and large cross-sections.

Note also the effect of the beam length, which is represented by the scatter of data at fixed cross-section, is almost negligible.

The fact that *n* is reduced for small cross-sections might be related to the lower tendency of these beams to activate STZ operations and local dilatation due to the reduced number of STZs. On the other hand, a high *n* can be related to a local atomic structure is more prone to activate shear transformation events whose interactions lead to an increment of strain hardening coefficient. However, the exact physical mechanism is not known, but an high *n* means that it becomes increasingly difficult to deform the specimen after yielding. This observation can be sustained by considering a greater number of STZs present in large cross-sections coupled with the high fragility index, which, in turn, might explain the presence of a homogeneous plastic deformation for large cross-sections as well.

Lastly, note that only Tian *et al.*[114] reported in the literature the presence of strain hardening for TFMGs, but using a much smaller beam size (section 4.2). The trend that we have shown here is quite unique and possibly creating new insight into the size-effect study of small scale metallic glasses, so far different for the bulk counterparts.

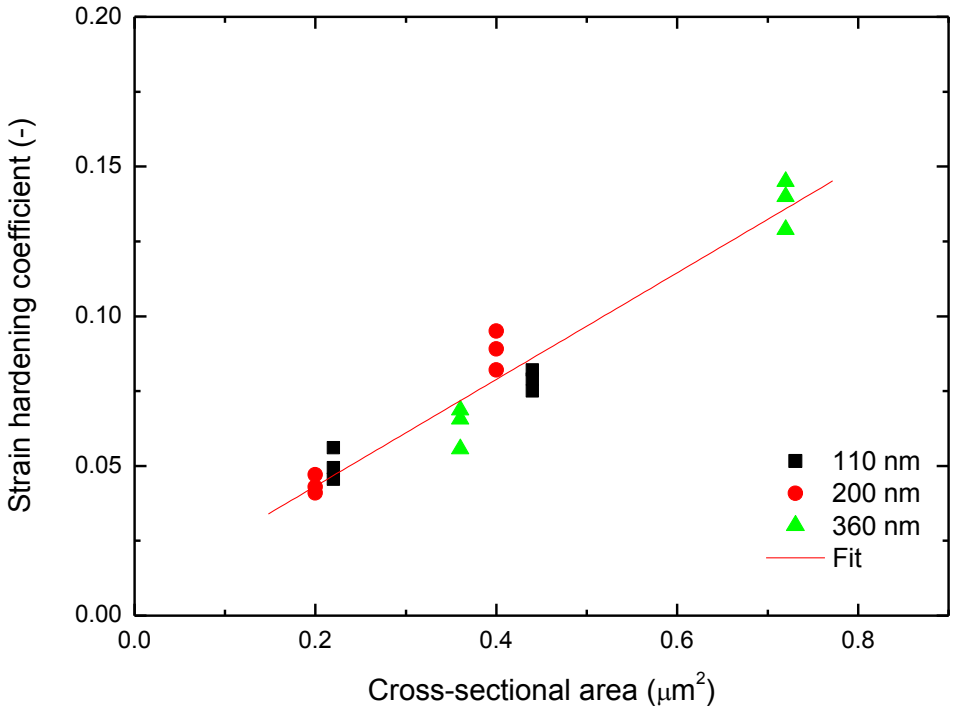

Figure 4.19 *– Evolution of the strain hardening coefficient as a function of the cross-sectional area.*

4.2.5 Viscoplastic behavior

In sections 4.1.1c and 4.1.2 we focused on the viscoplastic properties of TFMGs by using nanoindentation extracting the rate sensitivity of hardness and the activation volume carrying out the tests at different loading rates, using the methodology described in section 2.6.

The viscoplastic properties of TFMGs have been investigated by using the lab-on-chip technique as well. Specifically, for a particular test structure, once a stable position is reached in the force-displacement diagram (section 2.8.1), stress relaxation takes place with a kinetics depending on

the thermally activated deformation mechanisms related to the material microstructure and thickness [144, 146]. The test conditions with the lab-on-chip technique correspond to a creep test performed on a material attached to a spring. Figure 4.20 shows the schematic behaviour of one $Zr_{65}Ni_{35}$ specimen beam. Before the release step, the force (F) inside the actuator is maximum (F_0). If this actuator is released alone without being attached to the specimen beam, the force would be zero and the actuator would reach the u_{free} position. When the system actuator-sample is released, it reaches force equilibrium. As the actuator does not relax (as verified by measuring the displacement of test structures made of a SiN actuator over long periods of time [144]) the way this equilibrium evolves is due to the relaxation of the specimen beam (red dots in Figure 4.20).

The relaxation experiment is performed by measuring deformation at different time intervals (t_n). Both stress and strain vary with time. The strain rate sensitivity m (equation 4.8) and the apparent activation volume V_{app} (equation 4.9) can be extracted by following the stress-strain evolution of the specimen beams as

$$m = \frac{\partial \ln \sigma}{\partial \ln \dot{\varepsilon}_p} \ , \tag{4.8}$$

$$V_{app} = MkT \frac{\partial \ln \dot{\varepsilon}_p}{\partial \sigma} \ , \tag{4.9}$$

where σ is the stress in the beam, $\dot{\varepsilon}_p$ the plastic strain rate, M the so-called Taylor factor, ($\sqrt{3}$ for metallic glasses [41, 55]), k the Boltzmann constant, and T the temperature.

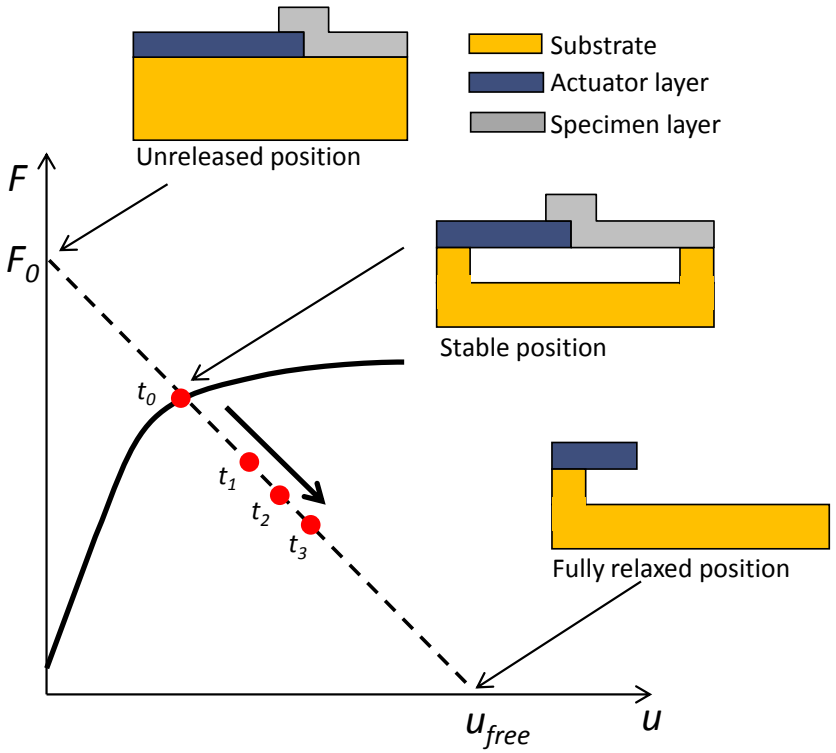

Figure 4.20 *– Force-displacement diagram for the actuator and the specimen beams with the equilibrium point attained during the release and three relaxation points (red dots). Adapted from [144].*

After successive measurements of one specific structure inside a SEM (section 2.8.1), the displacements (u) evolution with time is obtained. Hence, using equation 4.5, the time evolution of the total strain ε^{mech} and stress σ is obtained. The plastic strain is obtained by subtracting the elastic strain (σ/E) from the total strain. Then, the plastic strain rate is calculated by derivation with time, and finally the derivative of the plastic strain rate by the stress is performed [144]. However, as a first simple mean to analyse the displacements u versus time t data, a logarithmic variation is assumed in the form:

$$u(t) = A_1 \ln(A_2 t) \ , \tag{4.10}$$

where A_1 and A_2 are fitting parameters. As a matter of fact, imposing a logarithmic variation of u with t leads to a constant average activation volume independent of time.

We selected 4 time intervals to analyse stress relaxation, respectively t_0, t_1, t_2 and t_3 (Figure 4.20). Specifically, t_0 corresponds to the as released beams after a 3 hours' time – which approximately corresponds to the etching stop phase and the critical point dryer (section 2.8.2) – while t_1, t_2 and t_3 are different time intervals up to 51 days after the releasing. This choice has been dictated by the logarithmic kinetics of stress relaxation and to measure a significant variation of displacement (u).

Figure 4.21 shows the relaxation behavior of 25-μm long specimens with a thickness equal to 360, 200 and 110 nm, respectively (a), (b), and (c). Figure 4.21a-b shows the case of 1 μm-wide beam, while in (c) is reported a 2 μm-wide beam.

An in-depth analysis of Figure 4.21 reveals that:

- the relaxation phenomenon takes place only for stress larger than the yield stress. As a matter of fact, a very small scatter in the data is found in the elastic regime and mainly due to statistical errors when measuring the displacement in the SEM,
- the stress decrement due to relaxation follows a logarithmic kinetics. The stress drop is enhanced after the first week, while there is only a slight decrement after longer time (i.e. 51 days),
- the relaxation is slower when reducing the film thickness. For instance, the 360 nm-thick film (Figure 4.21a) shows higher relaxation kinetics (note the large gap in data from the as released and after 7 days), while for a similar temporal interval (8 and 11 days) the relaxation is reduced for the 200 and the 110 nm-thick specimens (Figure 4.22b-c).

The previous reported analysis can be applied also for other beam lengths and widths (Appendix B), revealing very similar trends.

Since relaxation takes place only after yielding, namely when the specimen is plastically deformed, a second independent estimation of the yield strength can be performed. Figure 4.22 shows the plot of the derivative of the displacement versus time divided by the length $(du/dt)/l$ as a function of the stress.

Specifically, in Figure 4.22 the specimen width is equal to 1 μm for 360 and 200 nm-thick beams (a) and (b), while it is equal to 2 μm for the 110 nm-thick specimen (c). Different lengths are examined as indicated in the inset of the Figure 4.22. During the elastic period (Figure 4.21) there is only a slight change in the measurement of the stress as a function of the time leading to $(du/dt)/l$ oscillating around zero. On the other hand, when relaxation takes place, $(du/dt)/l$ increases following a straight line. Hence, the yield strength can be estimated as the stress at interception of two lines, the first one $(du/dt)/l = 0$ and the second one which consider the relaxation. This result has been shown in Figure 4.22 for 25 μm-long beams.

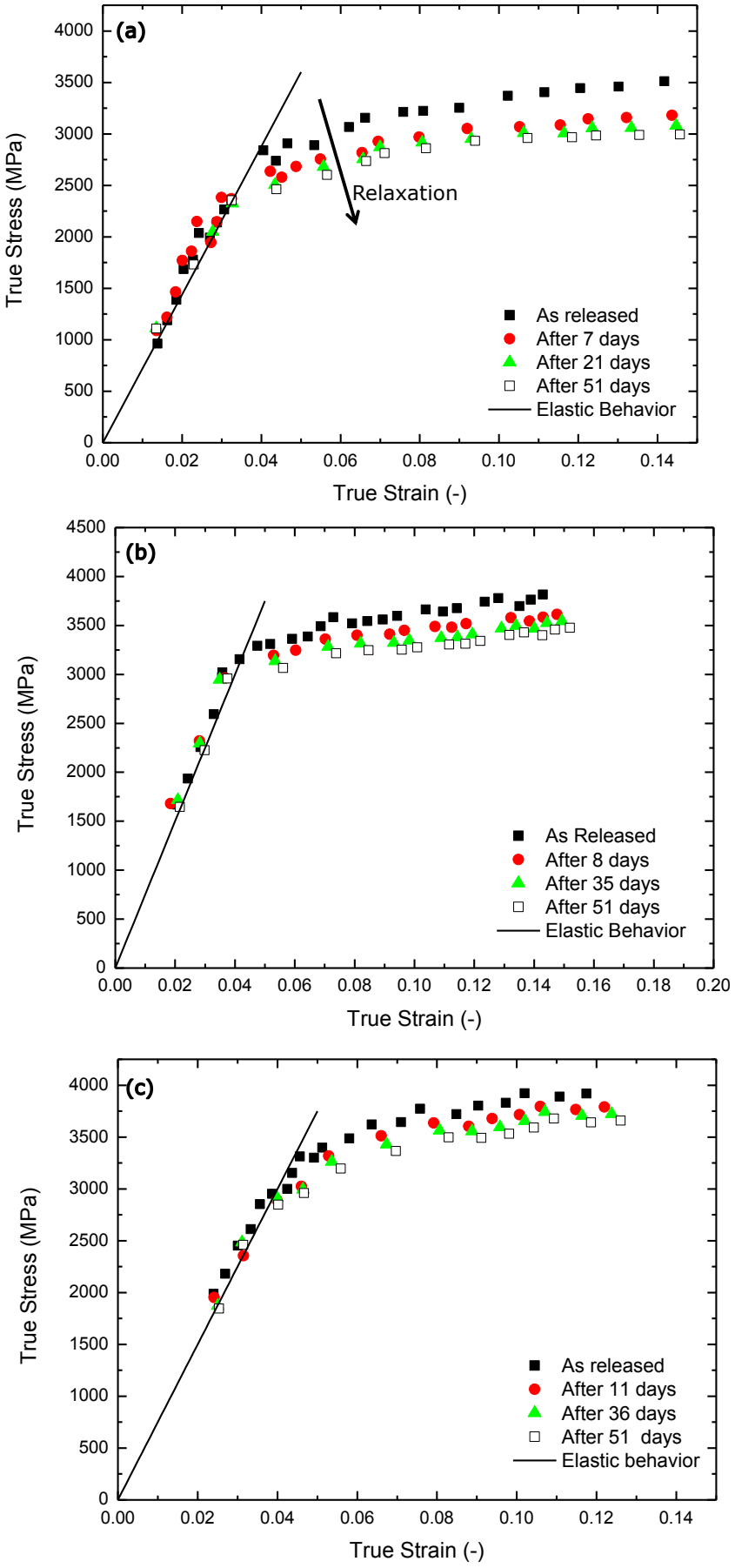

Figure 4.21 *– Stress relaxation for 360, 200, and 110 nm-thick beams, respectively (a), (b), and (c). The beam length is fixed and equal to 25 μm, while the width is 1 μm for (a) and (b), and 2 μm for (c).*

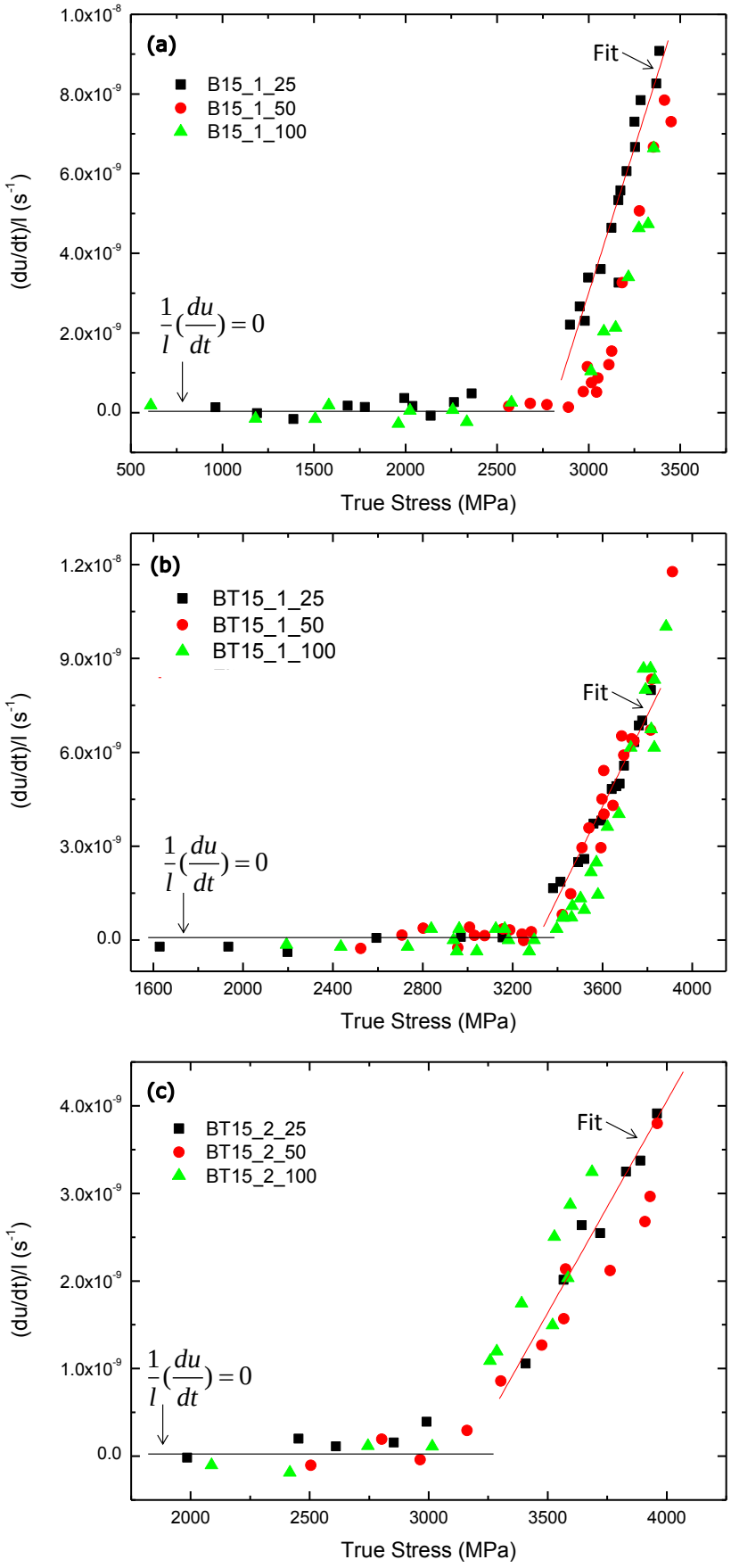

Figure 4.22 *– Plot of* $(du/dt)/l$ *as a function of the stress for a 360, 200, and 110 nm-thick specimen, respectively (a), (b), and (c). The specimen width is equal to 1 μm in (a) and (b) and 2 μm in (c). The fitted line for the 25-μm long beams is highlighted.*

Table 4.3 reports a comparison of the measure of the yield strength for the specimens in Figure 4.22 using two methods. The first one considers σ_y as point that deviates from the elastic behavior, while in the second method σ_y is calculated as the interception of two lines during relaxation experiments (Figure 4.22). Note the excellent agreement between both methods. This shows that the relaxation and plasticity mechanisms constitute one single phenomenon.

Specimen name	**Thickness (nm)**	**Cross-sectional area (μm^2)**	**σ_y tensile curves (MPa)**	**σ_y relaxation stress (MPa)**	**Difference (%)**
B15_1_25	360	0.36	2840	2778	2.20
B15_1_50	360	0.36	2931	2941	0.34
B15_1_100	360	0.36	2981	2969	0.40
BT15_1_25	200	0.2	3282	3275	0.21
BT15_1_50	200	0.2	3302	3338	1.1
BT15_1_100	200	0.2	3432	3429	0.10
BT15_2_25	110	0.22	3338	3278	1.80
BT15_2_50	110	0.22	3523	3504	0.54
BT15_2_100	110	0.22	3463	3476	0.37

***Table 4.3** – Estimation of the yield stress as a deviation from the elastic behavior or as the intersection of two lines after relaxation.*

Figure 4.22 also shows that the relaxation follows different kinetics depending on the level of plastic deformation involved. This fact is partly visible in Figure 4.21 as well. Specifically, it can be noted the $(du/dt)/l$ is not constant, but it increases at higher stress values meaning that the relaxation kinetics are enhanced for larger plastic deformations.

The extraction of the activation volume by exploiting specimen relaxation has been performed for different beams geometries as well as by considering the relaxation occurring for beams with the same geometry, but subjected to different stress levels, namely involving a change of the actuator length. Figure 4.23 shows the evolution of the average displacement as a function of time for a beam set of fixed geometry 25 μm x 1 μm x 360 nm, which corresponds to points in Figure 4.21a. The four different time intervals are respectively equal to 3 hours, 7 days 21 days and 51 days (Figure 4.21a). In Figure 4.23, full symbols correspond to beams that deform elastically without relaxation, while empty symbols correspond to beams which have been deformed plastically relaxing with time. The test number in the inset of Figure 4.23 indicates the number of the beam. The higher is the number, the higher is the deformation in the specimen. Figure 4.23 shows that the relaxation kinetics exhibits a logarithmic behavior as expected (equation 4.10). The data fitting with equation 4.10 (solid lines) is good ($R^2 > 0.988$) allowing the extraction of the coefficient A_1 and A_2 used for the calculation of the

average activation volume (equation 4.10). All other beams have the same relaxation kinetics (see the Appendix B).

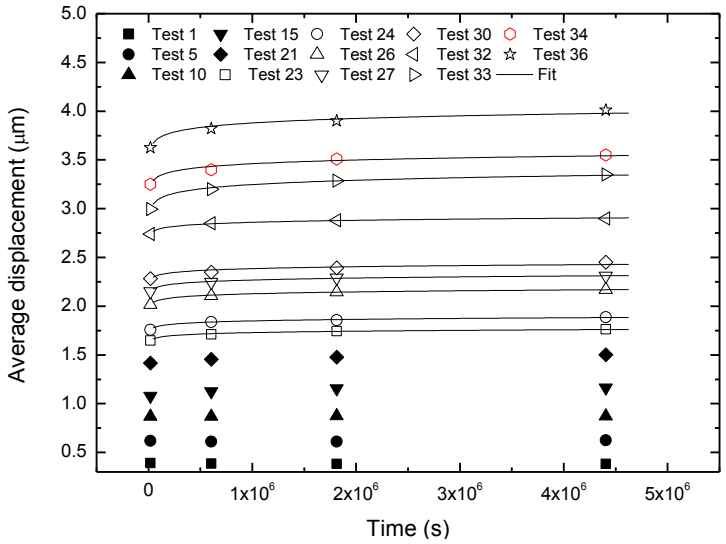

Figure 4.23 *– Average displacement vs time for a beam of 25 μm x 1 μm x 360 nm. Plastically deformed specimens (empty symbols) relax following a logarithmic kinetics as shown by the fitting lines using equation 4.10.*

Figure 4.24 shows the results of the average activation volume. Specifically, Figure 4.24a reports the evolution of the activation volume (V_{act}) as a function of the actuator length thus involving different stress and strain levels in the beam. The longer is the actuator, the higher is the stress produced in the beam (equation 4.5). Figure 4.24a reports the results for 25-μm long beams with different thicknesses and widths (see the inset), but analogous trends can be drawn for other beam lengths (Appendix B). It appears clear that for a fixed beam geometry, the activation volume is roughly constant, meaning that, although different stress and strain levels are involved, the elementary mechanisms activated are the same. Furthermore, even if there is a scatter between different beam geometries, the average activation volume is always between 100 and 200 $Å^3$. The value agrees with the results of nanoindentation reporting $V_{act} \sim$ 120-130 $Å^3$ (section 4.1.1c) even if a different loading configuration is involved. The overall data plotted as a function of the cross-sectional area are reported in Figure 4.24b, showing a slight variation with a value in between 100 and 200 $Å^3$, again in agreement with nanoindentation results.

The analysis of the viscoplastic behavior of $Zr_{65}Ni_{35}$ TFMGs by using the lab-on-chip technique provides some novel insight into the physics of deformation in these materials, while strengthening the results reported in section 4.2.4.

At first, we have to mention that – to the best of our knowledge – there are no studies which involve the analysis of relaxation phenomena of TFMGs. One key advantage of the lab-on-chip technique is that specimens stay attached to the actuator leading to stress relaxation over time without the use of other instruments. This kind of measure is difficult with compression test of micropillars or *in-situ* TEM tensile test. A change in local atomic arrangement due to stress relaxation is expected for metallic glasses which exhibit a liquid-like atomic structure (details in sections 1.1 and 1.2). Relaxation phenomena should be though as atomic redistribution caused by the application of an external stimulus (the stress of the actuator) which lead to free volume generation to best accommodate the imposed stress. Note that even after 51 days there are no evidences of

inhomogeneous deformations involving shear band activity, while all the deformation is homogeneously distributed within the specimen. Interestingly, we found that relaxation takes place only if plastic deformation occurs which corresponds to the activation of the irreversible STZ operations which therefore allow relaxation if a stress is applied. For these reasons, relaxation experiment can be used to estimate the yield strength. A thorough analysis reveals that activation volume is constant in between 110 and 200 $Å^3$, in agreement with nanoindentation. This result strengthens the analysis presented in section 4.2.4. As a matter of fact, a constant value of the activation volume suggests that the geometry of the beam does not affect the atomic arrangement, especially in terms of free volume and STZ size, quantities that are directly related to the activation volume.

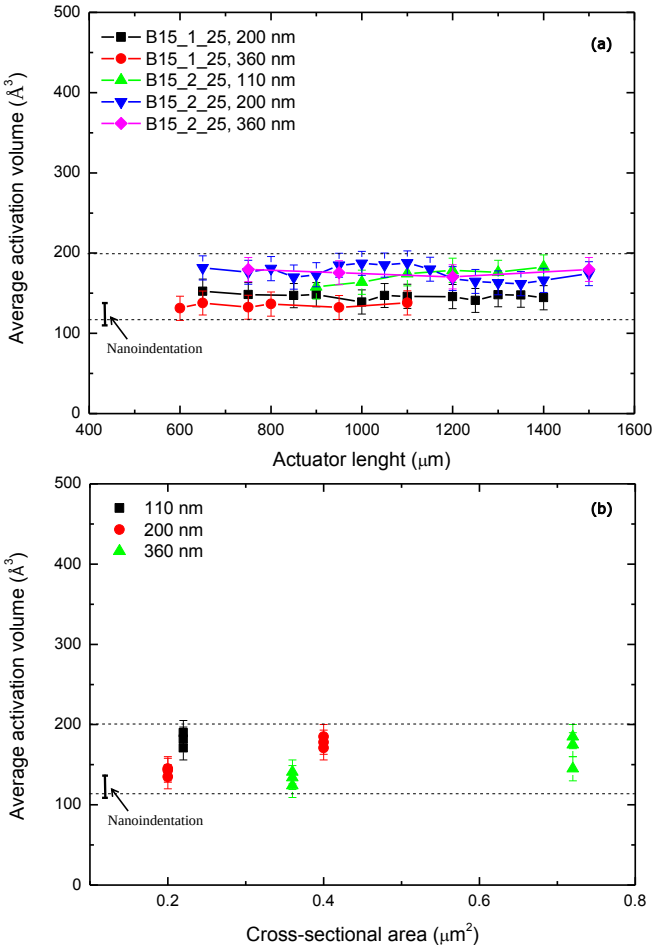

Figure 4.24 *– Average activation volume as a function of the actuator length and cross-sectional area, respectively (a) and (b). The average activation volume is constant and in between 110 and 200 $Å^3$.*

Lastly, it is worth to mention that the applied strain rate with the lab-on-chip is or the order of 10^{-9} s^{-1} with a slightly variation depending on the selected specimen geometry (Figure 4.21). This value is 7 decades slower with respect to the average one imposed by nanoindentation (0.025 s^{-1}). This further proves that the elementary mechanisms which carry plasticity (STZ operations) are the same. Hence, a change in the yield strength or strain hardening coefficient as a function of the cross-sectional area (section 4.2.4) have an *extrinsic* origin related to the enhanced difficulty of activation of STZ events for highly confined geometries (i.e. low cross-sectional areas).

4.3 Conclusion

In this chapter we focused on the elasto-viscoplastic properties of TFMGs by means of nanoindentation and uniaxial tensile test of freestanding beams.

Nanoindentation experiments carried out on different thicknesses for the composition $Zr_{65}Ni_{35}$ have shown an increment of the hardness (both with the CSM method and the standard indentation) for small thicknesses, combined with the enhanced formation of strain bursts and annular shear bands around the indent for large indentation depths on thicker films. This trend has been related to a thickness confinement of shear band formation. On the other hand, TFMGs have the same loading rate sensitivity and, consequently, the same activation volume, suggesting that films have a similar atomic order and free volume content as deduced also in Chapter III by analyzing the structural and elastic properties.

A compositional change involves a variation in hardness, rate sensitivity, and activation volume, increasing also the formation of strain bursts for Zr-rich specimen. These trends may be related to the variation of local order with the formation of Zr-Ni bonds favored for Ni-rich specimens, which also exhibit a larger activation volume in agreement with the enhanced thermodynamic fragility and FWHM reported in Chapter III.

The characterization of mechanical properties of freestanding $Zr_{65}Ni_{35}$ TFMGs has shown that the films can sustain large plastic deformation with the strength reaching the ideal value. Moreover, films are characterized by strain hardening. The yield strength and the strain hardening coefficient scale with the cross-sectional area with the ideal yielding and the lowest strain hardening coefficient reached for smaller cross-sections. On the other hand, larger cross-sections involve a drop of the yield strength (down to the expected value for a Zr-based BMG), while increasing the strain hardening coefficient. This means that elementary deformation mechanisms (STZ operations) are easily activated for larger cross-section. However, specimens do not fail via inhomogeneous deformation (i.e. shear bands), but homogeneous deformations is the leading mechanism independently on the cross-sectional area. While for small cross-sections the homogeneous deformation is related to the difficulty to activate the smaller number of dispersed STZs (leading to a yield stress close to the ideal value), for larger cross-section it is easier to activate STZs operations due to their higher number (reduced yield stress), but their interactions do not allow the generation of a single shear band event which can cause a catastrophic failure and thus leading to homogeneous deformation.

Once again, we stress the fact that one of the novel element of our analysis that is represented by the dependency of σ_y on the cross-sectional area (width times thickness) and not on a single dimension (i.e. the thickness). We successfully modeled this variation using the Griffith crack propagation criterion, strengthening the previous reported analysis.

The analysis of stress relaxation on freestanding beams has been provided to in-depth understand the viscoplastic behavior. It has been shown that relaxation takes place only if plastic deformation occurs, while the extracted average activation volume is constant and in between 110 and 200 $Å^3$. This evidence further indicates that films have the same atomic structure which is independent on the beam geometry. Hence, we suggest that the yield strength variation may be related to a change in STZ number for different cross-sections whose percolation control the yielding value.

Chapter V – Fracture of ZrNi thin film metallic glasses

In this chapter, we address the fracture behavior of ZrNi thin film metallic glasses (TFMGs). The fracture mechanisms for the bulk counterparts (BMGs) have been presented in Chapter I section 1.5.7, providing some key elements to understand the results in the case of thin films. Moreover, section 1.5.6 reports the tribological properties of BMGs and TFMGs analyzing the scratch behavior, which will be investigated for ZrNi TFMGs as well.

Here, we first present the results for the scratching of ZrNi TFMGs by investigating the effect of the thickness (700 and 300 nm), of the composition ($Zr_{65}Ni_{35}$ and $Zr_{85}Ni_{15}$), and of the scratching conditions reported in section 2.6.

Secondly, we investigate the fracture mechanisms of TFMGs deposited on a Si substrate using the method described in section 2.7. We model the fracture behavior as a function of film thickness and composition as well as by evaluating the effect of a SiO_2 capping layer covering the TFMGs surface.

Lastly, we analyze the fracture in tension of freestanding $Zr_{65}Ni_{35}$ TFMGs by completing the analysis presented in Chapter IV dealing with the evolution of the yield strength, the strain hardening coefficient and the viscoplastic behavior. We investigate the variation of the fracture strain as a function of the specimen cross-sectional area as well as of the free surface while showing the fracture profiles and the development of shear bands with the aim to improve the analysis reported in Chapter IV.

The objective of this chapter is to provide an extensive overview of the fracture mechanisms occurring in the case of ZrNi TFMGs as investigated by three different techniques.

5.1 Scratch resistance

In this section we analyze the scratch resistance of ZrNi TFMGs. Although there is a potential of TFMGs to be used as wear resistance coatings, there are not many studies dealing with the tribological and wear behavior. A review on this topic can be found in Chu *et al.* [33] and in section 1.5.6.

Here, we analyze the effect of thickness, composition and of the experimental parameters on the scratch resistance of ZrNi TFMGs with a particular emphasis on the scratch morphology and its evolution. As reported in section 2.6 – which summarizes the nanoscratch experimental conditions – two compositions have been studied: the fully amorphous $Zr_{65}Ni_{35}$ and $Zr_{85}Ni_{15}$ which show a dispersion of a crystalline α-Zr phase (section 3.1).

This choice has been dictated by the number of data obtained for $Zr_{65}Ni_{35}$ (Chapters III and IV) as well as by the idea to observe a very different scratch behavior if a fully amorphous structure is compared to a partially crystalline one, instead of comparing two fully amorphous films with a slight change in composition.

The effect of thickness has been addressed for the composition $Zr_{65}Ni_{35}$ involving 300 and 700 nm-thick films. Moreover, the effect of different loading ramps as well as the effect of different scratching velocities has been studied (section 2.6).

a) Effect of thickness and loading rate

Figure 5.1 shows the variation with the scratch distance of the coefficient of friction (COF), the loading and recovery curves and the scratch morphology for a 300 nm-thick film. The scratching has been conducted over a total length of 180 μm with a normal force linearly increasing from 0 up to 60 mN (0.33 mN/μm), while the scratch velocity was equal to 30 μm/s (section 2.6).

A convenient way to analyze the scratch results is to compare the COF evolution (Figure 5.1a) with the scratch morphology (Figure 5.1c). Specifically, it can be noted as follows:

- at the beginning of the scratch (zone 1), the COF increases from 0 up to 0.31, this corresponds to the tip gliding over the film under small almost elastic penetration as related to the high loading recovery, see zone 1 in Figure 5.1b. The inset 1 in Figure 5.1c shows the presence of few barely visible cracks,
- afterwards, the COF reaches a plateau with a constant value around 0.31-0.32. This corresponds to the film scratching involving plastic deformation and the formation of lateral cracks with a spacing that reduces when increasing the load, see the inset 2 of Figure 5.1c. Cracks develop with an angle in between 41 and 48° with respect to the scratch direction,
- if the normal load further increases, there is a reduction of the COF down to 0.21 (zone 3). This reduction is related to a decrement the lateral force. Note that the COF is defined as the ratio between the lateral and the normal force, with the last one increasing during the scan length. This means that the TFMG opposes a proportionally reduced resistance to the indent penetration and forward displacement, as justified by the intense cracking formation which increases in length and branching. Cracks are oriented at an angle in between 41 and 48°, then they follow the scratch direction (see the inset 3 of Figure 5.1). The maximum length of the entire crack is around 0.8 μm,
- when the penetration of the tip gets close to the interface with the substrate, the COF increases up to 0.3 again (zone 4) and then slightly reduces (zone 5). In zone 4, there is clear evidence of film delamination with the formation of a large lateral pile-up. The substrate scratching can be recognized in the SEM by the darker region in the middle of the scratch (see the inset 5 of Figure 5.1c),
- if the scratch velocity is reduced down to 3 μm/s we observe the same microstructural evolution, indicating that there are no significant effects of the scratching velocity in this range (an example is reported in the Appendix C).

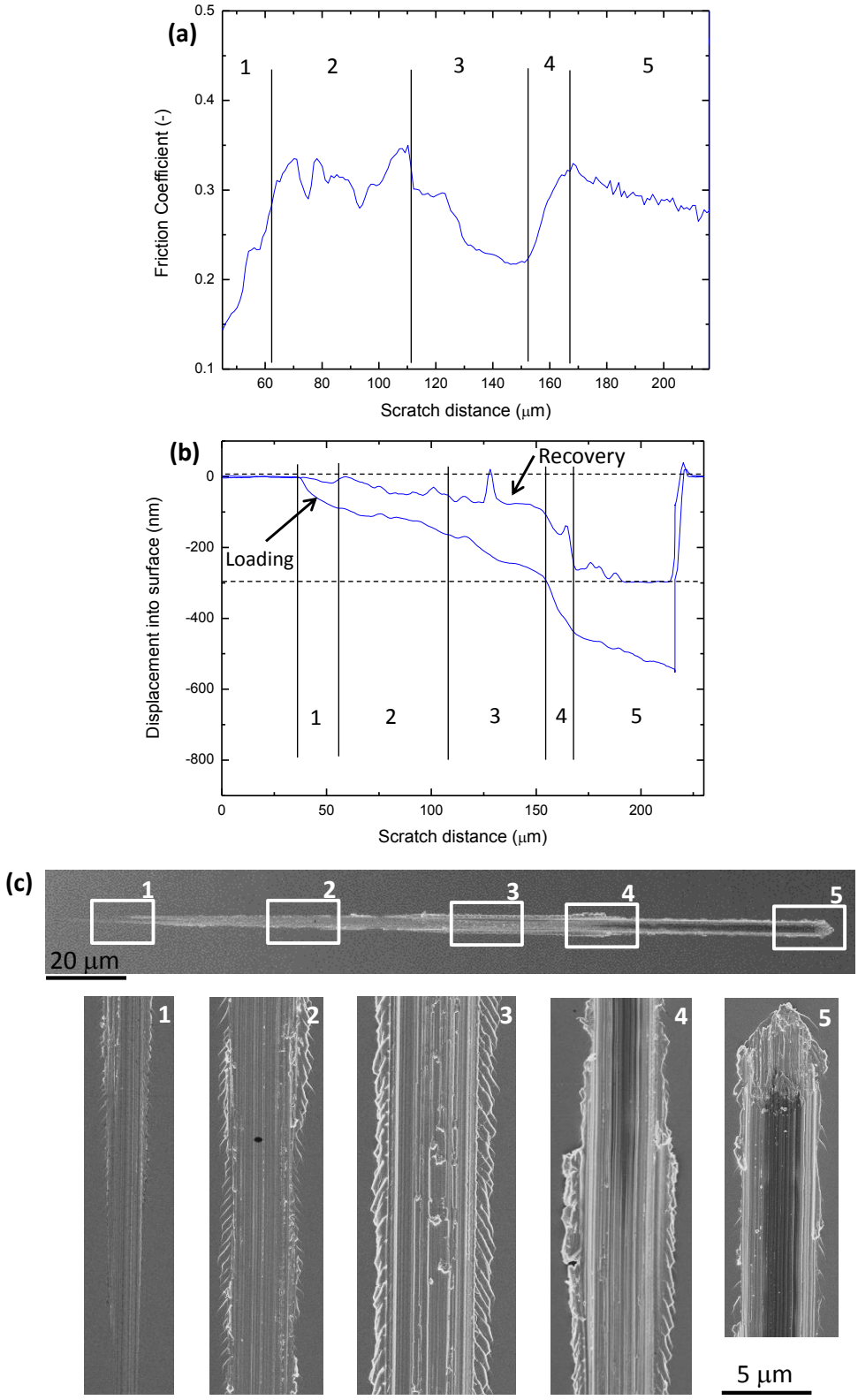

Figure 5.1 *– Evolution of the COF and of the displacement into surface as a function of the scratch distance, respectively (a) and (b); (c) the corresponding scratch morphology. The film thickness is equal to 300 nm. The scratch length is equal to180 μm with the loading increasing from 0 up to 60 mN with a constant velocity of 30 μm/s.*

Figure 5.2 shows the scratching of a 300 nm-thick film, with a different loading ramp. The scratch length is equal to 360 μm, while the normal loading increases for 0 to 60 mN, leading to a

loading increment of 0.17 mN/μm. The scratch velocity is fixed equal to 30 mμ/s, as in Figure 5.1. A longer scratch enables to observe better the morphological evolution which can be related to the COF variations. Specifically, Figure 5.2 shows that:

- at the beginning of the scratch the COF increases up to a plateau around 0.31 (zone 1). This corresponds to the elastic sliding regime and elastic deformation (see the recovery curve in Figure 5.2b). No cracks are observed,
- afterwards, the COF decreases reaching a plateau at around 0.17 (zone 2). Since the normal force linearly increases, this decrement should be attributed to an easier film scratching with the formation of lateral cracks oriented at around 43° with respect to the scratch direction,
- then, the COF sharply increases up to 0.4 followed by a decrement to a value of 0.21 (zones 3 and 4). This corresponds to the formation of more intense cracking, with smaller spacing and branching phenomena. The fact that this COF plateau is at a higher values with respect to the previous one (0.21 vs 0.17) is indicative of higher difficulty to move the tip (increment of lateral force). Cracks are oriented with an angle in between 41 and 48° with respect to the scratch direction and their maximum length is around 0.8 μm,
- close to the interface with the substrate, the COF increases up to 0.35 (zone 5) and then slightly reduces (zone 6). As reported in Figure 5.1, in zone 5, film delaminations are clearly observed with the formation of a large lateral pile-up. The substrate scratching can be recognized on the SEM micrographs by the darker region in the middle of the scratch (see the inset 6),
- if the scratching velocity is reduced down to 3 μm/s, the same microstructural evolution is observed indicating that there are no significant effects of the scratching velocity in this range.

Figure 5.3 shows the scratch of a 700 nm-thick film with the same condition as for Figure 5.1. The scratch length is equal to 240 μm, while the applied normal load range from 0 up to 80 mN, leading to a constant loading rate equal to 0.33 mN/μm. The scratch velocity is equal to 30 μm/s (as in Figure 5.1). Differences in scratch morphology have thus to be attributed to the film thickness and not to the loading condition. A thorough analysis of Figure 5.3 shows that:

- the COF exhibits a constant plateau at around 0.26 (zone 1). This zone corresponds to the elastic regime with the absence of cracks (Figure 5.3c, inset 1). However, when increasing the scratch depth, small cracks are formed and oriented at around 45° with respect to the scratch direction,
- when increasing the load, the COF reaches another plateau at around 0.29 (zone 2). This corresponds to the development of longer cracks (1.5 μm) with reduced spacing (inset 2a in Figure 5.3). Note also that cracks after an initial orientation at around 45° are oriented in the same direction of the scratch. The larger thickness favors lateral pile-up, as seen in the inset 2b of Figure 5.3, partly covering the lateral cracks,
- the initiation of substrate scratching is indicated by the COF increment up to 0.5 followed by the slight progressive decrement (zones 3 and 4). However, contrary to the results presented in Figure 5.1 and 5.2 we do not observe film delamination before reaching the substrate,
- very similar to the results reported in Figures 5.1 and 5.2, there are no morphological variations if the scratch velocity is changed to 3 mN/s.

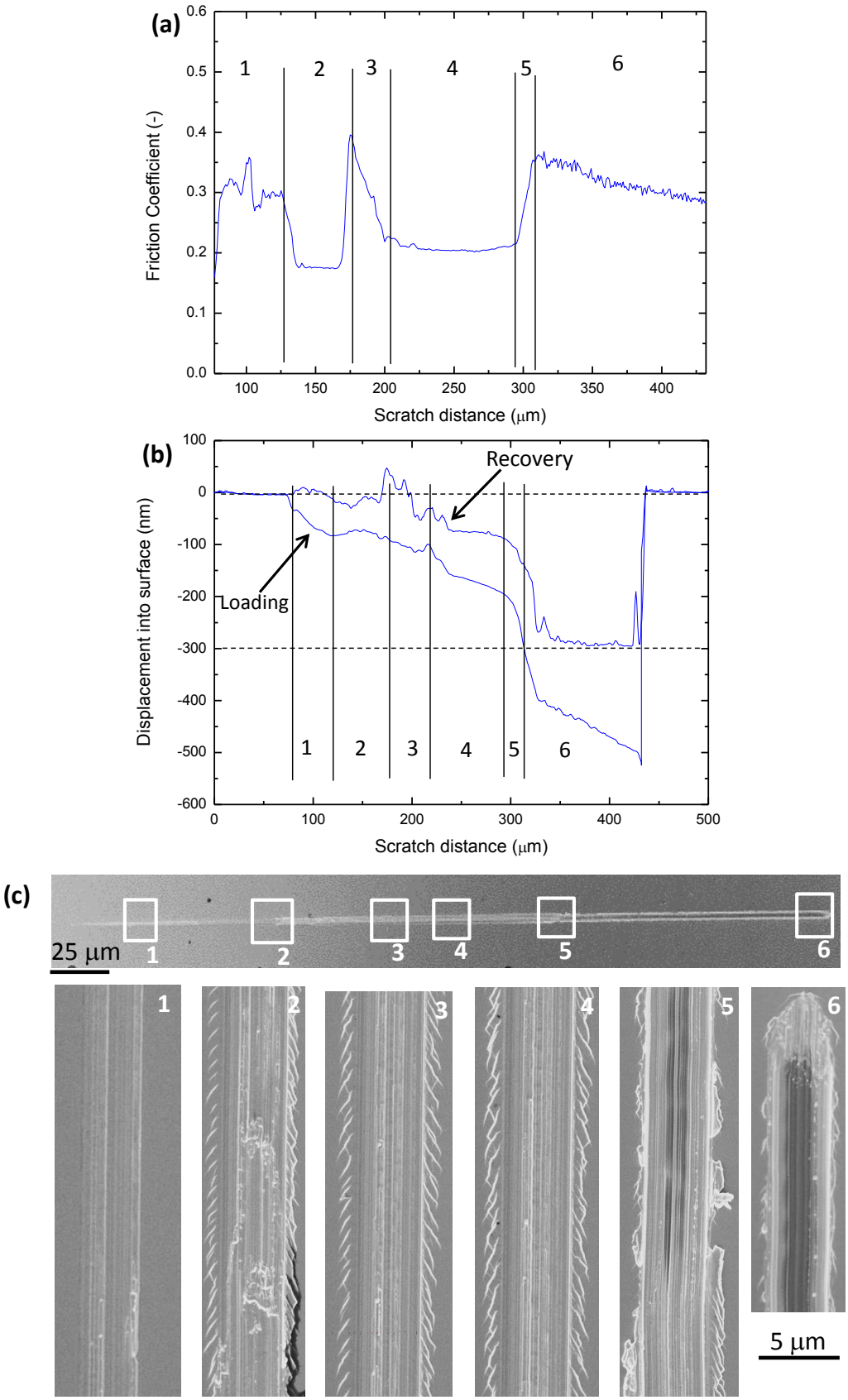

Figure 5.2 *– Evolution of the COF and of the displacement into surface as a function of the scratch distance, respectively (a) and (b); (c) the corresponding scratch morphology. The film thickness is equal to 300 nm. The scratch length of 360 μm with the loading increasing from 0 up to 60 mN with a constant velocity of 30 μm/s.*

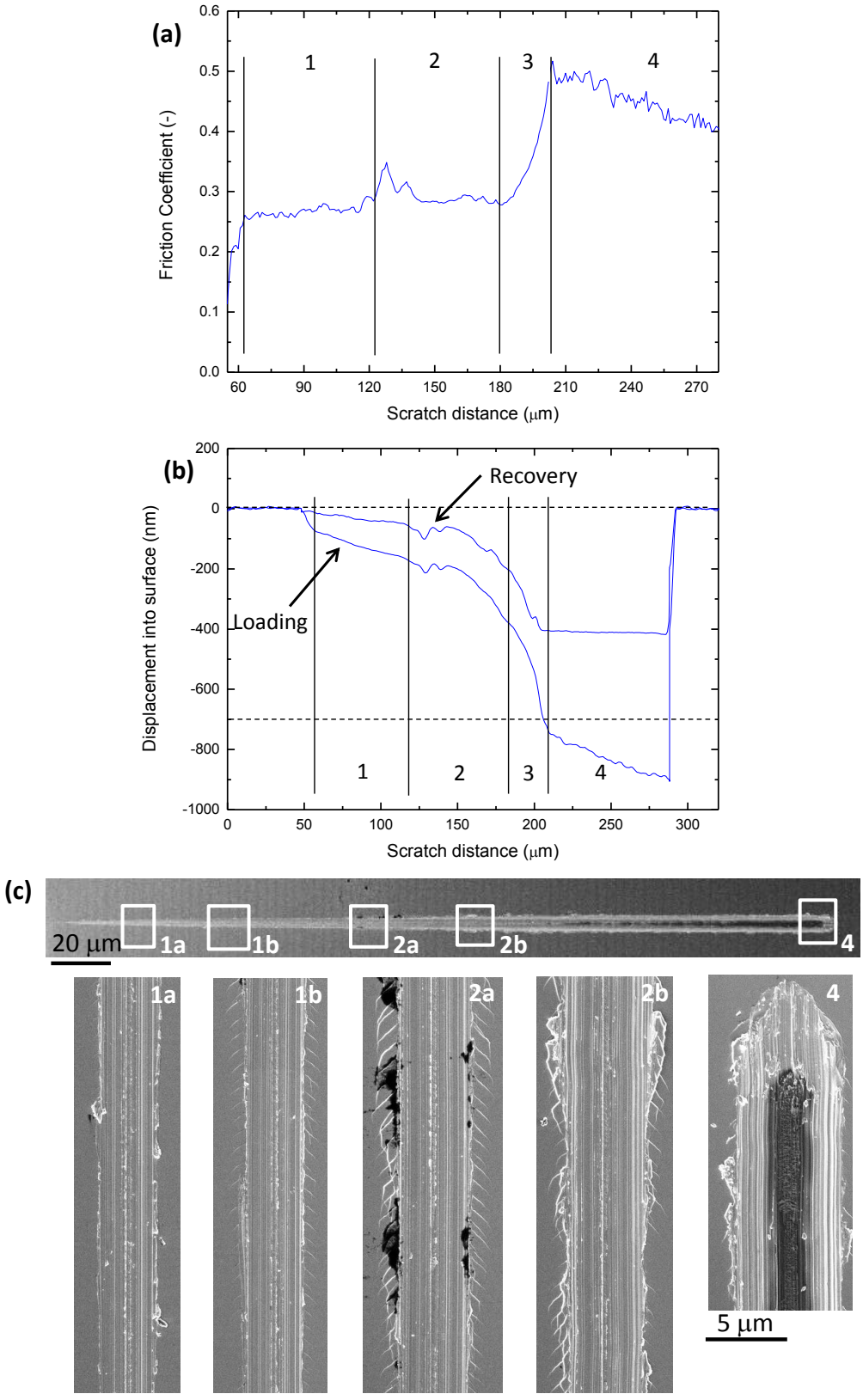

Figure 5.3 *– Evolution of the COF and of the displacement into surface as a function of the scratch distance, respectively (a) and (b); (c) the corresponding scratch morphology. The film thickness is equal to 700 nm. The scratch length is equal to 240 μm with the loading increasing from 0 up to 80 mN with a constant velocity of 30 μm/s.*

The scratch analysis of the 700 nm-thick film has been carried out also with a different loading ramp to reproduce the same as conditions reported in Figure 5.2 for a 300 nm-thick film. Specifically, the scratch has a length of 360 μm and the load ranges from 0 up to 60 mN (0.17 mN/μm), while the velocity has been fixed at 30 μm/s (Figure 5.4). An analysis of Figure 5.4 reveals that:

- the COF is characterized by two plateaus (zones 1 and 2), with an average value around 0.28 and 0.30, respectively. The corresponding morphological evolution starts with the elastic regime without cracking (inset 1a in Figure 5.4c), followed by crack formation (insets 1b and 2). The cracks are oriented at 45° with respect to the scratch direction and their spacing is reduced when increasing the normal load (inset 2). The cracks length increases with penetration depth reaching a maximum length of 1.5 μm,
- there is no film delamination, but an increased amount of pile up as the scratch gets deeper. When the substrate is scratched, the COF increases up to 0.5. Substrate scratching can be recognized by the darker region in the inset 4 of Figure 5.4c,
- as in Figures 5.1, 5.2, and 5.3, there are no morphological changes if the scratch velocity is reduced at 3 mN/s.

There seems to be some thickness effect on the scratch resistance. At first it can be noted that the normal force necessary to scratch the entire film down to the substrate is not proportional with the thickness. As a matter of fact, for a 300 nm-thick film the average normal force is equal to 35 ± 3 mN, while for a 700 nm-thick it is equal to 50 ± 3 mN. This non-linear behavior is indicative of a higher scratch resistance in the case of thinner film and can be explained on the basis of a thickness confinement as the for the increment of hardness obtained by nanoindentation (section 4.1.1). Again, this effect should not be thought in terms of a change of atomic arrangement or free volume content which are thickness independent (Chapters III and IV), instead it is an *extrinsic* effect and related to a thickness confinement. Moreover, a 300 nm-thick film has a reduced value of the lateral force since the COF reaches a plateau around 0.17 (Figure 5.2a). This means that – for a fixed value of normal force – a 300 nm-thick film necessitates of lower force for the tip advancement due to the reduced scratch depth and consequentially the reduced amount of film scratched.

The scratch mechanisms involved are very similar with a limited effect of the loading ramp and the scratch velocity. Specifically, for low scratch depths there is only elastic response followed by cracks formation oriented at around 45° with respect to the scratch direction (as also reported in section 1.5.6 for BMGs). By increasing the normal load, the crack length increases, while decreasing the spacing. Moreover, if the normal load increases, there is a tilt of the crack angle which starts at 45° and then become parallel to the scratch direction (Figures 5.1 – 5.4).

However, the cracks are longer for the 700 nm-thick film (1.5 μm), while being on average almost the half (0.8 μm) for the 300 nm-thick film. The cracks develop at lower normal load for thicker film, again indicating the lower scratch resistance. Moreover, for a 300 nm-thick film, delamination is observed when the tip reaches the substrate. This is not observed for a 700 nm-thick film which exhibit a progressive lateral pile up. An explanation arises considering the larger normal force necessary to scratch the thinnest film. As a matter of fact, when the substrate starts to be scratched, all the elastic energy is released leading to film delamination (insets 4 and 5 in Figures 5.1c and 5.2c, respectively). This is not the case for a 700 nm-thick film. To support this hypothesis we noted that the elastic recovery is enhanced for longer scratch distances for the 300 nm-thick film (Figures 5.1b and 5.2b). Again this effect strengthens the idea that size effects have an extrinsic origin.

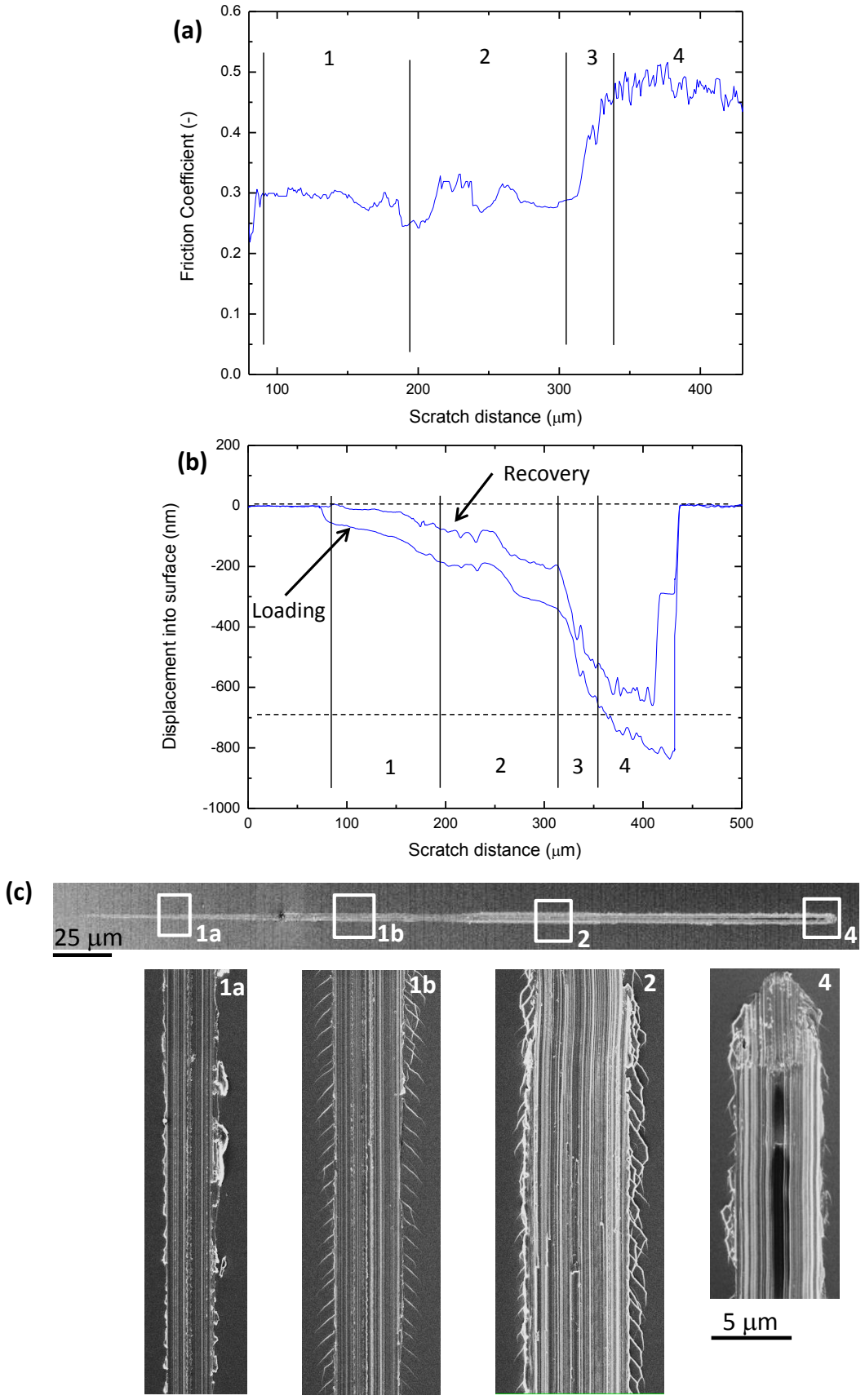

Figure 5.4 *– Evolution of the COF and of the displacement into surface as a function of the scratch distance, respectively (a) and (b); (c) the corresponding scratch morphology. The film thickness is equal to 700 nm. The scratch length is equal to 360 μm with the loading increasing from 0 up to 60 mN with a constant velocity of 30 μm/s.*

b) Effect of composition

Figure 5.5 shows the scratch results for a 700 nm-thick film with a composition $Zr_{85}Ni_{15}$ involving the presence of dispersed α-Zr nanocrystals within an amorphous matrix (Chapter III). The scratch conditions are the same as in Figure 5.3 with a scratch length of 240 μm and a normal load increasing from 0 up to 80 mN (0.33 mN/μm). The scratch velocity is equal to 30 μm/s.

Scratch mechanisms significantly differ from the results in Figure 5.3:

- the COF is almost constant and equal to 0.3 (zone 1), while increasing up to 0.6 when the substrate is scratched (zones 2 and 3). The scratch morphology involves no lateral cracks with scattered pile-up phenomena (insets 1a-c in Figure 5.5c) indicative of the progressive removal of chips attached to the tip during the scratch,
- when the substrate is scratched, there is an uniform lateral pile-up as visible in the inset 3 of Figure 5.5c, in which the substrate is the darker central region,
- there are no morphological changes if the scratch velocity is reduced down to 3 mN/s.

For the same $Zr_{85}Ni_{15}$ composition with a thickness of 700 nm, Figure 5.6 shows the scratch for a length of 360 μm and a normal load from 0 up to 60 mN, while the velocity is fixed at 30 μm/s, namely the same condition used in Figure 5.4.

The scratch behavior is very similar to what was reported in Figure 5.5 with an almost constant value of the COF around 0.3 (zone 1), followed by an increment up to 0.6 when the substrate is scratched (zones 2 and 3). The scratch morphology show the absence of lateral cracks, while reporting scattered later pile-up phenomena (insets 1a-c in Figure 5.6c). This pile-up is indicative of the progressive removal of chips attached to the tip during the scratch as probably indicated by the peaks in the zone 1 of the COF (Figure 5.6a). Furthermore, when the substrate is scratched there is an uniform lateral pile-up as visible in the inset 3 of Figure 5.6c, in which the substrate is the darker central region. Lastly, we do not observe any change if the scratch velocity is reduced to 3 mN/s.

The analysis of the compositional change reveals that the presence of a dispersed crystalline phase can strongly alter the scratch behavior. Specifically, the development of cracks during the scratch is a characteristic of fully amorphous composition (i.e. $Zr_{65}Ni_{35}$) and related to the formation of shear bands as the dominant mechanism to release the scratch energy. For a partially crystalline film, there is a marked ploughing effect with the chip attached to the tip and then progressively removed as the groove is produced, see the insets 1b and 1c in Figure 5.5c as well as the insets 1a and 1b in Figure 5.6. For this reason, the COF is constant at around 0.3, without changes indicative of a variation of scratch morphology as reported for $Zr_{65}Ni_{35}$ (Figures 5.3 and 5.4).

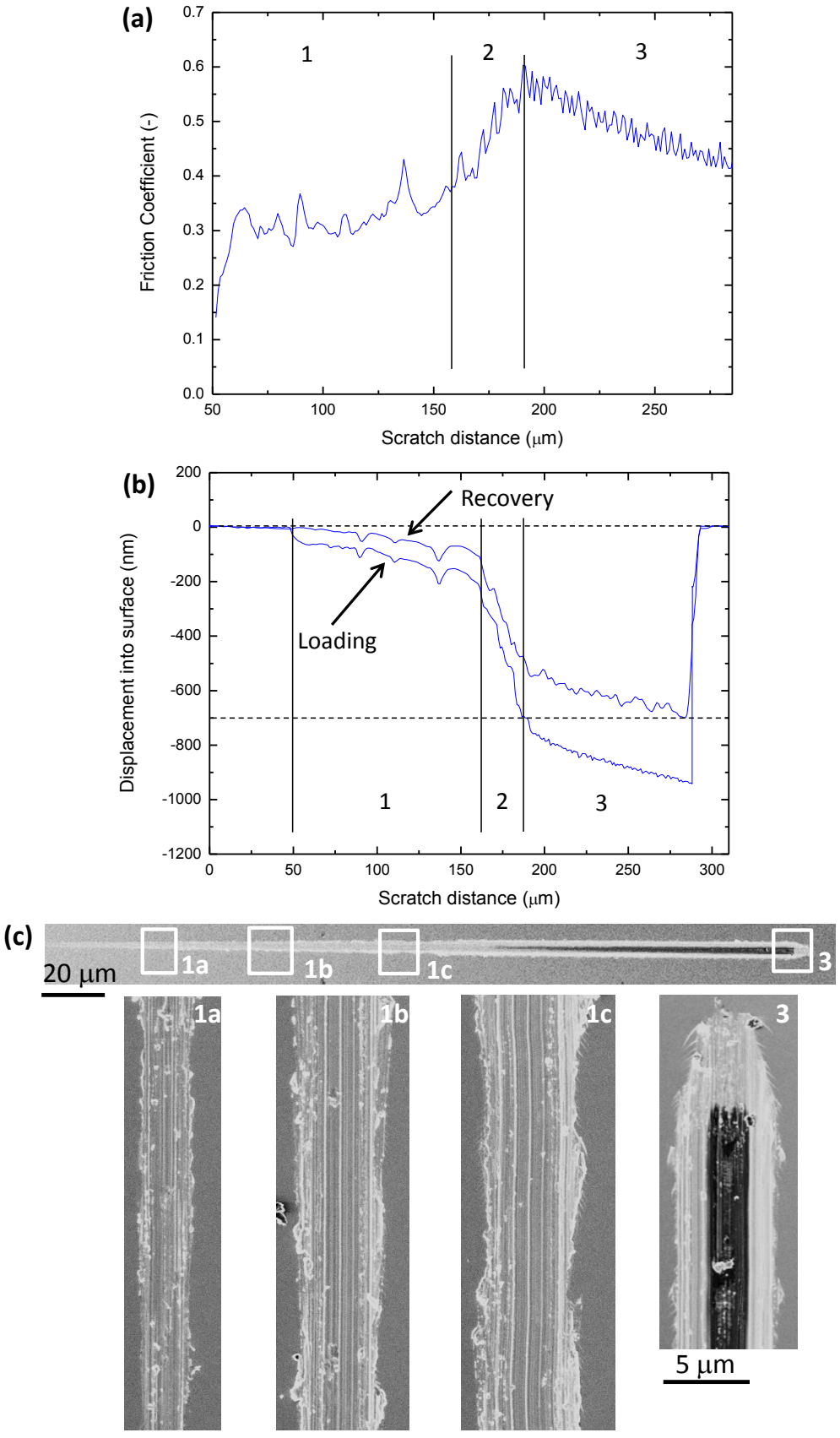

Figure 5.5 *– Evolution of the COF and of the displacement into surface for a* $Zr_{85}Ni_{15}$ *TFMG as a function of the scratch distance, respectively (a) and (b); (c) the corresponding scratch morphology. The film thickness is equal to 700 nm. The scratch length is equal to 240 μm with the loading increasing from 0 up to 80 mN with a constant velocity of 30 μm/s.*

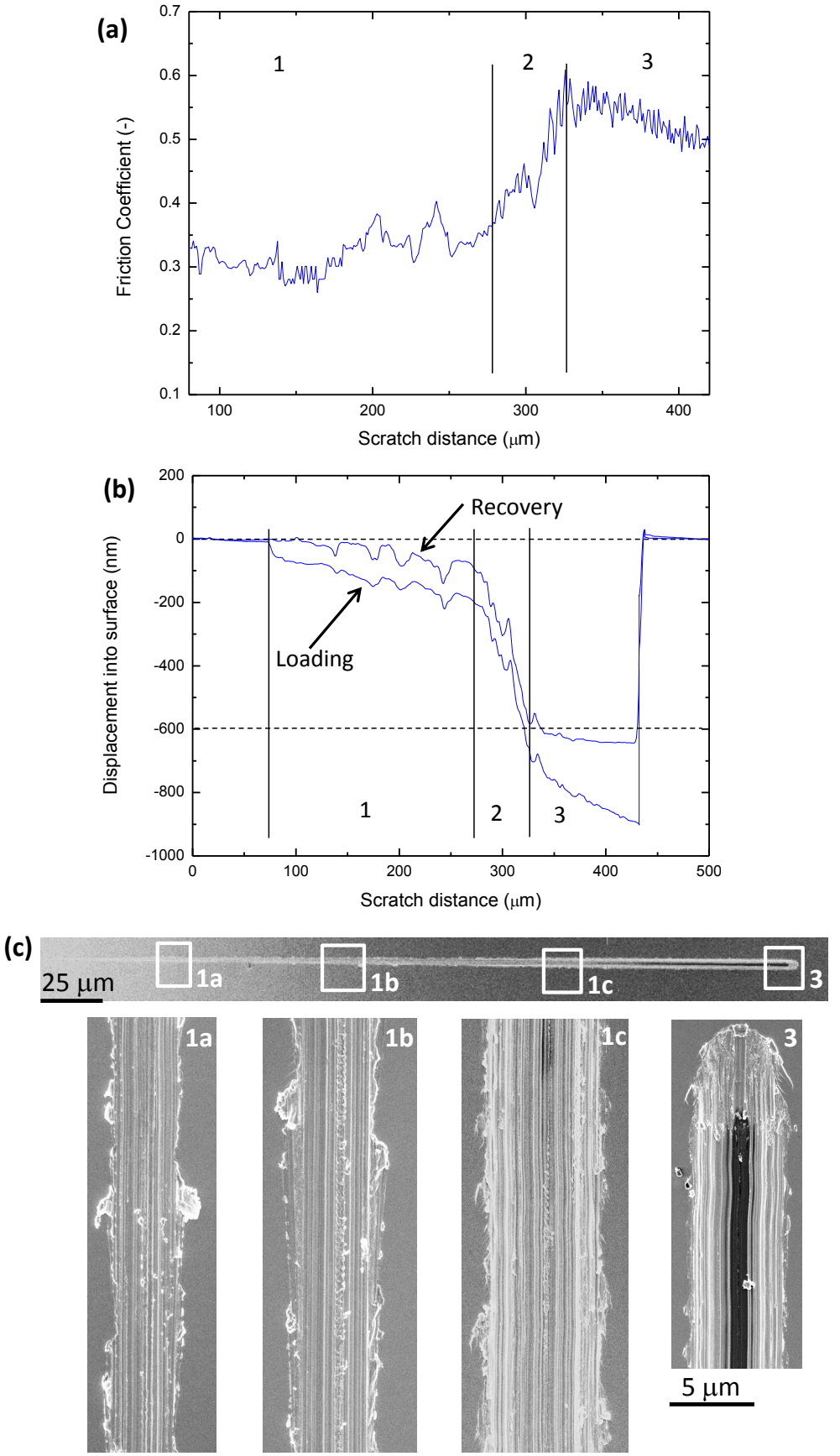

Figure 5.6 *– Evolution of the COF and of the displacement into surface for a $Zr_{85}Ni_{15}$ TFMG as a function of the scratch distance, respectively (a) and (b); (c) the corresponding scratch morphology. The film thickness is equal to 700 nm. The scratch length is equal to 360 μm with the loading increasing from 0 up to 60 mN with a constant velocity of 30 μm/s.*

5.2 Fracture of ZrNi TFMGs on a Si substrate

In this section we analyze the fracture mechanisms for $Zr_{65}Ni_{35}$ TFMGs deposited on a Si substrate. Most of this section directly reproduces a paper published in Scripta Materialia, Ref. [142], while extending the analysis considering the effect of a SiO_2 capping layer as well as the effect of composition.

It is worth noting that the theoretical background necessary to the understanding of the fracture behavior of BMGs is reported in section 1.5.7. Here, we insist on the fact that the extreme localization of deformation within narrow shear bands ($\sim$ 20 nm) can induce a local temperature rise well above the glass transition temperature (T_g) leading to a formation of a liquid layer. This leaves on the fracture surface dimples (alternatively called veins) or corrugations whose formation can be modeled by using the Argon and Salama model [95], recently adapted by Wang *et al.* [96] and Tandaiya *et al.* [91] (section 1.5.7).

Here, we use Argon and Salama model coupled with finite element simulations to investigate the effect of thickness on the fracture behavior of ZrNi TFMGs, while explaining the formation and size of corrugations and discussing the transition corrugation-mirror-like surface occurring for small thicknesses. Afterwards, we will confirm this analysis by exploring the effect of the deposition of an SiO_2 capping layer and of the change of composition.

The method used to address fracture of TFMGs deposited on a Si (100) substrate has been described in section 2.7: crack propagates from a shallow notch on the Si back face induced by a diamond tip, with the crack finally reaching the $Zr_{65}Ni_{35}$ film (Figure 5.7a). The loading configuration resembles a standard three-point bending test as reported in the case of BMGs in Refs. [86, 151].

a) Effect of thickness

The fracture surfaces are presented in Figure 5.7b-e [142]. The 300 and 400 nm-thick films show a uniform mirror-like surface with a thin folded layer at the top. The 520, 750 (not shown) and 900 nm-thick films show a regular corrugation pattern except for the top ~ 250 nm folded layer, Figures 5.7d and 5.7e. The average length (thickness direction) of the corrugation increases from 80 ± 5 to 100 ± 5 nm, respectively, for the 520 and 900 nm-thick films, similar to values reported by [62, 86, 96] for brittle BMGs, while the width of the corrugation slightly increases from 36 ± 3 to 48 ± 3 nm (Figure 5.8). A ~ 50 nm long flat region precedes the corrugation, corresponding to the shear displacement step needed to trigger cavitation, see also [52, 91, 152] and section 1.5.7. It is extremely difficult to determine the exact orientation of the shear displacement step due to the very small dimensions. We assume that it is inclined with respect to the normal direction to the interface, in agreement with results reported in literature [52, 91, 152].

Xi *et al.* [86] correlated the vein size (w) of several class of BMGs with the fracture toughness (K_c) through (section 1.5.7)

$$K_c = \sigma_y \sqrt{40w} \tag{5.1}$$

where σ_y is the yield strength. Recently, Madge *et al.* [62] and Wang *et al.* [92] confirmed this model by showing that brittle Fe and Mg-based BMGs ($K_c \leq 2$ MPa $m^{1/2}$) involve ~ 100 nm vein pattern size, while the vein dimensions increase up to 100 μm for tough Ti and Zr-based BMGs, $K_c \geq 50$ MPa $m^{1/2}$ (section 1.5.7). The hardness (H) has been measured by nanoindentation (section 4.1.1), decreasing

from 6.75 ± 0.1 GPa for the 520 nm-thick film to 6.35 ± 0.1 GPa for 900 nm-thick film [135]. The yield strength (σ_y) is taken equal to *H/3* (section 1.5 and Ref. [41]), i.e. ~ 2.2 GPa, in agreement with other Zr-based BMGs [62, 86]. Hence, the corresponding fracture toughness, estimated from equation 5.1, increases from 2.75 to 3 MPa $m^{1/2}$ (Figure 5.8).

It is worth noting that in section 4.2.4 we reported a strong dependency of σ_y with the cross-sectional area reaching values higher than 3200 MPa for very small cross-sectional areas (0.2 μm^2), while being close to 1800 MPa for larger ones (1.44 μm^2). Here, we consider σ_y equal to *H/3* because there is no a lateral confinement effect (i.e. the beam width in section 4.2.4). Moreover, in section 4.1.1 we have shown that *H* is constant at fixed indentation depth and normalized indentation depth as well, thus strengthening the validity of *H* measurement for the deposited thin films and therefore of the yield strength.

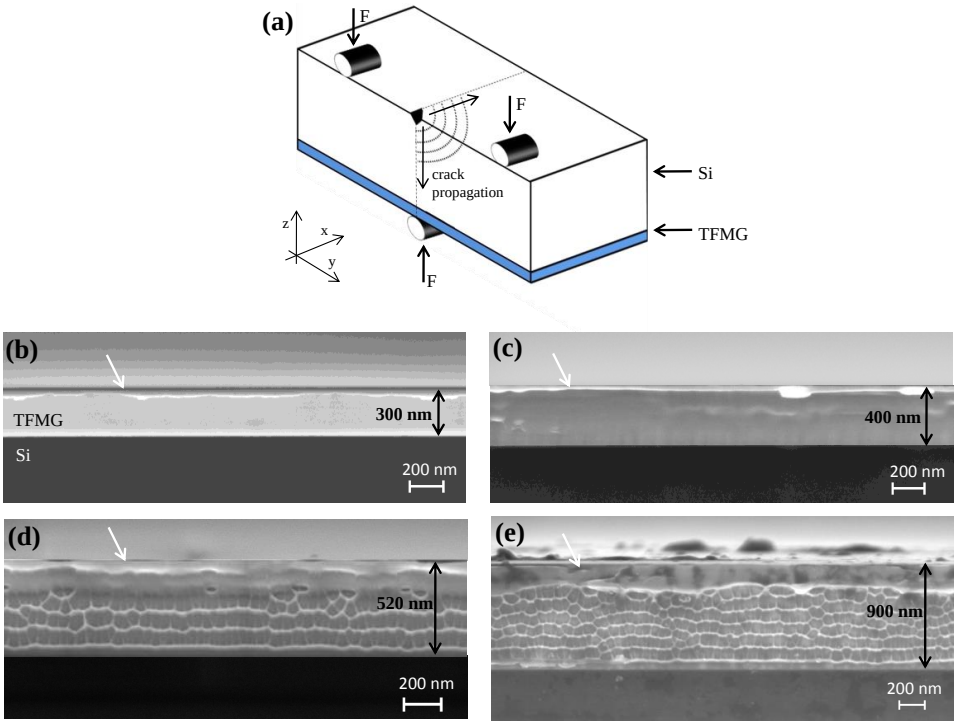

Figure 5.7 *– (a) Schematic representation of the crack propagation configuration for a TFMG deposited onto a Si wafer. The Figure is not to scale; the thickness of Si is equal to 380 μm, while the maximum thickness of TFMG is 900 nm. (b)-(e) SEM micrographs of fracture surface for $Zr_{65}Ni_{35}$ TFMGs with different thicknesses from (b) to (e), respectively, 300 nm, 400 nm, 520 nm and 900 nm. The Si substrate is the bottom dark region. A corrugation pattern appears for thicknesses above 500 nm only (d),(e), while a folded layer is observed for all thicknesses as indicated by white arrows.*

The fracture toughness (estimated using equation 5.1) is much lower than the values reported for Zr-based BMG [59, 62, 86], suggesting a major thickness effect when compared to the bulk (Figure 5.8). The fracture toughness of metallic glasses has been related to the Poisson ratio ν (section 1.5.4 and Refs. [59, 62]). The transition from brittle to ductile occurs at $\nu \sim 0.31$ in metallic glasses. A larger ν corresponds to a more incompressible material with a higher tendency toward shear dominated relaxation. Brillouin spectroscopy measurements (section 3.3) have given $\nu \sim 0.39$ independent of film thickness, in agreement with values reported for Zr-based BMGs [59]. Hence, a large fracture toughness should be expected for our alloy if in bulk form. The elastic modulus *E* is

equal to72 GPa (section 3.3), while the σ_y value ($\sim$ 2.2 GPa) is in agreement with the literature for Zr-based BMGs as well [62]. The origin of the particularly low fracture toughness and the reasons for the transition in the failure mechanism must thus be found elsewhere.

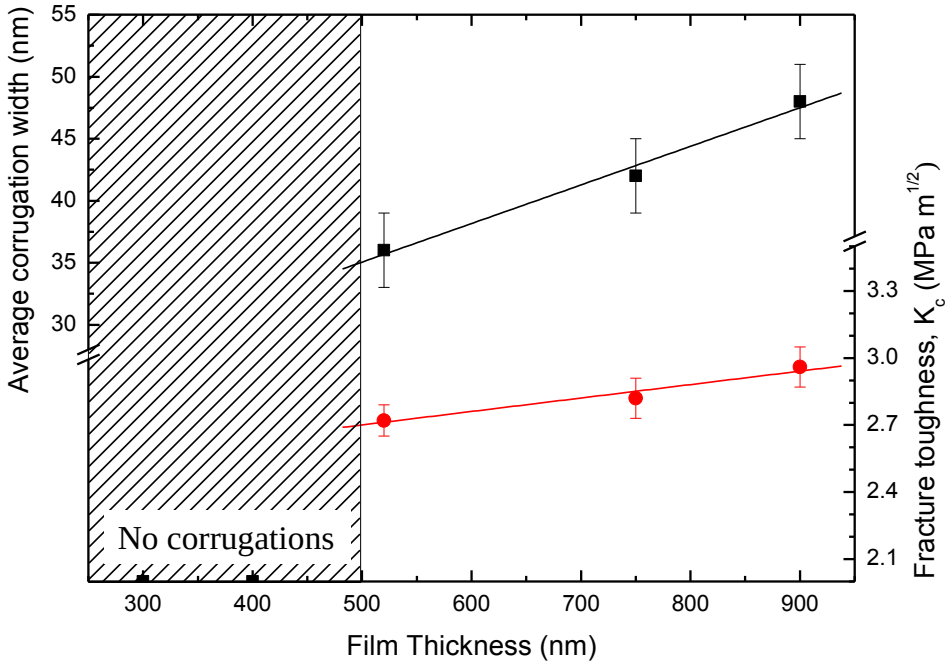

Figure 5.8 *– Thickness dependence of corrugation width and fracture toughness K_c estimated using equation 5.1, for $Zr_{65}Ni_{35}$ TFMGs.*

Zhang *et al.* [153] observed much smaller dimple sizes in Pd-based 5 to 10 μm thick TFMG, compared to BMGs. According to [86], the corrugation and vein size (w) is directly related to the fracture process zone (FPZ), thus a nm-scale dimple structure indicates small plastic zone, limiting the crack tip shielding. The lower bound of the critical energy release rate $G_c = \frac{K_c^2(1-\nu^2)}{E}$ is given by the intrinsic work of separation equal to 2 times the surface energy, χ [96]. Assuming $G_c \approx 2\chi \approx 2.24\ \mathrm{J/m^2}$ [91], a lower bound for K_c is 0.6 MPa $\mathrm{m^{1/2}}$ slightly below the obtained results (Figure 5.8). The Argon and Salama model [95], recently extended by Wang *et al.* [96] and Jiang *et al.* [93], is used to understand the development of corrugation pattern mechanism. A Taylor meniscus instability analysis [95], permitted by the liquid-like layer formation caused by the local heating due to shear bands development [52], states that an initial perturbation wavelength (λ_I) grows if

$$\lambda_I \geq 2\pi\sqrt{\chi / (\frac{d\sigma_H}{dx})} \tag{5.2}$$

where $\frac{d\sigma_H}{dx}$ is the stress gradient (or suction) ahead of the crack. More detailed non-linear analysis [95] reveals that the *dominant* wavelength (λ) is equal to $\lambda_I\sqrt{3}$. Once the initial perturbation (λ) is formed, the steady state wavelength (λ_S) evolves toward [95],

$$\lambda_S = 12\pi^2 A(n)(\frac{\chi}{\tau_y}) \tag{5.3}$$

where *A(n)* is the wavelength coefficient, which depends on the non-linearity exponent (*n*) (~ 1.3 for most metallic glasses) and τ_y is the yield stress in shear ($\tau_y = \sigma_y / \sqrt{3}$) [95, 96]. The competition between a dimple/vein or a corrugation mechanism can be deduced by comparing λ or ($\lambda_I \sqrt{3}$) and λ_S (Figure 1.28 shows a schematic of this mechanism).

If $\lambda_I \sqrt{3} > \lambda_S$, a meniscus instability develops leading to surface dimples [91, 93, 96]. If $\lambda_I \sqrt{3} < \lambda_S$, the perturbation is *frustrated* and will not develop into a steady furrow . This mechanism corresponds to the formation of a regular corrugation pattern involving cavitation ahead of the crack tip and further lateral coalescence of cavities [60, 151]. The choice between corrugation and dimple formation can be evaluated also by comparing the radius of the FPZ and $\lambda_I \sqrt{3}$ [93]. The FPZ radius is equal to half the corrugation or dimple width (*w*) since the perturbation cannot overcome the boundary of the FPZ [93] (Figure 1.28) as the suction stress ($d\sigma_H / dx$) reaches a maximum and then gets negative as shown in Figure 5.10. If $w/2 < \lambda_I \sqrt{3}$ the FPZ restraints the development of the meniscus instability leading to a corrugation pattern.

Finite elements simulations (Figure 5.9) were performed by Frédéric Lani at the Univerisité catholique de Louvain (UCL) to further analyze the data by calculating the local stress state and the extent of the FPZ ahead of the crack tip, see also Ref. [142] for supplementary information. These simulations are semi-quantitative, relying on the J_2 flow theory to represent the plastic behavior of the TFMG. Different thicknesses of TFMGs as well as various crack lengths for the 900 nm-thick film Figures 5.9f-h, were simulated under different K_I values. Figure 5.9a (and zoom in Figure 5.9h) and 5.9b show the plastic zone in terms of equivalent plastic strain contours for a crack in a 900 nm film located at 300 nm from the surface and for a 300 nm-thick film, respectively. The crack tip plastic zone and the compressive plastic zone at the inner fiber (caused by the bending) merge and lead to plastic collapse at $K_I \approx 2.2$ MPa $m^{1/2}$. For a 400 nm thick film, collapse occurs when $K_I \approx 2.6$ MPa $m^{1/2}$. Up to that point, the opening stress at the crack tip is high, typical of small scale yielding [142]. This ensures that the stress is similar up to this load to what is observed at the crack tip in a BMG. Contour plots of Figures 5.9c-h all correspond to $K_I = 2.2$ MPa $m^{1/2}$. Plastic collapse is thus taking place at a K_I on the order of the K_c measured experimentally. This means that the range of thicknesses under investigation covers the domain in which such a transition takes place. Plastic collapse involves a drop of the constraint and of the hydrostatic stress (and thus of the stress gradient, $d\sigma_H / dx$) which does not allow a cavitation mechanism to further develop. Therefore, we propose that the crack can propagate by protruding instability/cavitation within the FPZ, until the criterion for plastic collapse is met, explaining the absence of any patterns for the thinnest films and for the upper regions of the fracture surfaces for thicker films, Figures 5.7b-e. We anticipate that if collapse occurs, the failure mechanism is similar to the initiation process (first 50 nm in Figures 5.7d-e), namely a pure shear displacement.

The second question is to explain the low toughness compared to the expected bulk value, even if BMGs are constituted by several atomic species (section 1.3). In thin films, the volume available for plastic dissipation is fairly small. Furthermore, the bending loading configuration imposes a strong constraint on the maximum FPZ size. At $K_I \approx 2.2$ MPa $m^{1/2}$, the stress gradient ($d\sigma_H / dx$) driving the suction ahead of the crack tip is equal to $55 \cdot 10^3$ GPa/mm, independently of the film thickness (Figure 5.10a). The corresponding dominant perturbation wavelength $\lambda_I \sqrt{3}$ is equal to 49 nm, close to the width of the corrugation pattern of the 900 nm-thick film (Figure 5.8). The key point is that because the stress ahead of the crack tip necessarily drops to zero at the neutral axis, the hydrostatic stress can increase only over a portion of the thickness (Figure 5.10a).

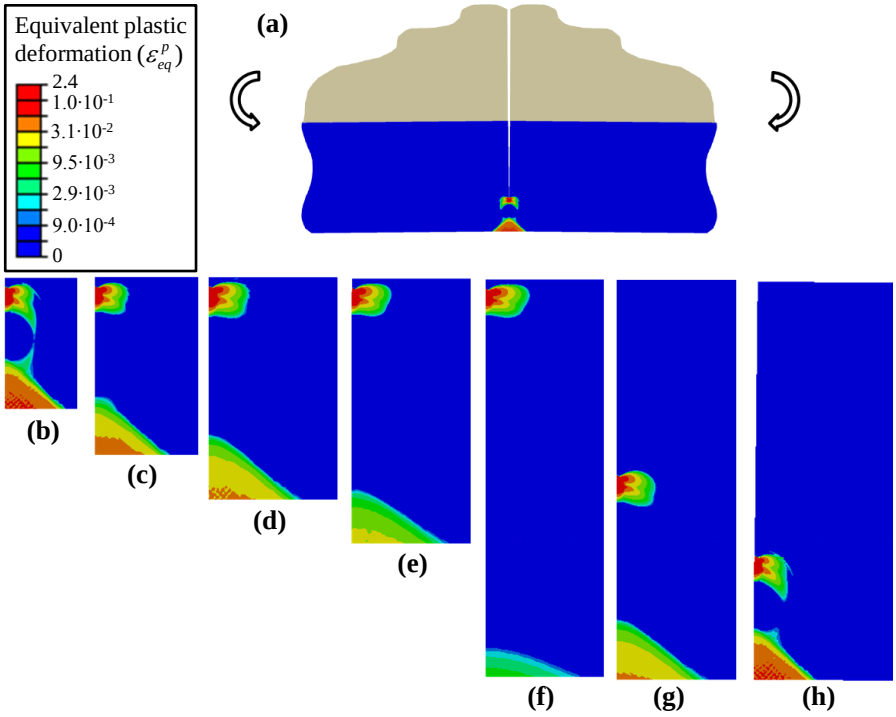

Figure 5.9 *– Finite element simulations of static cracks in TFMGs at K_I = 2.2 MPa $m^{1/2}$. (a) The illustrated zone is a zoom of the metallic glass film. The Si substrate (in grey) is entirely cracked. (b)-(h) Contour plots of the plastic zones in terms of effective plastic strain. (b) Layer thickness t = 300 nm, crack length a = 32 nm. (c) t = 400 nm, a = 32 nm. (d) t = 500 nm, a = 32 nm. (e) t = 600 nm, a = 32 nm . (f) t = 900 nm, a = 32 nm. (g) t = 900 nm, a = 450 nm. (h) t = 900 nm, a = 632 nm.*

Hence, the FPZ is limited to a length equal to a quarter of the thickness, in agreement with the measured corrugation length. As mentioned earlier, this is reminiscent to the thickness dependent toughness in thin metallic sheets where the FPZ size and thus dissipation scales with thickness [154]. To confirm this analysis, Figure 5.10b shows the variation of the Von Mises stress as function of the distance from the crack tip. The first plateau of about 60 nm is thickness independent and correspond to the FPZ ahead of the crack tip, again in agreement with the measured corrugation width. The critical wavelength for the development of a steady state perturbation λ_S is close to 130 nm, justifying – according with the previously reported criterion – the formation of the corrugation pattern Figures 5.7d-e. The corrugation formation is also justified by comparing the radius of the FPZ (equal to *w/2*) and $\lambda_I\sqrt{3}$: for all thicknesses, $w/2 < \lambda_I\sqrt{3}$. Furthermore, a limited lateral growth is expected as demonstrated by the corrugation width close to the predicted dominant wavelength $\lambda_I\sqrt{3}$ (see also section 1.5.7). As shown in Figures 5.7d -e, the transverse coalescence of cavities leaves marks on the valley of the corrugation pattern, while strong horizontal marks correspond to the edge of the FPZ. Finally, the transition wavelength below which no corrugation occurs is equal to 36 nm very close to the 37 nm reported in [96].

In summary, we have shown that the fracture of submicron ZrNi TFMGs occurs by a mechanism of corrugation with a width close to the dominant wavelength predicted by a meniscus instability model. This mechanism competes with pure shear deformation dominated cracking for small thicknesses and short ligaments. Even though evidences have been given for a higher ductility in thin films due to the high value of the Poisson ratio [110, 115], the fracture toughness is thickness dependent due to the lack of volume available for dissipation and geometric confinement, leading to a

low brittle like toughness level. This suggests that size effects on the fracture behavior have an *extrinsic* origin and related to a geometric confinement since no change in film atomic structure and free volume content has been found (Chapters III and IV). Note that a similar observations justify the nanoindentation behavior (Chapter IV) as well as the enhanced plasticity, the homogeneous deformation and the evolution of yield strength investigated with the lab-on-chip method (Chapter IV).

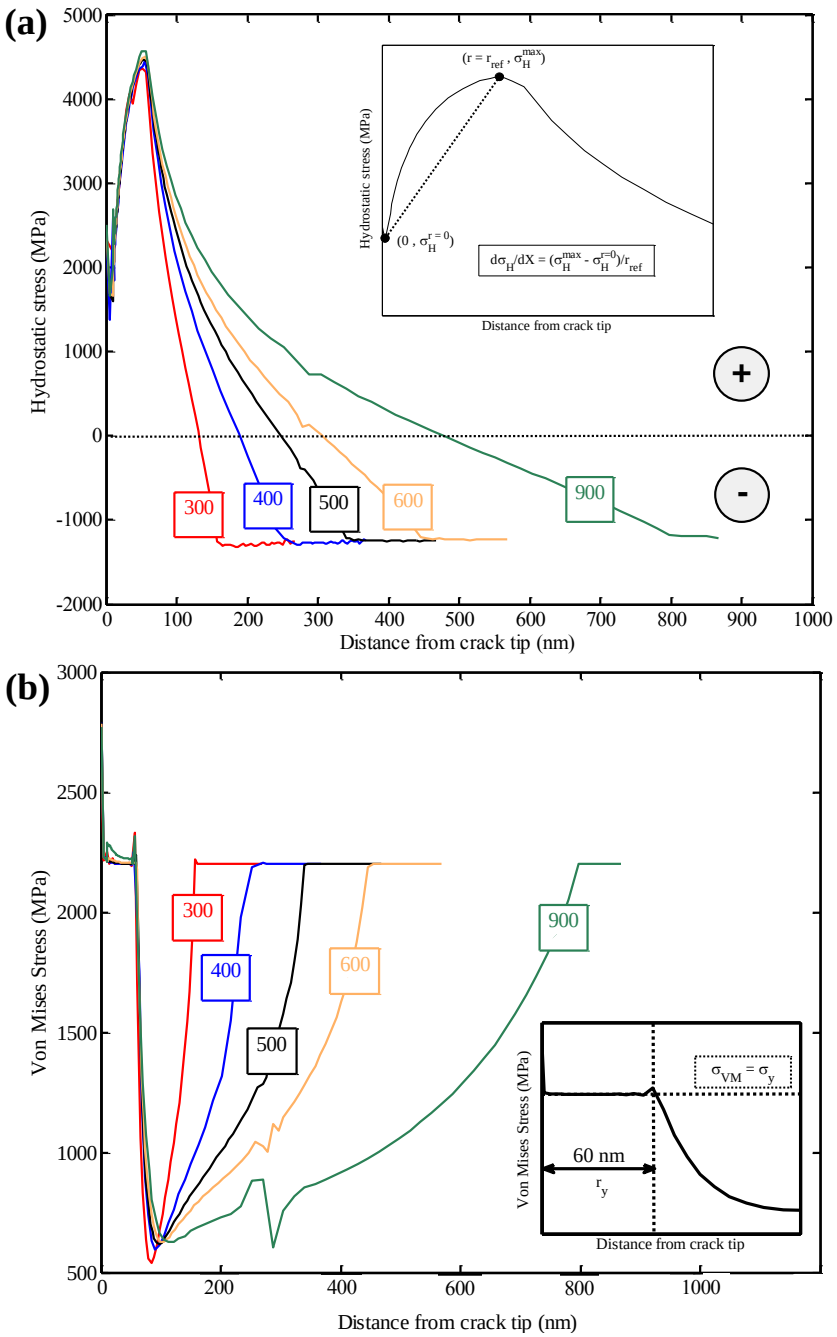

Figure 5.10 *– Stress fields obtained by finite element simulations. (a) Evolution of the hydrostatic stress as a function of the distance to the crack tip, ahead of the crack tip, for different TFMG thicknesses (300, 400, 500, 600 and 900 nm). The horizontal dotted line represents the boundary between tensile and compressive stress states, as expected in bending. In the inset, the calculation of the strain gradient. (b), Evolution of the Von Mises stress as a function of the distance to the crack tip, showing two plateaus, the first one corresponding to the plastic zone at the crack tip (60 nm, as clearly shown in the inset), and one to the compressive plastic zone of the bent layer.*

b) Effect of a SiO_2 capping layer on fracture

Here, we analyze how the cracking mechanisms of $Zr_{65}Ni_{35}$ TFMGs change when covering with a SiO_2 layer with the objective to confirm the previously reported analysis indicating as *extrinsic* (geometric confinement) the origin of size effects. More details are reported in Ref. [136].

The SiO_2 layer has been deposited immediately after the deposition of the 400 nm-thick ZrNi TFMGs to limit surface oxidation. The deposition system was the same DC-magnetron sputtering (Alliance Concept AC450) with a multiple target configuration (section 2.3). The target-substrate distance was 7 cm, while the background gas (Ar) pressure and the DC-power were fixed to 0.15 Pa and 500 W, respectively. The target was pure amorphous (purity > 99.9%) SiO_2. The SiO_2 growth rate was measured by mechanical profilometer and found equal to 0.7 nm/s.

Figure 5.7 shows a transition in fracture behavior for corrugation to mirror-like for thicknesses ≤ 400 nm. Finite element simulations (Figure 5.9) have shown that *plastic collapse* – namely the merging between the plastic zones ahead of the crack tip and the one due to bending configuration – occurs for small thicknesses (≤ 400 nm) preventing the cavitation and/or meniscus instability to develop and leading to a mirror-like surface such as in Figure 5.11a. Hence, the fracture behavior is intimately related to thickness confinement. In order to confirm this claim, we deposited a SiO_2 cap layer onto the TFMGs aiming to alter the fracture morphology by translating the compression zone within the SiO_2 in order to analyze possible changes in the fracture behavior of TFMGs. The fracture surface of a 400-nm thick $Zr_{65}Ni_{35}$ TFMGs coated with a 450 nm SiO_2 layer is shown in Figure 5.11b demonstrating the presence of a corrugated pattern with an average width (w) of ~ 38 nm, very close to the size exhibited by a 520 nm-thick film reported in Figure 5.8. The same 400-nm TFMG without SiO_2 capping did not show any corrugation but a flat mirror-like surface (Figure 5.11a). As expected, this abrupt change comes from the fact that the compressive zone due to bending lies in the SiO_2 layer, thus allowing the hydrostatic stress peak to develop over a region of the ZrNi film large enough for triggering a cavitation mechanism responsible for the observed corrugation pattern.

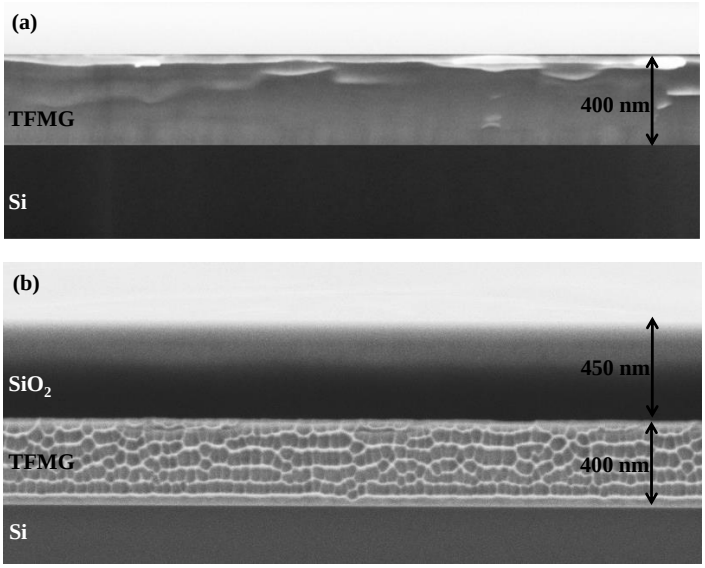

Figure 5.11 *– SEM micrographs of fracture surfaces for $Zr_{65}Ni_{35}$ TFMGs. (a) A mirror-like fracture surface is present for a 400 nm-thick because of the collapse of plastic zones ahead of the crack tip and due to bending configuration. (b) A corrugation pattern appears for a 400 nm-thick $Zr_{65}Ni_{35}$ film if coated by a SiO_2 cap layer since the bending plastic zone is moved in the SiO_2 layer.*

This proves again that the fracture mechanisms and the length scale over which they take place are dictated by extrinsic factors related to the loading configuration and external dimensions that set the constraint on the plastic zone size and on the magnitude of the stresses attained in the fracture process zone. The fracture toughness (K_c) – calculated using equation 5.1 – is equal to 2.7 MPa $m^{1/2}$ well below the expected value around 50 MPa $m^{1/2}$ estimated from a Poisson ratio of 0.39 for a BMG [59], but in agreement with results we obtained for TFMGs [142], Figure 5.8. As explained above, this low toughness is not a result of a particular atomic structure or of an intrinsic length scale effect on the mechanisms, but of the restriction on the plastic zone development due to the bending configuration and small thickness. This restriction on the plastic zone development is somewhat analogous to the substrate effect seen on the hardness in nanoindentation (section 4.1.1).

c) Effect of composition

Figure 5.12 shows the fracture surfaces of the different Zr_xNi_{100-x} TFMG compositions having an amorphous structure (Chapter III). As first, we noticed that all the films exhibit a corrugation pattern which covers approximately 3/4 of the film thickness leaving a smooth top region, so-called "folded layer" (see the effect of thickness section). These phenomena have been already discussed in section 5.2a and in Refs. [136, 142]. The corrugations are related to cavitation and the frustration of the meniscus instability mechanism, while the plastic collapse between the fracture process zone (FPZ) ahead of the crack tip and the compressive zone due bending leading to the formation of the folded layer (Figure 5.9). Figure 5.12 confirms that the mechanisms are globally the same for the different compositions. The $Zr_{65}Ni_{35}$ and $Zr_{75}Ni_{25}$ show essentially a similar corrugation morphology, while the $Zr_{42}Ni_{58}$ exhibits larger corrugations which are more reminiscent of the formation of a liquid layer dictating the process of cracking by a meniscus instability propagation, section 1.5.7 and Ref. [142]. This agrees with the more disorder character of this composition (see discussion in term of fragility index and activation volume in sections 3.3b and 4.1.2, respectively).

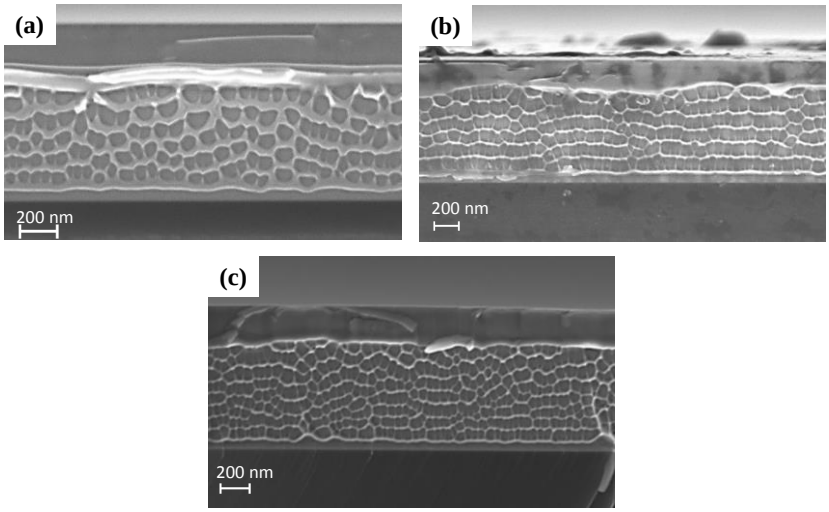

Figure 5.12 *– SEM micrographs of fracture surfaces for Zr_xNi_{100-x} TFMGs with a thickness of 800 nm. From (a) to (c) the compositions $Zr_{42}Ni_{58}$, $Zr_{65}Ni_{35}$, $Zr_{75}Ni_{25}$, respectively. All fracture surfaces show a corrugated pattern. The corrugation size increases when reducing the Zr content in the film, while folded layer on top surfaces is always present. The composition $Zr_{42}Ni_{58}$ (a) clearly shows a different morphology.*

The average corrugation width (*w*) increases from 43 nm up to 58 nm when reducing the Zr content in the film, thus leading to a change in fracture toughness – obtained using equation 5.1 – from 2.3 MPa $m^{1/2}$ up to 4.0 MPa $m^{1/2}$, and represented in Figure 5.13 [136]. Therefore, this further supports the idea that the fracture toughness is primarily set by the constraint on plastic flow development (section 5.2a-b and [136, 142]) since the same mechanisms are involved if the composition is changed.

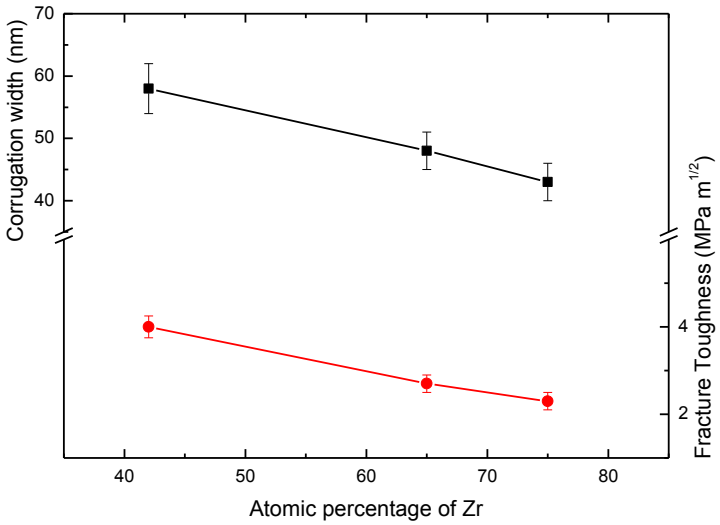

Figure 5.13 *– Evolution of corrugation width and the estimated fracture toughness for different ZrNi compositions.*

5.3 Fracture in tension

In this section we complete the analysis of size-effects affecting the mechanical response of freestanding $Zr_{65}Ni_{35}$ TFMGs as quantified by the lab-on-chip technique (Chapter IV). We will refer to Table 4.1 for the geometries of the studied specimens. As a short reminder, the specimen is named as "B15_*x*_*y*" where B indicates the "B" series (section 2.8.3), "15" is the width of the actuator (15 μm), while *x* and *y* indicate the width and the length of the specimen, respectively. The thickness of the specimen (110, 200, and 360 nm) is reported in Figure caption.

As mentioned in section 4.2 – depending on the ratio between the thickness of the actuator and of the specimen – the fracture is attained only for the most severe test conditions, namely a long actuator pulling on a specimen with a small width (equation 4.5). Table 5.1 summarizes the conditions for which the fracture occurs. Specifically, fracture is reached for 1 and 2 μm-wide beams in the case of a 110 nm-thick film whose mechanical properties are tested with 80 nm-thick actuator (high ratio actuator/specimen thickness), while in the case of the 200 and 360-nm thick specimens, the fracture occurs only for the 1 μm-wide beams (low ratio actuator/specimen thickness). In section 4.2, we have shown that non-broken specimens exhibit a large ductility and deform homogeneously, nevertheless the stress developed by the actuator does not allow inducing enough displacement to reach fracture. Hence, for these samples we have only a partial information (i.e. the maximum deformation) and they cannot be directly compared with the broken ones. For this reason, in this chapter we limit the analysis to the broken specimen as reported in Table 5.1.

The fracture strain obtained for the different specimen geometries is reported in Table 5.1 as well. First of all it can be noted that the fracture strain is much more than for conventional BMGs

(∼2% in the case of Zr-based BMGs, section 1.5.3 and Ref. [41]). The origin of such large fracture strain, only observed a few times in the literature, has been related to size effects positively affecting plastic deformation in small-scale metallic glasses (sections 1.6 and 4.2).

Actuator thickness (nm)	Specimen thickness (nm)	Specimen length (μm)	Specimen width (μm)	Fracture strain (%)
80	110	25	2	11.8
		50	2	10.9
		100	(1) – 2	(10.4) – 7.7
100	200	25	1	14.3
		50	1	12.7
		100	1	10.5
160	360	25	1	14.1
		50	1	11.5
		100	1	8.8

Table 5.1 *– Summary of the specimen geometries attaining fracture and the corresponding fracture strain.*

The effect of the specimen cross section and of the free surface on the fracture strain are reported in Figure 5.14. There is no effect of the cross-sectional area (Figure 5.14a) while the fracture strain is strongly dependent on the length of the beam (the points are vertically shifted). Nevertheless, if the results reported in Table 5.1 are plotted as a function of the specimen free surface (which takes into account the length of the specimen), a trend appears as illustrated in Figure 5.14b: the fracture strain increases when reducing the free surface. In Figure 5.14b the full symbols represent unbroken specimens of the same lab-on-chip series as reported in Table 5.1, while the "×" represents the fracture strain for the broken specimens (Table 5.1).

As already mentioned, the trend in Figure 5.14 differs from the evolution of the yield strength and of the strain hardening coefficient both scaling with the specimen cross-sectional area, while being almost constant with respect to the free surface (section 4.2). An explanation of the trend shown in Figure 5.14b considers the presence of dispersed defects whose absolute amount increase when investigating larger free surfaces. These defects should not be considered as macroscopic defects or flaws since they are not detectable with SEM and all the samples deform homogeneously. Moreover, the presence of a distribution of macroscopic defects would appear in the results reported in Figure 5.14, significantly increasing the scattering of the data and hiding the development of a clear trend, as reported in Figure 5.14b, with statistical effects. Instead, a broader distribution of shear transformation zone size (STZs, section 1.5.8) for samples with larger free surface enhances the likelihood of activation of shear transformation events which ultimately provoke fracture (section 1.5.8 and Refs. [3, 4]). For the sake of clarity, let us consider the stress-strain curve of a 360 nm-thick specimen 1 μm-wide and different lengths (Figure 4.11a). The yield strength is almost independent of the specimen length, while the fracture strain significantly varies (Table 5.1). Hence, while the activation of the macroscopic yielding requires the activation of irreversible STZ events which are strongly dependent on the cross-sectional area (section 4.2), the ease of the percolation of STZs for larger free surfaces (i.e. when the length is equal to 100 μm) limits the homogeneous development of the plastic

behavior. The specimen which maximizes the yield stress and the fracture strain is the 25 μm x 1 μm 200 nm (σ_y = 3280 MPa and fracture strain equal to 14.3%). Hence, even though we have shown that the films involve the same atomic structure independent of the thickness or of the geometry in general (Chapters III and IV), on average for larger free surfaces there is an enhanced probability of percolation of activated STZs events provoking a premature failure. Moreover, Figure 5.14b shows that specimen with different dimensions (but similar free surface) have very similar failure strains. This is the case for the 25 μm x 1 μm x 200 nm and 25 μm x 1 μm x 360 nm specimen (free surface around 60 μm^2), thus confirming the free surface dependency of the failure strain. Moreover, it is worth noting that all the investigated specimens deform homogeneously involving large plastic deformation before failure with no evidences of necking (section 4.2). This has been shown also for specimens which do not involve fracture and whose maximum strain can be very high, above 8-9% (Figures 4.11b, 4.13b, and 4.14c).

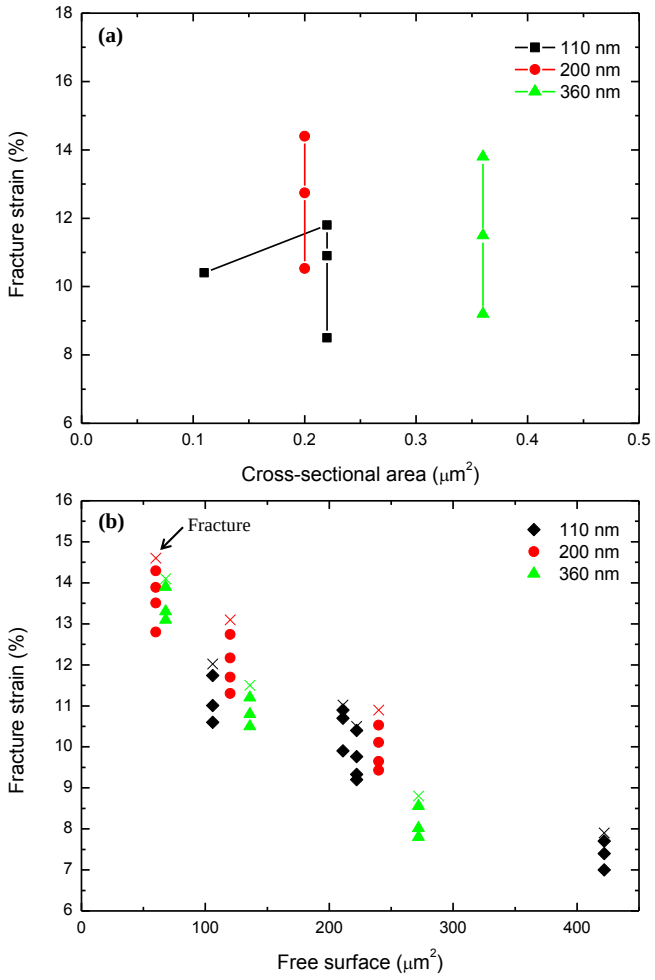

Figure 5.14 *– Evolution of the fracture strain as a function of the cross-sectional area (a) and free surface (b). In (b) the "×" indicates the fracture strain, while the full symbols indicate the total deformation of the last unbroken specimens.*

The analysis of fracture in tension is supplemented by SEM observations of broken specimens in order to strengthen some points of discussion addressed in section 4.2. Figure 5.15 shows a 360 nm-thick broken beam, with a width and an original length of 1 and 50 μm, respectively. Fracture does not occur at the overlap with the actuator nor in the vicinity of the dogbone edge (bottom rounded part).

Instead, fracture occurs at random position within the gauge length of the specimen beam depending on the stress level (imposed by the actuator) and on the statistical distribution of STZs size.

Cracking follows a straight line (inset 1 of Figure 5.15), at an angle with respect to the loading direction that is in between 0 and 65°. Specifically, in Figure 5.15 inset 1 the angle is close to 32°. However, it can be noted that there are no evidences of necking, instead, after a homogeneous deformation, the percolation of STZ events provoke a sharp fracture. As mentioned in section 1.5.7, BMGs exhibit a fracture angle in tension ranging between 48° and 65° with respect to the loading direction [41]. Here, we observe that the homogeneous deformation coupled with the micrometric size of the sample can significantly change the fracture angle enhancing statistical effects.

After fracture, the broken specimens bend down inside the bottom of the etched "pool" (Figure 5.15) whose depth – estimated from the Si (100) etching rate within a TMAH solution – is close to 17 μm (section 2.8.2). This fact, together with the abrupt release phase for the B structures (constant width of the actuator), produces a significant bending of the specimen close to the dogbone edge as reported in the insets 2 and 3. However, fracture never occurs in these regions.

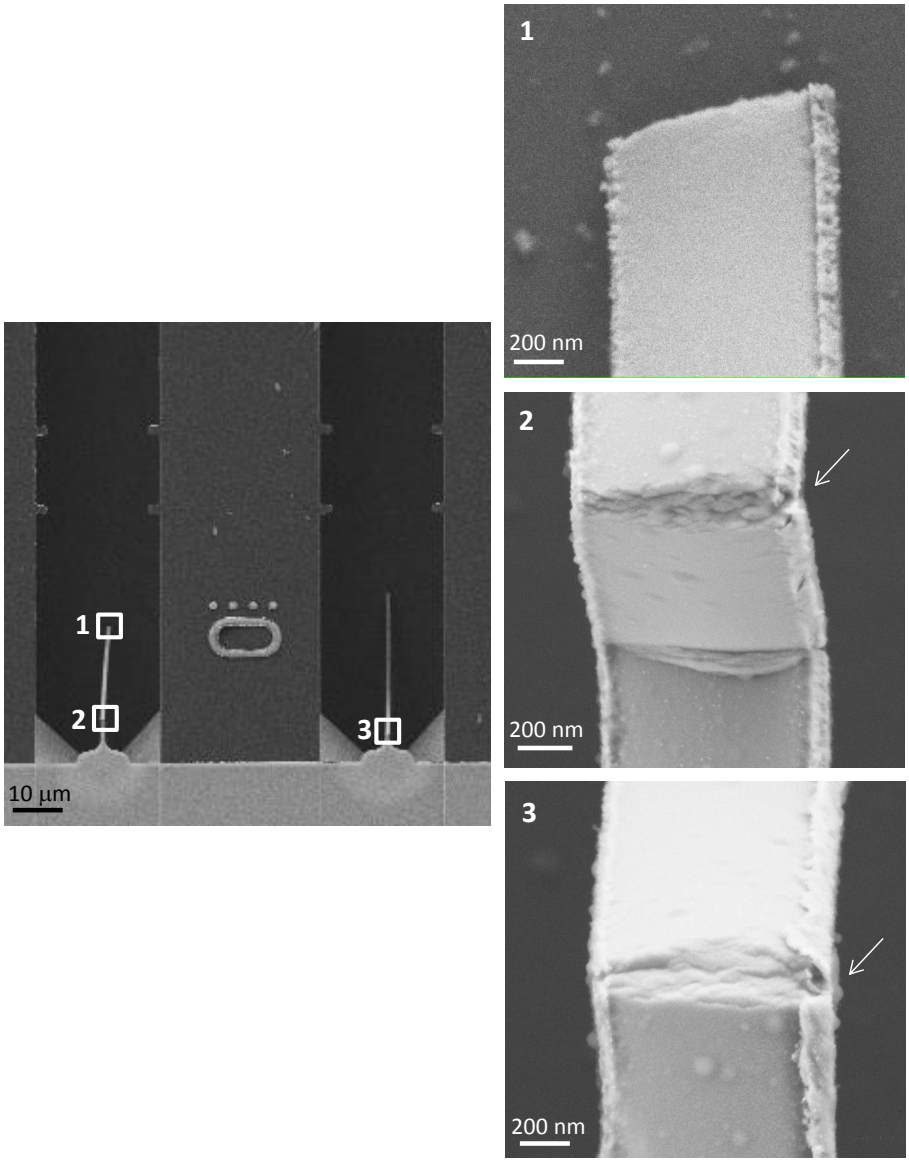

Figure 5.15 *– Broken 360 nm-thick beams. The fracture angle is close to 32° (inset 1), while insets 2 and 3 show a very high local deformation with formation of shear bands.*

The insets 2 and 3 of Figure 5.15 reveal an extremely high local deformation with the formation of shear bands within the entire cross-section. This phenomenon is observed for all the fractured beams. Shear bands originate for surface defects acting as local stress concentrators as indicated by white arrows in the inset 2 and 3 of Figure 5.15. This observation is in agreement with the experimental finding in the case of tension test of micropillars with artificially machined notches [111] as well as with theoretical analysis reported in Refs. [20, 60] and sections 1.5.3 and 1.5.8. Here, the intense shear bands activity is somehow related to the high plasticity reported for these specimens (Figure 5.14). As a matter of fact, the high thermodynamic fragility index reported for $Zr_{65}Ni_{35}$ TFMGs (sections 1.5.4 and 3.3a) involves a pronounced ability to form multiple shear bands whose interaction promotes plasticity. Moreover, the geometrical confinement for micrometric specimens involves a reduced likelihood of macroscopic defects which limits the risk of formation of a single shear band (especially if a tensile load is applied). Hence, both intrinsic (atomic structure) and extrinsic (geometrical confinement) factors are responsible for the homogeneous deformation and large plasticity (see also section 4.2). Lastly, the intense shear band activity justifies the high plastic deformation and the homogeneous deformation for specimens with large cross-sections which involve a yield strength close to the bulk counterpart (section 4.2.4).

Figure 5.16 shows two broken beams with a thickness of 200 nm, a width of 1 μm and an original length of 50 μm. The fracture angle is close to 10° (inset 1) even if there are statistical effects depending on the specimen and the defect distribution. Fracture occurs in the middle of the beam away from the overlap with the actuator and from the dogbone bottom edge. The insets 2 and 3 of Figure 5.16, which are magnification of the bent zone close to the dogbone bottom edge, reveal again the presence of an intense through-the-thickness shear band activity. Interestingly, the specimen bend and fold without breaking in this location, as clearly visible in the inset 2 of Figure 5.16. Again the evidence of the shear bands activity is related with the high plasticity observed in 200 nm-thick specimen too (section 4.2). As previously mentioned shear bands originate from superficial defects (similar to notches) which provide a local stress intensification, see the white arrow in the inset 3 of Figure 5.16.

The development of shear bands is observed also in the case of 110 nm-thick specimen as reported in Figure 5.17 for a 2 μm-wide beam having an original length of 50 μm. As in the previously reported cases, after fracture, the specimens bend down inside the Si etched “pool” and creates the development of the shear bands in the vicinity of the dogbone edge (inset 1 of Figure 5.17). Shear bands develop through the entire width even in the case of very small thicknesses and larger width (2 μm), thus explaining the origin of the extended plasticity (section 4.2). The extended homogeneous deformation (∼ 12%, Figure 4.14) , lead to a sharp fracture with an angle in close to 0° whose position is always within the specimen “core” avoiding the overlap with the actuator or the dogbone bottom edge.

As a conclusion, we strongly believe that the intense local plastic bending observed in all the specimens results from a dynamic effect taking place when the specimen breaks. Indeed, never observed before fracture, these very large local deformations prove again the large ductility of our specimens.

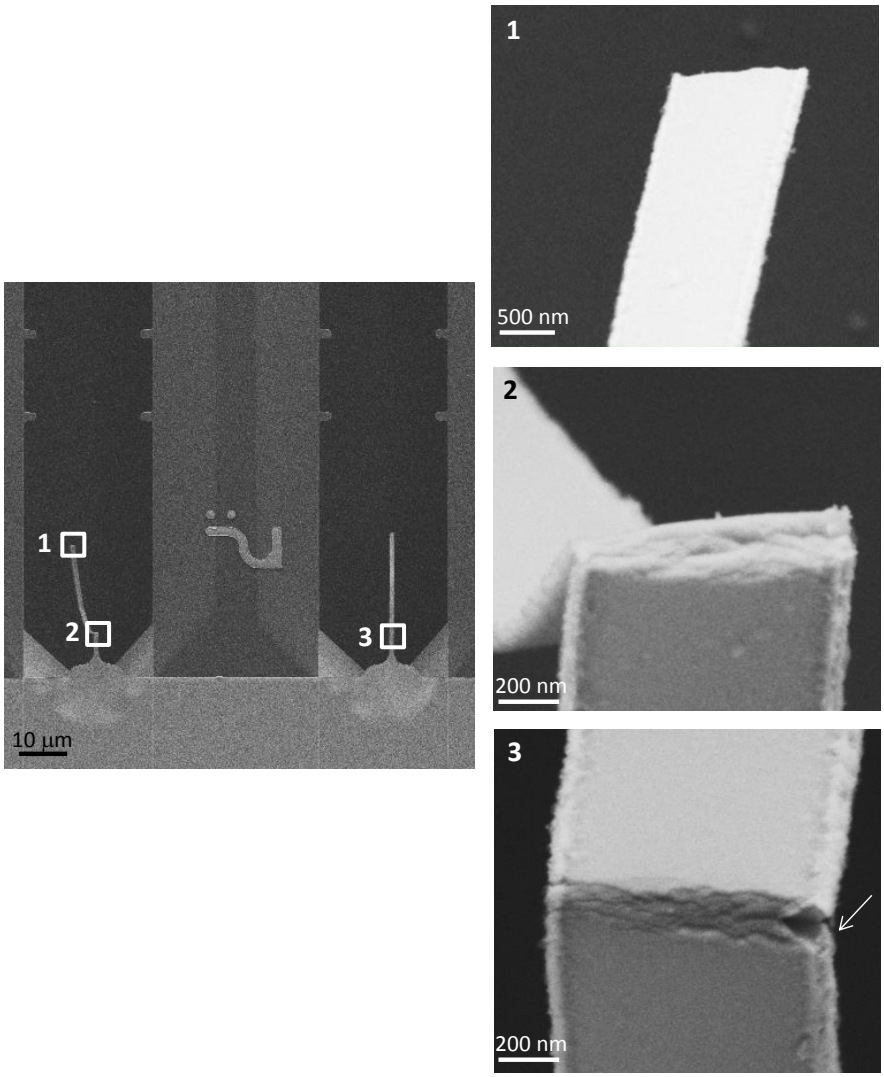

Figure 5.16 *– Broken 200 nm-thick beams. Inset 1 shows the fracture zone, while insets 2 and 3 report the very high local deformation with the trough-the-thickness formation of shear bands.*

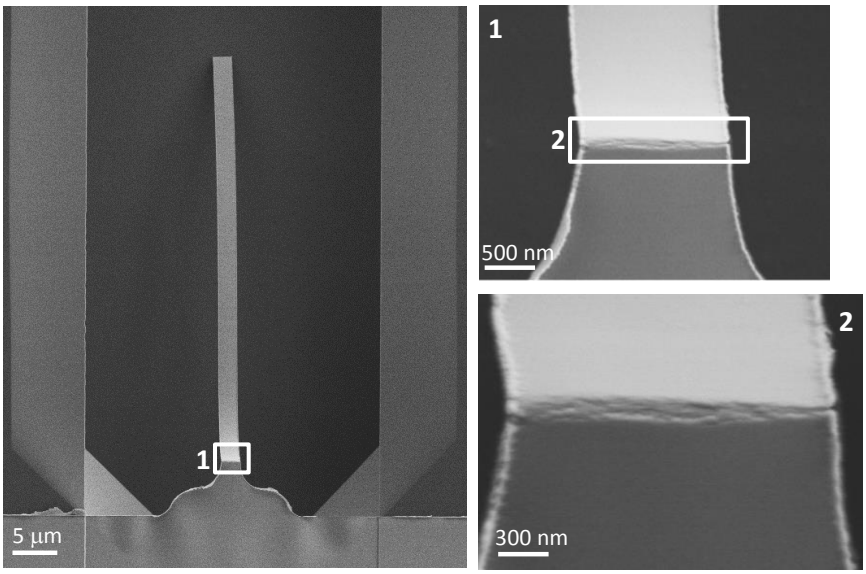

Figure 5.17 *– Fracture of a 100 nm-thick beam. Insets 1 and 2 highlight the development of shear band at the bottom edge of the dogbone.*

5.4 Conclusion

In this chapter, we have investigated the fracture mechanisms of ZrNi TFMGs by using different techniques in order to address failure from the viewpoint of the scratch resistance, of the fracture toughness in the presence of cracks and of the fracture strain in homogeneously deformed specimens.

A common feature for all the results is the effect of the geometrical confinement on the fracture behavior. This geometrical confinement is dictated by the thickness in the case of scratch and of fracture on a Si substrate, while it corresponds to the beam dimension for the lab-on-chip analysis.

The scratch analysis has shown that, even if the scratch morphology is thickness independent, there is a significant change in terms of the length of lateral cracks as well as of the normal force required to scratch the entire thickness. In particular, thinner films shows shorter cracking and they require, in proportion, an higher normal load to scratch the substrate.

Moreover, the thickness confinement plays a strong role in the fracture behavior. As a matter of fact, the thickness causes a transition in fracture surface from corrugation to mirror-like for thicknesses below 500 nm, while being responsible for the corrugation formation (high hydrostatic stress gradient) and the low fracture toughness as measured from the corrugation width. Furthermore, we show that if a SiO_2 capping layer is deposited on thinner film, a through-the-thickness corrugations appears instead of a mirror-like surface since the compressive zone due to bending is completely displaced within the SiO_2 layer. Again an extrinsic effect, since there are no changes in the atomic structure.

Lastly, small-size specimens investigated with the lab-on-chip technique involve an enhanced plasticity (with inversely scale with the free surface). The same confinement is responsible for the homogeneous deformation and the development of an intense shear bands activity at the dogbone edge of broken specimens.

These results suggest that size effects on fracture are related to thickness confinement and thus have an *extrinsic* origin, since we do not found any changes in terms of atomic arrangement (Chapters III and IV). Moreover, even though the atomic structure is comparable with the bulk counterpart (Chapters III and IV), there is a remarkable effect in terms of fracture behavior (which show corrugations instead of dimples) and large deformations (up 14.3%) for freestanding specimens.

Conclusion and Perspectives

The deformation and fracture mechanisms in ZrNi thin film metallic glasses (TFMGs) have been investigated with the aim to reveal the origin of mechanical *size effects*, namely the change of mechanical properties when reducing the size of the sample below the micrometer.

Chapter I has been devoted to a state-of-the-art description of the physics of the glassy state and analyzing the mechanical properties of BMGs at room temperature. Moreover, particular emphasis has been dedicated to literature review of size effects occurring in small scale metallic glasses, reporting major results, controversial trends as well as key elements to understand the evolution of mechanical properties and the deformation modes for small-scale specimens.

Chapter II has been dedicated to the deposition of ZrNi TFMGs and to the description of the characterization techniques. TFMGs has been deposited by DC-magnetron sputtering using a composite target in which Ni slices are inserted in a Zr matrix. This configuration enables to accurately tune film composition. Films have a uniform composition with the absence of impurities and the growth rate is linear. The surface is extremely smooth with an average roughness < 0.6 nm. The characterization of TFMGs involved several techniques aiming to study the structure and the mechanical properties as a function of thickness and composition. The description of the lab-on-chip technique to test mechanical properties of freestanding films constitutes the last part of this chapter, reviewing the basic principles and the fabrication process.

Chapter III focused on the analysis of the structural and elastic properties of ZrNi TFMGs with different thicknesses (from 900 down to 100 nm) and compositions ($Zr_{42}Ni_{58}$, $Zr_{65}Ni_{35}$, $Zr_{75}Ni_{25}$, and $Zr_{85}Ni_{15}$). The techniques involved were X-ray diffraction (XRD), transmission electron microscopy (TEM), X-ray reflectivity (XRR), surface Brillouin spectroscopy (SBS), picosecond ultrasonics (PU), and the measurement of the electrical resistivity. The link between composition and atomic structure has been analyzed, evaluating the effect of thickness as well.

Chapter IV has been dedicated to the analysis of the viscoplastic properties of ZrNi TFMGs. Nanoindentation has been carried out using both continuous stiffness measurement (CSM) as well as standard indentation. The viscoplastic properties have been studied by performing tests at different loading rate in order to the extract the activation volume. The second part of this chapter has been dedicated to the analysis of tensile tests on freestanding beams by using the lab-on-chip method. The stress-strain response has been extracted for different beam geometries, while the overall trends as a function of the beam cross-sectional area have been analyzed. Moreover, stress relaxation phenomena have been studied, obtaining a second estimation of the activation volume.

Chapter V analyzed the fracture behavior of ZrNi TFMGs. The first part, explored the scratch resistance by analyzing the effect of thickness, composition as well as different scratching conditions. In the second part, the fracture of TFMGs on a Si substrate has been reported analyzing the effect of a crack propagating from the Si back face. Lastly, the third part, completed the lab-on-chip results by looking fracture in tension.

Main results

a) Effect of composition at fixed thickness (800 nm)

- $Zr_{42}Ni_{58}$ and $Zr_{65}Ni_{35}$ specimens are fully amorphous, while Zr-rich specimens are characterized by the presence of a dispersed crystalline phase embedded in an amorphous matrix (Table 6.1). Small ($\sim$ 3 nm) and long ($\sim$ 60 nm) crystallites are found for $Zr_{75}Ni_{25}$ and $Z_{85}Ni_{15}$, respectively. For $Zr_{85}Ni_{15}$ the crystalline phase is the hexagonal α–Zr. The formation of this crystalline phase has been related to the lower system confusion for Zr-rich specimens,

- strong Zr-Ni bonds are formed in Ni-rich specimens (i.e. $Zr_{42}Ni_{58}$ and $Zr_{65}Ni_{35}$) which show an increase of all the elastic constants involving elastic, shear and bulk moduli as well as an increase of the mass density and a shift toward higher θ angles of the first sharp diffraction peak (FSDP), see Table 6.1. These results are confirmed by the larger nanoindentation hardness as well,

- a more disordered structure is found for Ni-rich specimens due to an enhanced entropic mixing contribution. This result has been confirmed by the higher values of the fragility index and of the full width at half maximum (FWHM) extracted from the first sharp diffraction peak (FSDP), see Table 6.1. Furthermore, nanoindentation results reveal that Ni-rich compositions are characterized by the presence of a reduced rate sensitivity of hardness leading to a larger activation volume as well as by a lower tendency toward strain burst formation in the indentation curve (Table 6.1). However, for all the investigated composition the fragility index is higher than 51 meaning that a large plastic deformation capacity ($\sim$ 10% in compression) should be expected,

- the electrical resistivity shows a parabolic profile with a maximum for the composition equal to $Zr_{53}Ni_{47}$ due to the enhanced confusion which limit the electron mean free path (Table 6.1). The Nagel and Tauc criterion effectively predicts the fully amorphous structure for $Zr_{42}Ni_{58}$ and $Zr_{65}Ni_{35}$ (higher system confusion) and the maximum electrical resistivity for $Zr_{53}Ni_{47}$ as well.

The composition effect on fracture and on the scratch behavior has been analyzed as well. Specifically, we show that the fracture morphology is characterized by the formation of corrugations whose size is influenced by the composition (even if the thickness confinement effect plays a major role). Moreover, the scratch behavior of $Zr_{85}Ni_{15}$ is completely different with respect to the amorphous compositions ($Zr_{65}Ni_{35}$) with the absence of lateral crack formation.

b) Effect of thickness at fixed composition ($Zr_{65}Ni_{35}$)

- $Zr_{65}Ni_{35}$ TFMGs involve a fully amorphous structure with no shift of the FSDP and no changes in FWHM for a thickness range from 900 down to 200 nm (Table 6.2),

Property	Technique	Evolution
Atomic structure	XRD – TEM	Crystallization phenomena for Zr-rich specimens
Position of FSDP	XRD	↑ for Ni-rich specimens
FWHM	XRD	↑ for Ni-rich specimens
Mass density (ρ)	XRR	↑ for Ni-rich specimens
Elastic constants (E. ν, μ, B)	SBS – PU	↑ for Ni-rich specimens
Fragility index (m_f)	SBS – PU	↑ for Ni-rich specimens
Hardness (H)	Nanoindentation	↑ for Ni-rich specimens
Strain rate sensitivity of hardness (m_H)	Nanoindentation	↓ for Ni-rich specimens
Activation volume	Nanoindentation	↑ for Ni-rich specimens
Strain burst formation	Nanoindentation	↓ for Ni-rich specimens
Electrical resistivity	4-points collinear probe	↑ for Ni-rich specimens

Table 6.1 *– Overall trends as a function of the composition.*

- the density, the elastic constants (elastic, shear and bulk moduli), the fragility index, and the electrical resistivity are thickness independent (Table 6.2),

- the rate sensitivity of hardness measured by nanoindentation is constant leading to a constant activation volume (110 – 130 $Å^3$). The activation volume estimated using the lab-on-chip technique is in agreement with nanoindentation results and it does not depend on the beam geometry (Table 6.2). It is worth noting that the applied strain rate imposed by the stress relaxation in the lab-on-chip technique is in between 6 up to 9 decades slower with respect to the average one imposed during indentation tests (0.025 s^{-1}). This means that the elementary mechanisms which carry plastic deformation – i.e. the shear transformation zones (STZs) operations – are the same and they are not dependent on the specimen geometry and on the applied load.

Hence, it is possible to assume that $Zr_{65}Ni_{35}$ TFMGs have a similar atomic structure. For this reasons, the origin of mechanical size effects should be *extrinsic* and related to a confinement effect in small-scale TFMGs.

Furthermore, it is worth noting that $Zr_{65}Ni_{35}$ TFMGs are characterized by the presence of strong Zr-Ni bonds (high elastic properties) as well as by the presence of a fragility index higher than 51, meaning that it can sustain large plastic strains due to the ease of shear bands formation whose interaction promotes large plastic strains.

Property	Technique	Evolution (value)
Atomic structure	XRD – TEM	Fully amorphous
Position of FSDP	XRD	Constant
FWHM	XRD	Constant
Mass density (ρ)	XRR	Constant (7.4 g/cm^3)
Elastic modulus (E)	SBS – PU – Lab-on-chip	Constant (72 GPa)
Poisson ratio (ν)	SBS – PU	Constant (0.39)
Shear modulus (μ)	SBS – PU	Constant (26 GPa)
Bulk modulus (B)	SBS – PU	Constant (113 GPa)
Fragility index (m_f)	SBS – PU	Constant (60)
Strain rate sensitivity of hardness (m_H)	Nanoindentation	Constant (0.026)
Activation volume	Nanoindentation – Lab-on-chip	Constant (110 – 200 Å^3)
Scratch behavior	Nanoscratch	Similar morphologies
Electrical resistivity	4-points collinear probe	Constant (186 μΩ cm)

Table 6.2 *– Constant properties of $Zr_{65}Ni_{35}$ a function of the film thickness or beam geometry (only for lab-on-chip specimens).*

Moreover, we have shown that:

- the hardness increases when reducing the thickness (Table 6.3),

- tensile test on freestanding TFMGs have shown that the films deform homogeneously with a total deformation that can be very large (above 14 %). The yield strength (σ_y) is dependent on the beam cross-section and not only on the film thickness (Table 6.3). Specifically, we show that σ_y approaches the ideal strength for small cross-sections (3300 MPa), while being close to literature reported values of Zr-based BMGs for larger ones (1800 MPa). The stress-strain response involves clear strain hardening which is more important for larger cross-sections (Table 6.3). On the other hand, we have shown that the fracture strain depends on the specimen free surface (Table 6.3), while the broken specimens are characterized by the presence of intense shear bands activity at the bottom edge of the dogbone,

- the fracture behavior of TFMGs on a Si substrate is characterized by a transition of the fracture mechanisms for thicknesses below 500 nm showing a mirror-like surface, while thicker films are characterized by the formation of corrugations (Table 6.3). The fracture toughness, estimated from the corrugations size, is below 4 MPa m$^{1/2}$ (Table 6.3), a value which is much smaller than the corresponding bulk counterpart (50 MPa m$^{1/2}$). Moreover, if a 400 nm-thick film is coated by a SiO_2 capping layer corrugations develops through all the thickness,

- thinner films need (in proportion) higher forces for reaching the substrate during scratch. Moreover, for thinnest films the lateral cracks are shorter and the film delaminates when the tip reaches the substrate (Table 6.3).

Property	Technique	Evolution
Hardness (H)	Nanoindentation	↑ for small thicknesses
Deformation mode	Lab-on-chip	Homogeneous (independent of beam geometry)
Yield stress (σ_y)	Lab-on-chip	↑ for small cross-sections
Strain hardening coefficient (n)	Lab-on-chip	↓ for small cross-sections
Fracture strain (ε_f)	Lab-on-chip	↑ for small free surfaces
Fracture mode	Fracture test on Si substrate	Transition corrugations to mirror-like surface for thicknesses < 500 nm
Fracture toughness (K_c)	Fracture test on Si substrate	< 4 MPa $m^{1/2}$
Scratch morphology	Nanoscratch	Longer cracks for thicker films without film delamination at the substrate interface

Table 6.3 *– Thickness or beam geometry-dependent properties of $Zr_{65}Ni_{35}$ TFMGs.*

Since we have shown that the films have a similar atomic structure, the origin of the size effects previously reported (Table 6.3), should be found elsewhere. Specifically, the observed changes have an extrinsic origin related to a confinement effect imposed by the thickness or by the beam geometry (i.e. the cross-section) for freestanding films.

The increment of hardness is related to the thickness confinement effect enhanced for thinnest films and which might prevent the development of mature shear bands during indentation. Similar results have been found in standard indentation tests conducted at fixed normalized indentation depth (25%) which demonstrate the absence of shear bands around the indent for samples experiencing a shallower penetration (i.e. 50 nm on a 200 nm-thick film).

For the same reason, we have shown that the geometrical confinement in small specimens analyzed with the lab-on-chip technique is responsible for the homogeneous deformation as well as for the evolution of the yield stress and of the strain hardening coefficient. Micrometer-scale beams are characterized by the absence of macroscopic defects (flaws or porosity) avoiding catastrophic failure via a single shear band events and explaining the homogeneous deformation with large plastic deformation. Moreover, we suppose that for low cross-sections there is a reduced amount of potentially actives STZs which can lead to an increase of the yield strength and a reduction of the strain hardening coefficient which is related to the ease of shear bands formation and their interaction. On the other hand, large cross-sectional beams involve a reduced yield strength which can arise from the ease of activation of the numerous STZs as also sustained by the increment of the strain hardening coefficient. It is worth noting that the evolution of the yield stress has been effectively modeled with an analysis based on the Griffith criterion coupled with a theoretical estimation of the ideal strength.

For large cross-sections, the development of intense plasticity is correlated to the high fragility index and the ease of shear-embryo formation and interaction. This description is confirmed by the trend of the fracture plastic strain which is dependent on the specimen free surface. As a matter of fact, the enhanced likelihood to find defects in large free surfaces limits the plastic behavior.

The fracture analysis of TFMGs on a Si substrate is strongly related to thickness confinement effect as well. The failure mechanism involves corrugations for the thickest films and a transition – at 500 nm thickness – with perfectly flat fracture surface. This change is related to the *plastic collapse* phenomenon occurring for thin films in which the plastic zone ahead of the crack tip and the compressive one due to bending merge together leading to a mirror-like surface. Moreover, we have shown that the origin of corrugation in thicker films is also dependent on the high stress gradient ahead of the crack tip which can frustrate the meniscus instability preventing the develop of dimples, while leading to cavitation. Moreover, the formation of corrugations have been justified using the Argon and Salama model as well as by fracture test conducted on a 400 nm-thick covered with a SiO_2 capping layer which pull the plastic zone due to bending outside the TFMGs providing corrugations even for a 400 nm-thick film.

Extrinsic size effects affect the scratch behavior as well. As a matter of fact, the length of the lateral cracks increases for thicker films which also require, in proportion, a reduced force to scratch the entire film and no delamination events are observed when the tip gets the substrate interface. This means that in a thinner film there is a larger amount of stored energy involving a limited crack growth and an abrupt release once the substrate surface is reached, leading to delamination.

The novelty of our results consists in the use of the lab-on-chip technique to extract film mechanical properties coupled with a thorough analysis involving a number of other techniques enabling the extraction of the entire mechanical behavior.

The lab-on-chip technique can be used to effectively extract the complete stress-strain response of TFMGs involving dimensions up to 100 μm-long and avoiding the use of focus ion beam (FIB). We have shown that there is a strong dependency of the main properties (σ_y, n, ε_f) on the beam geometry and this behavior was successfully modeled. Moreover, the lab-on-chip technique enables the analysis of the relaxation phenomena (which has never reported in literature for TFMGs) with the calculation of the activation volume.

Original results involved the fracture of thin film metallic glasses representing an unique case in the literature. However, the combination of several experimental techniques led to a complete and organic analysis of the entire mechanical behavior considering both the effect of the composition and the thickness, so far matter of intense debate in the scientific literature.

Perspectives

On a short term view, there are still several open issues whose analysis could strengthen the previously reported results and expand the research field especially with the lab-on-chip technique.

So far, it has been claimed that the deformation occurs homogeneously throughout the specimen without localization. The TEM analysis of elastically deformed beams and strongly plastically deformed films should provide fundamental novel elements to understand the physics of deformation of small-scale metallic glasses. Note that these tests have been already started in collaboration with Dr. Hosni Idrissi of the University of Antwerpen, nevertheless, up to now, we do

not have results yet due to the complexity of sample manipulation and data analysis which is very tricky for amorphous systems.

The analysis of mechanical properties with the lab-on-chip technique can be expanded with the analysis of different thicknesses and compositions as well. In the former case, it will be very interesting to investigate the behavior of a thicker film (i.e. > 500 nm) and to complete the analysis of the overall trends by considering other thickness and beam geometries. In the latter case, interesting results can arise from the analysis of the stress-strain response of other compositions (i.e. $Zr_{42}Ni_{58}$, $Zr_{75}Ni_{25}$, and $Zr_{85}Ni_{15}$). Lastly, the lab-on-chip technique enables the evaluation of the mechanical behavior of notched beams with different geometries and characterize the localization process. This analysis coupled with TEM observations can provide further insights into the deformation mechanisms occurring in TFMGs.

The mechanical properties of freestanding TFMGs can also be tested by other techniques. For instance, we develop freestanding cantilevers whose mechanical properties can be probed by bending test using nanoindentation. This analysis can be coupled with the observation of the formation of shear bands at the cantilever joint by using SPM or AFM. Moreover, the mechanical properties can be tested for different cantilever shapes (rectangular and triangular) and geometries. In this sense, a collaboration with the University of Rennes I started, but no results have been obtained so far.

Among the other studies a wider compositional range should be analyzed. For instance, we have shown that the composite sputtering target enables to deposit TFMGs with a composition ranging from pure Zr to $Zr_{42}Ni_{58}$. Nevertheless, we investigated only four compositions. The evolution of mechanical and physical properties as a function of a broader range of composition can reinforce the results, while providing thorough understanding on the composition effect on the atomic structure. As a first study, the analysis of scratching test for the compositions $Zr_{42}Ni_{58}$ and $Zr_{75}Ni_{25}$ will be easy to perform since samples are already available. However, on the long term it will be very inserting to have a complete view of the functional and mechanical properties as a function of the composition exploiting all the techniques presented in this thesis. Furthermore, the composite target geometry enables to deposit other metallic glasses such as ZrCu whose properties can be compared to the ZrNi investigated in this thesis.

On a longer term view, a thorough study functional properties of TFMGs remains a very open scientific field. In this thesis we investigated only the electrical resistivity showing how the variation of this property can be used to extract fundamental quantities such as the glass and the crystallization temperature, otherwise very difficult to measure for thin films. However, a more complete analysis can involve the analysis of electron mobility and the estimation of the carriers concentration. The analysis of magnetic and optical properties will be very interesting as well. As a matter of fact, specimens are very smooth with potential use as optical mirrors, while the magnetic properties can also be very interesting to probe due to the ferromagnetic behavior of Ni. It will be fascinating to analyze how these properties changes with the thickness and to explore completely new domains which can increase the potential use of TFMGs.

Lately, the analysis of the effect of heat treatment on the mechanical and functional properties of TFMGs can be very interesting as well. Understanding the crystallization behavior and how the properties vary compared to the more energetically favorable crystalline phase can open new scientific challenges and lead to new discoveries.

Appendix A – Nanoindentation results

In this appendix, additional nanoindentation results are provided in order to strengthen the discussion in Chapter IV (section 4.1), by giving the variation of hardness (H) as a function of the normalized indentation depth – namely the ratio between indent penetration and film thickness – for different loading rate $(\dot{P}/P)$. Note that using the CSM (continuous stiffness measurement) mode, $\dot{P}/P$ is kept constant during the test allowing to measure the rate sensitivity of hardness (m_H) and, hence, the activation volume (section 4.1).

Figure 4.1b shows the variation of hardness for an imposed loading rate equal to 0.05 s^{-1}. Specifically, H increases when reducing film thickness. The average H value – taken for an interval in between 10 and 20% – has been reported in Figure 4.1c.

Figure A1a-b shows the variation of H as a function of the normalized indentation depth for a loading rate equal to 0.02 and 0.1 s^{-1}, respectively. In a very similar way to what reported in Figure 4.1b, H increases when thickness decreases. The average hardness, calculated for a normalized indentation depth in the interval of 10 and 20% (vertical black lines) is used to extract the rate sensitivity reported in Figure 4.7.

As discussed in section 4.1, Figure A1a-b shows that there is no substrate effect since the hardness is constant at different normalized indentation depths. Moreover, it can be observed that H increases when reducing the thickness, a phenomenon which we have related to the enhanced difficulty for shear bands formation when the geometrical confinement (i.e. the smaller thickness) is enhanced.

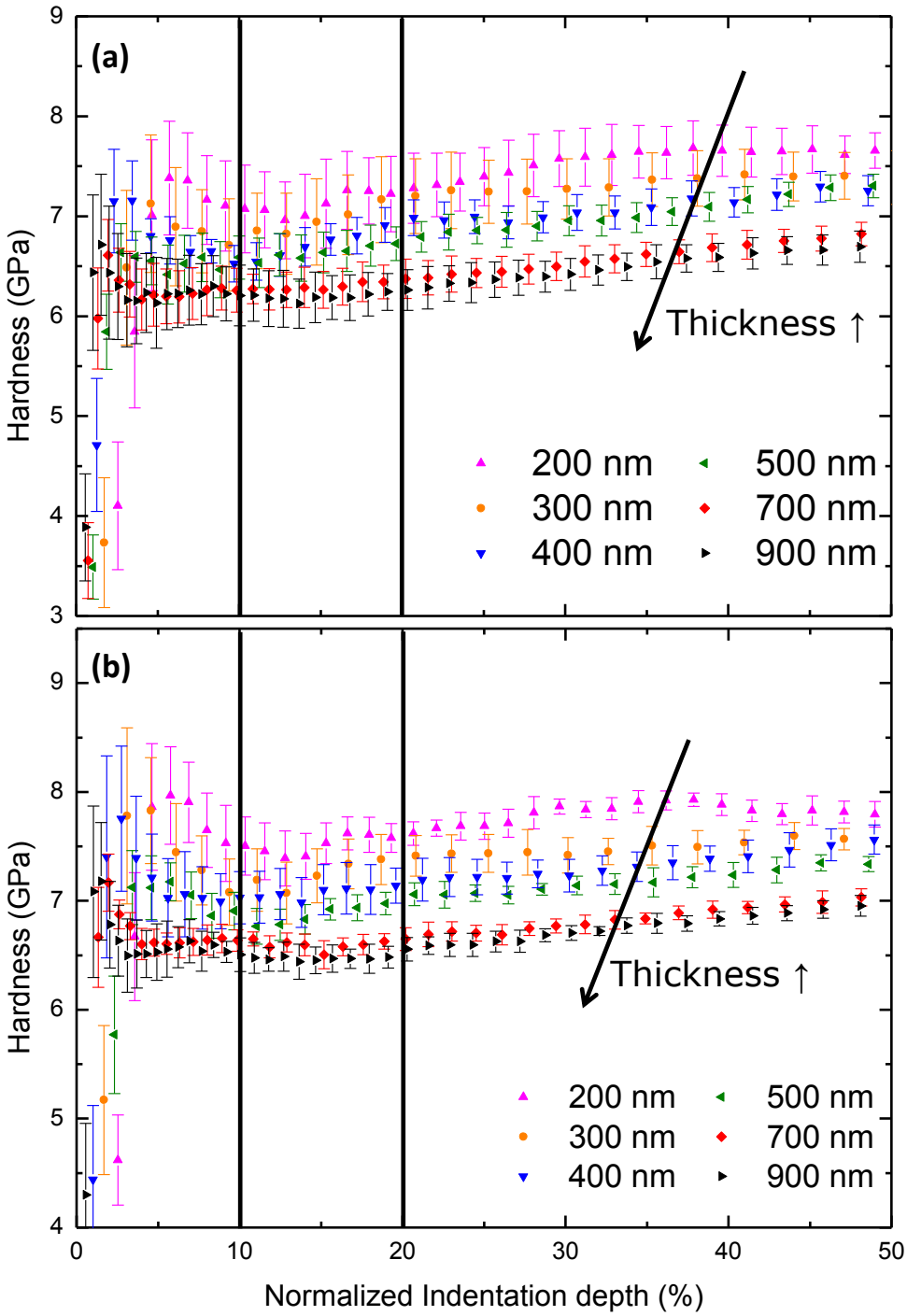

Figure A1 *– Variation of hardness as a function of the normalized indentation depth for different load rates, respectively of 0.02 s^{-1} and 0.1 s^{-1} (a) and (b). The vertical lines indicate the interval used for the extraction of the average hardness reported in Figure 4.7.*

Appendix B – Mechanical properties of freestanding $Zr_{65}Ni_{35}$ TFMGs

In this appendix, we provide additional results obtained using the lab-on-chip technique involving a uniaxial tension test of freestanding $Zr_{65}Ni_{35}$ thin film metallic glasses (TFMGs), see section 4.2.

a) Strain hardening analysis

Figure A2 shows the strain hardening analysis of a 200 nm-thick film with different lengths and widths. A Hollomon equation fits the data (equation 4.6) to extract the strain hardening coefficient (*n*). The extracted *n* values have been plotted as a function of the specimen cross-section in Figure 4.19 (red circles). As discussed in section 4.2, the strain hardening phenomenon is an unique feature of TFMGs and is closely related to the high fragility index enabling the formation of multiple shear bands. Figure A2b shows that the strain hardening is enhanced for larger beams.

The strain hardening analysis of a 110 nm-thick film is reported in Figure A3. Different specimen geometries are indicated in the inset. Data has been fitted using a Hollomon equation (equation 4.6) enabling the extraction of the strain hardening coefficient (*n*). As reported in Figure A2, 110 nm-thick TFMGs exhibit strain hardening enhanced for larger cross-sections (Figure A3b).

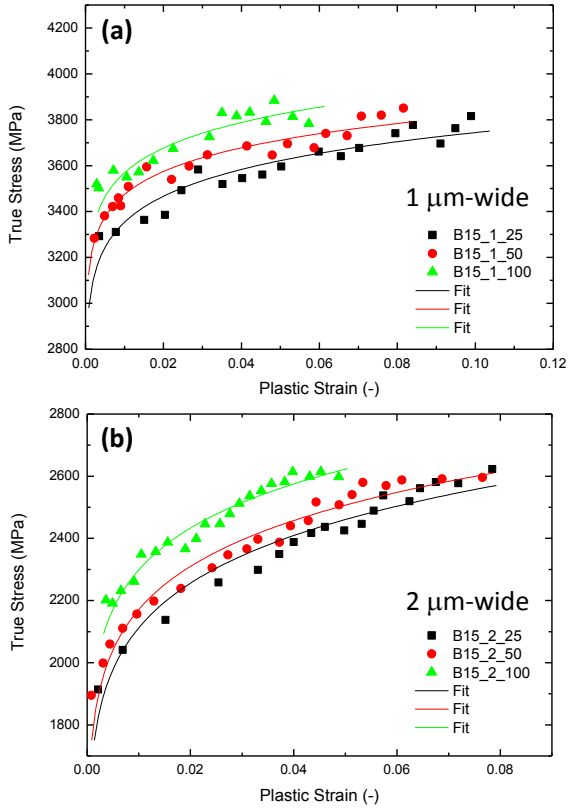

Figure A2 *– Strain hardening analysis of 200 nm-thick specimens. Data have been fitted with equation 4.6 (Hollomon fit) to extract the strain hardening coefficient.*

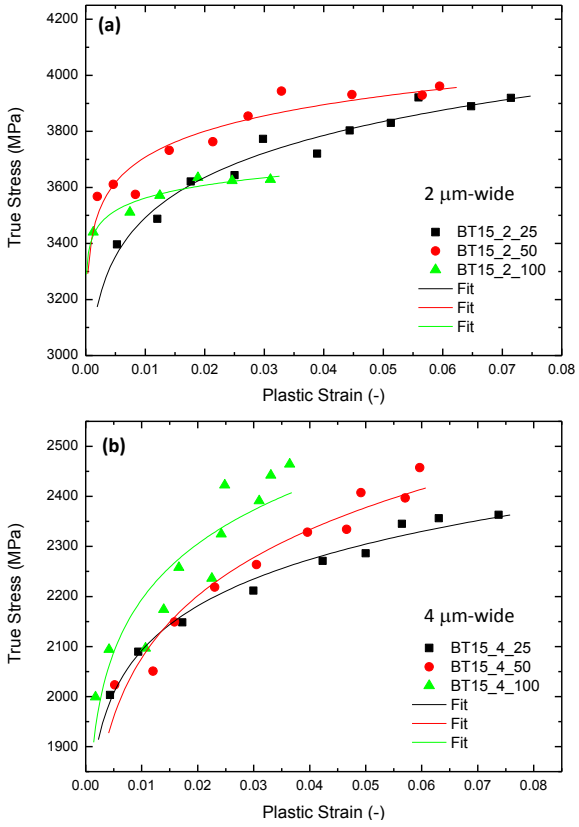

Figure A3 *– Strain hardening analysis of 110 nm-thick specimens. Data have been fitted with equation 4.6 (Hollomon fit) to extract the strain hardening coefficient.*

b) Relaxation stress-strain response for different beam geometries

In this section, we add the relaxation stress-strain curves for different beam geometries. The graphs here presented are complementary to Figure 4.21, while analyzing the relaxation for 50 and 100 μm-long beams with different thicknesses (360, 200 and 110 nm) and widths (1 and 2 μm).

Figure A4 shows the relaxation behavior of 50 μm-long specimens with a thickness equal to 360, 200 and 110 nm, respectively (a), (b), and (c). The width is equal to 1 μm for (a) and (b), and 2 μm for (c).

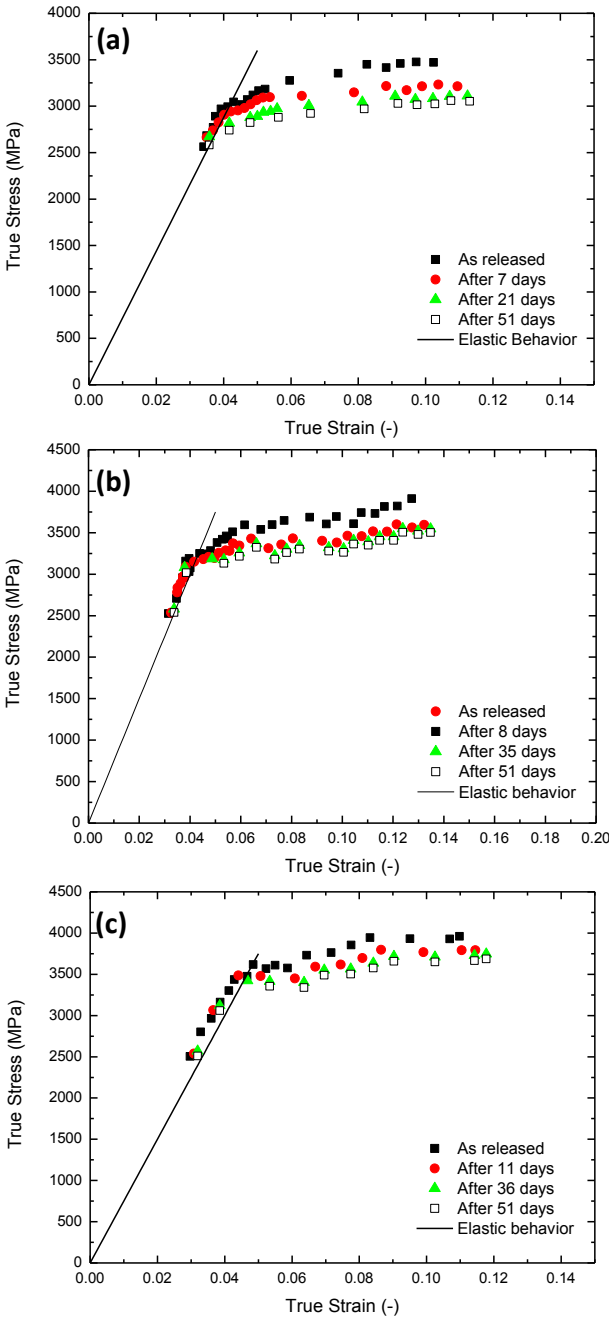

Figure A4 *– Stress relaxation for 360, 200 and 110 nm-thick beams, respectively (a), (b) and (c). The beam length is fixed and equal to 50 μm, while the width is equal to 1 μm for (a) and (b), and 2 μm for (c).*

As stated in section 4.2.5, relaxation takes place only after yielding and follows a non-linear kinetics with a stress drop enhanced during the first week after the release, while there is a smaller decrement for longer times enabling the extraction of the activation volume with the method reported in section 4.2.5.

Similar results are obtained for other geometries, Figures A5 to A8.

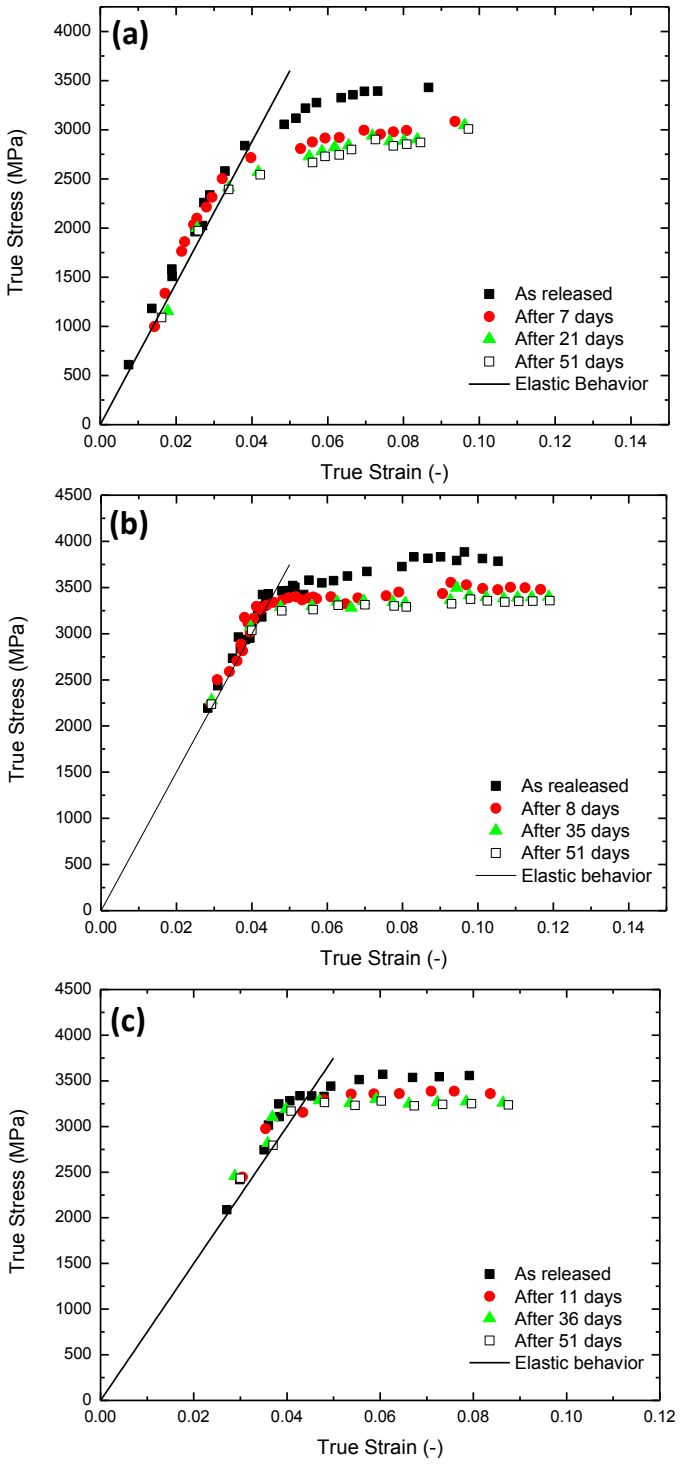

Figure A5 *– Stress relaxation for 360, 200 and 110 nm-thick beams, respectively (a), (b) and (c). The beam length is fixed and equal to 100 μm, while the width is equal to 1 μm for (a) and (b), and 2 μm for (c).*

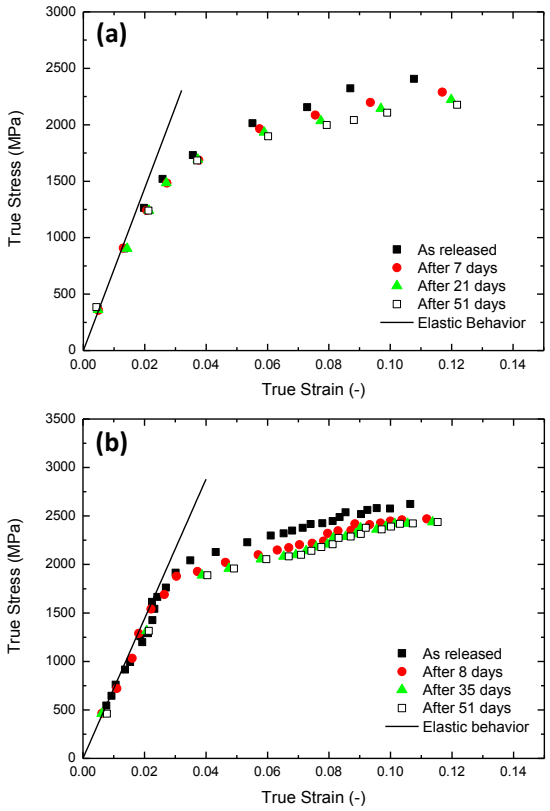

Figure A6 *– Stress relaxation for 360 and 200 nm-thick beams, respectively (a) and (b). The beam length is fixed and equal to 25 μm, while the width is equal to 2 μm.*

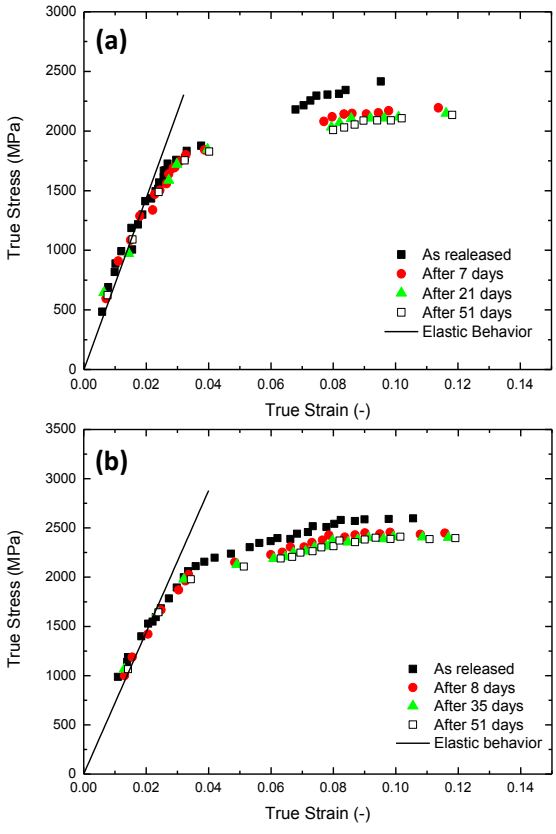

Figure A7 *– Stress relaxation for 360 and 200 nm-thick beams, respectively (a) and (b). The beam length is fixed and equal to 50μm, while the width is equal to 2 μm.*

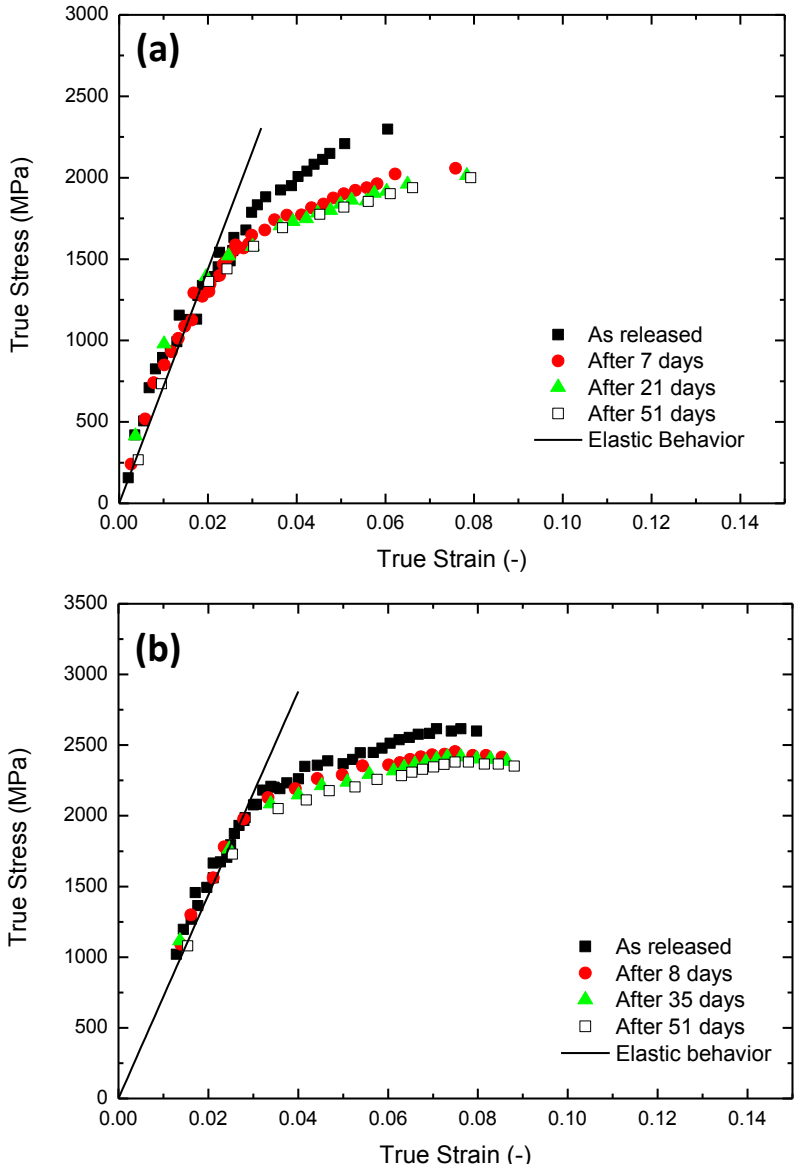

Figure A8 *– Stress relaxation for 360 and 200 nm-thick beams, respectively (a) and (b). The beam length is fixed and equal to 100 μm, while the width is equal to 2 μm.*

Figure A9 shows the relaxation kinetics for two beams with a geometry equal to 25 μm x 1 μm x 200 nm and 25 μm x 2 μm x 110 nm. As reported in Figure 4.23 (25 μm x 1 μm x 360 nm), the variation of the average displacement as a function of time follows a logarithmic kinetic as in equation 4.10, which enable to fit the data and obtain the values of the average activation volume with the procedure described in section 4.2.5.

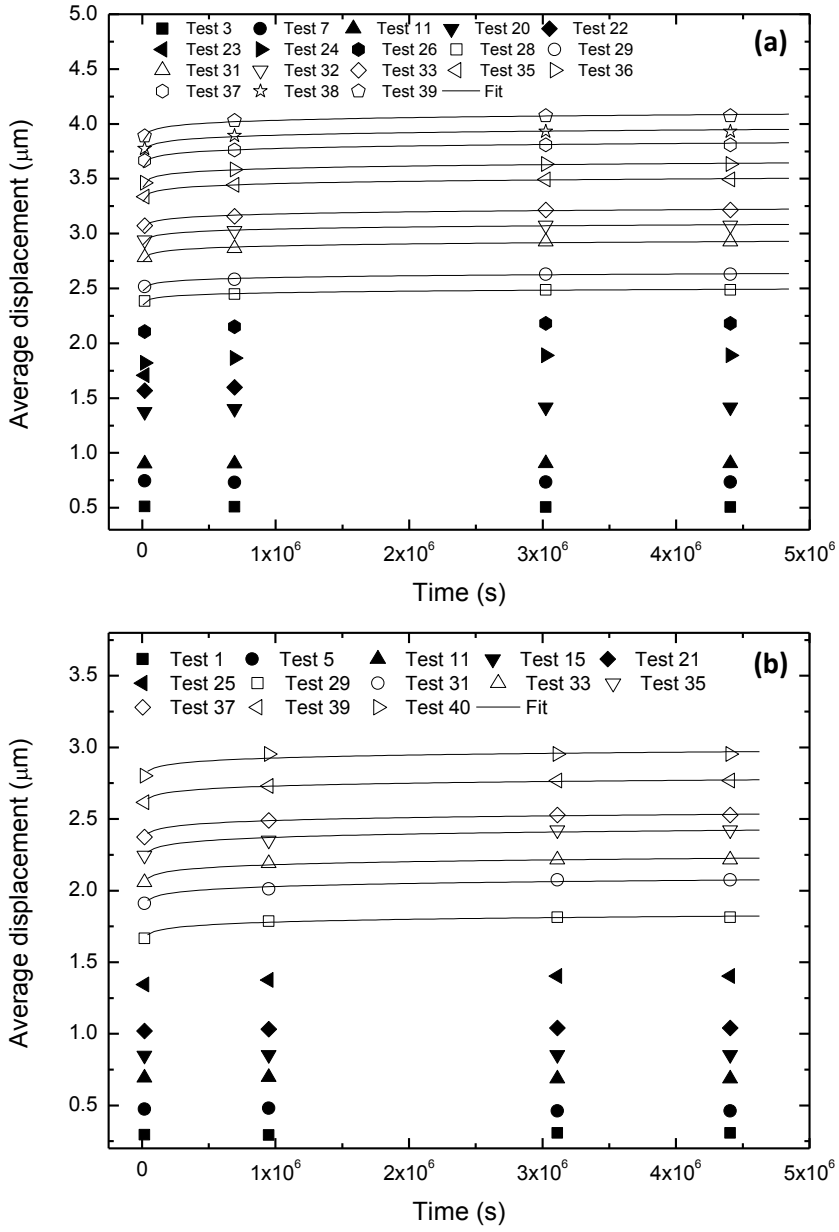

Figure A9 *– Average displacement as a function of the time for a beam of 25 μm x 1 μm x 200 nm and of 25 μm x 2 μm x 110 nm, respectively (a) and (b). Plastically deformed specimens (empty symbols) relax following a logarithmic kinetics as shown by the fitting lines.*

Figure A10 shows the calculated activation volume as a function of the actuator length (which is proportional to the applied stress) for 50 μm-long beams with different widths and thicknesses. For a fixed geometry, the activation volume is constant with values in between 110 and 200 $Å^3$. Similar results are reported in Figure 4.24a for 25 μm-long specimens.

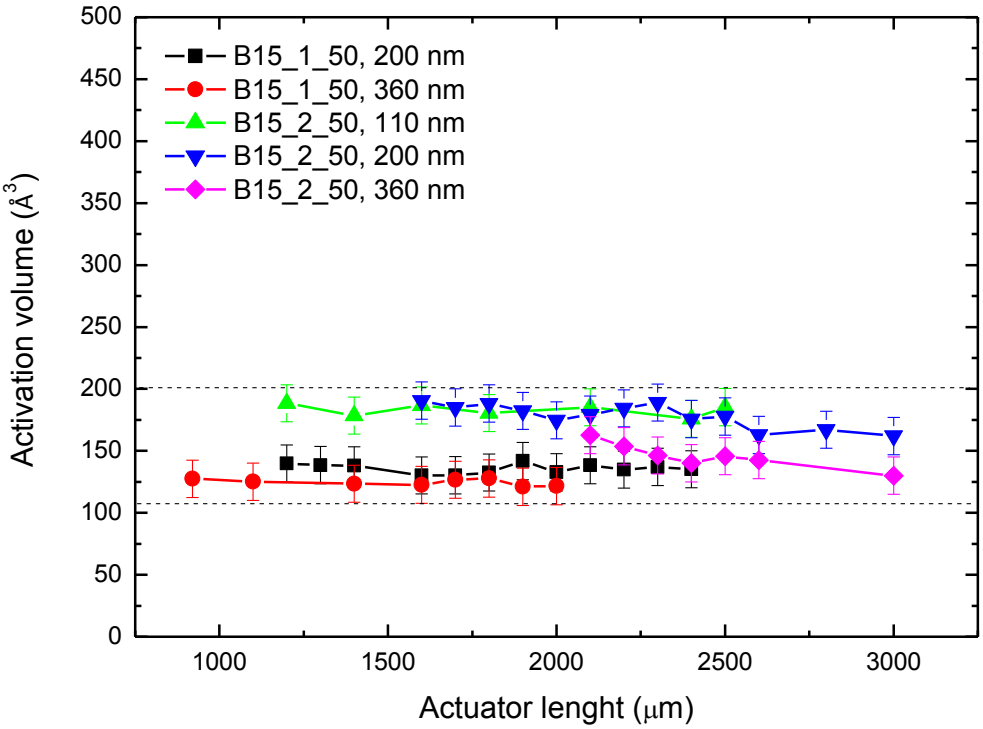

Figure A10 *– Average activation volume as a function of the actuator length for different beam geometries with a fixed length of 50 μm.*

Appendix C – Scratch resistance of ZrNi TFMGs

In this appendix, we provide additional nanoscratch results involving the effect of the scratch velocity. Specifically, we show the results for a scratch velocity equal to 3 μm/s for a 300 nm thick film with the same loading condition as in Figure 5.12. As a reminder, the normal load increases linearly from 0 up to 60 mN over a length of 180 μm.

The analysis of Figure A12, is very similar to Figure 5.1 involving the same film thickness and loading ramp, but a higher scratch velocity (30 μm/s). This indicates that, for the selected parameter, there are no appreciable changes in scratch morphology and its evolution. In Figure A11, it can be noted that:

- in zone 1, the COF increases from 0 up to 0.3 and then it stabilizes around 0.3. This corresponds to the tip glide over the film involving small penetration and elastic deformations, see for instance the high loading recovery in Figure A11b. Once the plateau is reached there is an enhancement of plastic deformation and the formation of lateral cracks whose spacing reduces increasing the load (inset 1 of Figure A11c). Cracks develop at an angle in between 41 and 48° with respect to the scratch direction,
- if the normal load further increases, there is a reduction of the COF down to 0.25 (zone 2). This reduction is related with a reduction of the lateral force necessary for the tip displacement. This means that the TFMG opposes a reduced resistance to the indent penetration and forward displacement, as justified by the intense cracking formation which increase in length and branching. Cracks are first oriented at an angle between 41 and 48° and then re-oriented parallel to the scratch direction (inset 2 of Figure A11). The cracks maximum length is around 0.8 μm,
- close to the interface with the substrate, the COF increases up to 0.4 (zone 3) and then slightly reduces (zone 4). In zone 3 there is film delamination with the formation of a large lateral pile-up. The substrate scratching can be recognized in the SEM by the darker region in the middle of the scratch (see the inset 5 of Figure A11c).

The same scratch features are found for a scratch velocity equal to 30 mN/s, as reported in Figure 5.1. Moreover, the effect of scratch velocity is not appreciable for all the other investigated thicknesses and compositions reported in Chapter V, Figures 5.2 to 5.6.

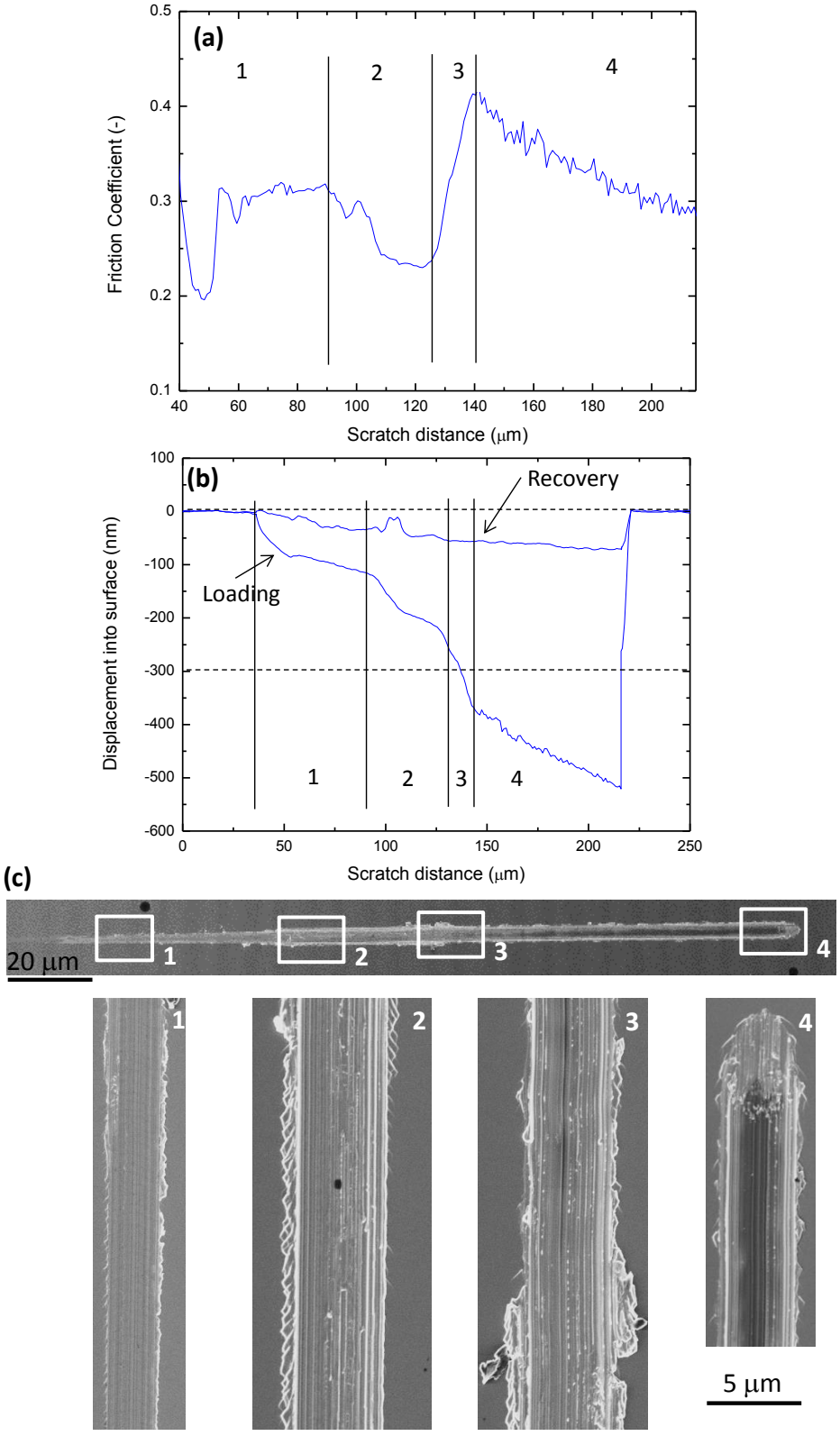

Figure A11 *– Evolution of the COF and of the displacement into surface as a function of the scratch distance, respectively (a) and (b); (c) the corresponding scratch morphology. The film thickness is equal to 300 nm. The scratch length is equal to 180 μm with the loading increasing from 0 up to 60 mN with a constant velocity of 3 μm/s.*

List of references

Publications in international journals:

1. **M. Ghidelli**, S. Gravier, J.-J. Blandin, T. Pardoen, J.-P. Raskin, F. Mompiou - *Compositional-induced structural change of ZrNi thin film metallic glasses deposited by magnetron sputtering*, Journal of Alloys and Compounds, 615, S348-351, (2014)
2. **M. Ghidelli**, A. Volland, J.-J. Blandin, T. Pardoen, J.-P. Raskin, F. Mompiou, P. Djemia, S. Gravier - *Exploring the mechanical size effects in $Zr_{65}Ni_{35}$ thin film metallic glasses*, Journal of Alloys and Compounds, 615, S90-S92, (2014)
3. **M. Ghidelli**, S. Gravier, J.-J. Blandin, J.-P. Raskin, F. Lani, T. Pardoen - *Size-dependent failure mechanisms in ZrNi thin metallic glass films*, Scripta Materialia 89, 9-12, (2014)
4. **M. Ghidelli**, S. Gravier, J.-J. Blandin, P. Djemia, F. Mompiou, G. Abadias, J.-P. Raskin, T. Pardoen, *Extrinsic mechanical size effects in thin ZrNi metallic glass films*, Acta Materialia 90, 232-241 (2015)
5. **M. Ghidelli**, S. Gravier, J.-J. Blandin, M. Coulombier, R. Vayerette, J.-P. Raskin, T. Pardoen, *Giant ductility of micrometer-sized freestanding metallic glass films*, in preparation, target: Nature materials

International conference and school contributions

1. **M. Ghidelli**, S. Gravier, J.-J. Blandin, P. Djemia, M. Coulombier, R. Vayerette, J.-P. Raskin, T. Pardoen - *Giant ductility of ZrNi thin freestanding metallic glasses films*, MRS Fall Meeting Boston (USA), 30 November 30 - 5 December 5, (2014) (Oral)
2. T. Pardoen, M. Coulombier, M.-S. Colla, G. Lemoine, R. Vayrette, **M. Ghidelli**, J.-J. Blandin, S. Gravier, L. Delannay, J.-P. Raskin - *Size dependent plastic localization in thin nanocrystalline or amorphous metallic films*, MRS Fall Meeting Boston (USA), 30 November 30 - 5 December 5, (2014) (Oral)
3. **M. Ghidelli**, S. Gravier, J.-J. Blandin, M. Coulombier, R. Vayerette, J.-P. Raskin, T. Pardoen - *On the elastoviscoplastic and fracture behaviour of ZrNi thin film metallic glasses*, Interuniversity Attraction Pole (IAP) plenary meeting, Ecole Royale Militaire, Brussels (Belgium), 17-18 November 2014 (Invited Oral presentation, 25 minutes)

4. **M. Ghidelli**, S. Gravier, J.-J. Blandin, P. Djemia, M. Coulombier, R. Vayerette, J.-P. Raskin, T. Pardoen - *Characterization of mechanical properties of thin ZrNi layers*, The second winfab scientific day, Université catholique de Louvain (UCL), Louvain-la-Neuve (Belgium), 17 October 2014 (Oral)

5. **M. Ghidelli**, J.-J. Blandin, T. Pardoen, F. Lani, J.-P. Raskin, F. Mompiou, P. Djemia, S. Gravier - *Size-dependent mechanical behavior of sputter-deposited $Zr_{65}Ni_{35}$ thin film metallic glasses*, ISMANAM 2014, Cancun (Mexico), 29 June - 04 July 2014 (Oral)

6. **M. Ghidelli**, J.-J. Blandin, T. Pardoen, J.-P. Raskin, S. Gravier - 5th IDS-FunMat training school, Spa (Belgium), 16-21 March 2014 (Oral + Poster)

7. **M. Ghidelli**, A. Volland, J.-J. Blandin, T. Pardoen, F. Lani, J.-P. Raskin, F. Mompiou, P. Djemia, S. Gravier - *Size dependent mechanics of thin ZrNi metallic glass films*, Interuniversity Attraction Pole (IAP) plenary meeting, Leuven (Belgium), 12 November 2013 (Poster)

8. **M. Ghidelli**, A. Volland, J.-J. Blandin, T. Pardoen, F. Lani, J.-P. Raskin, F. Mompiou, P. Djemia, S. Gravier - *Size dependent mechanics of thin ZrNi metallic glass films*, Nanomechanical Testing in Materials Research and development IV, Olhão (Portugal), 6-11 October 2013 (Poster)

9. **M. Ghidelli**, S. Gravier, J.-J. Blandin, T. Pardoen, J.-P. Raskin, F. Mompiou, P. Djemia - *Compositional-induced structural change of ZrNi thin film metallic glasses deposited by magnetron sputtering*, ISMANAM 2013, Torino (Italy), 30 June - 05 July 2013 (Oral)

10. **M. Ghidelli**, A. Volland, J.-J. Blandin, T. Pardoen, J.-P. Raskin, F. Mompiou, P. Djemia, S. Gravier – *Exploring the mechanical size effects in $Zr_{65}Ni_{35}$ thin film metallic glasses*, ISMANAM 2013, Torino (Italy), 30 June - 05 July 2013 (Oral)

11. **M. Ghidelli**, J.-J. Blandin, T. Pardoen, J.-P. Raskin, S. Gravier – 3rd IDS-FunMat training school, Annecy (France), 17-22 March 2013 (Oral + Poster)

12. **M. Ghidelli**, J.-J. Blandin, T. Pardoen, J.-P. Raskin, S. Gravier - 2nd IDS-FunMat training school, Anglet (France), 25-31 March 2012 (Oral)

Bibliography

[1] C. Suryanarayana, A. Inoue, Bulk Metallic Glasses, CRC Press, 2011.

[2] M. Ashby, A. Greer, Scr. Mater. 54 (2006) 321.

[3] A.L. Greer, Y.Q. Cheng, E. Ma, Mater. Sci. Eng., R 74 (2013) 71.

[4] J.R. Greer, J.T.M. De Hosson, Prog. Mater. Sci. 56 (2011) 654.

[5] P.M. Ossi, Disordered materials: An introduction, Springer Science & Business Media, 2003.

[6] P. Chaudhari, D. Turnbull, Science 199 (1978) 11.

[7] Y.-T. Cheng, W.L. Johnson, Science 235 (1997) 997.

[8] Y.Q. Cheng, E. Ma, Prog. Mater. Sci. 56 (2011) 379.

[9] W.D. Callister, Materials Science and Engineering, John Wiley & Sons Inc, 2007.

[10] A.L. Greer, Science 267 (1995) 1947.

[11] E. Ma, Z. Zhang, Nature Mater. 10 (2011) 10.

[12] J.D. Bernal, Nature 185 (1960) 68.

[13] P. Lamparter, Phys. Scr. T57 (1995) 45.

[14] S. Steeb, P. Lamparter, J. Non-Cryst. Solids 156-158 (1993) 24.

[15] D.B. Miracle, Acta Mater. 54 (2006) 4317.

[16] H.W. Sheng *et al.*, Nature 439 (2006) 419.

[17] H.W. Sheng *et al.*, Acta Mater. 56 (2008) 6264.

[18] Y.Q. Cheng *et al.*, Acta Mater. 56 (2008) 5263.

[19] Y. Cheng, H. Sheng, E. Ma, Phys. Rev. B: Condens. Matter 78 (2008) 014207.

[20] Y.Q. Cheng, A.J. Cao, E. Ma, Acta Mater. 57 (2009) 3253.

[21] D.B. Miracle, Nature Mater. 3 (2004) 697.

[22] Y.Q. Cheng, E. Ma, H.W. Sheng, Phys. Rev. Lett. 102 (2009) 245501.

[23] W. Klement, R.H. Willens, P. Duwez, Nature 187 (1960) 869.

[24] H.S. Chen, D. Turnbull, Acta Metall. 17 (1969) 1021.

[25] A. Inoue, T. Zhang, T. Masumoto, Mater. Trans. 30 (1989) 965.

[26] J.F. Löffler, Intermetallics 11 (2003) 529.

[27] M. Telford, Mater. Today 7 (2004) 36.

[28] A. Inoue, A. Takeuhi, Mater. Trans. 43 (2002) 1892.

[29] S.R. Nagel, J. Tauc, Phys. Rev. Lett. 35 (1975) 380.

[30] K.H.J. Buschow, N.M. Beekmans, Phys. Rev. B: Condens. Matter 19 (1979) 3843.

[31] K. Pekala, R. Trykozko, Appl. Phys. 22 (1980) 369.

[32] J. Antonowicz *et al.*, J. Appl. Phys. 115 (2014) 203714.

[33] J.P. Chu *et al.*, Thin Solid Films 520 (2012) 5097.

[34] A. Inoue, Acta Mater. 48 (2000) 279.

[35] A. Gebert *et al.*, Electrochimica Acta 53 (2008) 3403.

[36] H.S. Chen, Solid State Commun. 33 (1979) 915.

[37] J. Chu *et al.*, Phys. Rev. B: Condens. Matter 69 (2004) 113410.

[38] R. Morel, Y. Huai, R.W. Cochrane, J. Appl. Phys. 64 (1988) 5462.

[39] Z. Altounian *et al.*, Phys. Rev. B: Condens. Matter 27 (1983) 1955.

[40] I. Bakonyi, Acta Mater. 53 (2005) 2509.

[41] C.A. Schuh, T.C. Hufnagel, U. Ramamurty, Acta Mater. 55 (2007) 4067.

[42] M.M. Trexler, N.N. Thadhani, Prog. Mater. Sci. 55 (2010) 759.

[43] M. Chen, Annu. Rev. Mater. Res. 38 (2008) 445.

[44] F. Spaepen, Acta Metall. 25 (1977) 407.

[45] J. Schroers *et al.*, Mater. Sci. Eng., A 449-451 (2007) 898.

[46] A.S. Argon, Acta Metall. 27 (1979) 47.

[47] M.L. Falk, J.S. Langer, Phys. Rev. E 70 (2004) 011507.

[48] F. Shimizu, S. Ogata, J. Li, Acta Mater. 54 (2006) 4293.

[49] Z.F. Zhang, J. Eckert, L. Schultz, Acta Mater. 51 (2003) 1167.

[50] J.J. Lewandowski, A.L. Greer, Nature Mater. 5 (2006) 15.

[51] Y. Zhang, A.L. Greer, Appl. Phys. Lett. 89 (2006) 071907.

[52] D.T.A. Matthews *et al.*, Acta Mater. 56 (2008) 1762.

[53] J. Das *et al.*, Phys. Rev. Lett. 94 (2005) 205501.

[54] J. Xu, E. Ma, J. Mater. Res. 29 (2014) 1489.

[55] D. Pan *et al.*, Proc. Natl. Acad. Sci. U.S.A. 105 (2008) 14769.

[56] Z.F. Zhang *et al.*, Philos. Mag. Lett. 85 (2005) 513.

[57] Y. Yang, C.T. Liu, J. Mater. Sci. 47 (2011) 55.

[58] Z. Han *et al.*, Acta Mater. 57 (2009) 1367.

[59] J.J. Lewandowski, W.H. Wang, A.L. Greer, Philos. Mag. Lett. 85 (2005) 77.

[60] P. Murali *et al.*, Phys. Rev. Lett. 107 (2011) 215501.

[61] W.H. Wang, Prog. Mater. Sci. 57 (2012) 487.

[62] S.V. Madge *et al.*, Acta Mater. 60 (2012) 4800.

[63] J.D. Plummer, I. Todd, Appl. Phys. Lett. 98 (2011) 021907.

[64] S.J. Bull, J. Phys. D: Appl. Phys. 38 (2005) R393.

[65] W.C. Oliver, G.M. Pharr, J. Mater. Res. 19 (2003) 3.

[66] T. Burgess, M. Ferry, Mater. Today 12 (2009) 24.

[67] C.A. Schuh, T.G. Nieh, Acta Mater. 51 (2003) 87.

[68] C.A. Schuh *et al.*, Philos. Mag. 83 (2003) 2585.

[69] A.L. Greer *et al.*, Mater. Sci. Eng., A 375-377 (2004) 1182.

[70] C.A. Schuh, Mater. Today 9 (2006) 32.

[71] J.J. Pang *et al.*, Physica B 407 (2012) 340.

[72] D. Pan *et al.*, Appl. Phys. Lett. 95 (2009) 141909.

[73] H.S. Chou *et al.*, Appl. Phys. Lett. 93 (2008) 191901.

[74] Z.T. Wang, K.Y. Zeng, Y. Li, Scr. Mater. 65 (2011) 747.

[75] R. Ristić *et al.*, Croat. Chem. Acta 83 (2010) 33.

[76] R. Ristić, M. Stubičar, E. Babić, Philos. Mag. 87 (2007) 5629.

[77] N.V. Steenberge *et al.*, Scr. Mater. 56 (2007) 605.

[78] J. Fornell *et al.*, Int. J. Plast. 25 (2009) 1540.

[79] J.-i. Jang *et al.*, Scr. Mater. 64 (2011) 753.

[80] S.J. Bull, Surface and Coatings Technology 50 (1991) 25.

[81] S.J. Bull, Tribol. Int. 30 (1997) 491.

[82] V. Keryvin *et al.*, J. Phys. D: Appl. Phys. 41 (2008) 074029.

[83] F.X. Liu *et al.*, Surf. Coat. Technol. 203 (2009) 3480.

[84] P.-S. Chen *et al.*, Surface and Coatings Technology 231 (2013) 332.

[85] Y. Huang *et al.*, Intermetallics 18 (2010) 1056.

[86] X.K. Xi *et al.*, Phys. Rev. Lett. 94 (2005) 125510.

[87] V.Z. Bengus *et al.*, J. Mater. Sci. 35 (2000) 4449.

[88] C.J. Gilbert, V. Schroeder, R.O. Ritchie, Metall. Mater. Trans. A 30A (1999) 1739.

[89] C.A. Pampillo, Journal of Material Science 10 (1975) 1194.

[90] K.S. Nakayama *et al.*, Nano Lett. 8 (2007) 516.

[91] P. Tandaiya, R. Narasimhan, U. Ramamurty, Acta Mater. 61 (2013) 1558.

[92] G. Wang *et al.*, Phys. Rev. Lett. 98 (2007) 235501.

[93] M.Q. Jiang *et al.*, Scr. Mater. 62 (2010) 572.

[94] P.G. Saffman, G. Taylor, Proc. R. Soc. London 254 (1958) 312.

[95] A.S. Argon, M. Salama, Mater. Sci. Eng. 23 (1976) 219.

[96] G. Wang *et al.*, Acta Mater. 56 (2008) 5845.

[97] A.J. Cao, Y.Q. Cheng, E. Ma, Acta Mater. 57 (2009) 5146.

[98] Y.L. Z. Han, J. Mater. Res. 24 (2009) 3620.

[99] N. Bailey, J. Schiøtz, K. Jacobsen, Phys. Rev. B: Condens. Matter 73 (2006) 064108.

[100] Y.Q. Cheng, E. Ma, Acta Mater. 59 (2011) 1800.

[101] W.L. Johnson, K. Samwer, Phys. Rev. Lett. 95 (2005) 195501.

[102] C.A. Volkert, A. Donohue, F. Spaepen, J. Appl. Phys. 103 (2008) 083539.

[103] D. Tonnies, R. Maass, C.A. Volkert, Adv Mater 26 (2014) 5715.

[104] C.J. Lee, J.C. Huang, T.G. Nieh, Appl. Phys. Lett. 91 (2007) 161913.

[105] Y.H. Lai *et al.*, Scr. Mater. 58 (2008) 890.

[106] A. Dubach *et al.*, Scr. Mater. 60 (2009) 567.

[107] C.Q. Chen, Y.T. Pei, J.T.M. De Hosson, Acta Mater. 58 (2010) 189.

[108] O.V. Kuzmin *et al.*, Acta Mater. 60 (2012) 889.

[109] C.Q. Chen *et al.*, Phys. Rev. B: Condens. Matter 83 (2011) 180201(R).

[110] D. Jang, J.R. Greer, Nature Mater. 9 (2010) 215.

[111] X.W. Gu *et al.*, Nano letters 14 (2014) 5858.

[112] Q.K. Jiang *et al.*, Acta Mater. 61 (2013) 4689.

[113] Q.K. Jiang *et al.*, Scientific reports 2 (2012) 852.

[114] L. Tian *et al.*, Nat. Commun. 3:609 (2012) 1.

[115] L. Tian, Z.-W. Shan, E. Ma, Acta Mater. 61 (2013) 4823.

[116] H. Guo *et al.*, Nat Mater 6 (2007) 735.

[117] Q. Deng *et al.*, Acta Mater. 59 (2011) 6511.

[118] Y.H. Liu *et al.*, J. Appl. Phys. 112 (2012) 063504.

[119] F.F. Wu, Z.F. Zhang, S.X. Mao, Acta Mater. 57 (2009) 257.

[120] Y.D. Dong, G. Gregan, M.G. Scott, J. Non-Cryst. Solids 43 (1981) 403.

[121] A.I. Zaitsev *et al.*, Phys. Chem. Chem. Phys. 4 (2002) 6047.

[122] P. Nash, C.S. Jayanth, Bull. Alloy Phase Diagr. 5 (1984) 144.

[123] H. Turnow *et al.*, Thin Solid Films 561 (2014) 48.

[124] X.J. Liu *et al.*, Phys. Lett. A 373 (2009) 2488.

[125] T. Fukunaga *et al.*, Intermetallics 14 (2006) 893.

[126] L. Yang *et al.*, J. Appl. Phys. 102 (2007).

[127] A. Hirata *et al.*, Nature Mater. 10 (2010) 28.

[128] A. Volland, PhD theisis, Etudes des effets d'echelle sur le comportement mécanique de films minces en verre métallique, Institut National Polytechnique de Grenoble (2012)

[129] T. Burakowski, T. Wierzchon, Surface Engineering of Metals: Principles, Equipment, Technologies, CRC Press, 1998.

[130] S. Franssila, Introduction to Microfabrication, John Wiley & Sons Ltd, 2010.

[131] C. Cavallotti *et al.*, Cryst. Res. Technol. 40 (2005) 958.

[132] J.A. Thornton, J. Vac. Sci. Technol. A4(6) (1986) 3059.

[133] http://www.iap.tuwien.ac.at/www/surface/sputteryield

[134] M. Ghidelli *et al.*, J. Alloys Compd. 615 (2014) S348.

[135] M. Ghidelli *et al.*, J. Alloys Compd. 615 (2014) S90.

[136] M. Ghidelli *et al.*, Acta Mater. 90 (2015) 232.

[137] G. Signoriello *et al.*, in: 7th. Int. Conf: on Thermal, Mechanical and Multiphysics Simulation and Experiments in Micro-Electronics and Micro-Systems, IEEE, 2006.

[138] P. Djemia *et al.*, J. Appl. Phys. 90 (2001) 756.

[139] P. Djemia *et al.*, Solid State Commun. 106 (1998) 459.

[140] A. Kueny, M. Grimsditch, Phys. Rev. B: Condens. Matter 26 (1982) 4699.

[141] J. Goupy *et al.*, Surface and Coatings Technology 237 (2013) 196.

[142] M. Ghidelli *et al.*, Scr. Mater. 89 (2014) 9.

[143] A. Boé *et al.*, Thin Solid Films 518 (2009) 260.

[144] M. Coulombier *et al.*, The Review of scientific instruments 83 (2012) 105004.

[145] T. Pardoen *et al.*, Mater. Sci. Forum 633-634 (2010) 615.

[146] M. Coulombier, PhD thesis, Nanomechanical lab on-chip for testing thin film materials and application to Al and Al(Si), Université catholique de Louvain (2012)

[147] D. Ma, A.D. Stoica, X.L. Wang, Nature Mater. 8 (2009) 30.

[148] Y. Waseda, M. Ohtani, Z. Phys. B: Condens. Matter 21 (1975) 229.

[149] J. Hay, B. Crawford, J. Mater. Res. 26 (2011) 727.

[150] J. Hay, J. Mater. Res. 24 (2009) 667.

[151] X.X. Xia, W.H. Wang, Small 8 (2012) 1197.

[152] F. Jiang *et al.*, Acta Mater. 59 (2011) 2057.

[153] G.P. Zhang, Y. Liu, B. Zhang, Scr. Mater. 54 (2006) 897.

[154] T. Pardoen *et al.*, J. Mech. Phys. Solids 52 (2004) 423.

Abstract

Bulk metallic glasses are known for their superior strength performances with respect to crystalline counterparts, but also for a macroscopically brittle behaviour. Nevertheless, mechanical *size effects* have surprisingly been reported when reducing the specimen dimensions. In order to study such effects, the mechanical properties of thin $Zr_{65}Ni_{35}$ metallic glass films – deposited by DC magnetron sputtering – have been investigated for thickness ranging from 200 up to 900 nm. The mechanical behavior was studied for films deposited on Si substrate and for freestanding films as well. $Zr_{65}Ni_{35}$ films exhibit the same atomic structure as indicated by the absence of shift of diffraction peaks and by the constant values of the mass density, elastic properties, and activation volume. However, the cracking mechanisms of the film on the substrate are thickness dependent, resulting from a thickness confinement effect on the development of the plastic zone. The mechanical properties of freestanding films were investigated using an original technique of micro-tension controlled by internal stresses. Homogeneous plastic strains (up to 10 %) combined with very high stresses (up to 3500 MPa) were attained. The specimen cross-sectional area was the key parameter affecting the probability to get percolation of defects involved in the plastic deformation as confirmed by the constant value of the activation volume estimated analyzing stress relaxation phenomena. The effect of the composition on the mechanical properties has been investigated as well and, in this case, the changes in mechanical behavior were preferentially attributed to modifications of the metallic glass atomic structure.

Keywords: Metallic glasses; Thin films; Size effects; Mechanical properties.

Résumé

Les verres métalliques massifs sont connus pour leurs propriétés de résistance mécanique supérieures par rapport aux matériaux cristallins, mais aussi par une fragilité macroscopique. Cependant, des effets d'échelle sur le comportement mécanique ont été parfois reportés de manière inattendue lors de la réduction des tailles des échantillons. Afin d'étudier de tels effets, on s'est intéressé aux propriétés mécaniques de films minces en verre métallique de composition $Zr_{65}Ni_{35}$ et d'épaisseurs entre 200 et 900 nm ; les films étant obtenus par pulvérisation cathodique. Le comportement mécanique de ces films a été étudié à la fois sur substrat Si et sur des films libres. On montre que les films avec composition $Zr_{65}Ni_{35}$ ont la même structure atomique comme indiqué par l'absence de décalage des pics de diffraction et par des valeurs constantes de la densité, des propriétés élastiques, et du volume d'activation. Cependant, les mécanismes de fissuration varient avec l'épaisseur du film sur substrat, mais que cette variation résulte essentiellement d'un effet de confinement de l'épaisseur sur le développement de la zone plastique. Les propriétés mécaniques des films libres ont été étudiées en utilisant notamment une technique originale de micro-traction actionnée par contrainte interne. Dans ces conditions, des déformations plastiques importantes (jusqu'à 10%) combinées à des niveaux de contraintes élevés (jusqu'à 3500 MPa) ont pu être obtenues et on a montré qu'un paramètre important dans le contrôle des propriétés était l'aire de la section du film pouvant influencer la capacité d'obtention d'une percolation des défauts mis en jeu lors de la déformation plastique. Cela a été confirmé par des valeurs constantes du volume d'activation, estimé en étudiant les phénomènes de relaxation de la contrainte. L'effet de la composition du film sur les propriétés mécaniques a également été analysé et, dans ce cas, les variations de comportement mécanique ont été reliées à des modifications de la structure atomique du verre métallique.

Mots Clés: Verres métalliques; Films minces; Effets d'échelle; Propriétés mécaniques.